CHALMERS
UNIVERSITY OF TECHNOLOGY

Technologies for Ice Protection of Aircraft Air Intakes

Development of an Electric Propulsion Motor Cooling Inlet Ice Protection System using CFD, Droplet Impingement and Thermal Modelling

Master's thesis in Mobility Engineering

HALIME SELIMOGLU
TOMÁS VASCONCELOS

DEPARTMENT OF MECHANICS AND MARITIME SCIENCES
CHALMERS UNIVERSITY OF TECHNOLOGY
Gothenburg, Sweden 2024
www.chalmers.se

Master's thesis 2024

Technologies for Ice Protection of Aircraft Air Intakes

Development of an Electric Propulsion Motor Cooling Inlet Ice Protection System using CFD, Droplet Impingement and Thermal Modelling

HALIME SELIMOGLU
TOMÁS VASCONCELOS

CHALMERS
UNIVERSITY OF TECHNOLOGY

Department of Mechanics and Maritime Sciences
Division of Fluid Dynamics
Chalmers University of Technology
Gothenburg, Sweden 2024

Technologies for Ice Protection of Aircraft Air Intakes
Development of an Electric Propulsion Motor Cooling Inlet Ice Protection System using CFD, Droplet Impingement and Thermal Modelling
HALIME SELIMOGLU & TOMÁS VASCONCELOS

Supervisor: Pascal Isenegger, Heart Aerospace AB
Examiner: Carlos Xisto, Department of Mechanics and Maritime Sciences

Master's Thesis 2024
Department of Fluid Mechanics
Division of Mechanics and Maritime Sciences
Chalmers University of Technology
SE-412 96 Gothenburg
Telephone +46 31 772 1000

Cover: Picture of ES30.
Typeset in LaTeX
Printed by Chalmers Reproservice
Gothenburg, Sweden 2024

Technologies for Ice Protection of Aircraft Air Intakes
Development of an Electric Propulsion Motor Cooling Inlet Ice Protection System using CFD, Droplet Impingement and Thermal Modelling
HALIME SELIMOGLU & TOMÁS VASCONCELOS
Department of Mechanics and Maritime Science
Chalmers University of Technology

Abstract

As the aviation industry works towards a global commitment to net-zero carbon emission, a growing interest occurs in electric aircraft. The airstream-facing surfaces on aircraft in operational environments are susceptible to in-flight ice accretion, which has crucial effects on aircraft performance and operational safety. An electric engine on the aircraft creates unique challenges in dealing with ice accretion since typical ice protection sources such as bleed air or exhaust gases are not output from the electric motors. The main objective of this study is to investigate ice protection technologies for electric propulsion motor air intakes to ensure safe end energy-efficient flight without any icing hazards.

A generic model of a submerged cooling air intake is designed. Unlike typical cooling air inlets, the need for an ice protection system (IPS) is demonstrated by the in-flight icing simulations carried out by FENSAP-ICE due to the novel placement under an angled nacelle. Within the icing and flight envelopes, the required power for providing anti-icing to the air intake is calculated by a Simulink model, and the computed heat is validated to confirm that it is sufficient to avoid icing.

After evaluating various concepts, it is found that utilizing residual heat from the motor/inverter cooling system provides sufficient heat for anti-icing. However, implementation across the entire lip cross-section adds more complexity in comparison to other solutions. An electro-thermal IPS is identified as the more feasible option for smaller surfaces, such as inlet lips, in terms of power consumption, system complexity, and reliability.

Keywords: anti-icing, IPS, electro-thermal, electric aircraft, cooling air intake, ice accretion, power requirements.

Acknowledgements

First and foremost, we are deeply thankful to Heart Aerospace for giving us the opportunity and resources to conduct this research. The team provided inexhaustible guidance and profound interest, which made this work possible.

We owe profound gratitude to our supervisor, Pascal Isenegger, for his continuous guidance and invaluable support. Special thanks to Luciano Martinez Stefanini for generously sharing his insightful advice with us. Their exceptional expertise and dedication have been instrumental in shaping the direction and outcome of this research. We are also deeply grateful to Alain Cuenca and Alexandre Antunes; their proficient insights contributed to the quality and scope of the work.

Moreover, we would like to express our gratitude to our examiner, Carlos Xisto. His significant feedback and valuable guidance enriched our project, and the access to Chalmers's resources and technical support he provided substantially accelerated the work. We would like to acknowledge the contributions of Professor José Chaves Pereira from Instituto Superior Técnico in Lisbon to diverse numerical modeling aspects performed throughout this work.

We also want to thank Derya Su Sahin for her technical support. It significantly contributed to improving the quality of our thesis delivery.

Halime Selimoglu & Tomás Vasconcelos, Gothenburg, June 2024

Individual Acknowledgments

I would like to extend my heartfelt thanks to my family, Selimoglu and Efendiler. Your belief and encouragement have been the greatest source of my journey toward the master's degree. To my partner, Emil Callerfjord, this work would not have been possible without your steadfast support and unwavering belief in me. Your encouragement has played a pivotal role in my motivation. To my dear friends, especially G4, Silan, Mert(s), Isil, Idil, and Elif, thank you for always being there for me.

Halime Selimoglu

This work was the culmination of a long academic phase, made possible by the unconditional support of my family. They have been the pillars along this path, offering encouragement and belief in me. Their support during challenging moments when the path forward seemed uncertain is the reason why this work was achieved. I am also grateful to the friends I have met along the way. Their encouragement and shared experiences provided invaluable support. I dedicate this work to my family and friends especially, my parents, grandparents, and godfather; as well as Carlos, Kevin, Maria, and Rocío.

Tomás Vasconcelos

List of Acronyms

Below is the list of acronyms that have been used throughout this thesis listed in alphabetical order:

AGL	Above Ground Level
AoA	Angle of Attack
CAS	Calibrated Air Speed
CFD	Computational Fluid Dynamics
CM	Continuous Maximum
EASA	European Union Aviation Safety Agency
ESDU	Engineering Sciences Data Unit
FAA	Federal Aviation Administration
FAR	Federal Aviation Regulation
FOD	Foreign Object Damage
FPD	Freezing Point Depressant
GA	General Aviation
IATA	International Air Transport Association
IM	Intermittent Maximum
IPS	Ice Protection System
ISA	International Standard Atmosphere
LWC	Liquid Water Content
MEA	More Electric Aircraft
MED	Mean Effective Drop Diameter
MVD	Median Volumetric Diameter
NACA	National Advisory Committee for Aeronautics
NASA	National Aeronautics and Space Administration
TAS	True Air Speed

Nomenclature

Below is the nomenclature of indices, sets , parameters, and variables that have been used throughout this thesis.

Indices

w	water
v	vapor
a	air
sk	skin
s	ice
fp	far upstream on flat plate extending forward of inlet entry plane
fl	flush inlet
sc	scoop inlet
f	fairing of scoop inlet
pre	pre-entry force
r	ramp of flush inlet
sp	spillage drag
c	forward suction force
int	intrinsic net thrust
ice, rec	recovery factor stagnation
∞	freestream

Parameters

a	speed of sound (m/s)
D	drag (N)
q	power density (W/m^2)

q_{conv}	convective heat loss (W/m^2)
q_{evap}	evaporative heat loss (W/m^2)
q_{KE}	kinetic heat gain (W/m^2)
q_{sens}	sensible heat loss (W/m^2)
q_{aero}	aerodynamic heat gain (W/m^2)
m_{evap}	rate of surface water evaporation (kg/m^2s)
m_{imp}	rate of water droplets impingement (kg/m^2s)
k	thermal conductivity (W/mK)
L_v	latent heat of evaporation (kJ/kgK)
M	Mach number
Nu	Nusselt number
Pr	Prandtl number
Re	Reynolds number
h	heat transfer coefficient (W/m^2K)
C_p	specific heat (W/m^2K)
ν	kinematic viscosity (m^2/s)
μ	dynamic viscosity (kg/ms)
ρ	mass density (kg/m^3)
β	collection efficiency
V	freestream velocity (m/s)
T	temperature (K)
P	static pressure (Pa)
S	surface area (m^2)
R_h	relative humidity
R_c	recovery factor
t	airfoil thickness (m)
l	characteristic length (m)
c	chord length (m)
η	efficiency
Φ	rearward component of pressure force on the outside of streamtube (N)
Ψ	momentum flow in streamtube entering inlet (N)
τ	forward component of pressure force on inside of streamtube (N)

Contents

List of Acronyms **ix**

Nomenclature **xi**

List of Figures **xvii**

List of Tables **xxiii**

1 Introduction **1**
1.1 Background . . . 1
1.1.1 Aircraft icing . . . 5
1.2 Objective . . . 6
1.3 Scope . . . 7

2 Theory **9**
2.1 Aircraft Icing . . . 9
2.1.1 Flight in icing . . . 9
2.1.1.1 The icing atmosphere . . . 9
2.1.1.1.1 Cloud liquid water content . . . 9
2.1.1.1.2 Cloud types . . . 10
2.1.1.1.3 Variations with altitude . . . 11
2.1.1.1.4 Cloud droplet size distribution . . . 13
2.1.1.2 Physics of ice accretion . . . 14
2.1.1.2.1 Types of ice accretion . . . 14
2.1.1.2.2 Droplet impingement . . . 16
2.1.1.2.3 Heat balance in icing conditions . . . 20
2.1.1.3 Atmospheric design criteria . . . 24
2.2 Ice Accretion Modeling in Aerospace . . . 26
2.2.1 Aerodynamic flow solution . . . 28
2.2.2 Droplet impingement . . . 29
2.2.3 Ice accretion . . . 30
2.2.4 Blade Element Method . . . 32
2.3 Auxiliary Air Inlet Design . . . 35
2.3.1 Flush inlets . . . 35
2.3.1.1 Pressure recovery . . . 37
2.3.1.2 Comparison of ramp planform effect . . . 37
2.3.1.2.1 Operating at full mass flow . . . 37

2.3.1.2.2 Operating at maximum efficiency 37

3 Methods **39**
3.1 Concept Generation 40
3.2 Concept Selection 41
3.3 Concept Development 43
3.3.1 CFD Model 44
3.3.1.1 Geometry & domain 45
3.3.1.2 Mesh generation 48
3.3.1.3 Setup 49
3.3.1.4 Output 54
3.3.1.5 Mesh dependency study 55
3.3.1.6 Validation 60
3.3.2 Simulink model 66
3.3.2.1 Power computations 66
3.3.2.2 Computational model validation 68
3.3.2.2.1 Validation results 68
3.3.2.2.2 Evaporation term investigation 70
3.3.2.2.3 Aerodynamic heating term effect 71
3.3.2.3 IPS architectures 72
3.3.2.3.1 Electro-thermal IPS 73
3.3.2.3.2 Water-heated IPS 75

4 Results **77**
4.1 Concept Generation 77
4.1.1 Existing concepts 77
4.1.1.1 Pneumatic boot de-icing systems 77
4.1.1.2 Electro-thermal systems 78
4.1.1.3 Fluid ice protection systems 81
4.1.1.4 Electro-impulse de-icing systems 82
4.1.1.5 Hot air systems 84
4.1.1.6 Hybrid systems 86
4.1.1.7 Common usages of IPS 87
4.1.2 New concepts 87
4.2 Concept Selection 89
4.3 Concept Development 91
4.3.1 Critical icing conditions 91
4.3.2 Intake design 91
4.3.3 Ice accumulation on unheated inlet 93
4.3.4 Power requirements 101
4.3.5 Validation with simulations 106
4.3.6 IPS results 108
4.3.6.1 Electro-thermal IPS 108
4.3.6.2 Water-heated IPS 112
4.3.6.2.1 Liquid properties 112
4.3.6.2.2 Pipe configurations 113
4.3.7 IPS Selection 118

5 Conclusion **123**
5.1 Research Output 123
5.2 Future Development 124

Bibliography **125**

A Droplet impingement physics **I**
A.1 Droplet trajectory equation I
A.2 Modified droplet inertia parameter II

B Simulation conditions **VII**

C 3D surfaces **XI**

D Ice accretion results **XV**

List of Figures

1.1 Aviation's share of global CO_2 emissions from 1940 to 2021 [3]. 2
1.2 The progress towards the goal on fuel efficiency [4]. 2
1.3 Carbon emissions from aviation in the EU without any action and emissions-reduction goals set by the industry [4]. 3
1.4 Penetration of electrical systems by aircraft type [6]. 4
1.5 Electrical propulsion architectures [6] 4
1.6 Aircraft accidents involving icing [68] 5
1.7 Icing Research Tunnel, NASA Glenn Research Center [12]. 6
1.8 Electric propulsion cooling air inlet example (Heart Aerospace). . . . 7

2.1 Ice buildup in different liquid water content over an airfoil [22]. LWC = 0.30 g/m^3 and LWC = 1.14 g/m^3, respectively. 10
2.2 Stratiform (layer) clouds [16]. 10
2.3 Cumuliform (vertical) clouds [17]. 11
2.4 Cumulative variation with altitude for supercooled LWC from all cloud types [18]. 12
2.5 Altitude variation of horizontal extent of extended icing encounters in (a) layer (b) convective clouds [18]. 12
2.6 Frequency distribution of icing observations for various increments of temperature and pressure altitude [19]. a) Stratiform clouds, b) Cumuliform clouds. 13
2.7 Glaze or clean ice [27] 15
2.8 Rime ice [27]. 15
2.9 Mixed ice [28]. 15
2.10 The aerodynamic characteristics of the NACA 23012 airfoil under different ice shapes: lift coefficient (left) and drag coefficient (right) [29]. 16
2.11 Droplet impingement parameters [20]. 17
2.12 Droplet impingement parameters [20]. 18
2.13 Local impingement efficiency curve [20]. 18
2.14 Maximum local impingement efficiencies at the stagnation line, $\alpha = 0$ [31]. 19
2.15 Water catch efficiencies for various airfoils and geometric shapes [31]. 19
2.16 Local impingement efficiencies at different (a) chord length, (b) MVD [32]. 20

2.17 Local impingement efficiencies (continued) at different (c) freestream airspeed, (d) angle of attack [32]. 20
2.18 Aircraft total catch typical from 6 to 16% thick airfoils at $\alpha = 4$ degrees, with 20 μm MVD droplets. (all altitudes: strictly true for 10,000 ft and within 10% error between sea level and 20,000 ft [31]). . 22
2.19 Liquid water content factor vs median volumetric diameter [24]. . . . 25
2.20 Ambient temperature vs pressure altitude [24]. 25
2.21 Liquid water content factor vs cloud horizontal extent [24]. 26
2.22 Water film model. 31
2.23 Particle trajectory across a propeller disk [71]. 33
2.24 Force balance diagram on the blade section [71]. 33
2.25 Flush inlets [15]. 35
2.26 Rectangular ramp inlet on a 787 Dreamliner [64] 36
2.27 NACA curved-divergent ramp inlet on a 737 [63] 36
2.28 Flush inlet geometry parameters [15]. 36

3.1 Diagram of the methodology of the research. 39
3.2 The five-step concept generation method [59], page 120. 40
3.3 Concept evaluation ending with the concept selection [59], page 148. . 41
3.4 Concept evaluation process by Ulrich et. al. [59], page 149-150. . . . 42
3.5 Significant engine inlet ice protection selection considerations [49]. . . 42
3.6 Flow chart of the icing computations. 44
3.7 Initial geometry. 45
3.8 Shaft-like geometry to allow actuator disk modeling. 45
3.9 Domain size used for initial 2D simulation. 45
3.10 Lip geometry [65]. 46
3.11 Vortex development near the side walls of a divergent ramp NACA duct [72]. 46
3.12 Nacelle bottom view. 47
3.13 Nacelle side view. 47
3.14 Nacelle domain limits. 48
3.15 Mesh. 48
3.16 ES-30 flight envelope and icing envelopes. 51
3.17 Residuals convergence for 140 knots (KCAS) at 5000 feet. 52
3.18 Lip surface. 53
3.19 Heat transfer coefficient map using wall functions. 54
3.20 Impingement rate (m_{imp}) output from ICE3D (glaze ice) for test case 1. 55
3.21 Ice cover aft of the lip for 5000 feet, $M = 0.23$, $T_s = 270.15\ K$, $LWC = 0.574\ g/m^3$, $MVD = 20\ \mu m$. 55
3.22 Heat transfer coefficient contours on lip surface. 56
3.23 Velocity magnitude contours along the cross-section of the nacelle. . . 57
3.24 Heat transfer coefficient changes across mesh numbers. 58
3.25 Mass flow ratio across mesh refinements 59
3.26 Ram pressure recovery across mesh refinements 59
3.27 y^+ change across mesh numbers 60

3.28 NACA0012 leading edge heated zones [42]. 61
3.29 Predicted collection efficiency [42]. 62
3.30 Heat transfer coefficient distribution [42]. 62
3.31 Coarsest and finest meshes used for 2D validation 63
3.32 Film thickness distribution. 64
3.33 Pressure distribution convergence with mesh refinement 65
3.34 Flow chart for power calculations. 67
3.35 Energy balance terms validation at $T_{tot} = -20°F$ 68
3.36 Energy balance terms validation at $T_{tot} = -20°F$ in percentage of total heat required 69
3.37 Energy balance terms validation at $T_{tot} = 22°F$ 69
3.38 Energy balance terms validation at $T_{tot} = 22°F$ in percentage of total heat required 70
3.39 Energy balance terms validation at $T_{tot} = -20°F$ with different evaporation formulations. 71
3.40 Energy balance terms validation including aerodynamic term at $T_{tot} = -20°F$ 72
3.41 Varying power calculations for IPS architectures. 73
3.42 Electro-thermal IPS architecture. 74
3.43 Water-heated IPS architecture. 75

4.1 Cross-section of a pneumatic de-icing boot uninflated and inflated [40]. 77
4.2 Pneumatic deicing system for a twin-engine GA aircraft with reciprocating engines [40]. 78
4.3 Leading edge heater mat layout [41]. 79
4.4 Material and structure of ice protection area [57]. 79
4.5 Chordwise layout of the heaters [44]. 80
4.6 Illustration of TKS systems on the leading edge of the wing [45]. . . . 81
4.7 Fluid de-icing system [40]. 81
4.8 Basic circuit of electro-impulse systems [47]. 82
4.9 Electro-impulse de-icing system [48]. 83
4.10 Electro-impulse system layout [49]. 83
4.11 Hot-air de-icing system on the leading edge [40]. 84
4.12 Engine inlet bleed air ice protection system [50]. 85
4.13 Engine inlet hot air anti-icing capabilities during descent power at 15,000 ft altitude [50]. 85
4.14 Hybrid system of electro-impulse and electro-thermal ice protection systems [51]. 86
4.15 Hybrid system of hot-air and pneumatic ice protection systems [40]. . 86
4.16 First concept using waste heat. 88
4.17 Second concept using waste heat. 88
4.18 Third concept using waste heat. 89
4.19 Ice shapes at the different conditions and altitudes described in table B.4 94
4.20 Ice accretion on lip surface for test case 1 ($M = 0.23$, $T_s = 270.15\ K$, $LWC = 0.574\ g/m^3$, $MVD = 20$) 94

4.21 Collection efficiency variation with altitude and MVD for respectively test cases 1, 7, 8, 37 and 38 defined in table B.4 95
4.22 Velocity magnitude vectors for 0° of AoA. 95
4.23 Heat transfer coefficient variation along the lip surface for test cases 1, 13 and 37 defined in table B.4. 96
4.24 Water catch rate comparison between different altitudes for test cases 1, 13 and 37 defined in table B.4 97
4.25 Water catch rate variation with temperature for respectively test cases 1, 3 and 5 defined in table B.4 97
4.26 Ice thickness variation with CM/IM and MVD for respectively test cases 1, 2, 7, 8 in table B.4 98
4.27 Ice thickness variation with MVD for respectively test cases 1, 2, 13, 14, 37 and 38 defined in table B.4 98
4.28 Collection efficiency variation with inflow angle of attack ($M = 0.23$, $T_s = 270.15\ K$, $LWC = 0.574\ g/m^3$, $MVD = 20$) 99
4.29 Velocity magnitude vectors for 30° of AoA. 99
4.30 Ice accretion in 6 minutes for test case 1 ($M = 0.23$, $T_s = 270.15\ K$, $LWC = 0.574\ g/m^3$, $MVD = 20$) 100
4.31 Total power required for various altitudes in CM/IM while MVD = 20 μm. 101
4.32 Total power required for various altitudes in CM/IM while MVD = 40 μm. 102
4.33 Sensible heat flux vs ambient temperature in CM/IM while MVD = 20 μm. 103
4.34 Sensible heat flux vs ambient temperature in CM/IM while MVD = 40 μm. 103
4.35 Impingement rate, in CM/IM, MVD = 20 μm. 104
4.36 Parameters affecting impingement rate, in CM/IM, MVD = 20 μm. . 105
4.37 Energy balance terms at various temperatures and altitudes for CM, MVD = 20 μm. 105
4.38 Energy balance terms at various MVD and icing conditions. 106
4.39 Ice cover heated surface for test case 1 in table B.4 107
4.40 Ice cover heated surface for test case 7 in table B.4 107
4.41 Surface temperature distribution for test cases 1, 14, and 16 described in table B.4. 107
4.42 Ice thickness comparison with the heater on or off for test case 1 ($M = 0.23$, $T_s = 270.15\ K$, $LWC = 0.574\ g/m^3$, $MVD = 20$). 108
4.43 Electro-thermal IPS system implementation. 109
4.44 Effects of ambient temperature and heat required on thermal efficiency in electro-thermal IPS. 110
4.45 MVD and CM/IM effect on thermal efficiency in electro-thermal IPS. 110
4.46 Converged temperatures of heater layers at 10000 ft, -21.9°C, in IM, MVD = 20 111
4.47 Ethylene glycol-water mixture (60:40) properties [69]. 113
4.48 Circular pipe implementation on inlet lip. 113

4.49 Water mass flow effect on lip temperature and temperature drop in the pipe for the circular pipe. . . . 115
4.50 Effect of water temperature on lip temperature with different water flows for the circular pipe. . . . 115
4.51 C pipe implementation on inlet lip. . . . 116
4.52 Water mass flow effect on lip temperature and temperature drop in the pipe for the C pipe. . . . 117
4.53 Temperature drop in the pipe on lip temperature with different water flows for the C pipe. . . . 117
4.54 Effect of water temperature on lip temperature with different water flows for the C pipe. . . . 118
4.55 System components of water-heated IPS. . . . 119
4.56 Moody's diagram. . . . 120

A.1 Drag coefficient vs Reynolds number for a sphere [21]. . . . II
A.2 Droplet range ratio as a function of droplet Reynolds number [26]. . . . III
A.3 Comparison of droplet trajectories with respect to modified inertia parameter [20]. . . . IV
A.4 K_0 based on MVD for several chord sizes [20]. . . . V

C.1 Final nacelle design. . . . XI
C.2 Inlet view. . . . XII
C.3 Domain boundary conditions. . . . XII
C.4 Nacelle refinement zone near the inlet entry through the duct and exit. . . . XIII

D.1 Total pressure evolution across the duct for different conditions. . . . XV
D.2 Ice shapes at the different conditions and altitudes described in table B.4 . . . XVI
D.3 Heated surface ice accretion in 6 minutes for different test points. . . . XVII
D.4 Heat transfer coefficient contours on lip surface. . . . XVIII
D.5 Velocity magnitude contours along the cross-section of the nacelle. . . . XIX
D.6 Velocity magnitude change with AoA. . . . XX

List of Tables

2.1 Langmuir droplet size distribution [23]. . . . 14
2.2 Ice analysis codes and their main characteristics 28
2.3 Ramp coordinates for NACA curved-divergent planform [15]. . . . 36

3.1 Literature research map 41
3.2 Used mesh parameters. . . . 49
3.3 Used boundary conditions. . . . 50
3.4 Spatial discretization used across flow solutions. . . . 52
3.5 Model parameters used on DROP3D. . . . 53
3.6 Model parameters used on ICE3D. . . . 53
3.7 Mesh parameters for different regions. . . . 58
3.8 Heater zone discretization. . . . 62
3.9 Mesh refinement parameters. . . . 63
3.10 Spatial discretization 64
3.11 Validation inputs. . . . 68

4.1 Leading edge heater material properties [42]. . . . 80
4.2 Usages of ice protection systems. . . . 87
4.3 Inlet and lip focused common usage of existing IPS methods. . . . 87
4.4 Investigation of existing concepts for the air inlets of ES-30. . . . 90
4.5 Qualitative selection matrix. . . . 90
4.6 Simulation conditions. . . . 91
4.7 Inlet parameters. . . . 93
4.8 Outputs from flow solutions for CM and IM. . . . 101
4.9 Analyzed test conditions. . . . 106
4.10 Circular pipe properties. . . . 114
4.11 C pipe properties. . . . 116
4.12 Comparison of IPS architectures. . . . 121

A.1 Characteristic lengths for several bodies for calculation K_0 [20]. . . . IV

B.1 Coordinates of stations on x and y axes [65]. . . . VII
B.2 Experimental icing conditions from [42]. . . . VII
B.3 Thermal setup for icing condition evaluation [42]. . . . VIII
B.4 Test conditions. . . . X

1
Introduction

The airstream-facing surfaces on aircraft in operational environments are susceptible to in-flight ice accretion. This formation of ice has crucial effects on aircraft performance and operational safety. Icing encounters during flight can change the airfoil shape and disrupt the airflow, resulting in degrading maneuverability and stability and increasing drag. Of equal importance is protection against ice that accumulates on air intakes, which is vital for the proper operation of the engines and thermal management systems. The blockage of the intakes, potential ice shedding, or ingestion of ice cause hazardous risks of malfunction of onboard systems. As it is impractical for an aircraft to fly avoiding the icing conditions, aircraft icing has been a subject of study for many years [1].

As the aviation industry works towards a global commitment of having a net-zero carbon emission by 2050 [2], a growing interest occurs in electric aircraft. ES-30 is a hybrid-electric commercial aircraft that Heart Aerospace is building towards this sustainable aviation goal. Having an electric engine on the aircraft creates unique challenges in dealing with ice accretion. This collaborated research will investigate new ice protection methods and system configurations for the electric propulsion motor air intakes, based on a hybrid electric aircraft platform. This chapter will present the background, objective, and scope that will be addressed in this thesis work.

1.1 Background

Aviation has been the focus of society due to its high carbon emissions by increasing demand for air travel. Not only does aviation have a large negative effect on climate change through carbon emissions, but this amount is also increasing every year, as seen from the figure 1.1 [3]. This contribution to the global climate crisis has been observed especially during COVID-19 when air travel stopped for a while.

To address this problem, the International Air Travel Association (IATA) has set a list of goals with all the stakeholders in the aviation industry [2] in 2008:

- improving fuel efficiency by 1.5% per annum between 2005 and 2020,
- reaching a cap on net aviation emissions as carbon neutral growth from 2020,
- reducing net global carbon emissions by 50% by the year 2050 relative to 2005.

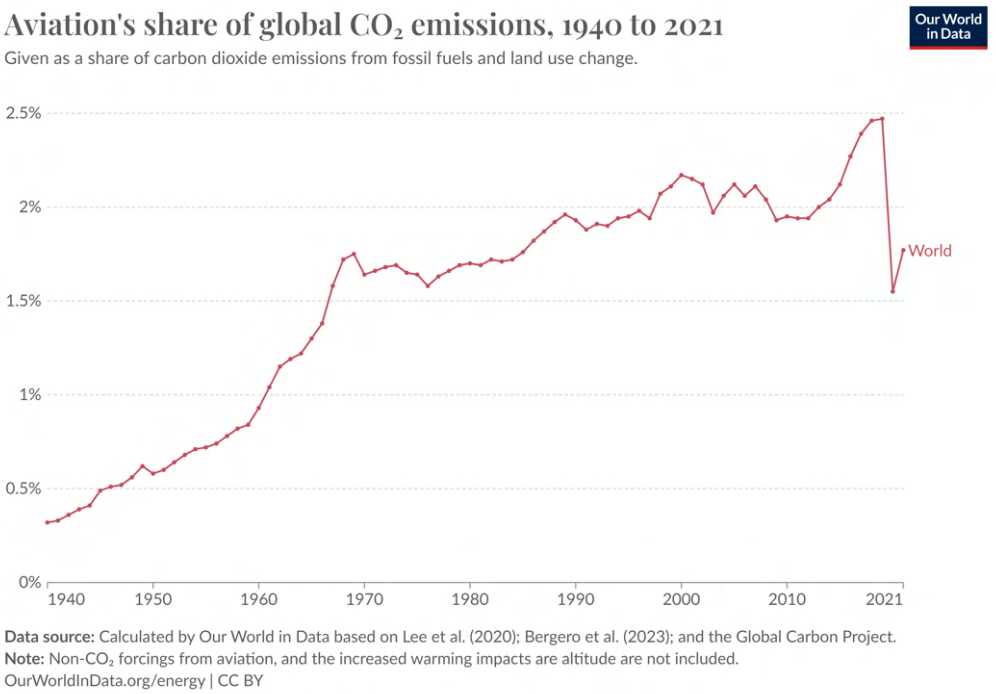

Figure 1.1: Aviation's share of global CO_2 emissions from 1940 to 2021 [3].

Figure 1.2 provides an overview of the progress towards the goal of fuel efficiency with an average improvement of 2.0% per year during 2009-2019 compared to a goal of 1.5% [4].

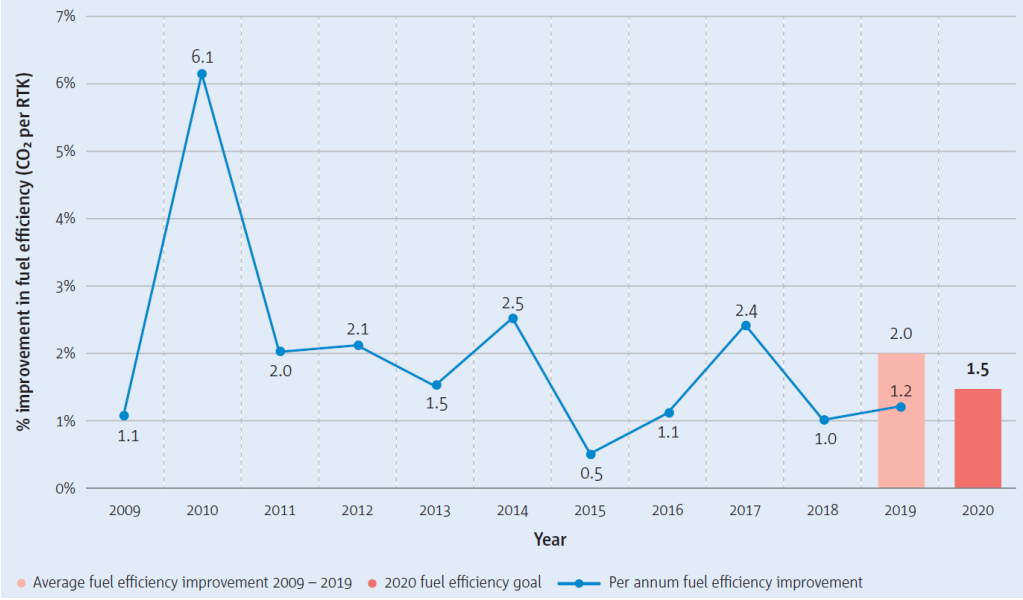

Figure 1.2: The progress towards the goal on fuel efficiency [4].

In 2021, five European associations published a Destination 2050 report [5] outlining a roadmap for the aviation sector. This agreement with the regulators has committed to the following:

- Assessing the feasibility of making 2019 the peak year for absolute CO2 emissions from flights within and departing from the EU.
- Reducing net CO2 emissions from all flights within and departing from the EU by 45% in 2030 compared to the hypothetical reference scenario.
- Reaching net zero CO2 emissions by 2050 from all flights within and departing from the EU.

According to the prediction of the industry, if no action is taken, the amount of carbon emissions will drastically scale up, as shown in figure 1.3 [4]. In the case of acting with known technology, operations, and infrastructure, this amount still ends up contributing significantly to overall global carbon emissions. The only solution to reach this goal is to develop new-generation technologies, including biofuels.

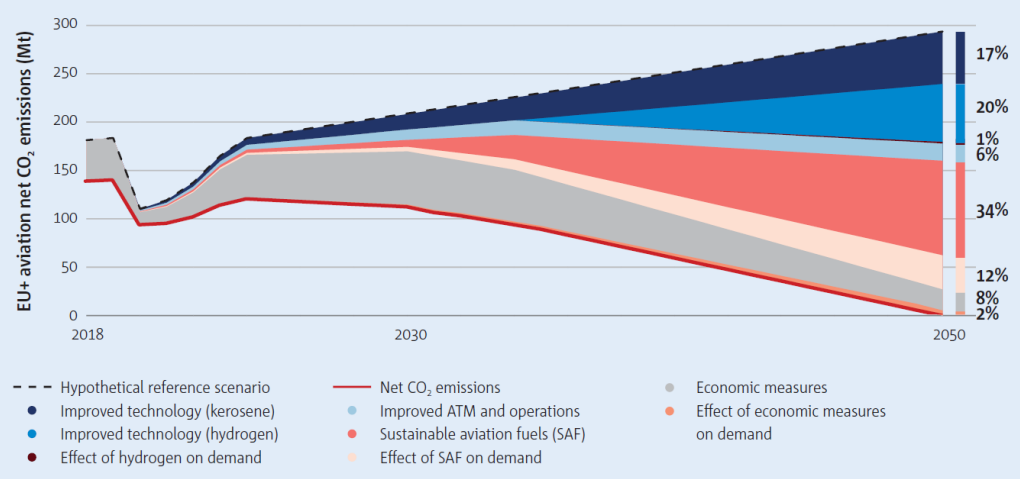

Figure 1.3: Carbon emissions from aviation in the EU without any action and emissions-reduction goals set by the industry [4].

In these conditions where new-generation technology needs are perceptibly clear, electrification in aviation evolved to become a strong option for the carbon-neutral goal. This change has manifested itself in two different paths. One of them is the More Electric Aircraft (MEA) concept, where electric equipment is installed successfully instead of a pneumatic, mechanical, or hydraulic system one by one [6]. The other method is Electric Propulsion, a revolutionary concept that recently gained publicity. Meanwhile, MEA can improve emissions to an extent, and electric propulsion can change aircraft architectures radically.

There are several reasons for evolving the More Electric Aircraft trend. While the hydraulic systems are robust and powerful enough to provide large forces, they have drawbacks from a maintenance cost perspective. Pneumatic systems are also not as efficient and have complicated systems as hydraulics. Another possible issue is the effect, identification, and resolution of leakages. It is complex and time-consuming to repair even if they are found. On the other hand, electrical systems are relatively flexible, light, and highly efficient. It can be said that a high level of electrification was applied in the first Boeing 737 flight in 1967 when cabin equipment and avionics

were designed by electrical systems. Another significant case is "Fly by Wire" (FBW) by Airbus A320, followed by Boeing 777 in 1994. FBW reduced the weight and created space by eliminating the mechanical connections and providing electrical transmission. Finally, the 787 was the first Large Commercial Aircraft to install an environmental control system, brakes, and a de-icing system powered electrically.

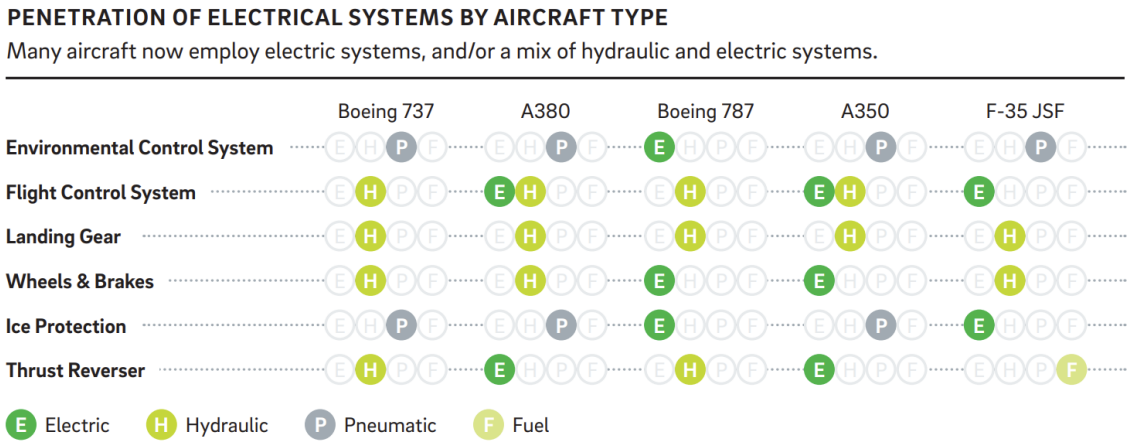

Figure 1.4: Penetration of electrical systems by aircraft type [6].

As a result of the advantages of electrification in aircraft systems in terms of less weight, higher reliability, lower maintenance costs, and higher efficiency, the MEA trend is expected to be implemented more day by day.

Electric Propulsion requires more radical changes than MEA. Three different architectures exist to provide electrical power, as shown in the figure 1.5 [6].

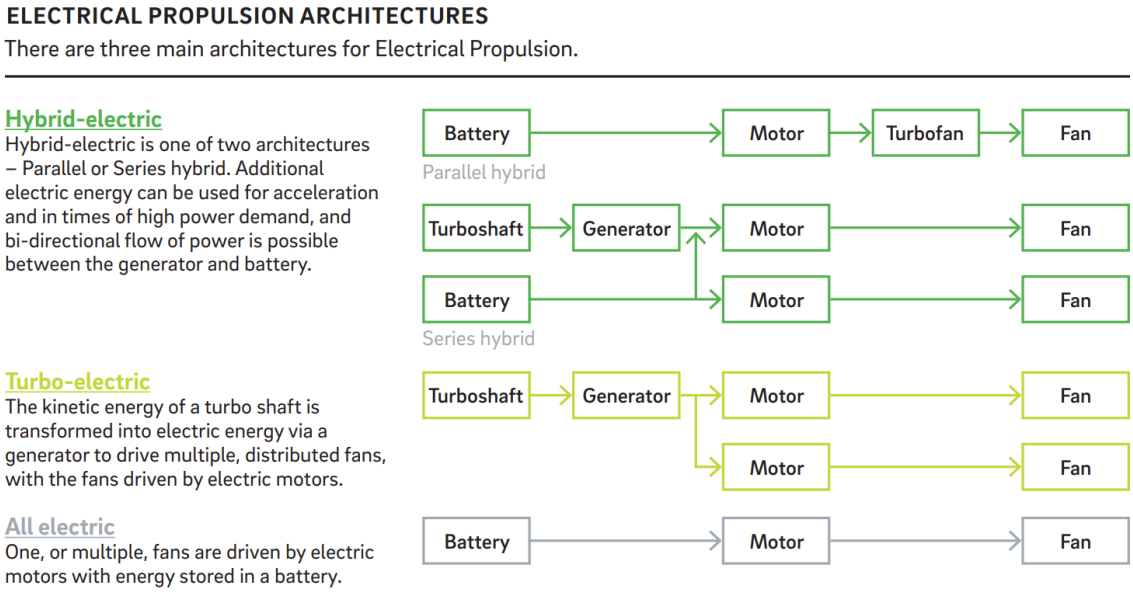

Figure 1.5: Electrical propulsion architectures [6]

Hybrid-electric can have either parallel or series hybrid configurations. This architecture operates a gas turbine engine where battery capacities are inadequate in

specific parts of the flight envelope. Hybrid-electric aircraft use electric motors either additionally in high thrust sections to contribute to thrust, such as takeoff or climb, or when the thrust is not that critical, such as cruise. The second configuration is a turbo-electric architecture where the electrical energy is transformed from a turboshaft and given to the electric motor-driven fans. The third configuration is to have purely electrical energy onboard. In this case, the range is apparently limited by the batteries' sizes and capacities. Heart Aerospace's ES-30 has a hybrid-electric configuration where the range allows it to complete a regional transport mission with gas engines and electric motors.

1.1.1 Aircraft icing

There are challenges in switching from an air-breathing engine to an electric powertrain. Air-breathing engines are a great source of hot bleed air, usually used to avoid icing on the airframe, especially on the inlets. The ES-30 has small turboprop engines mounted outboard on the wing, while inboard will be a pair of large electric motors [7]. Electric motors on the wing require different ice protection due to a lack of bleed air to protect the air inlets from icing since icing phenomena lead to 12% of total weather accidents as shown in figure 1.6. As power is the main concern in a hybrid-electric concept, efficient and feasible technologies are investigated in this research.

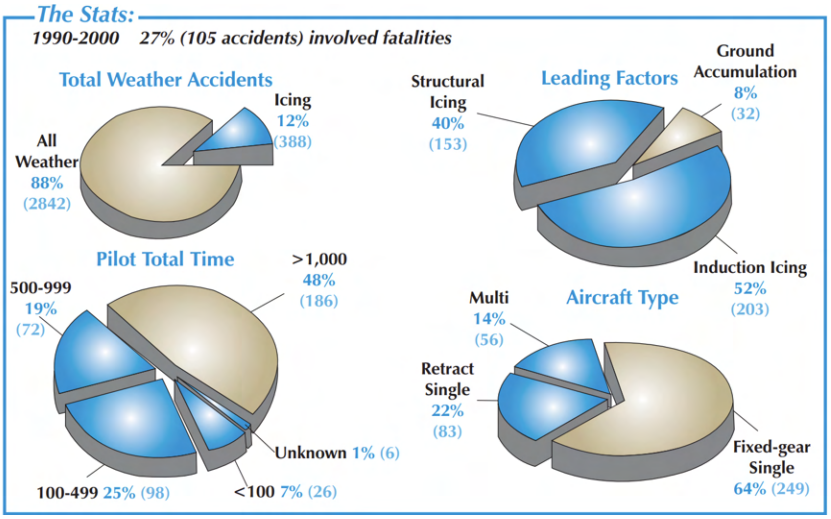

Figure 1.6: Aircraft accidents involving icing [68]

When an aircraft is in a humid and cold atmosphere, it may encounter supercooled water droplets. Upon striking the aircraft's surface, some of these droplets can freeze, leading to ice accumulation. This ice accretion modifies the airframe's original shape by impacting its aerodynamic performance. For instance, ice formation on the wings can lower the maximum lift coefficient and increase drag, potentially causing instability and increasing the risk of a crash. Furthermore, a minor accumulation of ice at a crucial spot could have a more detrimental effect on performance than a larger accumulation at a less critical area. Thus, investigating the icing mechanism

has a significant importance in flight safety.

Aircraft icing is an active research field with methodologies ranging from experimental analysis and numerical simulations to data-driven approaches. NASA conducted some tests investigating the impact of aircraft icing on stability [9], Papadakis et al. conducted experiments about the impact of icing on handling qualities and aerodynamic performance [10], wind tunnel tests are done to understand the effect of aircraft icing [11].

Figure 1.7: Icing Research Tunnel, NASA Glenn Research Center [12].

Even though the experimental study gives precise and realistic values, carrying out an experiment is costly and time-consuming. More research has been focusing on the numerical simulation approach. As the analytical solutions for aircraft icing is too complex to obtain, a mathematical model is implemented to study the aircraft icing numerically. For example, the LEWICE code [53], developed by the NASA Glenn Research Center, applied the Messinger icing model [33] to study the ice accretion for different flight conditions. FENSAP-ICE [52] implements a three-dimensional ice accretion solver which solves the Reynolds-Averaged Navier–Stokes (RANS) equation for airflow field and Messinger model for ice accretion.

While icing experiments are required for certifying the aircraft and have a significant cost, numerical models enable aircraft producers to predict the in-flight icing previously, design ice protection systems to a certain extent, and avoid wasting time and resources on conducting an experiment for every critical icing condition.

1.2 Objective

The research aims to explore various ice protection systems applicable to an electric propulsion cooling air inlet, which is shown in figure 1.8, and to develop safe and

energy-efficient solutions through the flight mission. Typical cooling submerged inlets usually do not require any ice protection due to no critical ice accretion. As distinct from typical submerged cooling inlets, this inlet will be located under an angled nacelle where it is more exposed to the airflow and icing. Additionally, the propeller effect on the ice accretion on the inlet is aimed to be investigated. First, a generic air inlet will be designed to simulate icing conditions on the CAD model. Then, the necessity for ice protection will be studied with CFD and ice accretion computations whether the inlet is exposed to critical icing encounters. Several ice protection system concepts will be proposed viable to EASA CS-25 certification [14] and be evaluated according to selection metrics. System implementations of ice protection systems will be outlined. As a result, the research provides novel insights into the conceptual design of hybrid-electric aircraft, which can be guiding in the mission of electrifying air travel.

Figure 1.8: Electric propulsion cooling air inlet example (Heart Aerospace).

1.3 Scope

This study is limited in several terms, such as inlet types and ice protection systems, due to hybrid-electric aircraft concept design. The air intakes are used to provide sufficient airflow for the cooling of the electric motors and inverters. These air intakes will be flush inlets due to the lower drag contribution preferences [15] at an angled location on the front side of the nacelles.

Various IPS solutions compatible with electric aircraft concepts will be assessed. The study is limited to a duration of five months, which affects the number of concepts investigated. Due to time constraints, the flow solution is simulated using the generic model with simplified assumptions.

2
Theory

2.1 Aircraft Icing

Ice formation has been a serious concern all along aviation history. There have been several research studies performed to explain natural icing conditions, mostly by the National Advisory Committee for Aeronautics (NACA) in the early years [8]. To manage the risks of flying in icing conditions effectively, the science of icing is explained broadly.

2.1.1 Flight in icing

Supercooled water droplets are contained in clouds, and ice will form during flight if liquid water impacts the airframe, which has a temperature below the freezing point. This formation deteriorates the smooth airflow over the airfoil, the ice accumulation decreases lift and increases drag on the wings, blocks the intakes, and causes the propeller to accrete ice. To design ice protection systems, in-flight icing in terms of meteorological parameters, ice accretion physics, and design criteria are introduced in this chapter.

2.1.1.1 The icing atmosphere

The shape, amount, and rate of ice accretion depend on the atmospheric conditions and the aircraft flight parameters such as speed, and angle of attack. Before analyzing the aircraft icing, being familiar with certain knowledge of icing characteristics is essential. Outside air temperature, cloud liquid water content, droplet size, and horizontal extent are the influencing factors that are going to be described in what follows.

2.1.1.1.1 Cloud liquid water content

Liquid water content (LWC) is the most critical parameter affecting the ice accumulating in aircraft icing. It is defined as the total mass of water inside all liquid droplets within a unit volume of cloud [20]. The common unit used for LWC is grams of water per cubic meter of air (g/m^3). An example of the effects of LWC on wing ice formation can be seen from the figure 2.1. Higher values of LWC result in a higher amount of impinging water around the surface. It is seen that higher LWC poses a threat to the aerodynamic profile of the airframe. Ice accumulation especially the horn-shaped ice buildup disrupts the streamlines around the aerodynamic

profile and gives rise to adverse effects on flight performance and power requirements for ice protection systems.

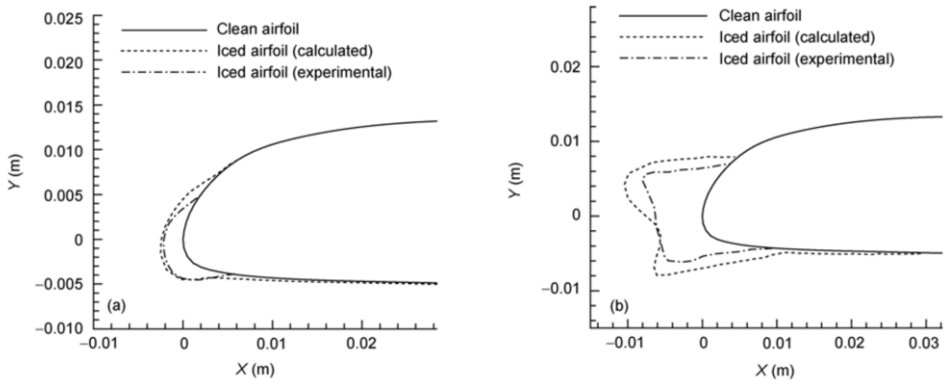

Figure 2.1: Ice buildup in different liquid water content over an airfoil [22]. LWC = 0.30 g/m^3 and LWC = 1.14 g/m^3, respectively.

2.1.1.1.2 Cloud types

In terms of aircraft icing, clouds can be classified as stratiform and cumuliform clouds.

Stratiform clouds can be defined as layer-type clouds and they are known for having an extensive horizontal coverage. They can be classified by the altitude they exist in. The high-level stratiform clouds ($\geq$20,000 ft) include mostly ice crystals and do not pose a risk for airframe icing. However, they should be evaluated for engine icing. The middle-level stratiform clouds (between 6,500 and 20,000 ft) are composed of both liquid and solid water content and are important for airframe icing. These clouds extend to a wide region and considering that the typical altitudes for cruise speed of transport-category turboprop aircraft are included in this altitude interval, a long exposure to icing is possible.

Figure 2.2: Stratiform (layer) clouds [16].

The low-level stratiform clouds (below 6,500 ft) as seen from the right side of the figure 2.2, have a place in aircraft icing. The severity of icing for these clouds is considered light to moderate. The most severe region is the upper parts of the clouds

where they contain the maximum liquid water concentration values. While both rime and glaze ice are observed in the stratiform clouds, rime ice forms generally. Types of ice are described in the section 2.1.1.2.1 in detail.

Cumuliform clouds are important in icing due to their high liquid water content (LWC) values, rapid development, and instability. These clouds form vertically and cover narrower regions than stratiform clouds do. These clouds are known as fair weather cumulus since they form in fairly good weather behind cold fronts where the warm air is forced upwards by collision with the cold air. However, they can form into cumulus congestus, which is seen on the right side of the figure 2.3, forming a cauliflower or tower-shaped cloud. The largest and most intense type of cumulus cloud are cumulus nimbus, which is known as a "thunderhead" as seen on the left side of the figure 2.3. They cause rain, thunder, lightning, or various forms of frozen precipitation. Icing in cumuliform clouds happens in short distances with a high liquid water content. In cumuliform clouds, usually glaze ice or a mixture of rime and glaze ice forms. Aircraft avoid this type of cloud due to the heavy shear winds, turbulence, and lightning risk.

Figure 2.3: Cumuliform (vertical) clouds [17].

2.1.1.1.3 Variations with altitude

There has been a flight for data acquisition on atmospheric icing conditions under 10,000 ft ($\sim$ 3048 m) in the winter months [18]. As seen from the figure 2.4, there are several altitude intervals prompting concerns due to rapid climbs in LWC such as between 4,000 ft ($\sim$ 1219 m) and 6,000 ft ($\sim$ 1829 m). This level represents the upper limits of the layer of turbulent mixing in wintertime. The figure 2.5 shows the horizontal extent concerning altitude for both cloud types. There are correlated relations as, for instance, the existence of cumuliform clouds strongly influences the LWC.

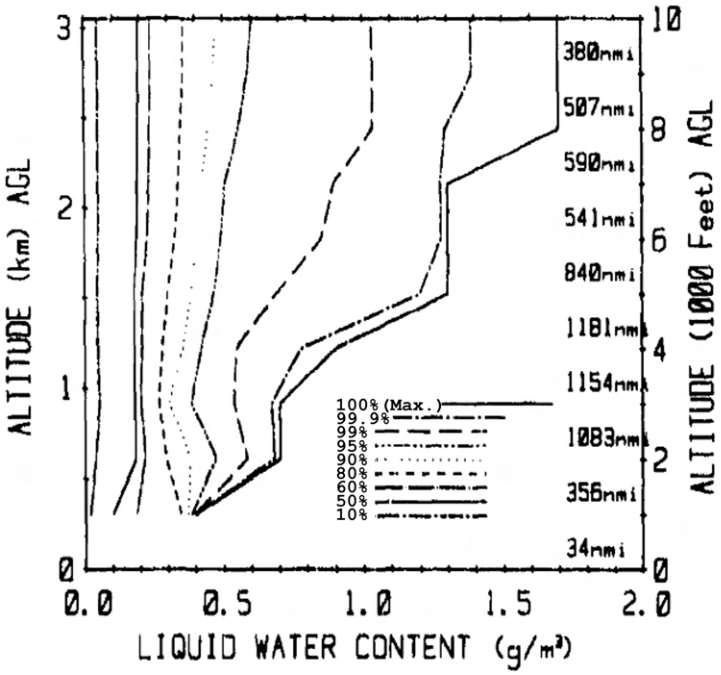

Figure 2.4: Cumulative variation with altitude for supercooled LWC from all cloud types [18].

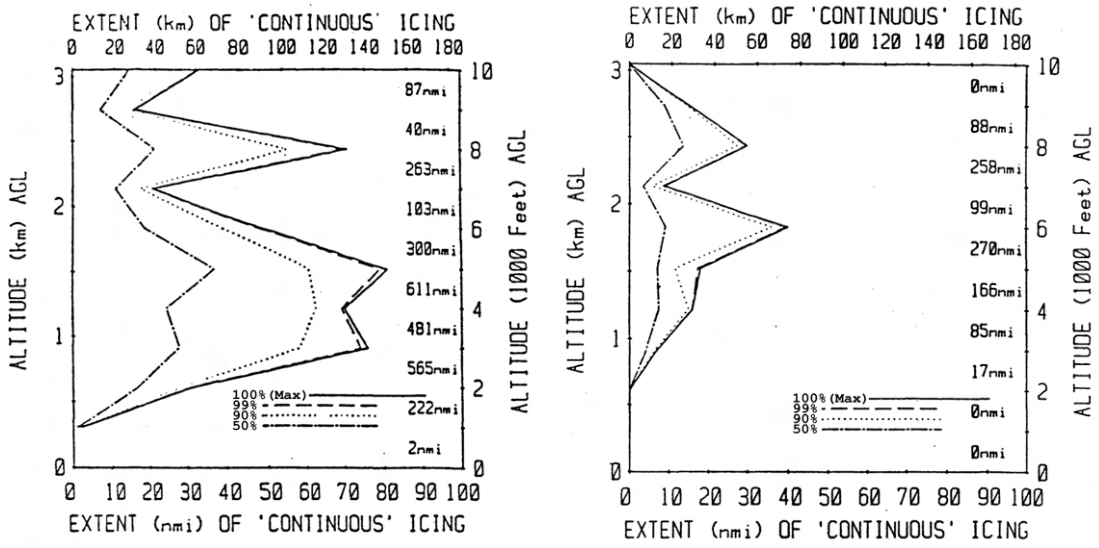

Figure 2.5: Altitude variation of horizontal extent of extended icing encounters in (a) layer (b) convective clouds [18].

Aircraft icing occurs mostly at altitudes lower than 22,000 ft ($\sim$ 6700 m) where the ambient temperature of the atmosphere is -22°F (-30°C). Over 22,000 ft altitude, icing is seen rarely since the fraction of supercooled water decreases with temperature, and only ice crystals are present. Apart from all the individual contributions of the altitude and temperature to the aircraft icing, an envelope can be generated to know where the icing is possible. This envelope is a helpful standard to provide critical

atmospheric inputs while analyzing the ice buildups and designing the ice protection system. Federal Aviation Regulation (FAR) contains the transport airworthiness requirements according to these cloud envelopes. Icing envelopes are shown within an altitude and temperature range for stratiform and cumuliform clouds according to observation data obtained by NACA. In the figure 2.6, the blue line frames these icing envelopes for continuous and intermittent maximum conditions, respectively. The numbers show the frequency distribution of icing observations at the specified atmospheric condition.

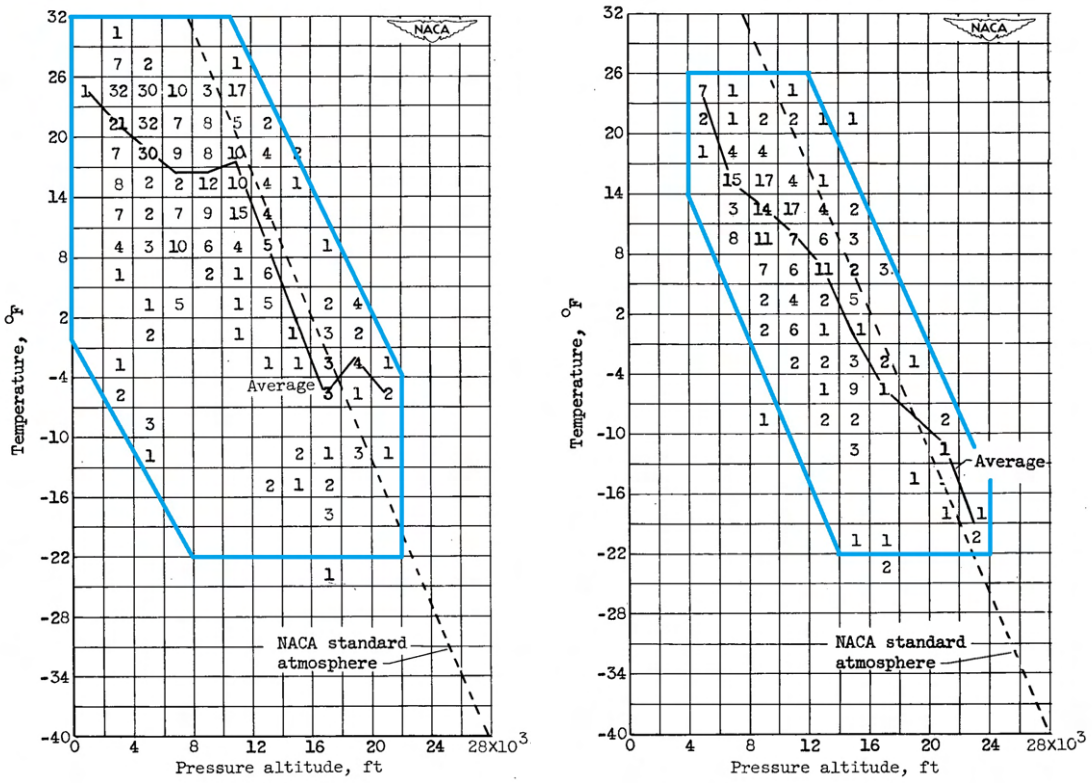

Figure 2.6: Frequency distribution of icing observations for various increments of temperature and pressure altitude [19]. a) Stratiform clouds, b) Cumuliform clouds.

As seen from the stratiform cloud envelope, icing rarely occurs below 0°F (-17°C) at low altitudes. The minimum temperature where the icing is observed is -22°F (-30°C) when the altitude increases to higher levels (up to 22,000 ft). The most frequent icing region is seen around 4,000 ft and 20 °F (-6°C) for CM icing conditions. On the other side, the cumuliform clouds do not cover as wide a region as the stratiform clouds. Different from the stratiform clouds, the envelope starts at 4,000 ft altitude for IM icing conditions up to 24,000 ft. The temperature range is also more restricted than stratiform clouds.

2.1.1.1.4 Cloud droplet size distribution

Clouds are composed of droplets that vary in size. This range of the distribution is mostly defined by median volume droplet diameter (MVD) which is also called mean

effective diameter (MED) in the older usage for the same parameter. It represents that half of a mass of volume of water in the cloud is larger than the MVD value and the other half of the droplets are smaller [20]. As the droplet sizes vary in the atmosphere, NACA researchers found that the Langmuir distribution represents the cloud droplet distribution well and it is typically used for certification purposes. In table 2.1, the likeliness of drop diameters increases with going from column A to E. For instance, column A shows a monodispersion case while columns D and E represent a condition that is more expected in the atmosphere. MVD has been proved to be a simple substitute that estimates the ice accretion computations well.

Table 2.1: Langmuir droplet size distribution [23].

Fractional LWC in Each Size Group %	Distribution(s) of drop diameter/MVD				
	A	B	C	D	E
5	1.00	0.56	0.42	0.31	0.23
10	1.00	0.72	0.61	0.52	0.44
20	1.00	0.84	0.77	0.71	0.65
30	1.00	1.00	1.00	1.00	1.00
20	1.00	1.17	1.26	1.37	1.48
10	1.00	1.32	1.51	1.74	2.00
5	1.00	1.49	1.81	2.22	2.71

MVD ranges between 10-30 μm typically and based on the data reviewed by FAA , the overall average value for stratiform (layer) clouds is about 15 μm and about 19 μm for cumuliform (convective) clouds [24]. The droplet sizes less than 15 microns cannot impinge on the airframe and continue flowing in the airstream. Therefore, the liquid water content consisting of these droplets does not contribute to ice accretion. This concept [25] of critical drop size diameter provides more precise ice accretion computations, and the regulations are developed accordingly not considering the small MVD values. The related standards are presented in the section 2.1.1.3 in detail.

2.1.1.2 Physics of ice accretion

The physics of ice accretion is explained in three steps. Due to atmospheric conditions, which type of ice to form is described with the results of different ice shapes and characteristics. Second, droplet impingement has been included mathematically. Most of the parameters that are going to be utilized in this research are defined in this chapter. Lastly, aircraft design criteria concerning certification standards are introduced and the significance of designing the ice protection systems according to critical conditions are discussed.

2.1.1.2.1 Types of ice accretion

The type of ice is significant in ice formation as it changes the aerodynamics differently due to distinct ice shapes. Ice is identified as clear, rime, or mixed. Based

on its shining appearance, clear ice is defined as glaze ice in the literature as the transparent part of the clear ice is called glaze [20]. Rime ice has an opaque and milky white appearance. Mixed ice is the combination of clear and rime ice, that has clear in forward and rime in aft areas [26] as seen from the figure 2.9. Rime ice tends to cover the airfoil profile having a spearhead or streamlined shape while clear ice tends to form a single- or double-horned shape depending on the flow angle.

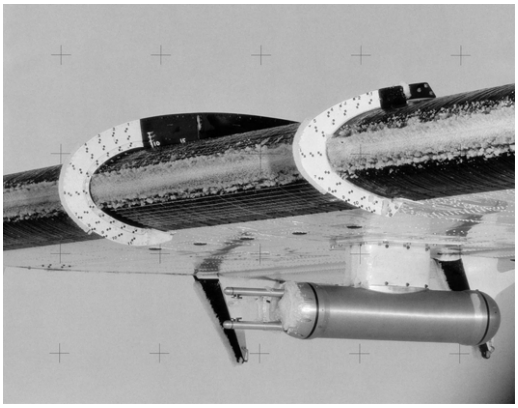

Figure 2.7: Glaze or clean ice [27]

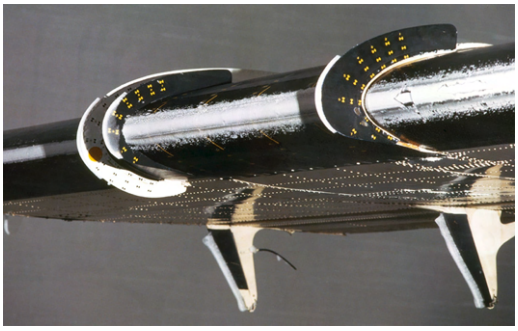

Figure 2.8: Rime ice [27].

Figure 2.9: Mixed ice [28].

Rime ice forms when the supercooled droplets freeze on impact to the airframe and the place where the ice is going to accumulate is highly predictable. The white

color comes from the air trapped between the ice and the airframe. This type of low-density ice forms when the droplets are small, and the air temperature is low; consequently, the liquid water content is low. Rime ice is generally brittle and it can be displaced easily by the de-icing protection systems.

Clean ice, on the other side, does not form on impact. Supercooled droplets merge with other droplets and they spread aft slowly covering more regions of the wing and finally freeze. Clear ice forms when the air temperature approaches the freezing point (0 °C) by the large droplets which have a high LWC. Since a sheet covers the surface without any air trapped in between, the ice structure becomes quite solid. If the ice accumulation continues, horn shapes start to occur disrupting the airflow. This shape has enormously adverse effects on lift and drag characteristics. The figure 2.10 shows that while the airfoil has a stall angle around 15°, glaze ice decreases it to around 9°. Rime ice does not affect the aerodynamics as negatively as glaze ice does. Rime ice formation also decreases the stall angle but only to around 13°. In terms of drag characteristics, it can be seen that clear ice influences the flow field dramatically and increases the drag at least three times more than the rime ice formation.

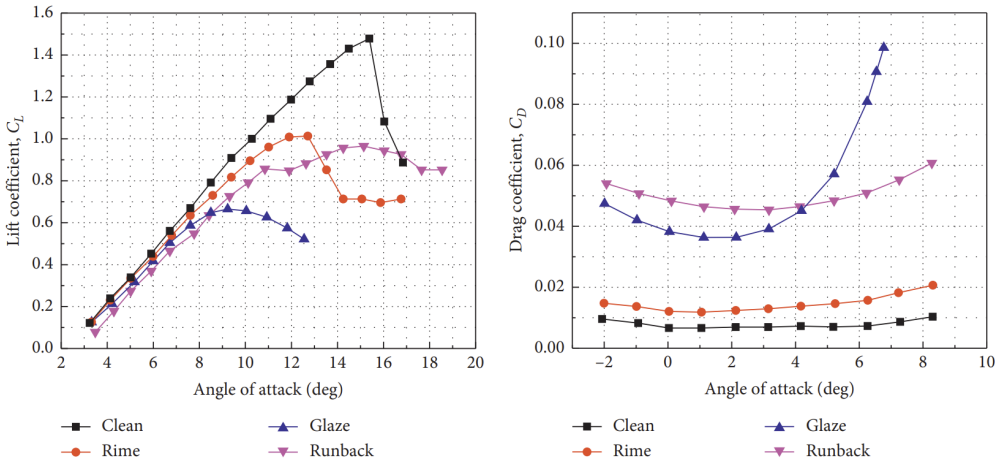

Figure 2.10: The aerodynamic characteristics of the NACA 23012 airfoil under different ice shapes: lift coefficient (left) and drag coefficient (right) [29].

2.1.1.2.2 Droplet impingement

Supercooled droplets in the cloud will strike the aircraft during flight. If they impinge on the surface, ice starts building up. The path that droplets follow until they hit the surface is called a droplet trajectory.

The physical and mathematical fundamentals of two-dimensional representations of a wing cross-section and a circular cylinder are going to be explained here. Computer codes calculating the droplet impingement will be addressed in the section 2.2.

Droplet impingement parameters

Parameters related to droplet impingement computations are going to be defined in this chapter. In the figure 2.11, the droplet impingement is illustrated over an airfoil. h, in the upper drawing, is the projected height of the airfoil, which depends on the angle of attack. In the lower drawing, $S_U, S_L, \Delta Y_0, E$ are shown. S is denoted as the length along the airfoil surface. S = 0 usually represents the leading edge and the stagnation point if convenient. S_U and S_L are defined as the length of the upper and lower surface of the airfoil showing the impingement limits, respectively. The Y-axis is taken at a distance where the flow is unaffected by the existence of the airfoil. The point where the droplet path and Y-axis intersect is the point of Y = 0. The same trajectories are taken to the Y-axis for the upper and lower impingement limits and named the locations as Y_U and Y_L. The distance between these points is defined as $\Delta Y_0 = Y_U - Y_L$ and named as the freestream impingement width.

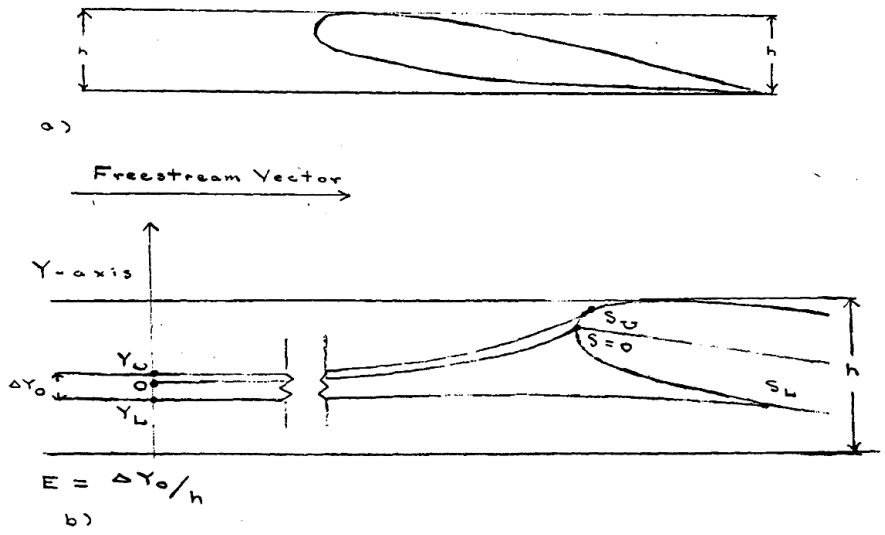

Figure 2.11: Droplet impingement parameters [20].

The total impingement efficiency (or known as collection efficiency, as well), E, is defined as

$$E = \frac{\Delta Y_0}{h} \tag{2.1}$$

where E defines the proportion of liquid mass coming from the Y-axis and impinging amount of droplets on the airfoil. In the equation 2.1, ΔY_0 and h are nondimensionalized and they will be dimensionalized through dividing by the chord length. However, the notation will stay the same.

For the local impingement (or collection) efficiency, β, the figure illustrates the derivative perspective of a droplet impinging on the airfoil surface over a length δS.

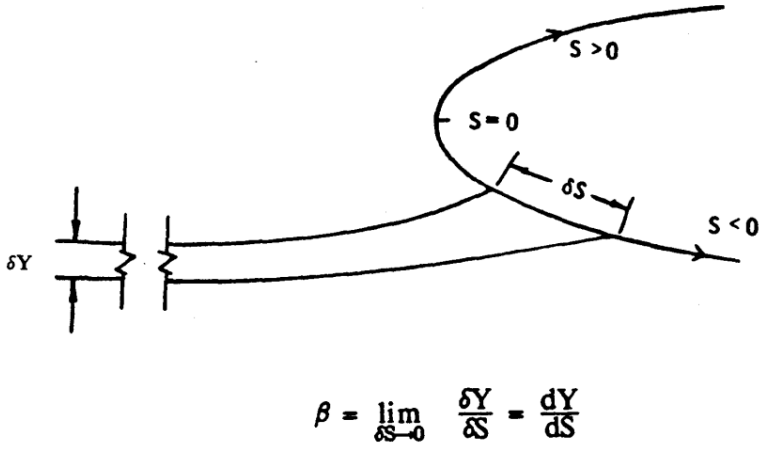

Figure 2.12: Droplet impingement parameters [20].

The local impingement efficiency is defined as

$$\beta = \frac{dY_0}{dS} \tag{2.2}$$

The maximum local impingement efficiency over the airfoil is defined as β_{max} and computed as,

$$\Delta Y_0 = \int_{S_L}^{S_U} \beta \mathrm{ds} \tag{2.3}$$

The local impingement efficiency along the airfoil surface can be seen from the figure 2.13. The curve starts from the lower surface of the airfoil, passes the stagnation point where β peaks, and continue with a dramatic decrease at the end for the upper surface of the airfoil. This trend is directly affected by the angle of attack. While there is zero angle of attack, a symmetrical graph is expected for the two sides of the stagnation line.

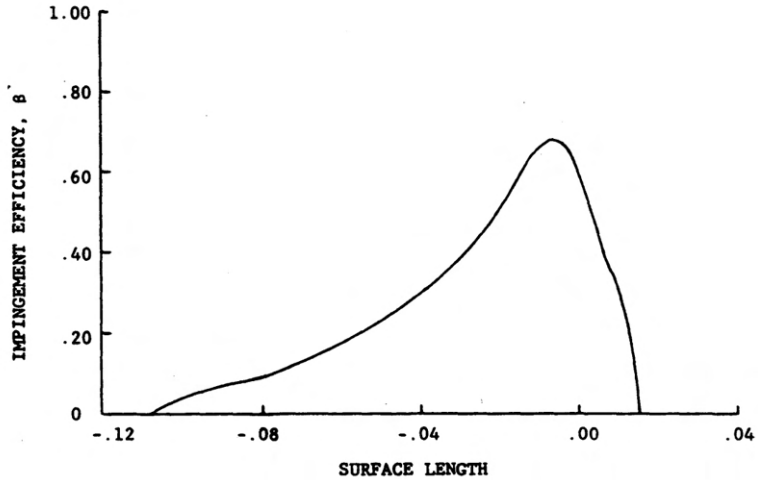

Figure 2.13: Local impingement efficiency curve [20].

There are many factors affecting the local collection efficiency. The figure 2.14 shows the maximum local impingement efficiencies for several bodies and the figure 2.15 shows the water catch efficiencies for various airfoils and geometric shapes.

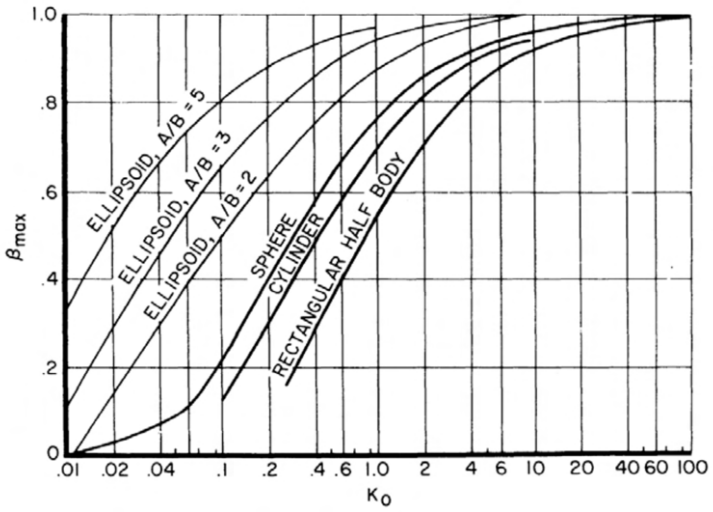

Figure 2.14: Maximum local impingement efficiencies at the stagnation line, $\alpha = 0$ [31].

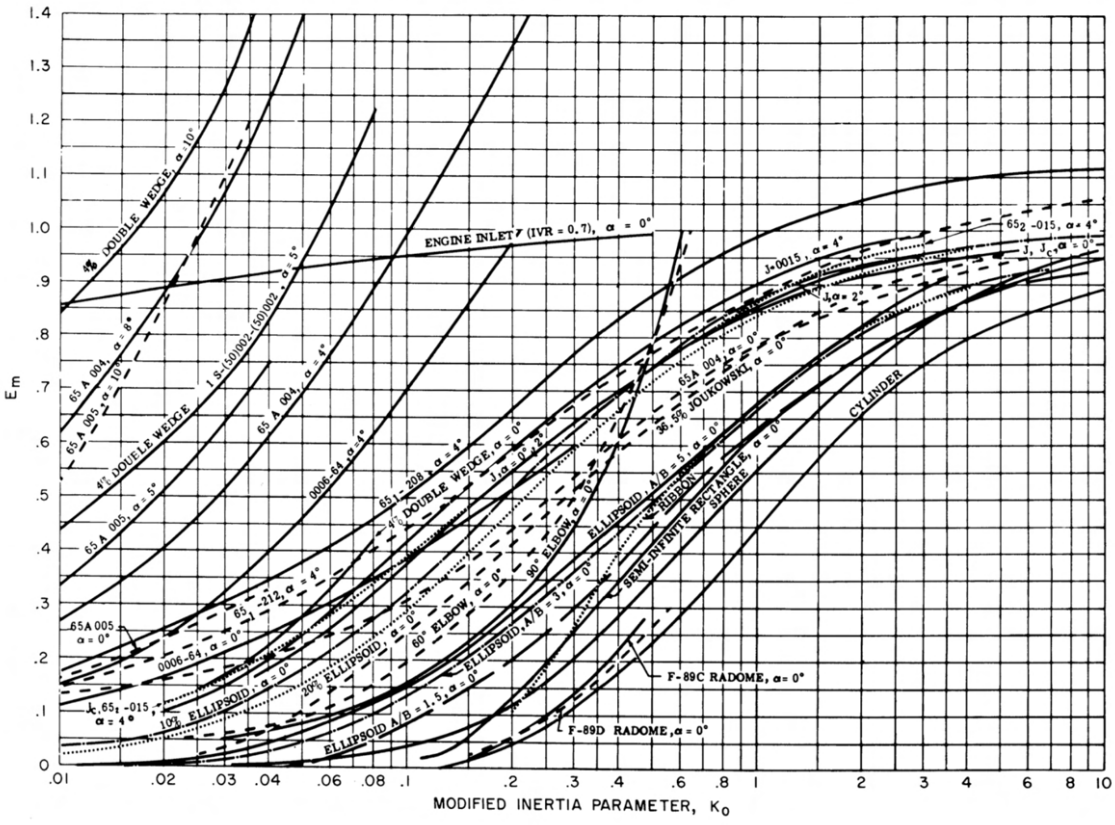

Figure 2.15: Water catch efficiencies for various airfoils and geometric shapes [31].

Other effects of more factors such as chord length, droplet diameter, freestream airspeed, and angle of attack are shown in figure 2.16 and 2.17.

Droplet diameter and airspeed are directly proportional to local collection efficiencies. Smaller MVD and lower airspeed results in lower β while chord length is inversely proportional, shorter chords result in larger impingement efficiencies. The angle of attack affects the local collection efficiencies differently throughout the airfoil surface. The collection efficiency peak point is at the stagnation line when there is no angle of attack and it moves by the direction and quantity of the angle of attack. When the quantity increases, the collection efficiency expands in the rest of the airfoil surface instead of piling up at the stagnation point.

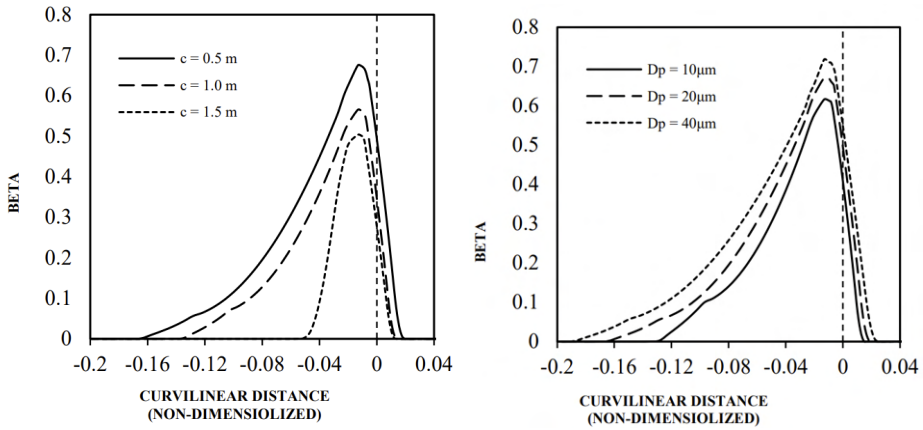

Figure 2.16: Local impingement efficiencies at different (a) chord length, (b) MVD [32].

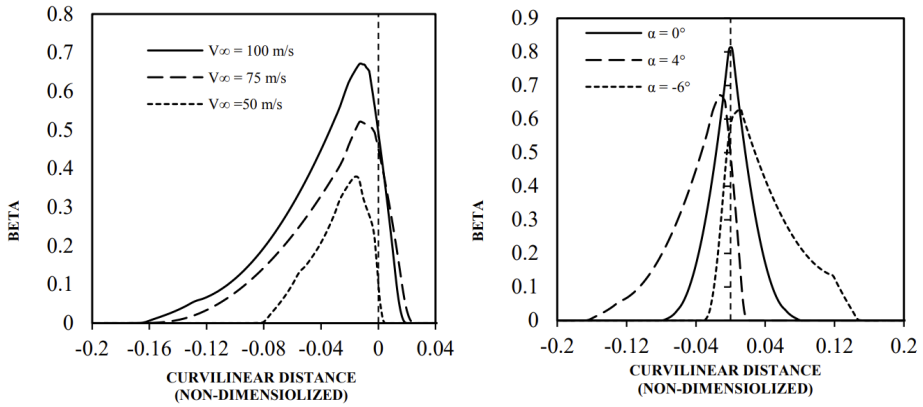

Figure 2.17: Local impingement efficiencies (continued) at different (c) freestream airspeed, (d) angle of attack [32].

2.1.1.2.3 Heat balance in icing conditions

In icing conditions, heat balance between the airframe and the atmosphere is explained by the extended Messinger model [33]. The power required for continuously

heated surfaces can be expressed by an energy balance given in the equation 2.4 for each surface element of the wing. As the anti-icing method keeps the surface temperature above the freezing point, the heat balance is simplified by neglecting the runback heat of enthalpy since the runback is also maintained at a constant temperature. Main contributors to balancing the heat losses from the surface are defined as sensible heating, convective cooling, evaporative cooling, kinetic heating, and aerodynamic heating.

$$\dot{q}_{\text{anti-icing}} = \dot{q}_{\text{sensible}} + \dot{q}_{\text{convection}} + \dot{q}_{\text{evaporation}} - \dot{q}_{\text{kinetic}} - \dot{q}_{\text{aero}} \tag{2.4}$$

$\dot{q}$ represents the heat flux per unit area for each term in the equation 2.4 and has a unit of W/m^2K.

Sensible heating

Sensible heating term comes from heating the impinging droplets to keep them in the liquid state. This heat term keeps the runback water to stay as water and avoid secondary icing.

$$\dot{q}_{\text{sensible}} = \dot{m}_{local}\, c_{p_{\text{w}}} \left(T_{\text{sk}} - T_{amb}\right) \tag{2.5}$$

where c_{p_w} is the specific heat of water and T_{sk} and T_∞ are the skin and ambient temperature, respectively. $\dot{m}_{local}$ is the mass flow of the impinging droplets per unit of time and surface, which can be abbreviated as $\dot{m}_{imp}$ and known as the intensity of ice accretion, too [34]. It can be calculated from the equation 2.6.

$$\dot{m}_{local} = \beta\, \text{LWC}\, V_\infty \tag{2.6}$$

where β is the collection efficiency as mentioned in the equation 2.2, LWC is the liquid water content, and V_∞ is the freestream velocity.

As explained in the section 2.1.1.2.2, collection efficiency is a function of droplet size, aircraft speed, airfoil parameters, and atmospheric conditions. On the other side, Krammer and Scholz [35] presented an equation to approximate the collection efficiency valid for the airfoils with a relative thickness of 6 to 16% at an angle of attack of $\alpha = 4°$.

$$\beta = 0.00324 \left(\frac{V_\infty}{t}\right)^{0.613} \tag{2.7}$$

This equation is adapted from the figure 2.18 for a 15% Joukowski airfoil for a specific scenario. This estimation is true for a droplet diameter of 20 microns and an altitude of 10,000 ft. The applications of the altitudes from sea level to 20,000 ft, the error will be less than 10%. This equation is helpful for the first approximations in preliminary design. For greater accuracy, the more refined K_0 and collection efficiency method should be preferred which are presented in the figure 2.15 and equation A.12.

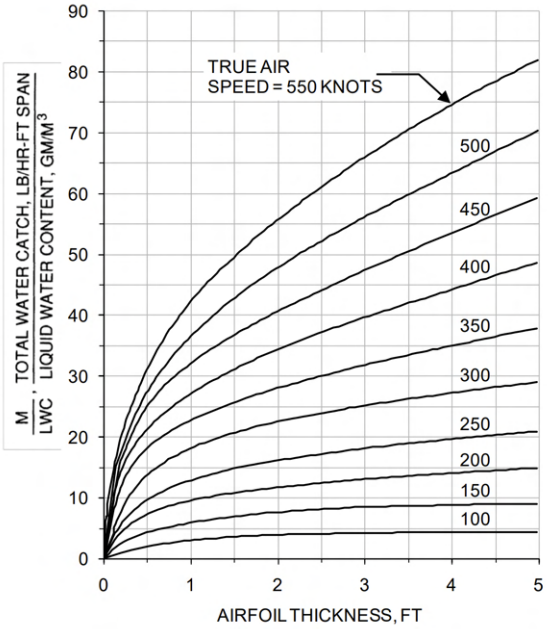

Figure 2.18: Aircraft total catch typical from 6 to 16% thick airfoils at $\alpha = 4$ degrees, with 20 μm MVD droplets. (all altitudes: strictly true for 10,000 ft and within 10% error between sea level and 20,000 ft [31]).

Convection

The ice-accreting surface is cooled by the convection to the airstream. This heat loss can be expressed as,

$$\dot{q}_{\text{convection}} = h_0(T_{\text{sk}} - T_{\text{amb}}) \tag{2.8}$$

where h_0 is the heat transfer coefficient, expressed in the equation 2.9

$$h_0 = \frac{Nu\, k}{l} \tag{2.9}$$

where Nu is the Nusselt number, k is the thermal conductivity of air, and l is the characteristic length. Since icing mainly occurs in the vicinity of the leading edge of the airfoil, the characteristic length is taken as twice the nose radius [36].

The methodology to calculate the relevant heat transfer coefficient is significant to apply the correct flow situation. First, depending on the flow geometry such as a flat plate, a sphere, or a cylinder, different approaches will be followed. Then, the Reynolds number will affect the boundary layer and determine if the flow is laminar or turbulent. In addition, it should be determined whether the appropriate condition requires the local or surface average coefficient [37]. While the heat transfer coefficient formulation remains the same, the Nusselt number included in that equation varies concerning the categories in this methodology.

The geometry to compute the flow conditions around the lip of the leading edge is estimated as a circular cylinder where the fluid motion is normal to the axis of

the cylinder. Having the nose diameter as the characteristic length corroborates this geometry assumption, as well. Thereafter, the Reynolds number is necessary to define the accurate Nusselt number correlation, which is expressed as,

$$Re = \frac{\rho\, V_\infty\, l}{\mu} \tag{2.10}$$

where the ρ is the density, and μ is the dynamic viscosity of the air.

While the Reynolds number affects the Nusselt number correlations for the flows over a flat plate, there is one single comprehensive equation by Churchill and Bernstein [38] given in the equation 2.11 covering the entire range of Reynolds number, as well as a wide range of the Prandtl number for the circular cylinders.

$$Nu = 0.3 + \frac{0.62 Re^{1/2}\, \mathrm{Pr}^{1/3}}{\left[1 + (0.4/\,\mathrm{Pr})^{2/3}\right]^{1/4}} \left[1 + \left(\frac{Re}{282,000}\right)^{5/8}\right]^{4/5} \tag{2.11}$$

where Pr represents the Prandtl number and is expressed as,

$$Pr = \frac{c_{p_a} \mu}{k} \tag{2.12}$$

where the c_{p_a} is the specific heat of air.

Evaporation

Evaporative cooling from the surface of the water to the airstream is expressed with the equation 2.13.

$$\dot{q}_{\text{evaporation}} = \chi \left\{ e\left(T_{\text{sk}}\right) - e\left(T_{amb}\right) \right\} \tag{2.13}$$

where the χ is the evaporation coefficient and defined in the equation 2.15, e is the nonlinear saturated water vapor pressure function which is required at the temperature of skin and ambient, respectively. There are several equations approximating the saturated water vapor pressure function, the approximation used as a function of temperature in Kelvin is expressed in the equation 2.14.

$$e(T) = 2337 \exp\left\{ 6789 \left[\frac{1}{293.15} - \frac{1}{T}\right] - 5.031 \ln\left[\frac{T}{293.15}\right] \right\} \tag{2.14}$$

The evaporation coefficient from the equation 2.13 is given as

$$\chi = \frac{0.622\, h_0\, L_E}{c_{p_a}\, P_0\, Le^{2/3}} \tag{2.15}$$

where L_E is the latent heat for the evaporation, P_0 is the ambient pressure, and Le is the Lewis number which is defined in the equation 2.16.

$$Le = \frac{1}{Pr} \tag{2.16}$$

Kinetic heating

The kinetic heating term contributes to the energy balance as a heat gain due to the kinetic energy of impinging supercooled droplets.

$$\dot{q}_{\text{kinetic}} = \dot{m}_{\text{local}} \frac{V_\infty^2}{2} \tag{2.17}$$

Aerodynamic heating

Due to the friction between the droplet and the air in the boundary layer over the surface, this term will contribute to the energy balance as a heat gain. It can be mentioned as viscous or frictional heating besides aerodynamic heating.

$$\dot{q}_{\text{aero}} = R_c h_0 \left[\frac{V_\infty^2}{2c_{p_a}^2} \right] \tag{2.18}$$

where R_c represents the recovery factor expressed as,

$$R_c = 1 - 0.99 \left(1 - Pr^n\right) \tag{2.19}$$

where n is $\frac{1}{2}$ for laminar boundary layer and $\frac{1}{3}$ for turbulent boundary layer.

2.1.1.3 Atmospheric design criteria

Aircraft design must meet regulatory requirements ensuring air carrier certifications. Heart Aerospace aims to certify its ES-30 under EASA CS-25 requirements. For aircraft icing, the FAA report "Engineering Summary of Airframe Icing Technical Data", ADS-4 [26], and Federal Aviation Regulations, Part 25, Appendix C [24] are going to be the main bases for regulatory data. Icing envelope design criteria depend on LWC, MVD, ambient temperature, flight altitude, horizontal cloud extent, and cloud type. The stratiform and cumuliform clouds are defined and explained in section 2.1.1.1.2, and icing conditions are differentiated with these cloud types. The stratiform (layer) clouds are defined in continuous maximum (CM) icing conditions and the cumuliform (vertical) clouds are investigated in intermittent maximum (IM) icing conditions. CM and IM icing conditions have been considered for airframe icing and IM icing conditions have traditionally been considered for engine ice protection.

FAR 25 Appendix C has six figures and they have been used since 1964 for selecting the atmospheric design criterion related to the icing clouds. These figures estimate the probable maximum (99%) of the liquid water content for an average value of horizontal extent, ambient temperature, and droplet size in the cloud. Figure 2.19 shows the estimation of the liquid water content values with respect to ambient temperature which ranges between 0 to -40 °C and median volumetric diameter which ranges between 15 to 40 μm.

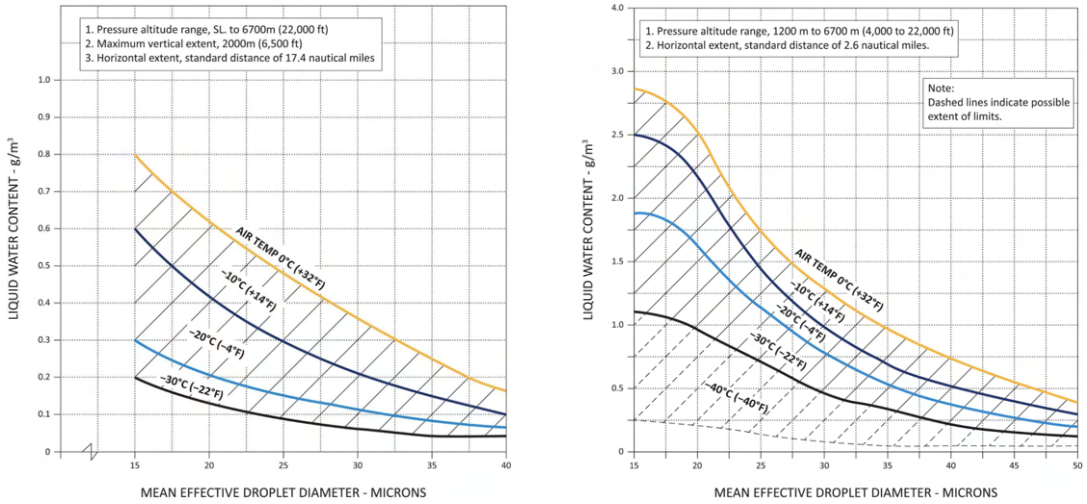

(a) CM icing conditions **(b)** IM icing conditions

Figure 2.19: Liquid water content factor vs median volumetric diameter [24].

Currently, a 20 μm MVD is used generally to compute the airframe ice accumulation for the reference (17.4 nmi) or longer exposure distance [24]. Another analysis is done with the 40 μm MVD to compute the chordwise impingement limits of the ice accretion of an airfoil. Meanwhile, the Advisory Circular [39] recommends that the entire range of MVD should be considered up to 40 μm over the distance up to 17.4 nmi at least.

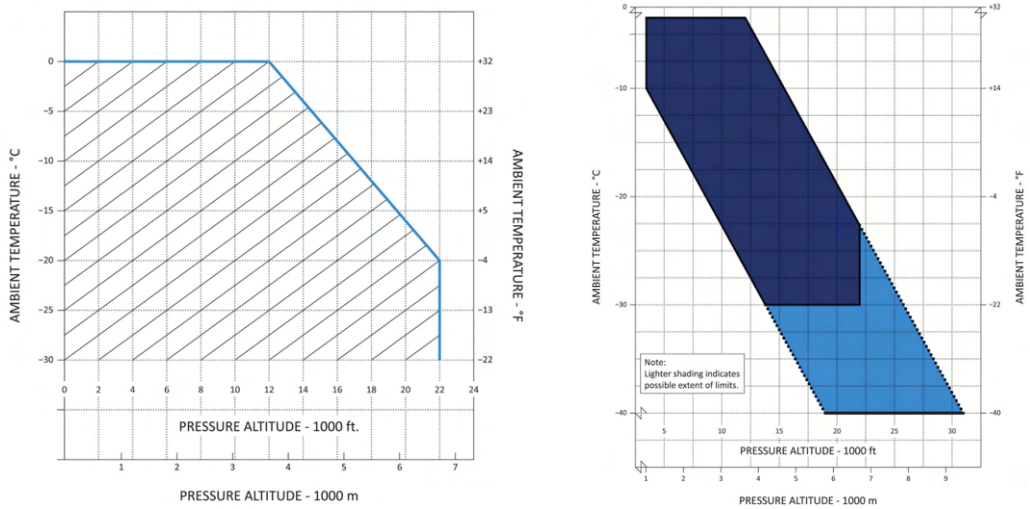

(a) CM icing conditions **(b)** IM icing conditions

Figure 2.20: Ambient temperature vs pressure altitude [24].

For instance, figure 2.19 (a) shows the LWC in CM icing conditions with respect to MVD at a reference distance of 17.4 nautical miles (nmi). This reference distance is 2.6 nautical miles (nmi) for IM icing conditions as shown in figure 2.19 (b). In case of a need for designing for a longer or shorter flight extent, a liquid water content

factor is used to correct the LWC value depending on the cloud's horizontal extent different than the reference distance. This is because longer averaging distances will result in lower maximum values of LWC as an average over the total exposure distance [24]. These correction factors are indicated for CM and IM icing conditions in the figures 2.21, respectively.

The choice of exposure distance depends on the different applications. One application is to compute the ice accumulation through a long exposure distance around 100 or 200 miles [26]. For this use, the corresponding LWC value for the specified icing conditions and atmospheric data are obtained from figure 2.19. Then, the LWC values are corrected with the correction factors obtained from the figure 2.21. Another application is to compute the ice buildup during a 45-minute hold condition. For this scenario, the LWC value is taken at its full value from the figure 2.19 within the reference horizontal extent.

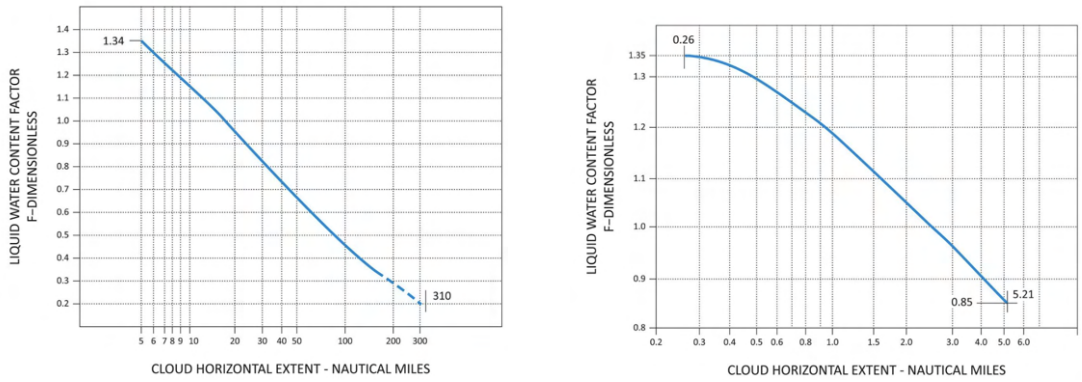

(a) CM icing conditions **(b)** IM icing conditions

Figure 2.21: Liquid water content factor vs cloud horizontal extent [24].

2.2 Ice Accretion Modeling in Aerospace

Experimental testing is required from certification authorities like EASA/FAA to fly into known icing conditions, nonetheless, this can become a costly step for a company in the pursuit of aircraft certification, this pushed the development of more accurate computational tools to analyze ice accretion on aircraft's surfaces which allows to reduce costs in the certification process since IPS could be designed to be more efficient, resulting in fewer iterations of it during the experimental testing phase (Certification by Analyses). Today, they are part of the certification process of an aircraft and can be presented to certification authorities as part of the certification process, with flight testing still being mandatory.

To mitigate risks, various icing codes were developed by companies and research institutes. The state of the art today consists of different approaches that need to be chosen carefully depending on the problem that one wants to analyze, a summary of different icing codes and their main characteristics is shown in table 2.2.

Probably the most well-known and studied code to date is NASA's LEWICE [53], which applies a time-stepping procedure to calculate the shape of ice accretion. It is a potential flow field solver, making it a quick and reliable procedure for surfaces like wings, vertical and horizontal stabilizers at low angles of attack where viscous effects have a lower influence on the flow characteristics over these surfaces; however, on flows where viscous and 3D effects greatly affect the flow behavior like vortex structures, these solutions can prove unreliable and more complex analysis might need to be performed.

NASA's LEWICE also has a 3D version, which is only available for use in the USA but looks into improving solver accuracy by considering these effects which can still have a significant impact, like over highly swept wings.

FENSAP-ICE was initially developed by Newmerical Technologies International (NTI) [52] and later acquired by Ansys, Inc., which quickly raised to one of the leading codes for ice accretion analysis. Differently from LEWICE, FENSAP-ICE starts by solving the 3D Reynolds Averaged Navier-Stokes equations for steady or unsteady compressible flow, inviscid or viscous, for which the flow can be laminar or turbulent. Turbulence here can be modeled by one or two-equation models. This modeling, of course, increases the computation time compared to the simpler potential flow code used by LEWICE, but higher accuracy can thus be achieved for certain types of flow characteristics as described earlier. The main modules employed by FENSAP-ICE for ice accretion analysis are described below,

- FENSAP - Flow Solver
- DROP3D - Water Droplet/Ice Crystal Impingement
- ICE3D - Ice Accretion and Water Runback

DROP3D is the 3D Eulerian water droplet impingement solver. It uses fine-grain partial differential equations for particle velocity and water concentration. Thus, in a single-shot approach, it can compute these variables as well as droplet velocity vectors, water catch efficiency distributions, impingement patterns, shadow zone characteristics, and impingement limits over the entire domain.

ICE3D is the ice accretion model of the FENSAP-ICE system, also based on fine-grain partial differential equations for the complex thermodynamics of ice formation, outputting the displaced 3D grid after ice accretion. Therefore, it can be used to restart FENSAP with the new grid, allowing one to analyze the effect on the aerodynamics of the ice accretion if this is a critical issue for the surface at the test.

Besides this module, FENSAP-ICE also employs conjugate heat transfer (CHT3D), which couples airflow convection and heat conjugation through solids for dry-air heat transfer calculations and in conjunction with droplets impact and ice accretion for wet-air anti-icing calculations, allowing for complete anti-icing IPS design.

Table 2.2: Ice analysis codes and their main characteristics

	Development	Solver Type	Dimension
LEWICE	NASA	Potential Flow	2D/3D
FENSAP-ICE	NTI/Ansys	Lagrangian/Eulerian	3D
ONERA3D	ONERA	Eulerian	3D
PoliMIce	Politecnico di Milano	Lagrangian	3D

Due to the nature of this problem, it was initially established that a 2D simplification would possibly not capture all the relevant characteristics of the flow of the analyzed problem, thus the possibility of using an exclusively 2D analysis software like LEWICE was discarded.

FENSAP-ICE was thus the chosen software to perform this analysis, which is available for use at Chalmers.

Figure 3.6 shows the procedure used for the flow and icing analyses made throughout this work using FENSAP-ICE.

This type of approach to icing analysis can be more time-consuming because different solvers are used independently instead of modeling all the physics into a single simulation setup, which can also increase user input errors since they can cascade down the solver modules; nonetheless, at the same time it as the great benefit of allowing testing for similar flow conditions without the need of resolving all the flow structures each time a smaller parameter change is performed.

2.2.1 Aerodynamic flow solution

The initial airflow solution is obtained either directly on FENSAP or Fluent. Since flow variables will predominantly describe the droplet behavior it is of great importance to correctly capture all the phenomena involved in the actual flow. Because of this, it was decided to compute the flow solutions first on Fluent and then export them into FENSAP-ICE, which allowed a higher degree of control over these flow characteristics.

Fluent is a finite volume method solver (Eulerian) that employs similar flow models as used by FENSAP, but provides more modeling options that can increase simulation fidelity to the real case scenario.

The continuity 2.20, momentum 2.21 and energy 2.22 equations are solved over a discretized domain.

$$\frac{\partial \rho}{\partial t} + \nabla \cdot (\rho \vec{v}) = S_m \tag{2.20}$$

$$\frac{\partial}{\partial t}(\rho \vec{v}) + \nabla \cdot (\rho \vec{v} \vec{v}) = -\nabla p + \nabla \cdot (\overline{\overline{\tau}}) + \rho \vec{g} + \vec{F} \tag{2.21}$$

$$\frac{\partial}{\partial t}(\rho E) + \nabla \cdot (\vec{v}(\rho E + p)) = \nabla \cdot \left(k_{\text{eff}} \nabla T - \sum_j h_j \vec{J}_j + (\overline{\overline{\tau}}_{\text{eff}} \cdot \vec{v}) \right) + S_h \tag{2.22}$$

The choice of turbulence model depends on considerations such as the physics involved in the flow, the established practice for a specific class of problem, the level of accuracy required, the available computational resources, and the amount of time available for the simulation.

FENSAP-ICE limits the use of turbulence models to one and two-equation models, which thus were used along most of the computations with k-ϵ RNG being used whenever the flow and thermal boundary layers are not intended to be solved until the wall and the k-ω SST otherwise.

The k-ϵ RNG [66] is used due to its characteristics of adding swirl effect corrections into the turbulence generation parameter k, enhancing thus the accuracy for swirling flows, which can affect the flow characteristics over the inlet lip due to its position at the aft of the propeller disc, nonetheless, this variation of the standard k-ϵ model also provides an analytically derived formula for the effective viscosity that shows to be more accurate for low Reynolds number flows, being the case due to the low flight speed and characteristic lengths. All of this can result in higher accuracy, which as stated previously is of high importance to decrease the error cascade.

The k-ω SST [66] is widely used and accepted as RANS closure formulation, with the main difference being solving directly the flow until the wall. It employs the $k-\epsilon$ model far from the walls and a new formulation in near-wall regions, avoiding thus wall functions. The downside of this model is the known required $y+ \leq 1$ which in some cases might be difficult to achieve.

2.2.2 Droplet impingement

The Eulerian droplet impingement model consists of the RANS equations augmented by the droplets' (or crystals') continuity and momentum equations,

$$\frac{\partial \alpha}{\partial t} + \vec{\nabla} \cdot \left(\alpha \vec{V}_d \right) = 0 \tag{2.23}$$

$$\frac{\partial \left(\alpha \vec{V}_d \right)}{\partial t} + \vec{\nabla} \left[\alpha \vec{V}_d \otimes \vec{V}_d \right] = \frac{C_D \text{Re}_d}{24K} \alpha \left(\vec{V}_a - \vec{V}_d \right) + \alpha \left(1 - \frac{\rho_a}{\rho_d} \right) \frac{1}{Fr^2} \tag{2.24}$$

With the droplet Reynolds number (Re_d), the inertial parameter (K) and the Froude (Fr) being defined as,

$$\mathrm{Re}_d = \frac{\rho_a d V_{a,\infty} \left\| \vec{V}_\mathrm{a} - \vec{V}_d \right\|}{\mu_a} \tag{2.25}$$

$$K = \frac{\rho_d d^2 V_{a,\infty}}{18 L_\infty \mu_a} \tag{2.26}$$

$$Fr = \frac{\|V_{a,\infty}\|}{\sqrt{L_\infty g_\infty}} \tag{2.27}$$

FENSAP-ICE also allows one to choose the droplet drag coefficient correlations, offering four different models,

- Water Default - Empirical correlation for flow around spherical droplets.
- Water Stokes law - Flow around an isolated sphere is valid for very small Re_d (<1).
- Water extended Reynolds - Extended version of the default model for higher droplet Reynolds number.
- Snowflakes - Oblate spheroids used to calculate the collection efficiency of snowflakes.

Another important modeling aspect to be accounted for is the droplet size, as fixing a certain droplet size is an incorrect procedure. For this Langmuir [23] did extensive research on droplet size distributions in clouds, and based on his work DROP3D allows one to choose between monodisperse, Langmuir (A, B, C, D and E) 2.1, Appendix O or a custom distribution.

Instead of solving both air and droplets simultaneously as in a multi-phase flow, FENSAP-ICE solves this separately since the density of water is a thousand times higher than air, solving then the equations in a segregated manner.

The reference conditions for the droplet calculation should remain equal to the airflow solution.

For this appendix, C conditions are chosen (continuous max or intermittent max), based on a certain air static temperature, which will then fix a certain curve on figure 2.19, then an MVD and droplet distribution are defined, fixing the LWC.

2.2.3 Ice accretion

Impinging droplets will contaminate every surface that they impact, this phenomenon can be modeled by a thin liquid film with its height to be determined in every grid point on the solid surfaces, knowing the thermodynamic conditions, part of the film may freeze, evaporate, or sublimate.

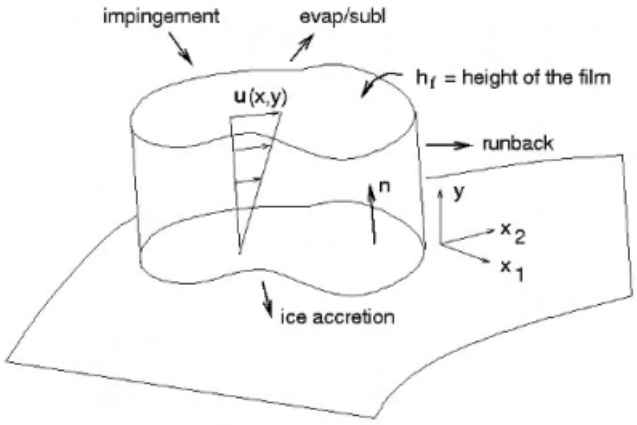

Figure 2.22: Water film model.

A system of two PDEs is solved on all solid surfaces, the first equation solves the mass conservation while the second employs the energy conservation equation.

$$\rho_f \left[\frac{\partial h_f}{\partial t} + \vec{\nabla} \cdot (V_f h_f) \right] = V_\infty LWC\beta - \dot{m}_{\text{evap}} - \dot{m}_{\text{ice}} \tag{2.28}$$

$$\begin{aligned} \rho_f \left[\frac{\partial h_f c_f \tilde{T}_f}{\partial t} + \vec{\nabla} \cdot \left(\bar{V}_f h_f c_f \tilde{T}_f \right) \right] = & \left[c_f \left(\tilde{T}_\infty - \tilde{T}_f \right) + \frac{\left\| \vec{V}_d \right\|^2}{2} \right] V_\infty LWC\beta \\ & - L_{\text{evap}} \dot{m}_{\text{evap}} + \left(L_{\text{fusion}} - c_s \widetilde{T} \right) \dot{m}_{ice} + \sigma\varepsilon \left(T_\infty^4 - T_f^4 \right) \\ & - c_h \left(\tilde{T}_f - \tilde{T}_{\text{ice,rec}} \right) + Q_{\text{anti-icing}} \end{aligned} \tag{2.29}$$

For equation 2.28 the terms on the right-hand side correspond respectively to the mass transfer by water droplet impingement (source), by evaporation, and by ice accretion (sink).

For equation 2.29, the first three terms on the right model are the heat transfer generated by impinging supercooled water droplets, by evaporation, and ice accretion, whereas the last three terms are the radiative, convective, and 1D conductive heat fluxes.

Various icing models such as glaze ice, rime ice, or water film can be used. The glaze ice model is used whenever the stagnation temperature is close to 0°C, forming a type of ice that is visually clear since it is composed of zones of water as solidified and others where a liquid film still exists, this can be observed in the figure 2.7. For low temperatures, the water droplets will immediately freeze trapping air inside the ice structure and giving it the distinct white color of rime ice as can be seen in figure 2.8.

The last model is not used in this analysis as it only deals with temperatures significantly higher than freezing.

The reference icing conditions should be equal to those of the airflow and droplet solutions, with ICE3D only using the reference air Reynolds and Mach numbers for verification purposes.

The icing simulation is then performed at icing air temperature which can be different from the air static temperature used on the previous solvers. Nonetheless most of the time these two parameters are indeed equal but this option comes with the great benefit of allowing simulation of different icing conditions using a single air solution.

The recovery factor (REC) is used to introduce the effect of energy losses due to friction when computing the total temperature being defined as equation 2.30. ICE3D uses then the empirical formula defined in 2.31 to estimate this value.

$$T_{\text{ice,rec}} = T\left[1 + (REC)\frac{\gamma - 1}{2}M^2\right] \tag{2.30}$$

$$REC = \text{Pr}^{1/3} \tag{2.31}$$

The ice density can be defined by three independent models: a constant value, the Macklin formula (equation 2.32), or the Jones (glaze) formula (equation 2.33)

$$\rho_s = 378 + 425\log_{10}(R_M) - 82.3\left(\log_{10}(R_M)\right)^2 \text{ for } 0.2 < RM < 170 \tag{2.32}$$

$$\rho_s = \left\{ \begin{array}{ccc} 0.21{R_M}^{0.53} & R_M \leq 10 & \\ R_M/\left(1.15R_M + 2.94\right) & 10 \leq R_M \leq 60 & (\text{in g/cm}^3) \\ 0.84 & R_M \geq 60 & \end{array} \right) \tag{2.33}$$

With R_M being defined as,

$$R_M = -\frac{d \cdot \left\|\vec{V}_d\right\|}{2\tilde{T}_{\text{wall}}} \tag{2.34}$$

With these variables set, the ICE3D solver employs an explicit time-marching scheme requiring only the specification of two parameters: the total number of time steps (ice accretion time) and the actual time step, which, due to its unsteady behavior needs to satisfy a Courant number lower than one to avoid numerical instabilities, the time step can be automatically set within ICE3D being able to compute the ideal time step for each iteration.

2.2.4 Blade Element Method

The blade element method is based on a 2D analysis of different sections of a propeller blade allowing one to predict the performance of a certain propeller blade configuration easily.

The propeller is divided into several independent sections along the length, and for each section, a force balance is applied which involves the lift and drag with the

thrust and torque produced by the section, similarly, a balance of axial and angular momentum is applied. This creates a system of nonlinear equations that can be solved iteratively for each blade section, and finally by summing the contributions of each blade section an estimate of the propeller performance can be obtained.

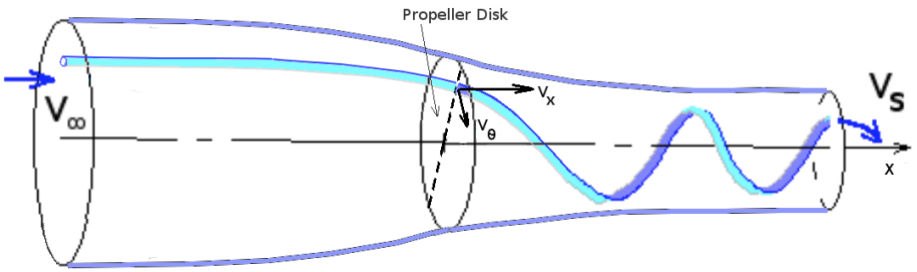

Figure 2.23: Particle trajectory across a propeller disk [71].

This method does not account for 3D phenomena, like shed tip vortices and the effect that they have on performance. Being a 2D analysis, radial-induced velocities due to angular acceleration are also neglected, for this reason, this method usually over-predicts thrust and under-predicts torque, resulting in a 5% to 10% error over the real data.

For the analyzed altitude cases, the thrust required for each of the altitudes and flight speeds is known. Then, by fixing the propeller geometry, the pitch can be iteratively changed until both values converge, with the possibility of giving a 5-10% increase to account for the previous non-modeled effects. With these the values for the swirl factor b highlighted in equation 2.37 can be obtained and given as an input to the fan boundary condition.

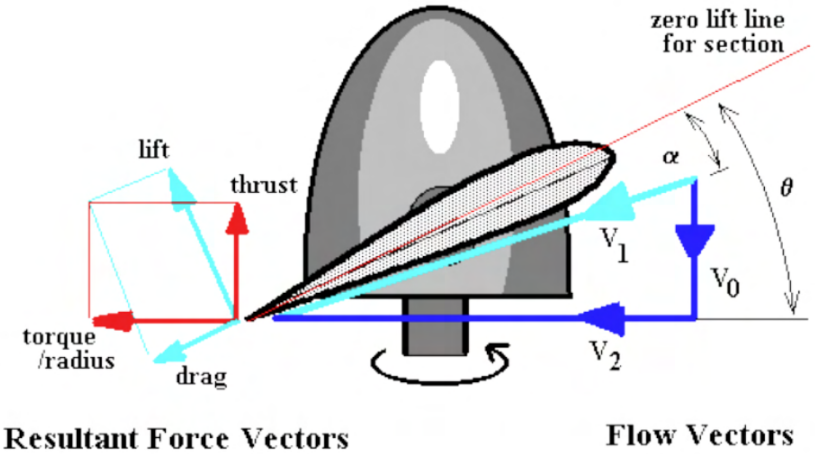

Figure 2.24: Force balance diagram on the blade section [71].

The local flow velocity and the angle of attack for the blade section are then given by equation 2.36, whereas the axial and angular momentum conservation can be

applied both for axial and circumferential directions, with the change in momentum passing through the propeller disk being equal to the trust produced by that blade element, this can be written with equation 2.39. Applying Bernoulli's equation and conservation of momentum, it can be shown that the axial velocity at the disk will be the average of the freestream and slipstream velocities 2.35, making the last step change into equation 2.39.

$$V_0 = \frac{V_\infty + V_s}{2} \tag{2.35}$$

$$V_1 = \sqrt{V_0^2 + V_2^2} \qquad \alpha = \theta - \tan^{-1}\left(\frac{V_0}{V_2}\right) \tag{2.36}$$

$$V_\theta = b\Omega r \qquad V_x = V_\infty(1+a) \tag{2.37}$$

For the angular momentum, it comes that by considering it in conjunction with the axial velocity change the angular velocity in the slipstream will be twice the value at the propeller disk. Thus the change in torque can be written as,

$$\Delta T = \quad \rho.2\pi r.dr \cdot V_0 \times (V_s - V_\infty) \tag{2.38}$$

$$= 4\pi r \rho V_\infty^2 (1+a)a \cdot dr \tag{2.39}$$

$$\Delta Q = \quad \rho.2\pi r \cdot dr \cdot V_0 \times \left(V_{\theta(\text{ slipstream }) } - V_{\theta(\text{ freestream }) }\right) \times r \tag{2.40}$$

$$\Delta T = \frac{1}{2}\rho V_1^2 c \left(C_L \cos(\varphi) - C_D \sin(\varphi)\right) B \cdot dr \tag{2.41}$$

$$\Delta Q = \frac{1}{2}\rho V_1^2 c \left(C_D \cos(\varphi) + C_L \sin(\varphi)\right) B \cdot r \cdot dr \tag{2.42}$$

With these formulations defined, the process runs now in an iterative way, starting with an initial guess for the axial and angular inflow factors, a and b, and then using these to find the flow angle on the blade using equation 2.36, and the blade section properties to estimate the element thrust and torque with equations 2.41 and 2.42, then by equaling these equations to 2.39 and 2.40 a finer estimate for the inflow factors can be achieved and given as an input to the next guess until convergence is achieved.

It is observed during code implementation that convergence is not guaranteed using this method since it is a nonlinear system of equations. If convergence-enhancing techniques are not used and nonlinear airfoil section properties (considering stall, for example) are used, reaching convergence can be much more difficult.

With convergence achieved, thrust and torque coefficients can now be computed, as well as the propeller efficiency and advance ratio; these quantities are defined as in equations 2.43.

$$C_T = \frac{T}{\rho n^2 D^4} \qquad C_Q = \frac{Q}{\rho n^2 D^5} \qquad \eta_{\text{prop}} = \frac{JC_T}{2\pi C_Q} \qquad J = \frac{V_\infty}{nD} \tag{2.43}$$

2.3 Auxiliary Air Inlet Design

The design of the engine and cooling inlets requires a rigid trade-off to meet the aerodynamic performance requirements of the aircraft. A variety of research has been done on the ideal inlet geometry for specific conditions. There are two methods to provide the necessary airflow to the auxiliary equipment. One of them is to bleed the required air from the main engine air diffuser [62]. This method provides high-pressure air to the system, but a larger inlet and, consequently, a larger duct system has to be implemented due to the increasing amount of airflow. More issues like distortion and stability of the flow should also be considered. The other method is to have a separate auxiliary inlet which has the purpose of only providing this auxiliary airflow to the equipment. This separate inlet prevents the main engine design from becoming more complicated with this auxiliary function. On the other hand, these separate inlets may have poor pressure recovery characteristics. As in this research, an inlet geometry is designed with respect to the scope of the electric propulsion cooling of Heart Aerospace's ES-30, and the second method is followed. Flush inlets are explained in terms of pressure recovery and drag characteristics in this section to move on with the suitable inlet geometry according to the need.

2.3.1 Flush inlets

As the research focuses on inlets that are cooling the electric motors of ES-30, the required mass flow ranks as an intermediate value. Due to lower drag characteristics, a flush inlet is preferred to design to meet these requirements. In this chapter, two basic flush inlet types are introduced as given in figure 2.25 and table 2.3.

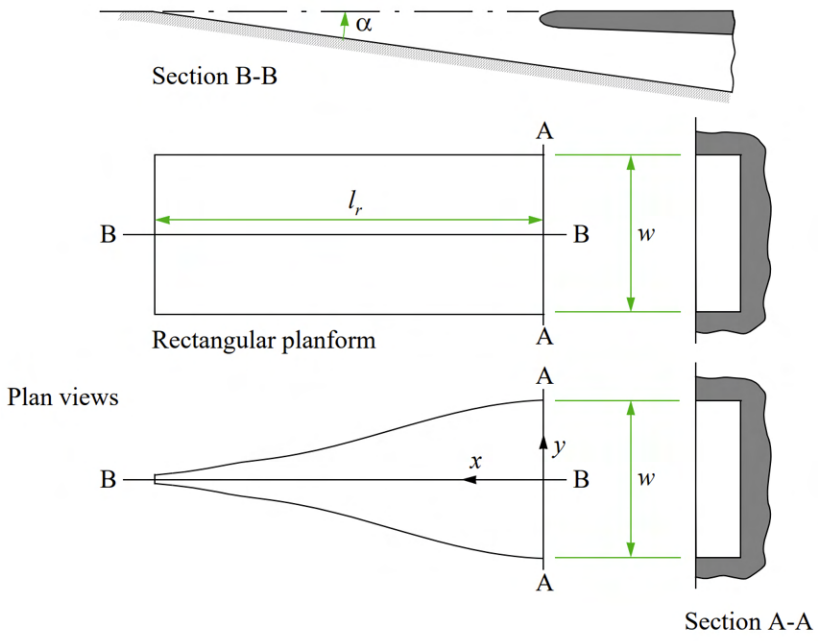

Figure 2.25: Flush inlets [15].

Table 2.3: Ramp coordinates for NACA curved-divergent planform [15].

x/l_r	0.0	0.1	0.2	0.3	0.4	0.5	0.6	0.7	0.8	0.9	1.0
$2y/w$	1.0	0.996	0.916	0.766	0.614	0.466	0.388	0.312	0.236	0.158	0.085

One of the two basic flush inlet types is an inlet which has a rectangular ramp planform as shown in the figure 2.26 on a 737 Dreamliner [64]. This inlet is rather easier to manufacture. The second design is an inlet that has a NACA curved-divergent ramp with an extremely swept planform that is shown in figure 2.27 on a 737 [63]. This sweep aims to generate strong vortices on the ramp sides to thin the boundary layer on the center of the ramp with the purpose of decreasing pressure loss. Even though these vortices also cause losses, the net result is a higher pressure recovery compared to other inlets.

Figure 2.26: Rectangular ramp inlet on a 787 Dreamliner [64]

Figure 2.27: NACA curved-divergent ramp inlet on a 737 [63]

A method for predicting the drag of certain types of flush inlets is developed in ESDU [15]. The drag calculations are valid for ramp angles, $\alpha \leq 11.5°$. From the derivations [15], the best pressure recovery comes from an inlet width-to-depth ratio of around 4 and a ramp angle of 7°. The derivations of flush inlet designs are done by following the notations presented in figure 2.28.

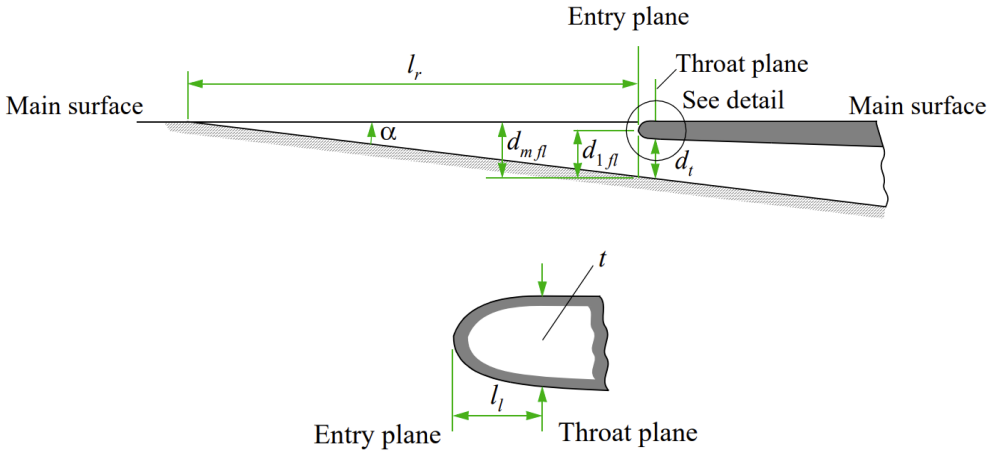

Figure 2.28: Flush inlet geometry parameters [15].

2.3.1.1 Pressure recovery

For the curved-divergent inlets, the ram pressure efficiency is highly dependent on the boundary layer thickness to throat-to-height ratio, θ/d_t. When the geometry is fixed, this efficiency varies with the mass flow and has a peak value, η_m. The modified mass flow ratio, which is defined as $\mu = \dot{m}d_{1fl}/\dot{m}_0 d_t$ has a specific value at this peak value of η_m. This value can be calculated from ESDU.

2.3.1.2 Comparison of ramp planform effect

The effect of ramp planform is compared with a rectangular, a curved-divergent, and an intermediate case of straight-divergent ramp with a closure ratio of 0.25. The rectangular ramp generates the lowest drag in every mass flow while having lower pressure recovery in the lower mass flow values. Between curved-divergent and straight-divergent ramps, the curved-divergent has a higher pressure recovery in the lower mass values while having a little more drag.

2.3.1.2.1 Operating at full mass flow

A flush inlet with a curved-divergent ramp that operates at full mass flow is sized similarly to the rectangular ramp. However, the dimensions might be overestimated since the ramp planform can mitigate the boundary layer effect.

2.3.1.2.2 Operating at maximum efficiency

There is a special process for the inlets designed to operate at maximum efficiency given in the ESDU.

These two operations are compared with the same parameters where the drag coefficient and pressure recovery characteristics are presented in the ESDU. In every mass flow, the inlet that operates at full mass flow has a 15% lower drag than the inlet operating at maximum ram pressure efficiency. On the other hand, the full-mass-flow inlet has an 18% lower efficiency. Therefore, it is significant to consider the priority and role of the inlet to move on with the sizing.

3
Methods

The research is carried out by merging two methodologies and adapting them to the current task. One of them is a concept development process developed by Ulrich et al. [59], and the other methodology for a design and innovation process is presented by Design Council [60], which is called the Double Diamond. A general layout of this concept development process is shown in the diagram 3.1.

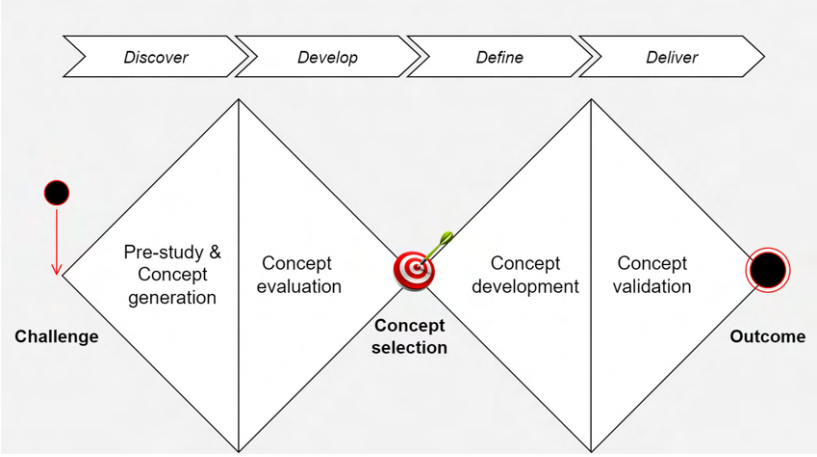

Figure 3.1: Diagram of the methodology of the research.

The solution to a challenge starts with a pre-study discovering the problem. In this initial part, defining the purpose and scope is a must to understand the problem within the boundaries. For instance, designing an ice protection system for an aircraft is an extensive topic. The type of aircraft, the airframe component to protect from the ice, and the icing conditions to consider are some limiting examples. The aim and scope as given in the sections 1.2, 1.3, ensure the generated concepts are specific to the needs. After this definition, the target specifications are going to be established. This process contains four steps:

1. Listing of metrics.
2. Collecting competitive benchmarking information.
3. Setting ideal and marginally acceptable target values.
4. Reflecting on the result and the process.

A list of metrics in this research is constituted from a variety of sources. The flight and atmospheric conditions are provided by Heart Aerospace and the geometry of the model is built from the theoretical basis according to the need of ES-30.

Benchmarking is to explore existing solutions that are already in the market and being used. To develop a suitable ice protection system on an electric aircraft air intake for cooling purposes, research is conducted on typical ice protection systems that are used on the same type of inlets. Ideal and marginally acceptable target values are defined with respect to the need and capacity of the ES-30. They guided the solution through the design process. The reflection step is to ensure all the target values are possible to achieve with the defined metrics or not that unfamiliar with the existing solutions. This planning step is discussed with the industrial supervisor at Heart Aerospace to confirm the initial target specifications.

3.1 Concept Generation

The research continues with the concept generation step after the pre-study. Five steps for this part are defined by Ulrich et. al. [59] as shown in the diagram 3.2.

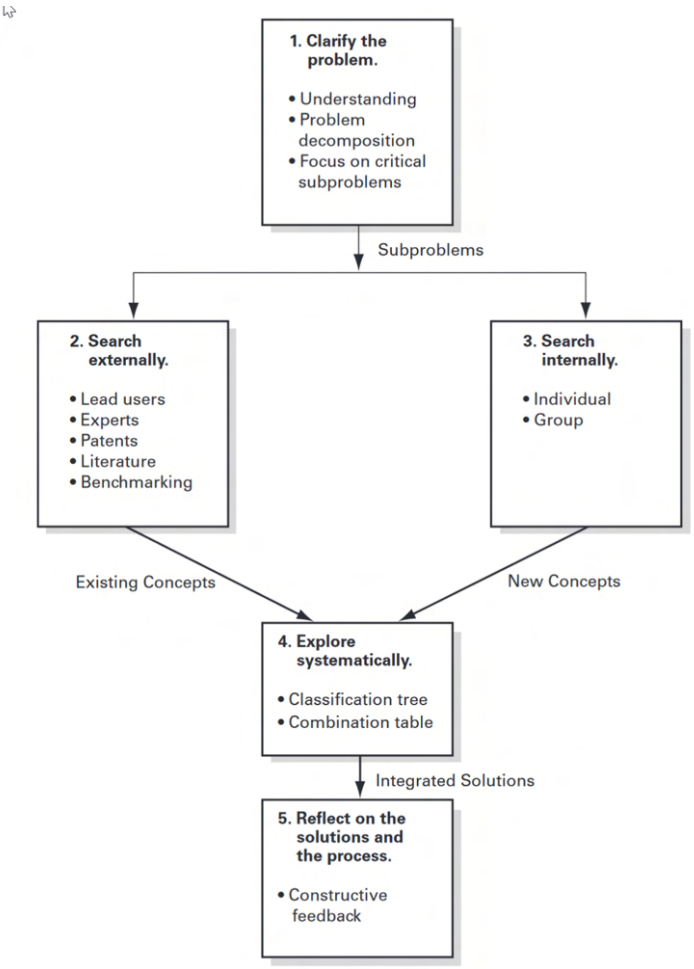

Figure 3.2: The five-step concept generation method [59], page 120.

Concept generation starts with clarifying the problem by decomposing it into sub-problems and focusing on the critical ones. In this research, the most feasible ice protection system solutions are expected according to the selection metrics. The

solution is limited as the aircraft does not have compressors, consequently bleed air as most aircraft have. This process continues with the search externally and internally. As the external sources, literature research has been done. The investigated topics are shown in the table 3.1.

Table 3.1: Literature research map

General	Icing on intakes	Intake design and analysis	Thermal modelling and IPS
Atmospheric icing	NACA inlet icing	Air intake lip design	Battery cooling systems
Ice accretion on aircraft	Ram inlet icing qualifications	Intake aerodynamics	Ram air heat exchanger
Icing conditions CS-25	Power estimation for anti-icing	CFD analysis of air intake	Thermal management system
Icing certification and standards	Air intake protection grids	Submerged air intake design	System architecture of thermal management
Ice protection systems	Icing testing on intakes	Numerical simulation of aircraft icing	Environmental control system of aircraft
Electric/hybrid aircraft ice protection	Computational integration of icing physics	Validation of ice accretion codes	Liquid/air cooling systems

While the external search diversifies around this map, the internal search has been done with the Heart Aerospace team regularly. The preferences due to simplicity, energy consumption, feasibility for the implementation in the nacelle, and the implementation are discussed. Representative system architectures are used throughout this concept generation process.

3.2 Concept Selection

A representative schema of the concept selection part is given in the figure 3.3.

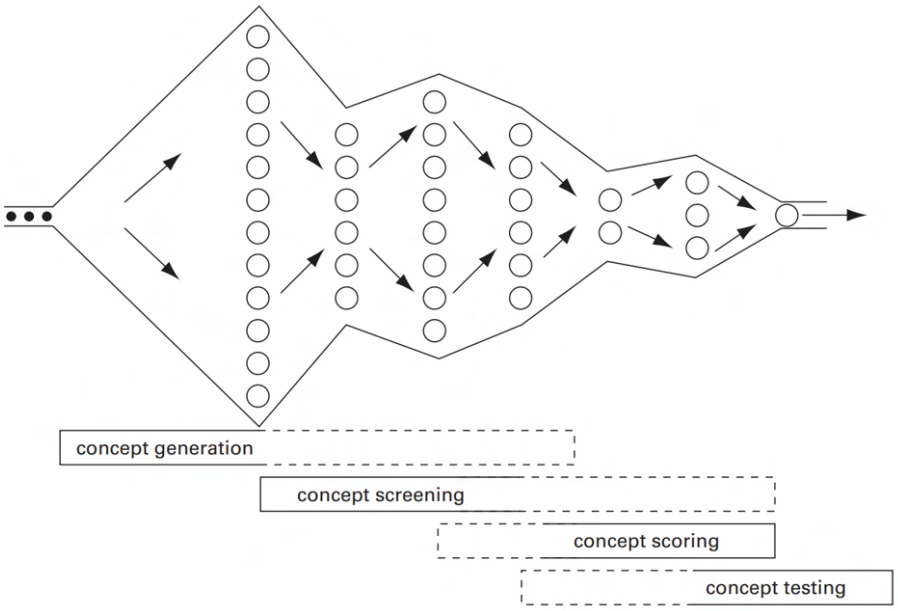

Figure 3.3: Concept evaluation ending with the concept selection [59], page 148.

It starts with the concept screening and moves on with the concept scoring. For both steps, a decision matrix is requisite where the criterion in the concept screening

allows rather simpler evaluation and elimination. In the concept scoring, an elimination can be done after rating and ranking the concepts in detail.

Ulrich suggests following a six-step process for evaluating the concepts which is given in figure 3.4.

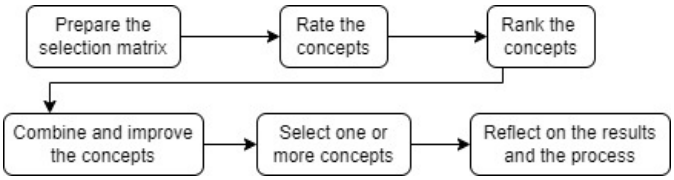

Figure 3.4: Concept evaluation process by Ulrich et. al. [59], page 149-150.

The selection matrix is significant to compare the relative strengths and weaknesses of the concepts. in this research, the selection criterion plays an important role in implementing the solution to a novel product. Those key indicators are defined in the result part of concept evaluation in section 4.2. An example list of selection considerations for the engine inlet ice protection systems is given in the Icing Handbook [49], shown in the figure 3.5.

	Hot Air Anti-Icing	Hot Air De-Icing	Electro-Impulse De-Icing	Fluid Anti-Icing	Fluid De-Icing	Electro-Thermal Anti-Icing	Electro-Thermal De-Icing	Pneumati De-Icing
Aerodynamic effects of ice cap		X	X		X		X	X
Aerodynamic effects of runback ice	X					X		
Ice ingestion (de-icing)		X	X		X		X	X
Ice ingestion (runback)	X					X		
Bleed air penalty	X	X						
Weight penalty	X	X	X	X	X	X	X	X
Weight for additional electrical power generation						X	X	
Power penalty	X					X	X	
Fluid costs				X	X			
Maintenance costs	X	X		X	X	X	X	X
Non-recurring costs	X	X	X	X	X	X	X	X
Fluid ingestion and toxicity				X	X			
EMI			?			X	X	
Noise	?	?	X					
Fatigue	?	?	X					
Development risk			X	X	X	X	X	

Figure 3.5: Significant engine inlet ice protection selection considerations [49].

As the criteria are evaluated by only existing or not in the figure 3.5, it can be an example of the concept screening. In the concept scoring, the selection matrix includes a more detailed evaluation such as weights of the criterion or a wider scale of scores. For instance, a weight penalty can be significantly critical for the performance of an aircraft while the noise affects the pleasant travel of the passengers.

After rating and ranking the concepts, the net scores list the most preferable options. In this stage, it is valuable to check if it is possible to combine any of the concepts and reach an improved solution. As the selection matrix identifies the strengths and weaknesses, it is easier to distinguish a strong feature of one solution and merge it with another strong concept that would be upgraded by it.

3.3 Concept Development

To come up with innovative and suitable ice protection system architectures, it has to be known how critical the ice accretion is in the specified region. This part of the concept generation is carried out with an analysis and computation process which is given as a flow chart in the figure 3.6.

There are several types of inputs used, such as flight inputs, which are taken from ES-30's flight information [61]. Using this flight envelope, the icing atmosphere inputs that ES-30 is going to experience are obtained by intersecting with the FAR icing envelopes given in the figures 2.20. The critical conditions to simulate and design the inlet accordingly are explained more in the result section of 4.3.1. According to the purpose of the inlet, the inlet geometry is designed with the flight and atmospheric inputs and the characteristics of the inlet such as pressure recovery or drag characteristics. The following method is explained theoretically in the section 2.3.

With the inlet geometry, the aerodynamic flow solution is obtained. While there are many ice accretion softwares, they are explained and compared in the section 2.2. As the ice accretion software used in this research is FENSAP-ICE, the flow solver is chosen as ANSYS Fluent so as not to have any problems with the flow implementation. For the droplet impingement analysis, DROP3D is used with the flow field obtained by ANSYS Fluent. Then, ICE3D has given the ice accretion shape around the inlet by iterating the droplet impingement data taken from DROP3D. The detailed methodology of the flow solution is explained in the next section.

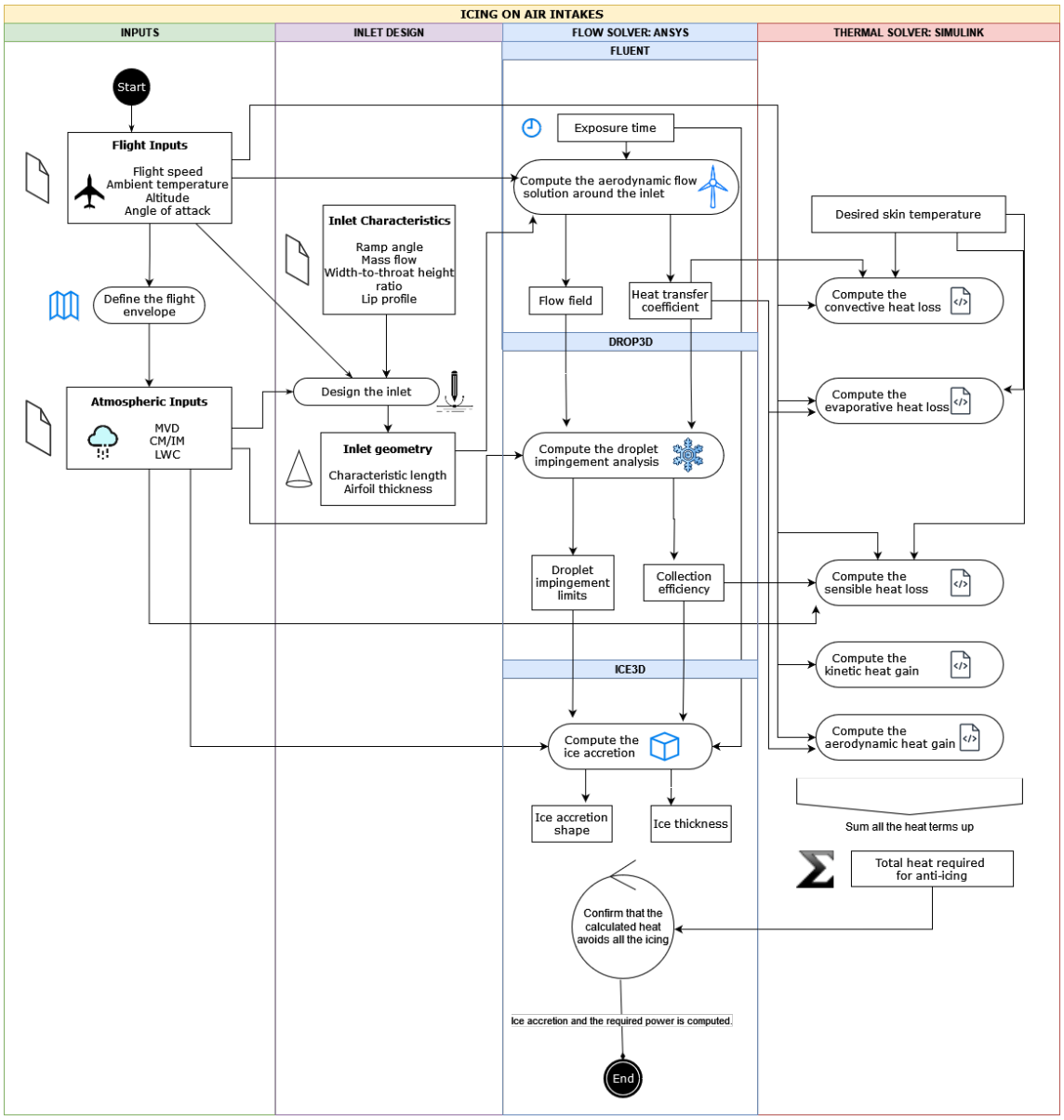

Figure 3.6: Flow chart of the icing computations.

3.3.1 CFD Model

It was previously introduced that Fluent is used as the main flow solver due to the higher modeling freedom that it gives. Alongside it, FENSAP-ICE is then used to get the actual icing results for this work.

Specific experimental data for this test setup is not publicly available, making its validation challenging, for which one can only rely on good modeling and the mitigation of numerical errors. To mitigate numerical errors a 2D model was set containing a NACA0012 airfoil profile, being a well-studied profile [42], the validation of this experimental setup with the computational one.

After this initial analysis and validation with the paper [42], an increase in modeling confidence could be achieved.

Then, moving towards the final subject to be studied, simpler inlet designs 3.7 and 3.8 are started to be analyzed towards the final test solution given in the Appendix C.1 and C.2 at each design.

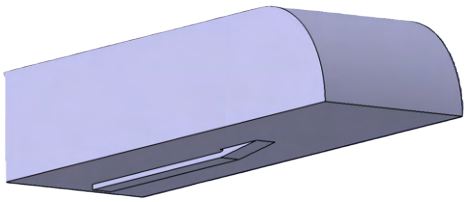

Figure 3.7: Initial geometry.

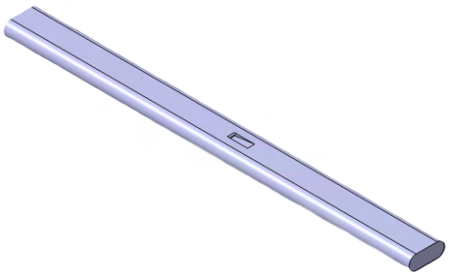

Figure 3.8: Shaft-like geometry to allow actuator disk modeling.

3.3.1.1 Geometry & domain

For the initial 2D analysis setup, a NACA0012 geometry is used, with the airfoil profile having the same geometry parameters used in [42]. For the domain, it is important that its limits extend as far as possible or that no disturbances by the imposition of the boundary conditions at the far-field are felt on the airfoil. Thus, the domain size is an important consideration to take into account to decrease numerical error and improve accuracy. For this, a domain that extends 24 chords downstream of the airfoil and 12 chords either upstream of it or perpendicularly of it, due to C shaped domain, is used 3.9

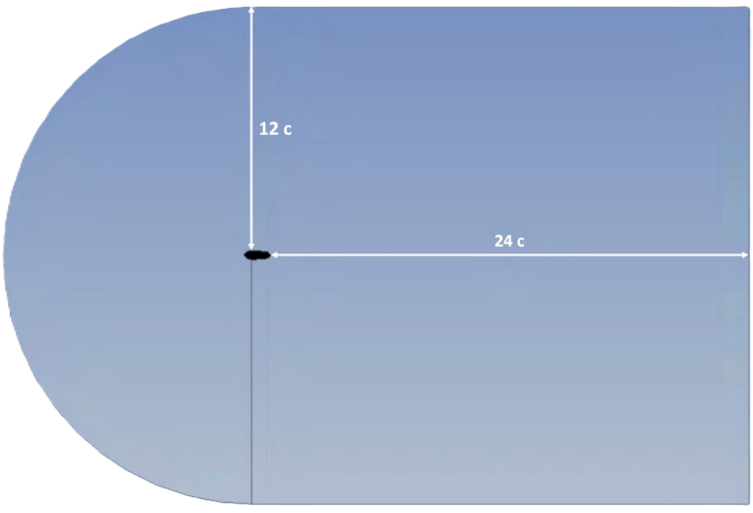

Figure 3.9: Domain size used for initial 2D simulation.

In the NACA duct case, the inlet geometry is built based on the guidelines provided by ESDU 86002 [15], this document focuses on either the mass flow characteristics or efficiency of this type of inlet, meaning that it provides general dimensioning to achieve a certain performance but the actual lip design, meaning the coordinates are not available, thus another document [65] which has available the lip construction coordinates as seen in figure 3.10, the respective coordinates for each station are shown in Appendix B.1.

Two common types of ramps can be used in these designs, either parallel or divergent 2.25. Heart Aerospace requires that one should be able to open or close mechanically this inlet based on cooling needs, thus it is chosen that a parallel ramp duct would be more feasible to implement the said mechanism later.

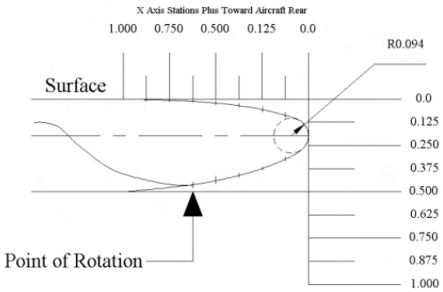

Figure 3.10: Lip geometry [65].

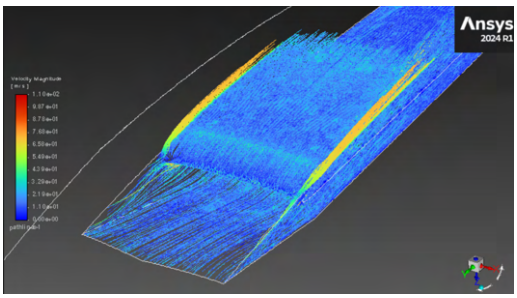

Figure 3.11: Vortex development near the side walls of a divergent ramp NACA duct [72].

This comes with an increase in aerodynamic drag and mass flow penalties since the vortices generated near the exterior wall corners as seen in figure 3.11 are weaker, which is the main working principle of it. They do not push as much mass flow into the inlet, which can make these vortices develop through the outside part of the nacelle, increasing thus the aerodynamic drag.

The lip coordinates that are previously referred to need to be multiplied by the desired inlet entry height, for which fixing the desired aspect ratio defines the remaining inlet geometry parameters.

Initially, various geometries were used, and then iteratively the design was modified, as modeling approached a more real test scenario. The final design in figures 3.12 and 3.13 was achieved and used to perform this analysis.

It is known that these types of inlets for normal applications, meaning free stream faced, surface submerged, and without any meaningful flow disturbances, are highly dependent on the boundary layer growth, resulting in momentum loss inside of the boundary layer and affecting the achieved mass flow. Their positioning on a surface, especially when compared to experimental results, can be of high importance as studied by [73]. However, since this inlet will be positioned on the aft of the propeller, which is directly affected by the swirl motion of the fluid behind it, the boundary layer growth influence can be assumed of less importance as compared to the swirl

effect that creates flow asymmetries on the inlet as well as changing the droplet impingement distribution. For this reason, the model represented in figure 3.13 was built and used for most of the work. This model aims to represent the full nacelle of the ES-30 including the propeller, modeled here as an actuator disk boundary condition.

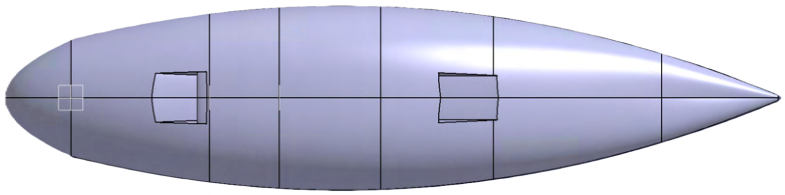

Figure 3.12: Nacelle bottom view.

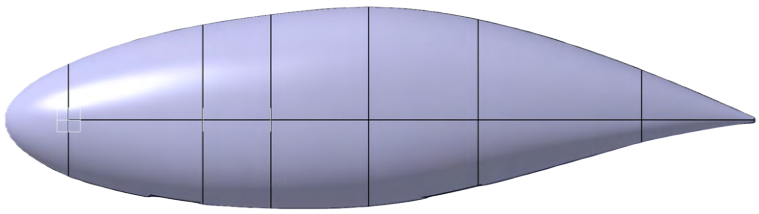

Figure 3.13: Nacelle side view.

The ES-30 propeller diameter, marked as D, is used as an interface surface to model the actuator disk, whereas the rest of the domain's physical limits are defined in figure 3.14. Alongside the physical limits, 3 different refinement zones were used in places where higher gradients are expected, leading to a need for finer mesh, their dimensions can also be observed in figure 3.14 as in Appendix C.4 for the inlet region near the nacelle surface.

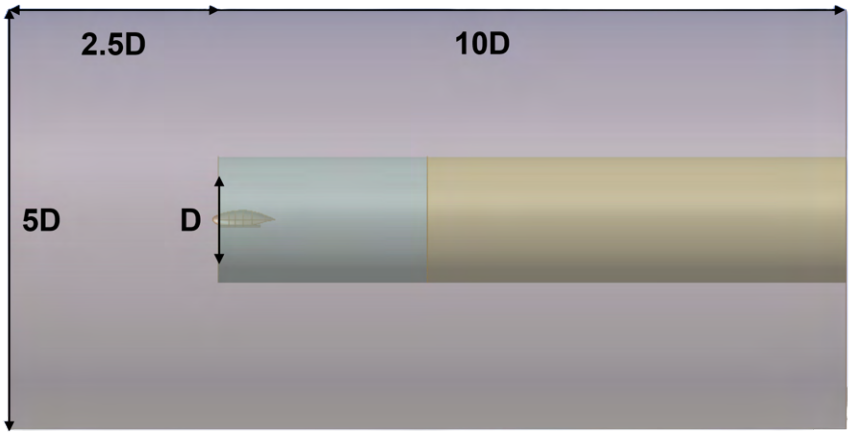

Figure 3.14: Nacelle domain limits.

3.3.1.2 Mesh generation

The integrated ANSYS mesh generator module was used to discretize the domain, for which table 3.2 represents the main parameters used to create it. Convergence issues arose while doing computation, for which a mesh improvement was made, especially in near-wall areas where high gradients were affecting the solution, this was fixed by using the said refinement zones with a higher number of elements or by using other computational techniques, such as the pressure velocity coupling method. Better convergence was also verified by using the polyhedral mesh option in Fluent [66], nonetheless, FENSAP-ICE is only able to read tetrahedral or quadrilateral 3D meshes, thus the polyhedral element technique was not used, even if it showed significant improvements in solution convergence due to its higher number of surfaces which spread information across the domain faster.

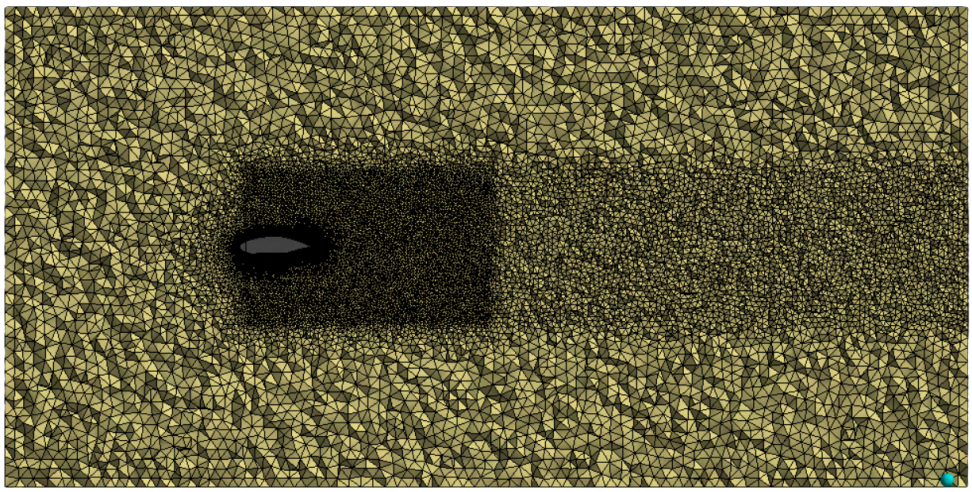

Figure 3.15: Mesh.

These mesh configurations result in an average y+ on the near-wall regions of 110 and 32 in the near lip area. Because of this, this mesh is intended to use wall functions to solve the flow in near-wall regions, as well as the thermal boundary layer, this is computationally cheaper to do and the accuracy of this near-wall model has been the focus of a lot of work across the years, nonetheless, it still represents a model and higher model fidelity ones should be tested to compare the results obtained by both solutions for comparison and validation purposes.

Table 3.2: Used mesh parameters.

Mesh Parameter	Element Size (mm)	Number of Divisions	Growth Rate	Region
Body Sizing	250	-	1.2	Exterior Domain
Body Sizing	125	-	1.2	Near Wake Region
Body Sizing	100	-	1.2	Far Wake Region
Body Sizing	50	-	1.05	Propeller Surface
Face Sizing	5	-	1.1	Duct Wall Region
Face Sizing	5	-	1.2	Nacelle Near Wall Region
Face Sizing	2.5	-	1.1	Aft Nacelle Near Wall Region
Face Sizing	1	-	1.1	Lip Near Wall Region
Edge Sizing	-	50	1.1	Ramp Point of Rotation Region

3.3.1.3 Setup

The setup performed on Fluent was done using a segregated pressure velocity coupling and the turbulence modeled with $k - \epsilon$ RNG and standard wall functions, introduced earlier, with the assumption that the flow is fully turbulent after the propeller disk surface.

The energy conservation equation is used to enable modeling of the flow as an ideal gas, avoiding then using a constant air density since different flow solutions were performed for different flight altitudes.

The applied boundary conditions are specified in table 3.3, while Appendix C.3 shows the respective details of these surfaces.

Being a low-flight speed aircraft, it is known that the maximum Mach number will be approximately 0.3, for which it is then expected that some regions of the flow will have locally higher Mach numbers. Nonetheless, it is expected that due to the geometry shape this increase in velocity was not going to be high, which proved to be true later. Velocity magnitude vectors in figure 4.22 show that maximum velocity occurs near the ramp entry with the average flow field velocity being considerably below the maximum value and in the vicinity of the compressible flow criteria, supporting the previous statement. For this reason, it was assumed that the error induced by compressibility effects was low; thus, the velocity inlet boundary condition was used.

Table 3.3: Used boundary conditions.

Surface Name	Boundary Condition Type
Inlet	Velocity Inlet
Outlet	Pressure Outlet
Farfield	Pressure Farfield/Velocity Inlet
Nacelle	Wall
Propeller	Fan

Boundary conditions were applied based on the used test matrix, marked with blue and green dots, in figure 3.16. These test points and their characteristics are resumed in Appendix B.4.

In total, 38 different icing test points were evaluated, for which it was assumed that the biggest change in the flow solution was coming from either the velocity or altitude changes. Three different flow solutions were performed for three different altitude steps studied.

Figure 3.16 represents the flight envelope of the ES-30 intersecting with continuous maximum and intermittent maximum icing envelopes, with these different test points, marked in red triangles for intermittent maximum conditions and blue circles for continuous maximum conditions, these represent the points accessed during the analysis.

One extremely relevant modeling aspect is the swirling momentum given to the flow by the propeller, this can be modeled in different ways either by using the complete geometry of the propeller blades and defining a dynamic mesh that interacts with the static mesh due to the rotation of it, which eventually comes at the cost of higher computational resources but can provide better accuracy, or if one is willing to compromise loss of accuracy to lower computational cost, an actuator disk model can be implemented where an infinitesimal surface is created in the domain, then a pressure change occurs across it due to the gaining of angular momentum. These parameters need to be calculated and given as input to the solver, for this the blade element method introduced in section 2.2.4 was used.

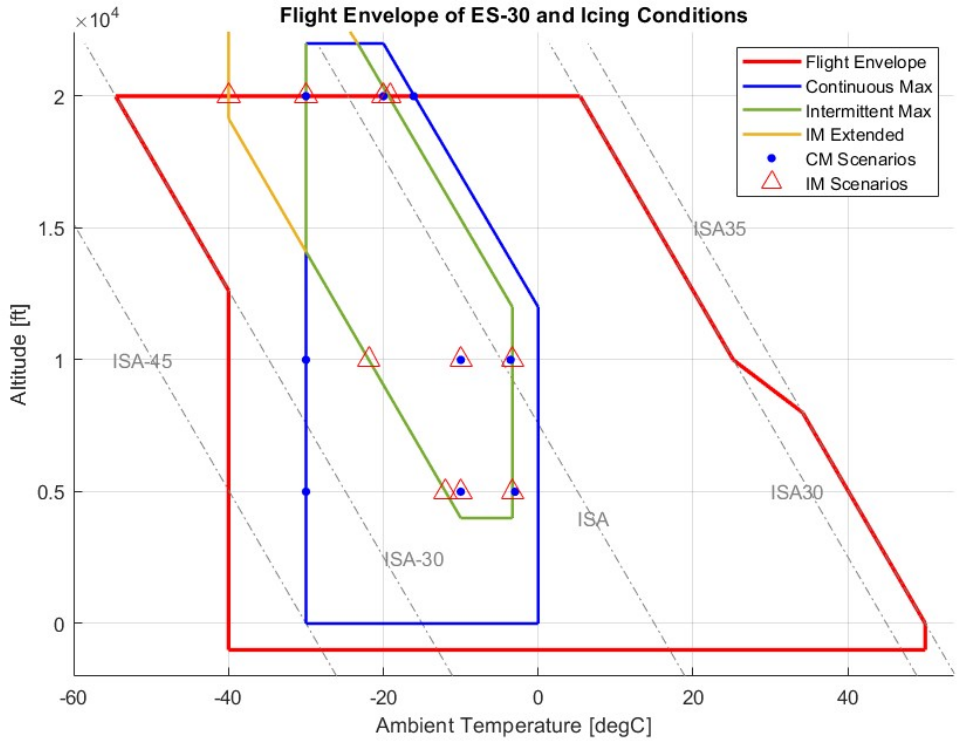

Figure 3.16: ES-30 flight envelope and icing envelopes.

The used pressure-velocity coupling scheme was SIMPLE for most test scenarios, which requires more iterations to achieve convergence but improved numerical stability, since the flight speeds are low, achieving at cruise altitude Mach 0.3 which is in the boundary of compressible flow assumption. The coupling between the physics phenomena can be assumed to be low, making the use of a coupled solver unnecessary.

The spatial discretization was done as defined in table 3.4, with the under-relaxation factors being maintained with the standard solver values. For the initialization procedure, the full multigrid initialization method was used which by creating n grid levels, allows a better initial solution estimation by solving these n grids from coarser to fine, this then helps to increase the convergence rate which is beneficial for the used pressure velocity scheme, additional details for this initialization method can be found in [66]. For the turbulent kinetic energy and dissipation rate since the $k - \epsilon$ RNG model was used which is more prone to unstabilize on adverse pressure gradients, these quantities were first discretized using a first-order upwind scheme, and after stabilizing the solution a second-order upwind approach to enhance solution accuracy. No time discretization technique is used since a steady state solution was achieved with the residuals for a cruise speed of 140 knots (KCAS) and an altitude of 5000 ft being shown in figure 3.17.

Table 3.4: Spatial discretization used across flow solutions.

	Spatial Discretization
Gradient	LSCB
Pressure	SO
Density	SOU
Momentum	SOU
Turbulent Kinetic Energy	FOU/SOU
Turbulent Dissipation Rate	FOU/SOU
Energy	SOU

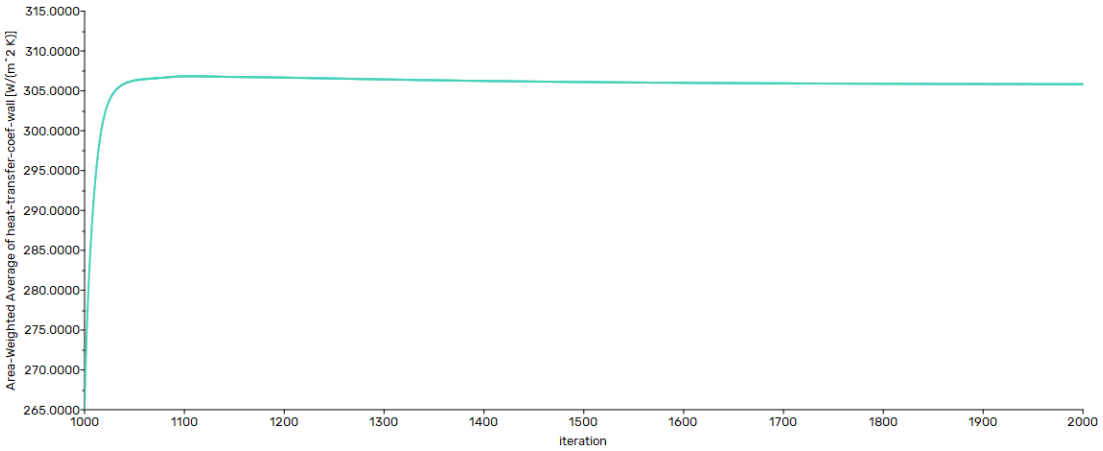

Figure 3.17: Residuals convergence for 140 knots (KCAS) at 5000 feet.

FENSAP-ICE setup was performed using 2 of the previously introduced models, DROP3D and ICE3D respectively. DROP3D receives the grid and solution files from Fluent and then the following parameters in table 3.5 were chosen, whereas for the conditions the module receives the air velocity, static pressure, static temperature, and droplet diameter, for which using Appendix C [14] it can define the LWC, water density was kept at 1000 kg/m^3 and the Langmuir D droplet distribution was used for every test point. The module also requires the input of the droplet initial solution, which should be equal to the airflow velocity inlet conditions given to Fluent if dry initialization is not used.

For the boundary conditions, the reference conditions from Fluent were imported adding now the LWC content in the atmosphere. The fan boundary condition was disabled since the flow solution already has these influences modeled, which is affecting the pressure and velocity values across this boundary.

Table 3.5: Model parameters used on DROP3D.

Physical model	Droplets
Particle Type	Droplets
Droplet drag model	Water - Default
Particle Thermal Equation	Disabled
Vapor Model	Disabled
SLD	Disabled
Particle Reinjection	Disabled
Body Forces	None

For the ICE3D module, the used model parameters can be found in table 3.6. Glaze ice or rime ice models were used accordingly depending on if the icing temperature was near 0 degrees Celsius, and later to verify the Simulink model if heat flux boundary conditions were applied to the lip surface. The conditions were kept similar to the DROP3D module, where besides the ones already introduced, ICE3D also receives input of the temperature recovery factor which is kept at 0.9, following equation 2.19, and the ice density type was changed between Jones rime or Jones glaze accordingly as before.

In this module, only the wall boundary conditions were defined, with all of them kept as adiabatic except for the lip surface, which was changed between 0 heat flux and a target heat flux for model verification. Lastly, the time of ice accretion varied between 6 and 8 minutes.

Figure 3.18: Lip surface.

Table 3.6: Model parameters used on ICE3D.

Ice - Water model	Glaze - Advanced or Rime
Heat Flux Type	Classical
Concavity Fix	70 degrees
Roughness Output	Disabled
Beading	None
Compute EID	Enabled/Disabled
Ice Crystals	Disabled
Ice Shedding	Disabled
Body Forces	None

3.3.1.4 Output

Heat transfer coefficients are computed through Fluent over the lip surface area and fed into Simulink, which previously was computing it using cylindrical surface empirical correlations [37]. The aerodynamic effect of the inlet design is not evaluated in this work, therefore, no more variables are extracted from Fluent.

On FENSAP-ICE, the outputs from DROP3D are the collection efficiency of each cell surface on the nacelle alongside the near-wall LWC content. Then ICE3D uses these values to compute the mass of water caught by each cell surface and then uses the thermal energy equation to determine if freezing occurs or not. After this final solver module, different properties can be extracted. For the focus of this work, the following properties are interpreted as the most important for model validation and IPS initial design.

- β - Collection Efficiency
- h - Heat transfer coefficient
- m_{local} - Rate of Water Impingement
- Ice Thickness
- Ice Shape
- Total air temperature

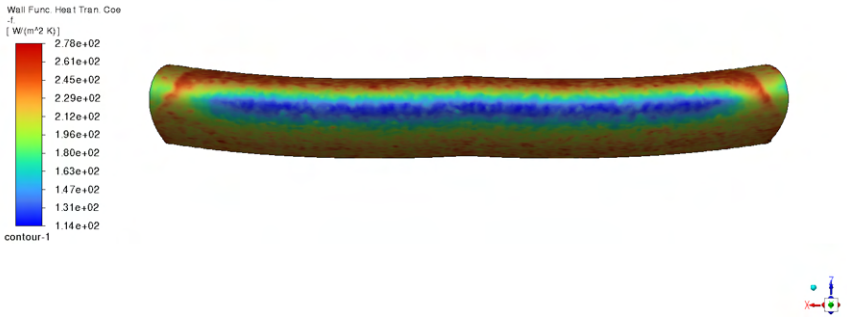

Figure 3.19: Heat transfer coefficient map using wall functions.

When glaze ice conditions are used, ICE3D needs to compute the extended icing data introduced in 2.2.3 for this, and based on the ice accretion rate new values for HTC are computed.

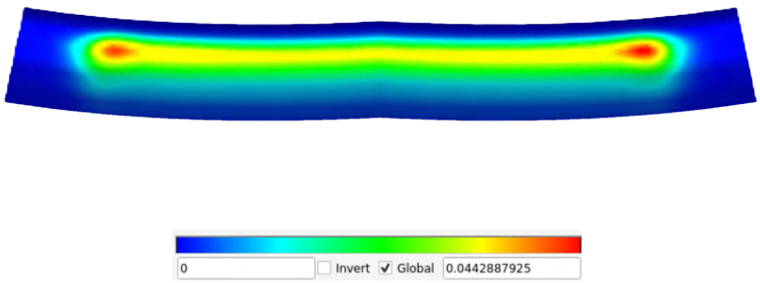

Figure 3.20: Impingement rate (m_{imp}) output from ICE3D (glaze ice) for test case 1.

The computed wall function HTC, which is defined by using empirical wall correlations to estimate the temperature profile in near-wall regions, then for adiabatic conditions the near wall temperature gradient can be calculated and consequently the heat transfer coefficient estimate originating the colormap surface shown in figure 3.19.
From figure 3.20, it is possible to observe the asymmetry (although subtle) on the mass of impinging water on the surface caused by the swirl motion of the fluid; this is dependent on the collection efficiency. One can also obtain from ICE3D the actual ice map of the surface, which for these same conditions can be observed in figure 3.21.

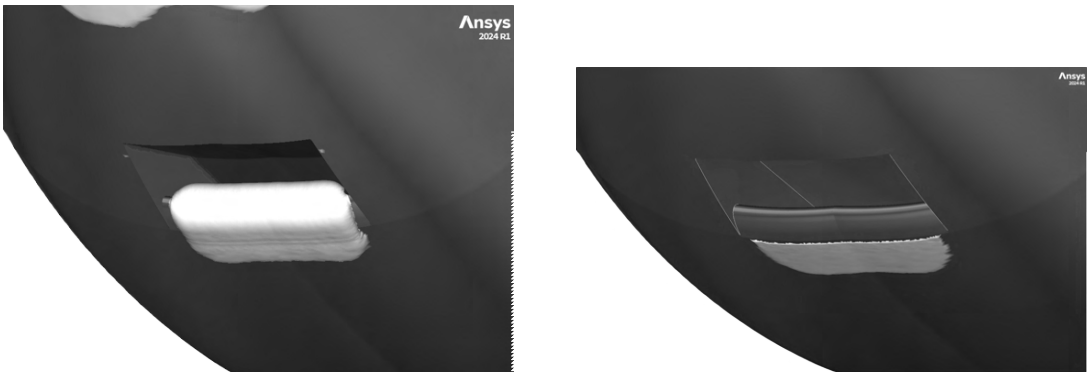

(a) Unheated. **(b)** Heated.

Figure 3.21: Ice cover aft of the lip for 5000 feet, $M = 0.23$, $T_s = 270.15\ K$, $LWC = 0.574\ g/m^3$, $MVD = 20\ \mu m$.

3.3.1.5 Mesh dependency study

Mesh dependency studies were performed to evaluate solution convergence. It is a critical part of any computational simulation process, it ensures the minimum mesh size not to have variation on the coefficients caused by the mesh, ensuring its accuracy and reliability.

For the study, 5 meshes were generated for the same domain having the refinement zones stated in 3.7. The first mesh evaluated has a size of 4.7 million elements, with the main parameters being also described in table 3.7; after this, the size of each

refinement zone is proportionally decreased until the total number of elements is roughly doubled. The same procedure is applied to the remaining meshes. The 5 meshes had then respectively 4.7 (Number 1), 11.6 (Number 2), 20.5 (Number 3), 50.8(Number 4), and 67.7 (Number 5) million elements.

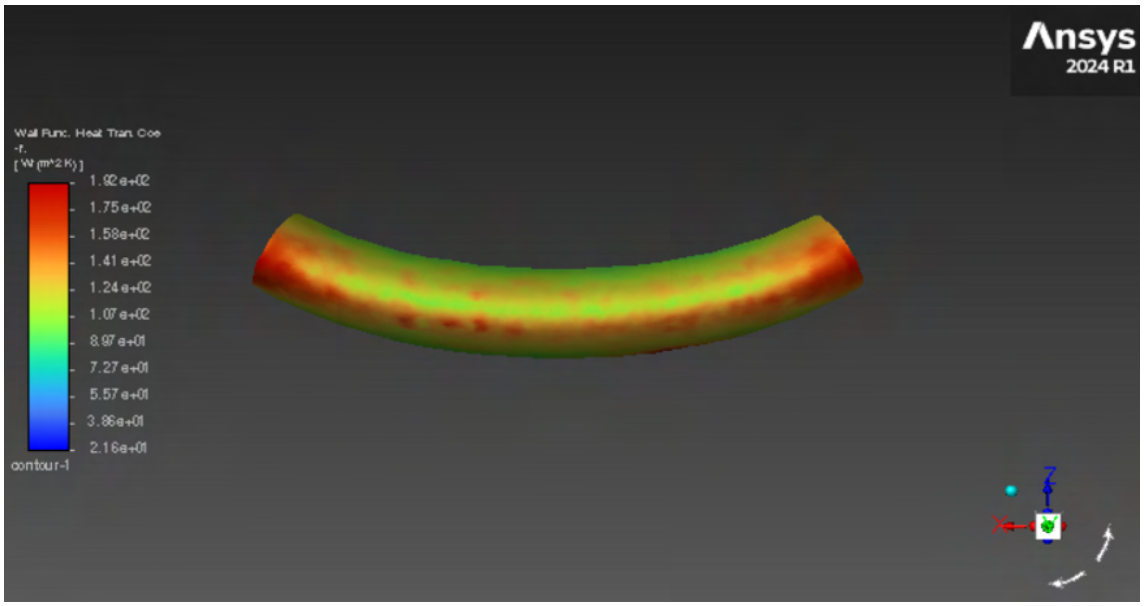

(a) Mesh number 1.

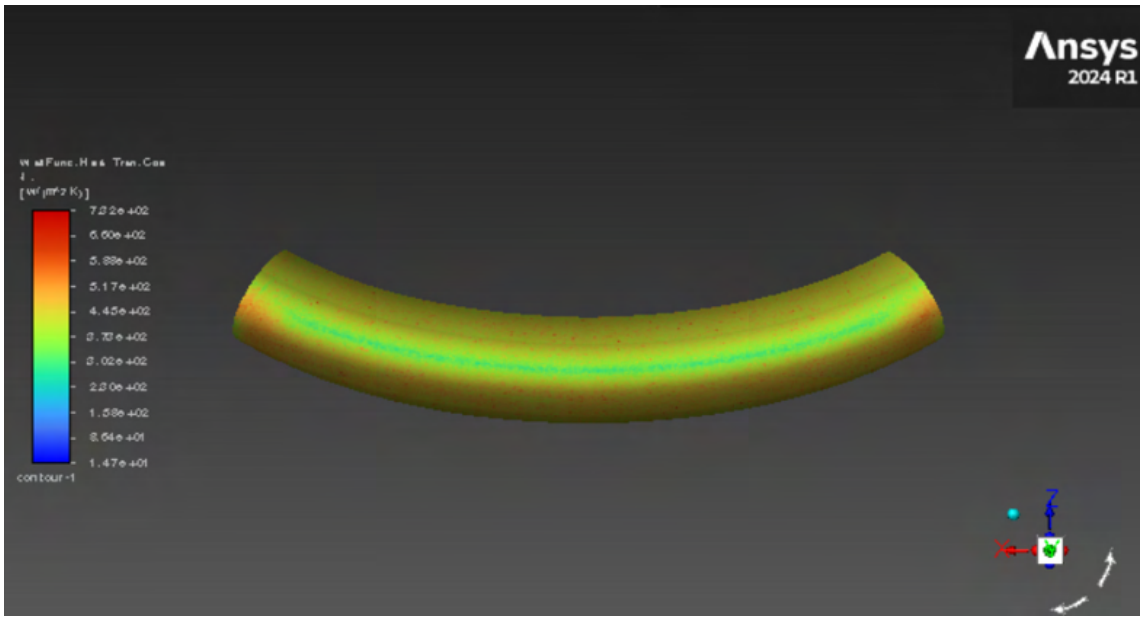

(b) Mesh number 5.

Figure 3.22: Heat transfer coefficient contours on lip surface.

Figures 3.22 and D.4 show the lip heat transfer coefficient contours change across mesh refinements while figure 3.24 shows the weighted average of the value on the lip's surface across the different studied meshes. This plot shows unexpected behavior, especially in mesh number 5 where it was expected convergence of the heat

transfer coefficient into the value range obtained in mesh numbers 3 and 4. Since the boundary layer did not change across mesh refinements, the computed heat flux should not show these large variations. This means that near wall zones especially in mesh number 5 are creating numerical errors, possibly due to mesh quality near the interface between the lip and the side walls of the ramp where the parabolic surface from the lip intersects tangentially the side wall creating high skewness elements in these zones.

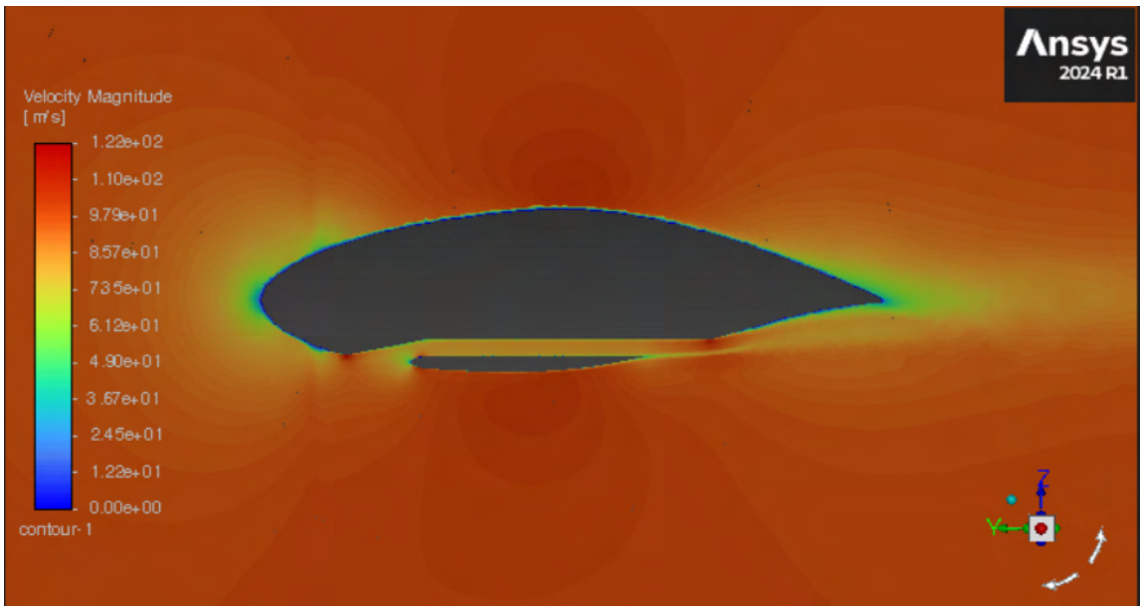

(a) Mesh Number 2

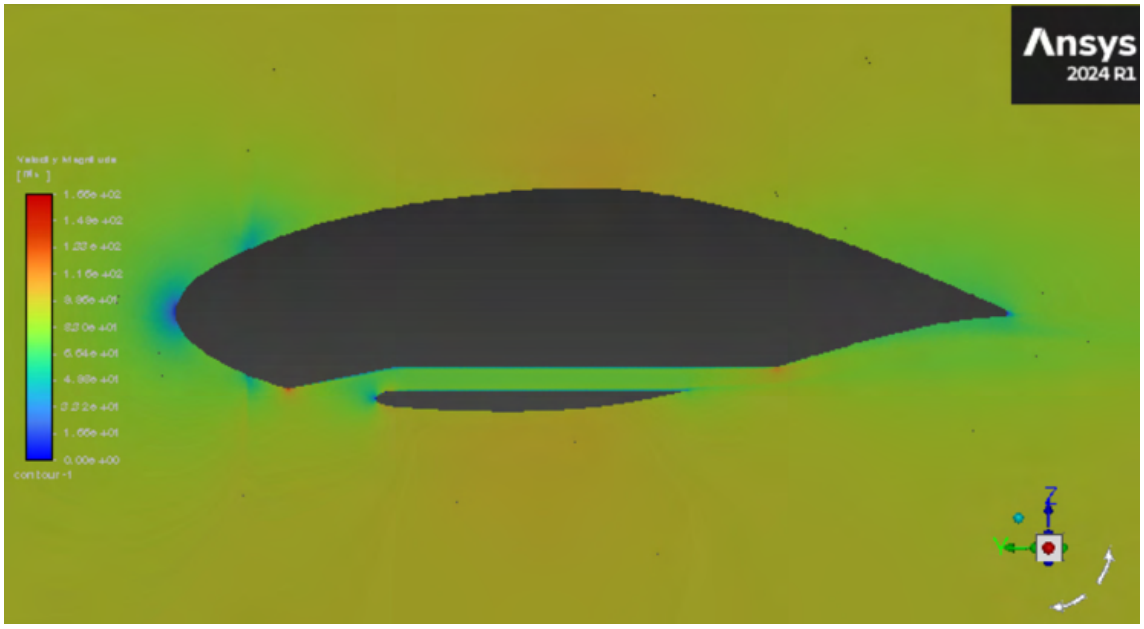

(b) Mesh Number 5

Figure 3.23: Velocity magnitude contours along the cross-section of the nacelle.

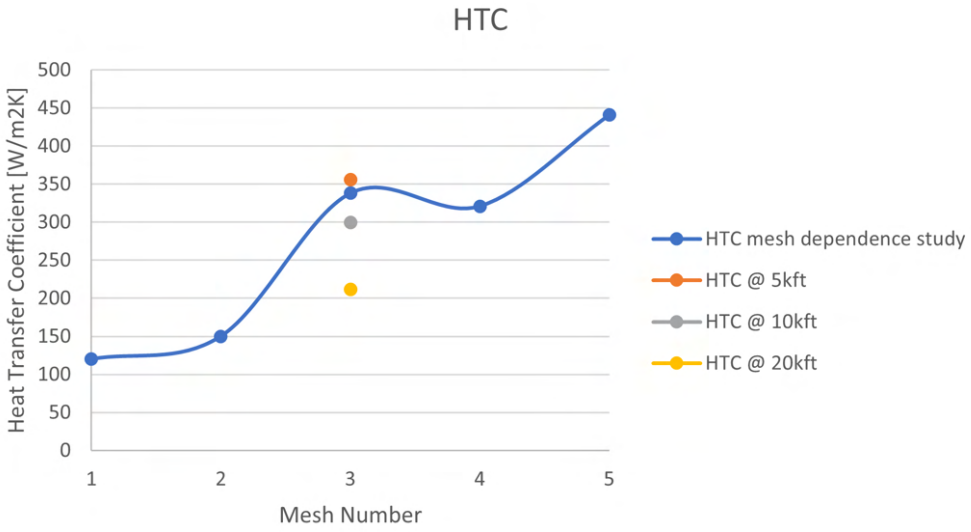

Figure 3.24: Heat transfer coefficient changes across mesh numbers.

Figure D.5 shows the velocity magnitude contours differences between mesh numbers 2 and 5, where it is possible to observe the increase in near-wall mesh refinement and the velocity change across the propeller surface near the spinner. Table 3.7 represents the regions of the domain where mesh refinements were applied, alongside the sizing type, the used element size for mesh number one, and the mesh elements growth rate.

Table 3.7: Mesh parameters for different regions.

Region	Sizing Type	Element Size (mm)	Growth Rate
General	-	400	1.2
Near Wake	Volume meshing	200	1.2
Far Wake	Volume meshing	400	1.2
Duct	Volume meshing/Surface meshing	50	1.2
Propeller Face	Surface meshing	50	1.05
Nacelle	Surface meshing	50	1.2
Lip	Surface meshing	50	1.2
Duct Walls	Surface meshing	50	1.2

The mass flow ratio on the duct was also evaluated by taking the area-weighted average of the velocity magnitude and air density at the duct's entry throat and a-dimensionalized with the inlet parameters of velocity magnitude and density for the same reference throat cross-sectional area. A similar behavior to the heat transfer coefficient here is also shown. This mass flow is only dependent on the flow velocity magnitude inside the duct and the local density since the air was modeled as an ideal gas. High gradients captured across mesh refinements can capture more accurately the vortex formations, which can lead to significant density changes, which can explain some of the initial behavior captured between Mesh 1 and 3. The mass flow, similar to the heat transfer coefficient, does not show a convergent behavior due to the reasons stated before.

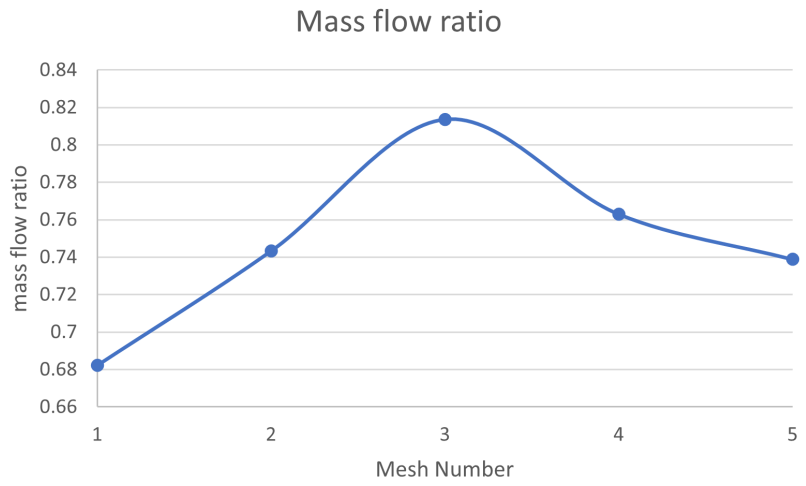

Figure 3.25: Mass flow ratio across mesh refinements

The ram pressure recovery can also be evaluated by knowing the difference between the total and static pressures on the duct throat and domain inlet, respectively. Its evolution through the mesh refinements can be seen in figure 3.26 where the grey dotted line represents the maximum efficiency for a rectangular platform inlet operating at the respective mass flow ratio conditions. The behavior shown in this plot is also unexpected and in tendency with the previous plots, with the source of the variations coming from larger variations of pressure inside the duct with the inlet's total and static pressures staying approximately constant across mesh refinements, meaning that the pressure losses inside the duct are driving this large changes. Isosurfaces for total pressure variation across the duct can be observed in D.1.

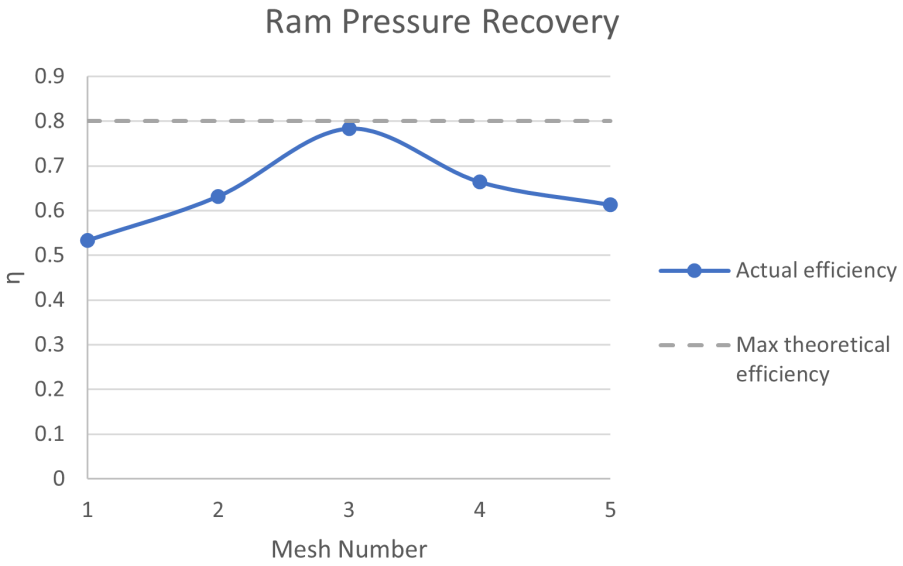

Figure 3.26: Ram pressure recovery across mesh refinements

y^+ (y-plus) is an important non-dimensional wall distance parameter in computational fluid dynamics that is crucial when dealing with wall-bounded flow simulations. It plays a significant role in accurately resolving the boundary layer characteristics and determining wall shear stress, heat transfer, and near-wall turbulence. The value of y^+ is determined based on the chosen turbulence model, as it influences the treatment of the viscous sublayer and the fully turbulent region of the boundary layer, figure 3.27 shows the change in y^+ across meshes. The large initial change in y^+ can be the source of the large variations in the quantities calculated above due to the chosen turbulence model and the use of wall functions. After mesh number 3 the y^+ was not decreased as much and kept above 20 to avoid issues arising from the blend region of the boundary layer ($5 \leq y^+ \leq 10$).

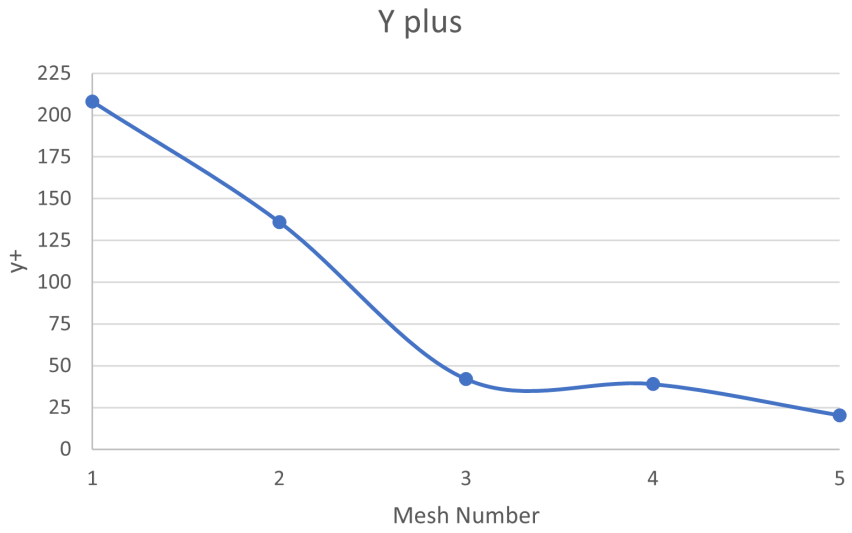

Figure 3.27: y^+ change across mesh numbers

During the mesh refinement study, some issues were identified that may impact the accuracy and reliability of the flow solutions. These issues manifested as unexpected behavior in the results, suggesting a lack of mesh independence, which is crucial for ensuring the validity of the computational model.

To address these concerns, further investigations need to be conducted. The focus of these investigations will be to evaluate the mesh refinement process and to implement necessary adjustments to achieve mesh-independent results.

3.3.1.6 Validation

Validation is an important aspect of every computational study, which is normally achieved by comparing the simulation results with experimental data. However, experimental data available to the public for this setup is scarce or not in the public domain, especially with the angled nacelle placement. Therefore, it is chosen to validate the data against more common examples used in the literature, where the degree of confidence in the model setup can be assured before going into a full-scale

version.

For this, the NACA0012 airfoil is analyzed computationally and validated against the results obtained by Al-Khalil [42], the same document used to validate the Simulink model and also used by many researchers and code developers to validate their results.

Having done thorough experimentation on the icing of different geometries protected with either anti-icing or de-icing IPS, this work allowed the creation of a better understanding of different icing scenarios and the correspondent heat fluxes required on these surfaces to prevent build-ups and validation of them with other computational codes like LEWICE.

The experimental study [42] used a 6 ft ($\approx 1.82\ m$) span airfoil, with a chord of 36 inches ($\approx 0.91\ m$) which is fitted with an electro-thermal ice protection system in the leading edge. The leading edge is removable and covered 10 inches ($\approx 0.254\ m$) in chord integrating thus the IPS. The total heated spanwise length is 3 feet ($\approx 0.91\ m$), and the total heated wrap distance in the chordwise direction is 7.75 inches ($\approx 0.197\ m$) at the end of the heated area an 8-inch span, guard heater is installed covering 12 inches ($\approx 0.3048\ m$) of wrap distance. This resulted in to maintain as much as possible of the airfoil clean of ice, preventing airflow disturbances that could affect the measurements. Heater zones are discretized as shown in figure 3.28 and used to validate temperature distributions across the surface.

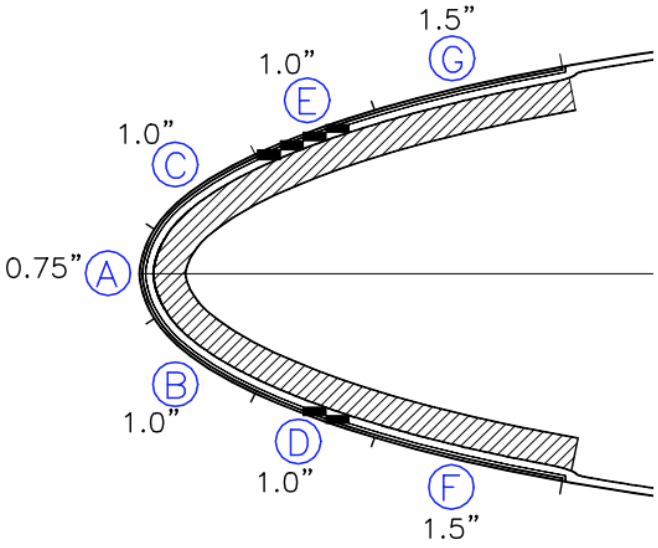

Figure 3.28: NACA0012 leading edge heated zones [42].

The two main parameters to validate with Al-Khalil experiments are the heat transfer coefficient distribution and the collection efficiency β. Figures 3.29 and 3.30, represent the plots achieved by Al-Khalil in his experiments which were also used here either to validate the simulation setup.

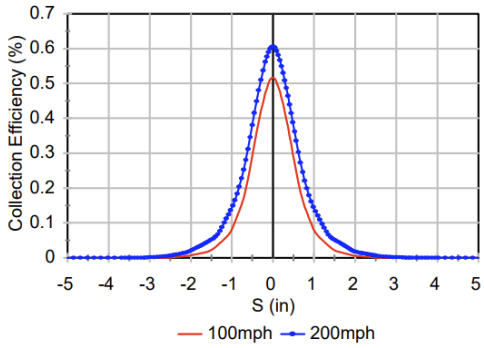

Figure 3.29: Predicted collection efficiency [42].

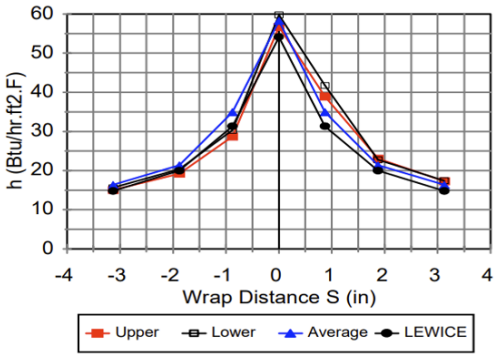

Figure 3.30: Heat transfer coefficient distribution [42].

Al-Khalil's experimental testing is performed following the test matrix in Appendix B.2 and B.3.

The heater zones are discretized over the airfoil domain. The table 3.8 represents the distances covered by the heater zones in Al-Khalil's experiment and the ones created for the simulation environment with the associated relative error. This error arises due to the number of points used to discretize the airfoil which do not exactly coincide with the heater limit zones.

Table 3.8: Heater zone discretization.

	Exp(mm)	Sim(mm)	Total Distance from LE (mm)	Error (%)
Zone A	9.52	9.66	9.52	1.47
Zone B	25.4	26.63	34.92	4.84
Zone C	25.4	26.63	34.92	4.84
Zone D	25.4	22.76	60.32	10.39
Zone E	25.4	22.76	60.32	10.39
Zone F	38.1	40.71	98.42	6.85
Zone G	38.1	40.71	98.42	6.85

Four mesh refinements are made, resulting in a total of five meshes used; figure 3.31 shows the coarser and most fine meshes used for this analysis. The used mesh parameters can be found in figure 3.9; the number of elements is increased by approximately a factor of two except between the first and second meshes, where a factor of 10 was used. The number of elements on the airfoil is increased progressively, as well as the near wall element size, to achieve a $y+ \leq 1$ for mesh 5, which allowed the use of the $k-\omega$ turbulence model to fully solve both the thermal and airflow boundary layers without the use of wall functions.

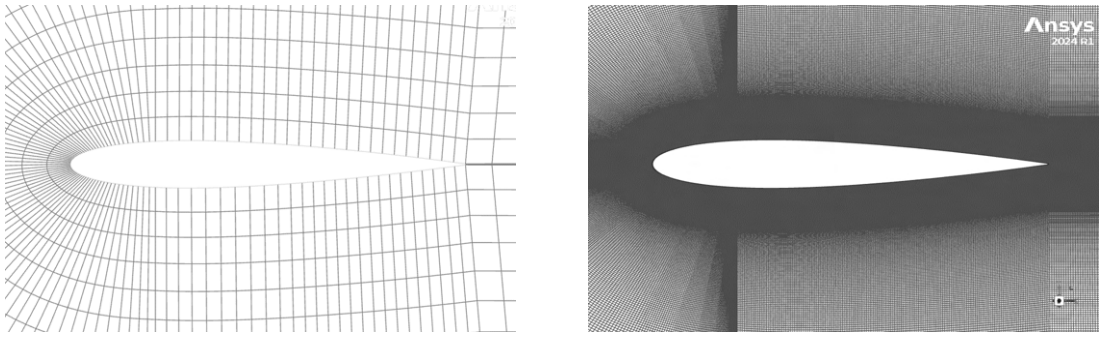

(a) Coarse **(b)** Fine

Figure 3.31: Coarsest and finest meshes used for 2D validation

Table 3.9: Mesh refinement parameters.

Mesh Number	Growth Rate	Number of Elements	Elements on Airfoil	y+
1	1.1	23043	73	
2	1.1	246761	183	1050
3	1.1	514513	457	230
4	1.1	1097273	914	35
5	1.1	2462118	1829	<1

NACA0012 is a well-studied profile, for which in this test scenario a 2D simplification can be assumed. This allows the saving of computational resources and decreases the solution time. That is why, a 2D mesh is built, However, since FENSAP-ICE is exclusively a 3D-based solver the input of 2D meshes is not possible, all the meshes are already constructed, and the validation parameters could be obtained without the use of an ice accretion module; it is chosen to carry on with the analysis through fluent using the multiphase flow setup. The angle of attack is kept at 0° as this covers most of the test cases in [42].

A fluent setup is performed for a steady-state solution using the highest mesh resolution the $k-\omega$ SST turbulence model applied to the mixture. For the multiphase model, the Eulerian inhomogeneous model is used. Two phases are created: one for air and the other for water, where the diameter of the droplets is selected to be 20 microns.

For phase interaction, the heat transfer coefficient is chosen to be Nusselt number-based. Film modeling is also used since FENSAP-ICE also computes it. For this phase accretion and a phase concentration of 3.9E-4 kg/m^3 are selected to represent the same LWC used in [42] experiments.

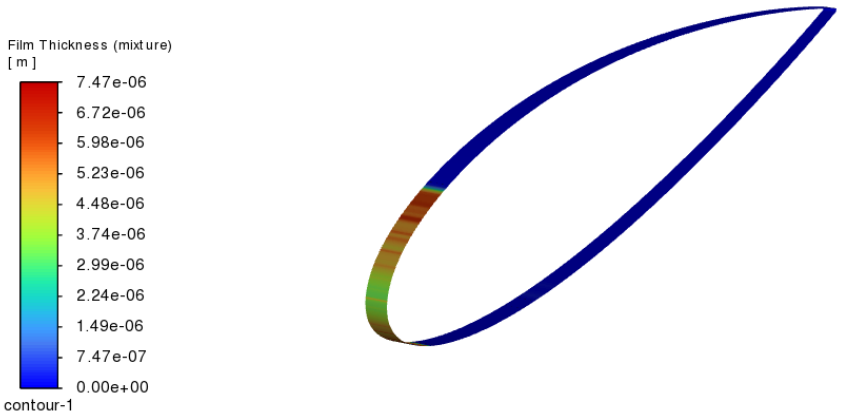

Figure 3.32: Film thickness distribution.

The rest of the setup followed similar modeling settings as it is used for the full nacelle simulation, with the solution methods involving a phase coupled SIMPLE scheme for the pressure velocity coupling, the spatial discretization in table 3.10 is used, with under relaxation factors kept as standard.

Table 3.10: Spatial discretization

Gradient	Least Squares Cell Based
Pressure	PRESTO!
Momentum	Second Order Upwind
Volume Fraction	First Order Upwind
Turbulent Kinetic Energy	Second Order Upwind
Specific Dissipation Rate	Second Order Upwind
Energy	Second Order Upwind

The mesh refinement study is performed using the refinement parameters of the table 3.9, with figure 3.31 showing the coarse and fine meshes used.

NACA0012 has a well-known pressure distribution plot for which Ladson [74] did extensive testing at NASA's Langley Research Center, obtaining data for different Reynolds conditions and angles of attack for free or forced transition scenarios. The data obtained by Ladson that matches best the Reynolds and angle of attack used in the experimental conditions by Al-Khalil is plotted in figure 3.33 against the obtained simulation results for the coefficient of pressure. To estimate the heat transfer coefficient, Al-Khalil used different thermocouples set to maintain a certain temperature with these, and by knowing the power input into the thermocouple an estimation of the heat transfer coefficient can be made. In a simulation environment, this can be achieved by fixing the walls as adiabatic, and then, since numerically, the near-surface temperatures are known, the heat transfer coefficient can also be estimated.

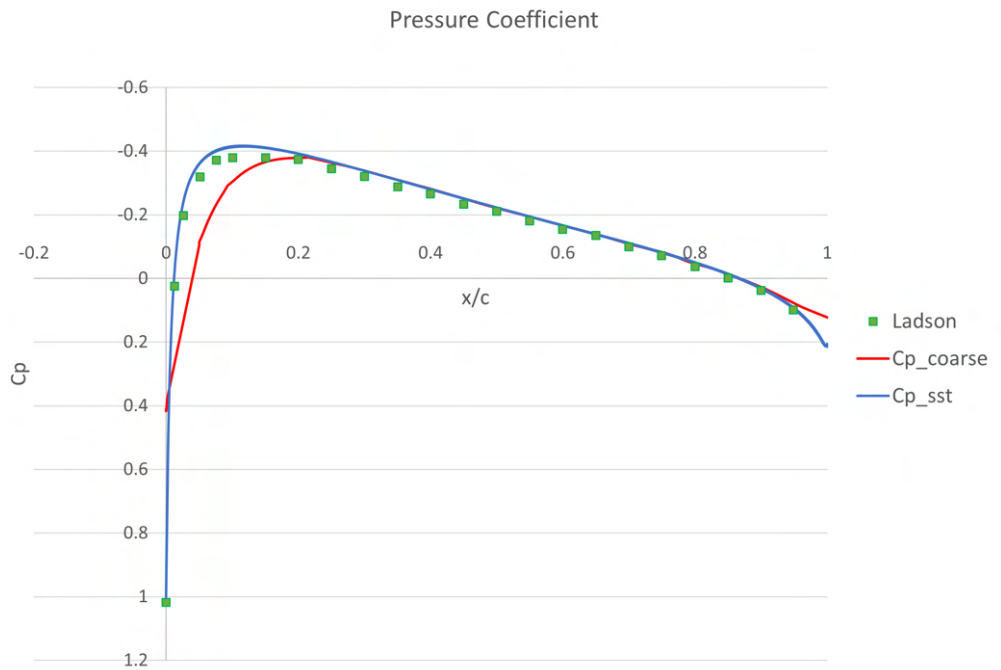

Figure 3.33: Pressure distribution convergence with mesh refinement

3.3.2 Simulink model

Two different methods to avoid icing should be explained. One of them is called "anti-icing" where the ice is prevented from being formed along the mission. The other method is "de-icing," where the ice is eliminated after it is formed. Selecting these ice protection modes is up to several parameters such as the size of the area to be protected and the ice accumulation tolerance of the relevant area. As long as the accumulated ice does not yield a huge aerodynamic degradation, de-icing is preferred to minimize the required power. However, anti-icing is mandatory for areas that cannot endure any ice accretion for safety reasons. In some practices, both anti-icing and de-icing modes are installed, which is referred to as hybrid.

As the ice-accumulated region is a small area, the anti-icing method is implemented to avoid ice accretion and shedding and simplify the analysis without any transient heating effects. The computations to calculate the required power for anti-icing are performed in Simulink which is a block diagram environment for Model-Based Design. It is used for the computing algorithm of the power requirements and the ice protection system modeling.

3.3.2.1 Power computations

The power required to avoid icing on the inlet and heat balance theory explained in the section 2.1.1.2.3 are followed in the Simulink model. Flight and atmospheric inputs are given according to selected critical icing conditions given in section 4.3.1. Heat transfer coefficient and collection efficiency values for each simulation condition are obtained from CFD simulations described in the section 3.3.1.3, then given to the model as the inputs.

A flow chart representing the Simulink model is presented in figure 3.34.

- The Lapse Rate Model is a Simulink block implementing the mathematical representation of the lapse rate atmospheric equations. It is customized by different ISA deviations representing the boundaries of icing conditions for each flight altitude.
- Another Simulink block used is the Ideal Airspeed Correction from the Aerospace Blockset. For different atmospheric conditions, true airspeed is computed through this block.
- Thermal conductivity is implemented in a block from the empirical data [43]. Interpolation is used for any required temperature values that have no equivalent conductivity values.
- Prandtl and recovery factor functions are given in the equations 2.12 and 2.19, respectively. Depending on the cloud types, two different icing conditions can be considered. Liquid water content can be obtained with the ambient temperature and MVD inputs by the models converting the figures 2.19 into a lookup table.

The power terms are calculated with the equations given in the section 2.1.1.2.3 and summed up to obtain the total power required to avoid icing.

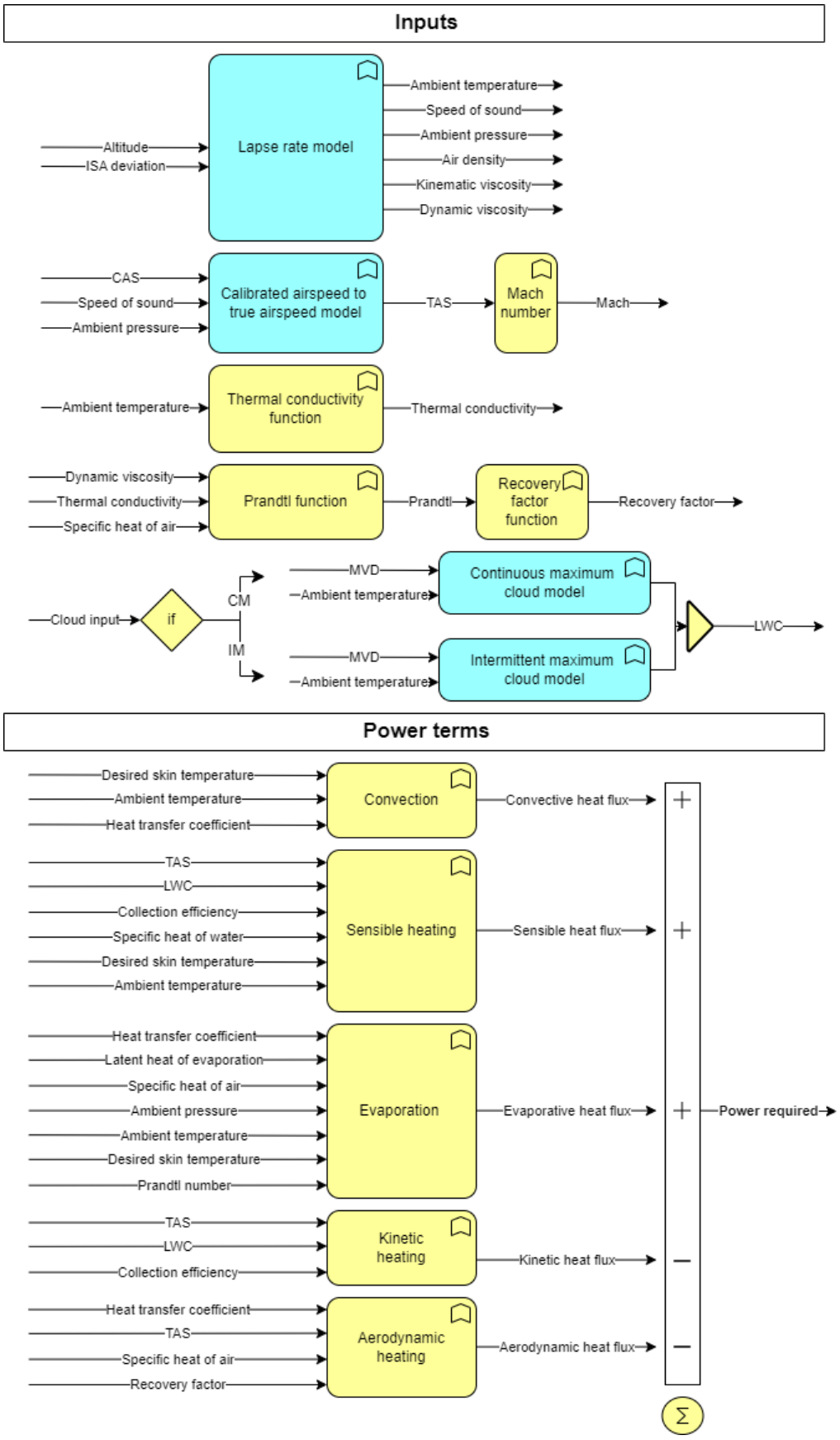

Figure 3.34: Flow chart for power calculations.

3.3.2.2 Computational model validation

Ice protection systems are critical components for flight safety. There are several suggested power values [31] and estimation methods [35]. They are validated by simulation and testing after the conceptual design. Due to the time and cost limitations, the computations are validated along with the experimental program done by Al-Khalil [42]. Both evaporative and running-wet methods are experimented and for various total temperatures, velocities, LWCs, MVDs, and angles of attack as given in the Appendix B.2. For two specific scenarios which are warm and cold atmospheric conditions, the percentages of energy balance terms are calculated for various surface temperatures.

Table 3.11: Validation inputs.

	Article values	SI units
Heat transfer coefficient	40 $Btu/hr.ft^2°F$	227.13 W/m^2K
LWC	0.39 g/m^3	0.39 g/m^3
Collection efficiency	0.5	0.5
Velocity	200 mph	89.41 m/s
Temperature	-22°F and 20°F	-30°C and -6.67°C

In the model, the ambient temperature is obtained by altitude and ISA deviation inputs as shown in the flow chart 3.34. To match the validation temperatures, a flight altitude is selected as 15000 ft where icing occurs at both temperatures. ISA deviations are arranged accordingly. Lastly, since the data is given in W/in^2 and $°F$ in the article, the results are matched in this unit.

3.3.2.2.1 Validation results

The required power values are calculated for the condition given in the table 3.11.

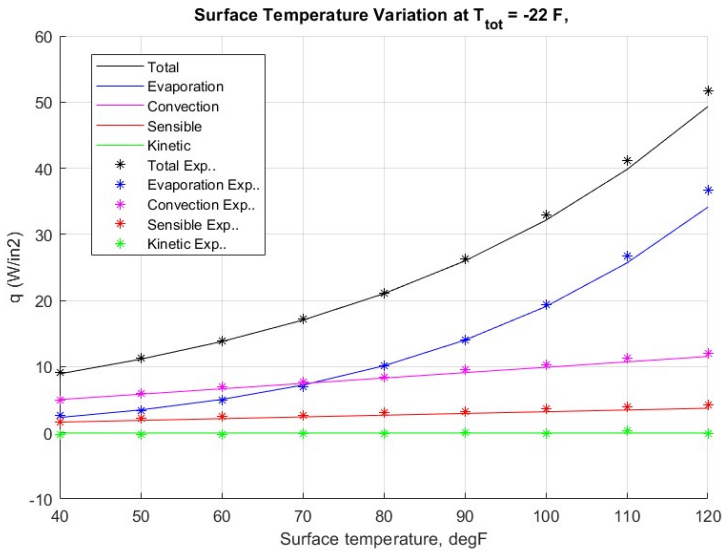

Figure 3.35: Energy balance terms validation at $T_{tot} = -20°F$

The figure 3.35 shows the calculated and experimental energy balance terms in the cold scenario. For the lower surface temperatures, the model predicts almost identically. When the surface temperature increases, there is a small margin that can be acceptable due to a little lower estimation of evaporation.

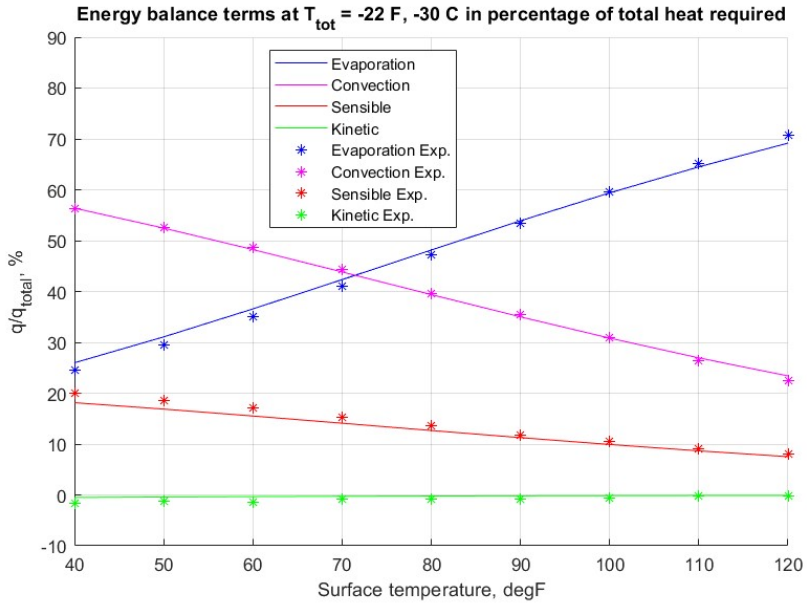

Figure 3.36: Energy balance terms validation at $T_{tot} = -20°F$ in percentage of total heat required

Figure 3.36 shows the energy balance terms in the percentage of heat required. It is seen that the model runs collaterally.

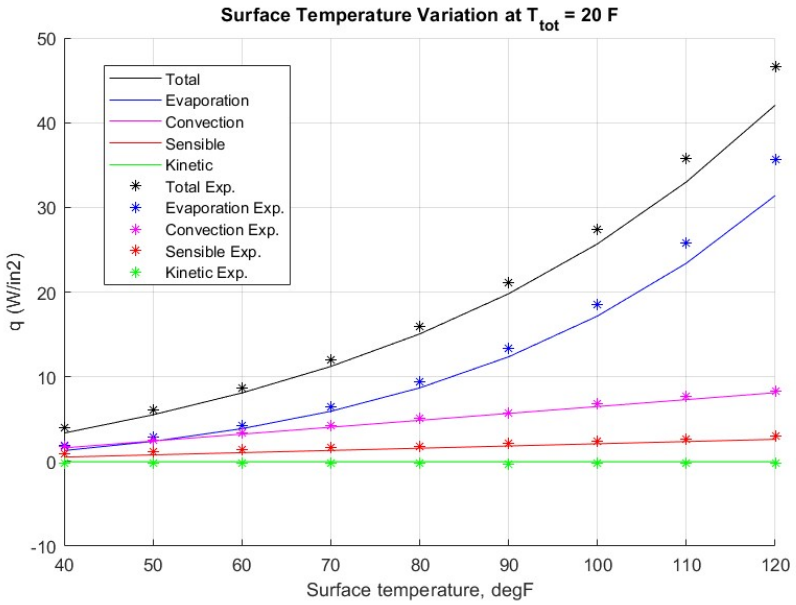

Figure 3.37: Energy balance terms validation at $T_{tot} = 22°F$

The warm scenario results are shown in the figures 3.37 and 3.38. In this condition, the model predicts well in lower surface temperatures. For the higher surface temperatures, the evaporation term underestimates a maximum of approximately 10%. As higher surface temperatures are required, usually in the evaporative mode, and lower surface temperatures are sufficient for running-wet mode which will be conducted in the designed inlet, it can be said that the model is validated with the experimental data.

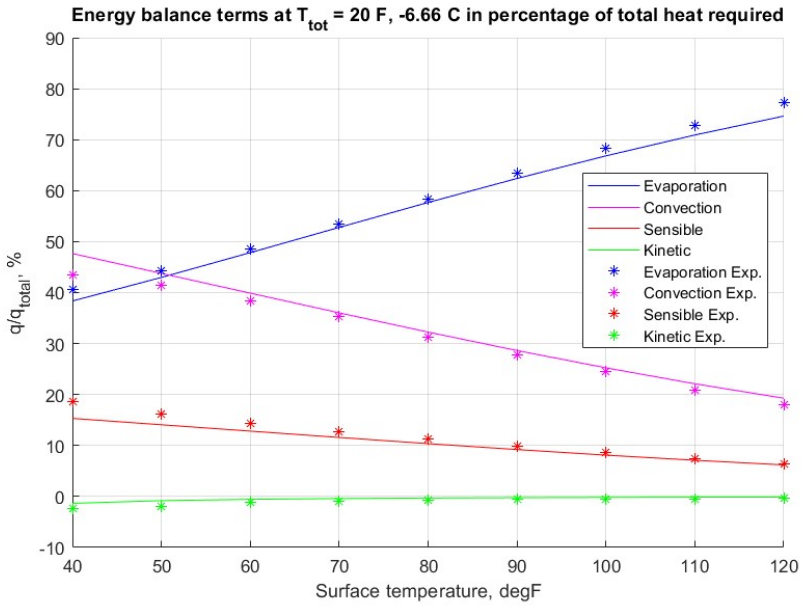

Figure 3.38: Energy balance terms validation at $T_{tot} = 22°F$ in percentage of total heat required

3.3.2.2.2 Evaporation term investigation

There is a variety of research done to calculate the power requirements for anti-icing and not all of them follow the same theoretical background. In the literature review, several different evaporation terms have been encountered. As the research of Al-Khalil has experimental data to validate, those terms are investigated and compared with the results.

The first evaporation term is used in the estimation of parting strip requirements by Krammer and Scholz [35]. The term is

$$\dot{q}_{\text{evaporation}} = 0.7 h_0 L_e \frac{R_h e_\infty - e_{\text{surf}}}{p_\infty c_{p,\text{ air}}} \tag{3.1}$$

where e is the water vapor pressure function calculated from Goff-Gratch equation [67], and 0.7 is an empirical factor. The second evaporation term is from the Aircraft Icing Handbook [20] where the final term in the equation 3.7 is obtained with the presented equations 3.2, 3.3, 3.4, 3.5.

$$\dot{m}_{evap} = g\Delta B \tag{3.2}$$

$$g = \frac{h_c}{C_{P_{air}}} \left(\frac{Pr}{Sc}\right)^{0.667} \tag{3.3}$$

$$\Delta B = \frac{B_1}{B_2} \tag{3.4}$$

$$B_1 = \frac{P_{v,Surf}}{T_{Surf}} - \left(\frac{P_T}{P_S}\right) \frac{P_{v,\infty}}{T_T} \tag{3.5}$$

$$B_2 = \frac{1}{0.622} \frac{P_T}{T_T} - \frac{P_v, Surf}{\mathrm{T}_{Surf}} \tag{3.6}$$

$$\dot{q}_{evaporation} = \dot{m}_{evap} L_e \tag{3.7}$$

The last evaporation term is presented in the theory section 2.1.1.2.3 from the Messinger model [33].

These terms give the following results shown in the figure 3.39. Krammer and Scholz's evaporation term overestimates the evaporation compared to experimental data. On the other side, the Icing Handbook's evaporation term underestimates it. This is why, Messinger's evaporation term is used in the research that estimates the evaporative heat flux perfectly as shown in the figure 3.35.

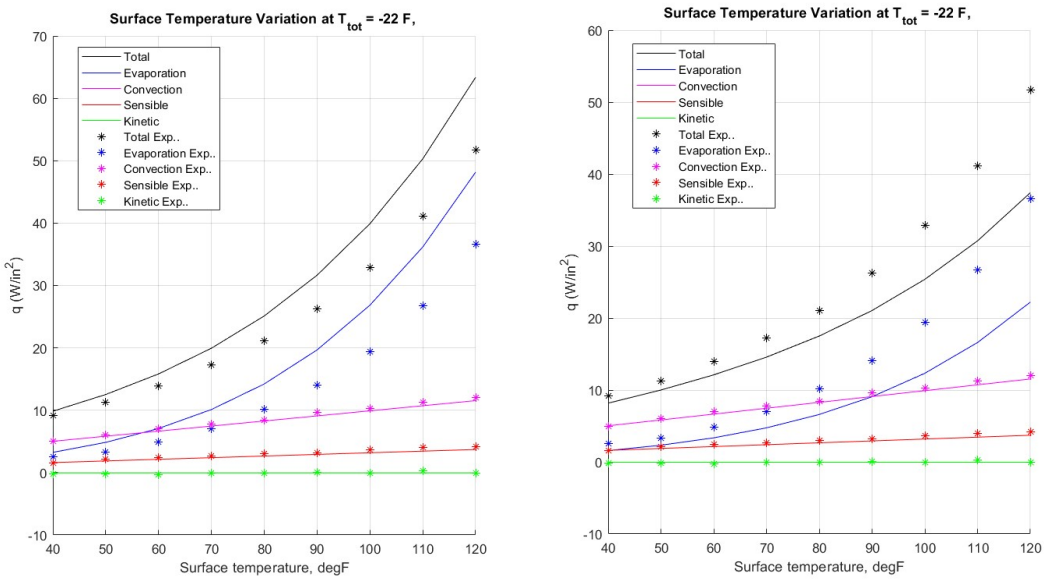

Figure 3.39: Energy balance terms validation at $T_{tot} = -20°F$ with different evaporation formulations.

3.3.2.2.3 Aerodynamic heating term effect

In the heat balance model, Al-Khalil does not include aerodynamic heating assuming the term has a very small effect which is also confirmed after validating the calculations with the model of the article, which is seen from figure 3.40.

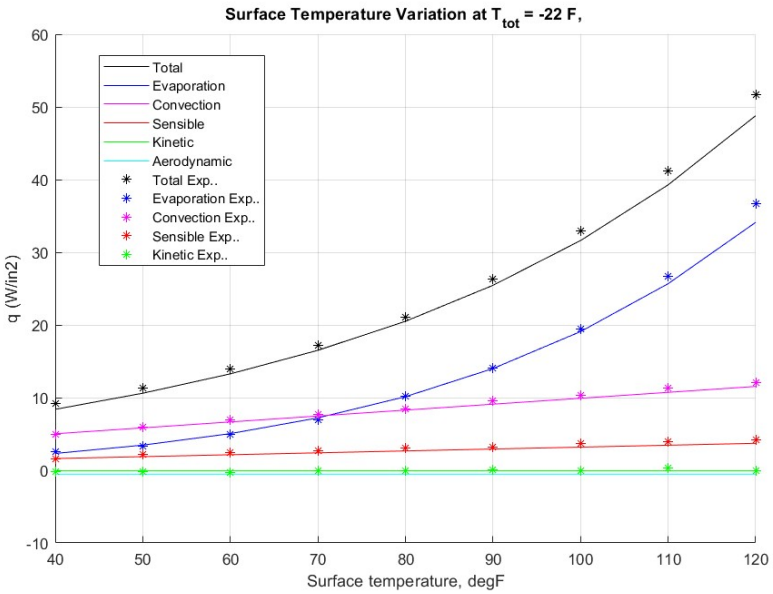

Figure 3.40: Energy balance terms validation including aerodynamic term at $T_{tot} = -20°F$

That is why, even though it is omitted in this validation to match the model, the aerodynamic heating contribution is included in the real model.

3.3.2.3 IPS architectures

Simulink is used to build two different IPS concepts. As suggested in the section 3.1, one existing concept and one new concept are introduced after searching both externally and internally. For the existing concepts, the most suitable method for this type of inlet is selected from the common usage of IPS, summarized in the section 4.1.1.7. An electro-thermal solution is built with the heater pads covering the inlet lip. As the new concept, a thin pipe is passed through the inlet lip with a hot glycol-water solution coming from the air-water heat exchanger which is used for the cooling system.

The power required for anti-icing is calculated with the principle of keeping the skin or surface temperature above a certain value. As the evaporative mode requires a lot of energy as explained in the section 4.1.1.2, the running-wet mode is selected. A conservative running-wet surface temperature is 40°F (around 4.5°C) [31]. That is why, a temperature of 5°C to calculate the required power to keep above this surface temperature is selected. The skin temperature is a constant target value in power computations in the flow chart 3.34. In the IPS architectures, it is implemented as a variable to see if the computed power is truly sufficient to surmount the desired skin temperature. This is the reason that skin temperature and all the parameters it affects are highlighted in blue in figure 3.41. This flow chart is identical for both IPS architectures.

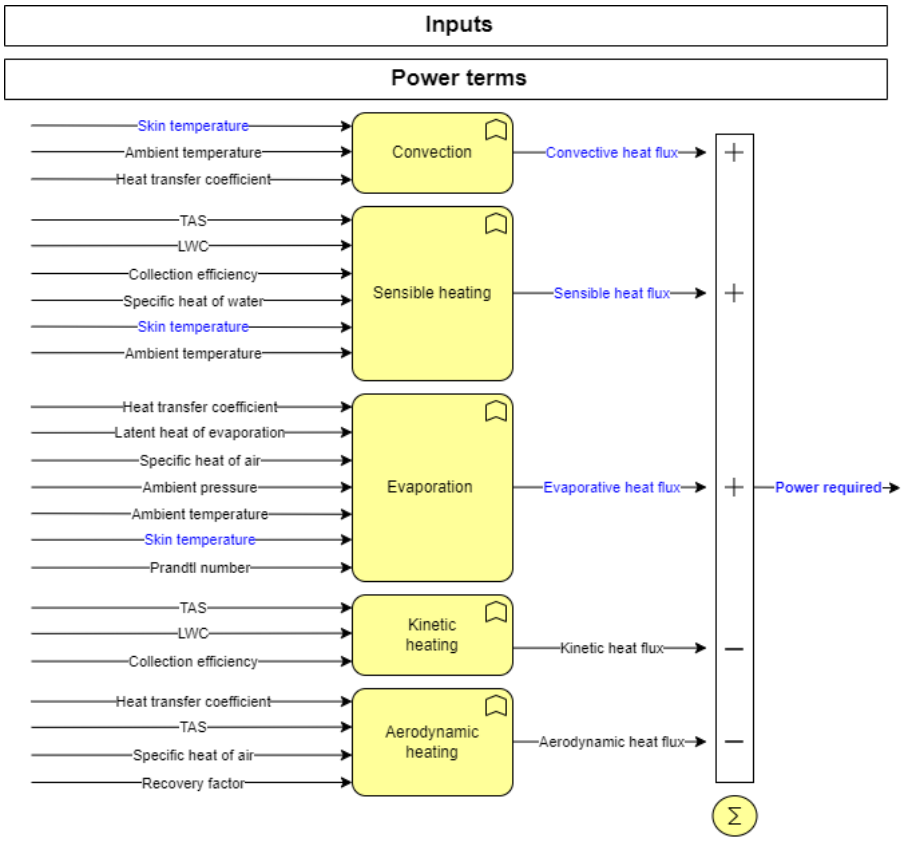

Figure 3.41: Varying power calculations for IPS architectures.

3.3.2.3.1 Electro-thermal IPS

A typical electro-thermal IPS solution is given in the section 4.1.1.2 where an example of heater material structure is shown in figure 4.4. The leading edge is covered with the same structure for this inlet. Thermal representation in Simulink for the electro-thermal IPS is shown in the figure 3.42.

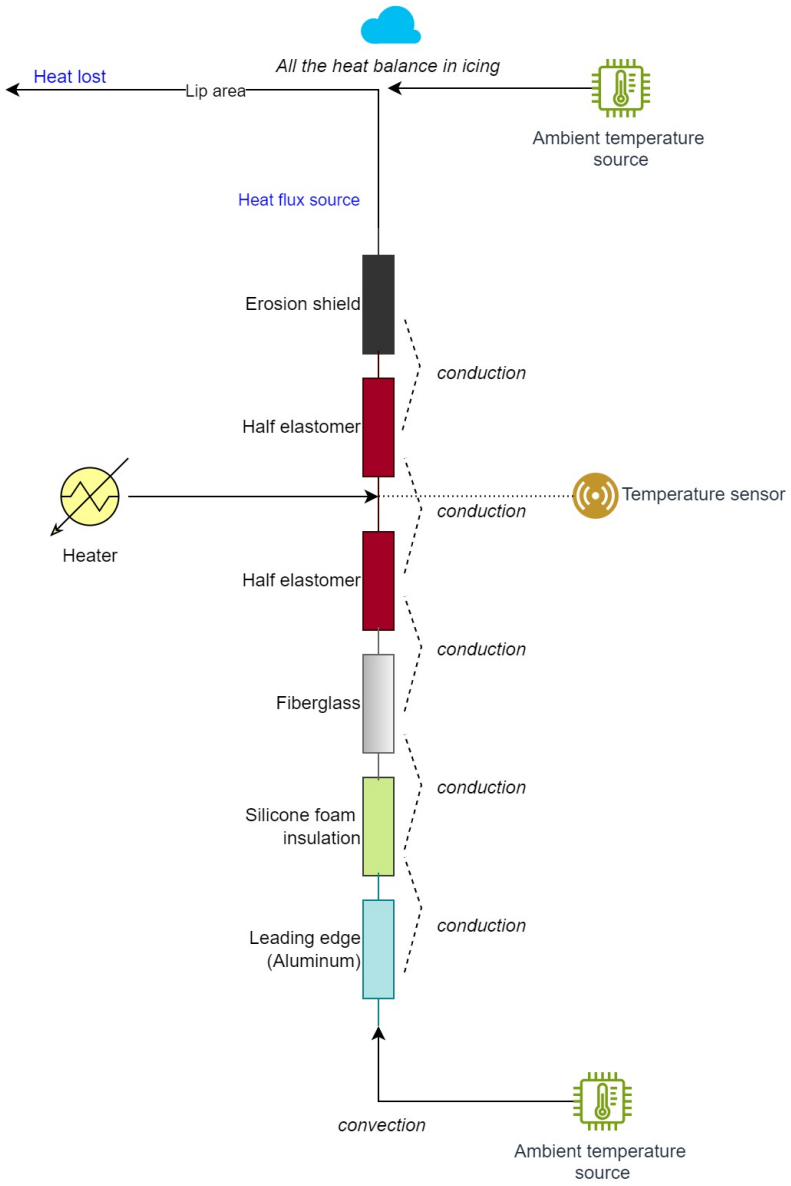

Figure 3.42: Electro-thermal IPS architecture.

The required power as a variable due to changing skin temperature is inserted as a heat flux source. Since the power required obtained from the figure 3.41 is the power per surface area $[kW/m^2]$, the total heat flux is calculated by the lip area obtained from the CAD design. This heat flux is given as a source to the system representing the heat lost from the surface due to icing conditions such as convection, evaporation, etc. Then, the heater structure is implemented including conduction through their different material properties, taken from the table 4.1. As the heater element is placed in between the elastomer, the elastomer is divided into two parts to expose this effect of installment. The heater element supplies a constant value of heat flux. It is obtained from the power calculations as presented in the chart 3.34 and described in the section 2.1.1.2.3, and it is increased by a factor to account for the heat flux to the inner surface of the inlet lip. This efficiency factor is calculated for all the simulation conditions and the lowest value is set. The inside of the structure

is enclosed by the typical leading-edge material which is aluminum. The heating circuit is completed with the air inside conservatively assumed to be at ambient temperature. Temperature sensors are foreseen to monitor performance and protect the material from overheating. The skin temperature is defined as a variable and fed into the system.

3.3.2.3.2 Water-heated IPS

The purpose of this new concept is to use the existing heat coming from the electric propulsion system. A water-glycol solution heated by the electric motors during the mission is connected to the inlet lip with a pipe instead of going to the air-cooling heat exchanger directly.

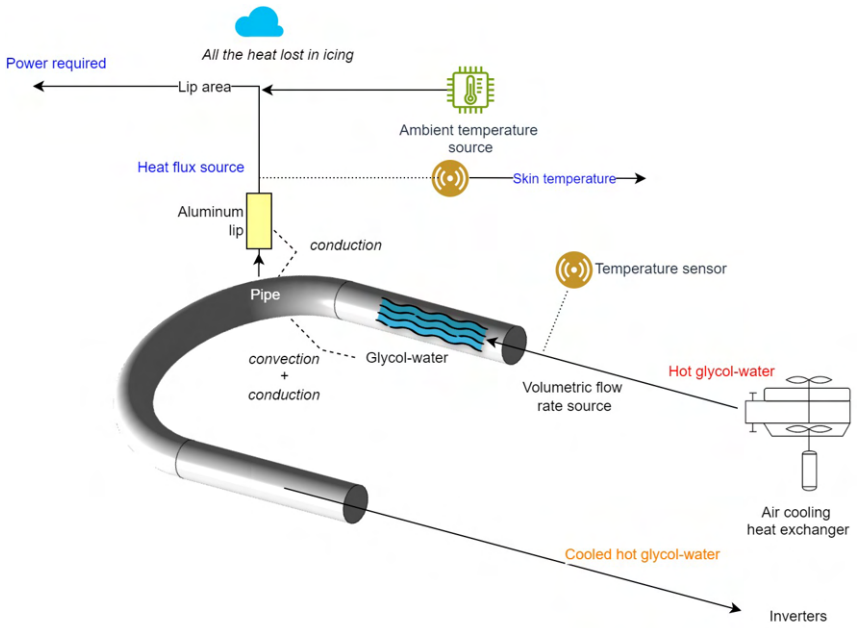

Figure 3.43: Water-heated IPS architecture.

4

Results

4.1 Concept Generation

After the literature study and theoretical background, several concepts are built. As the figure 3.2 addresses, both existing and new concepts are generated to expand the solution scale.

4.1.1 Existing concepts

To avoid all the hazardous icing phenomena that aircraft will experience during flight, aircraft manufacturers implement various ice protection methods in ice-accumulated areas. There are several ice protection systems in terms of operational principles. In the following chapter, pneumatic boot de-icing systems, electro-thermal systems, fluid ice protection systems, fluid electro-impulse de-icing systems, and hot air systems are discussed with their typical procedures and places of use.

4.1.1.1 Pneumatic boot de-icing systems

A pneumatic boot is a concept of breaking the ice cohesion by inflating the tube in a boot that covers the surface of the accumulated ice. The purpose is to disrupt the solid ice bond and let the aerodynamic or circumferential forces wipe the ice chunks away.

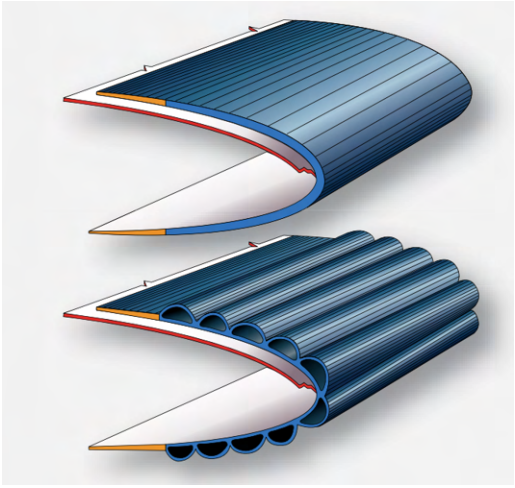

Figure 4.1: Cross-section of a pneumatic de-icing boot uninflated and inflated [40].

The orientation of tube installation is usually spanwise as shown in figure 4.1, but the chordwise configuration has been applied for particular designs as well. The spanwise orientation increases the drag more than the chordwise; however, the chordwise can experience manifold hardships [20]. These boots are used only for the de-icing method as the aim is to create a crack in the ice momentarily and the aerodynamic shape of the inflated tubes is not sustainable.

To provide the tubes to inflate, an example of a pneumatic system is shown in the figure 4.2.

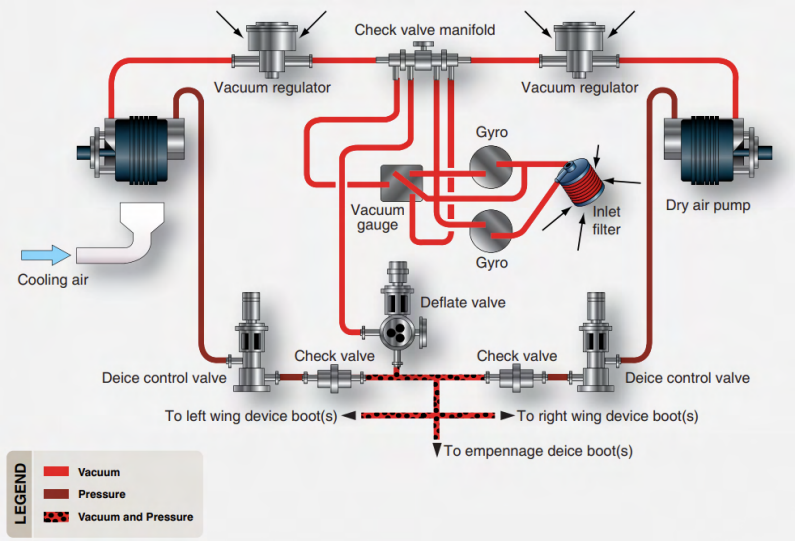

Figure 4.2: Pneumatic deicing system for a twin-engine GA aircraft with reciprocating engines [40].

Next to the boots, a regulated pressure source, a vacuum source, and an air distribution system should be implemented. The other components to support these and complete the system implementation are a solenoid which are deice control valves in the figure 4.2, relief and control valves, air filters, switches, a timer to repeat the deice cycle, and electrical interface such as circuit breakers. When the tubes are uninflated, the deflate valve is opened through the path check valve manifold and vacuum regulator. Gyroscopic components on the dry air pump side keep the boots at optimum suction level and the boots stick to the aircraft surface. When the switch is pushed on, either the bleed air from the compressors or the air from the dry air pump, as in figure 4.2, inflates the boots. The reason to use the bleed air is to avoid adding another engine-driven air pump.

4.1.1.2 Electro-thermal systems

An electro-thermal ice protection system operates by heating the water impingement region by supplying electrical energy from resistance heaters. The purpose is to keep the surface temperature above the freezing temperature and avoid ice formation or melting of the bond between accumulated ice and protected structure. This IPS can be implemented in various parts of the airframe for both anti-icing and de-icing

modes. The places protected by the electro-thermal anti-icing method are usually critical to ice accretion since the power required to protect large regions might not be afforded. For the cases where the anti-icing is not adequate, the electro-thermal de-icing can accompany the anti-icing as shown in figure 4.3. An electro-thermal anti-icing system also has two categories in terms of operation evaporative or running-wet. Evaporative systems as the term implies, supply energy sufficient to evaporate all the water droplets over the surface. Meanwhile, the running-wet systems supply the energy sufficient to avoid freezing over the surface. The melted water can freeze again on the unheated surface at the aft which is called runback ice. This type of operation has the possibility of creating critical scenarios where the water runoff or the runback ice can damage the aircraft components. That is why, for instance, running wet is not preferred on a turboprop or turbojet inlet to protect the propulsion systems from any ice or water ingestion.

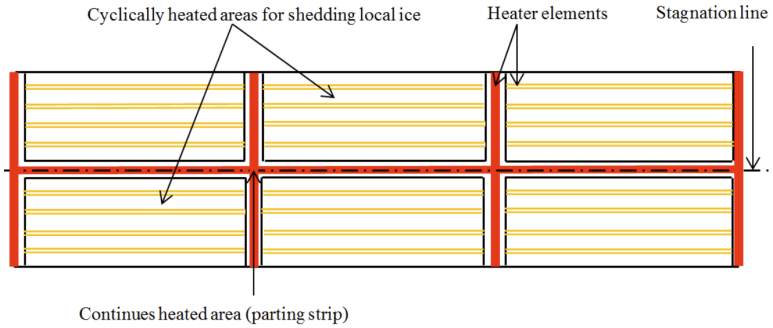

Figure 4.3: Leading edge heater mat layout [41].

In a typical heater structure, electrical resistance elements are sandwiched by a dielectric material, while the outer surface of the airframe is protected by a rain and hail-resistant material as an erosion shield. Since the heat input also goes back into the leading edge skin, a thick layer of insulator material is installed to serve as an electrical and thermal insulator to protect the inner structures. An example composition for the materials and structure of the ice protection area is investigated by Al-Khalil [42] in figure 4.4.

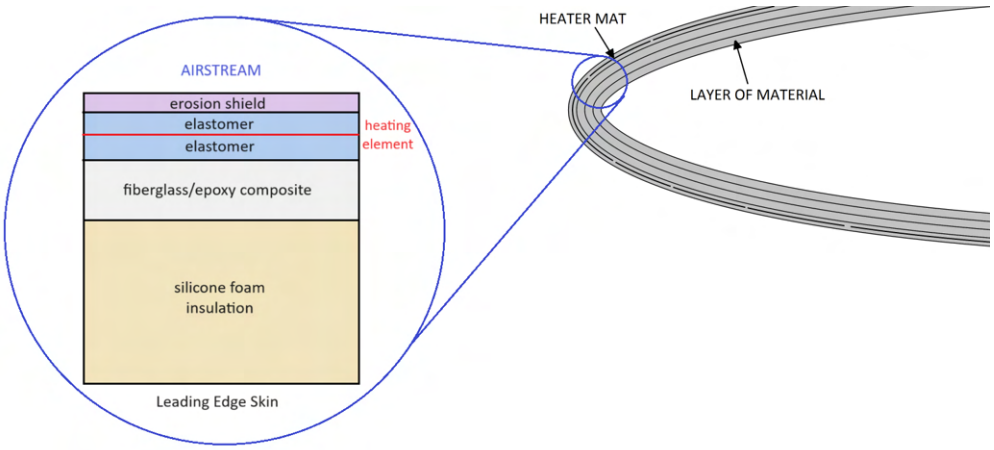

Figure 4.4: Material and structure of ice protection area [57].

This multilayer structure for electro-thermal ice protection is installed on a NACA 0012 airfoil with a chord of 0.914 m and tested in the NASA GRC Icing Research Tunnel. The heat conductivity, heat capacity, density, and thickness values are taken from the setup of Al-Khalil [42] shown in the table 4.1.

Table 4.1: Leading edge heater material properties [42].

Material	Heat conductivity (W/mK)	Density (kg/m^3)	Heat capacity (J/kgK)	Thickness (mm)
Heating element (alloy 90)	40.991	8906.3	385.2	0.013
Erosion shield (SS 301 HH)	16.258	8025.3	502.4	0.2
Elastomer (Cox 4300)	0.256	1384.0	1256.0	0.56
Fiberglass/Epoxy composite	0.294	1794.1	1570.1	0.89
Silicone foam insulation	0.121	648.8	1130.4	3.43

Electro-thermal anti-icing is implemented usually on most air data probes, ice detectors, and engine P2/T2 sensors. Water lines, turboprop inlet cowls, and windshields of transport category aircraft are also continuously heated electro-thermally. Mostly small and important regions are chosen for this method as the required power is high for heating the whole wing. Moreover, the heating element can be easily installed in these small areas as the electrical wiring for the power supply does not require much space and the route is easy to draw between the existing structure. The power source for these systems is either the engine-driven or the auxiliary power source driven.

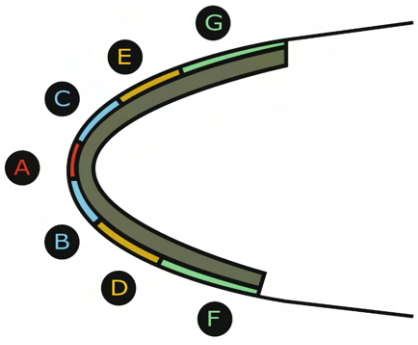

Figure 4.5: Chordwise layout of the heaters [44].

Due to different ice impingements on different locations of the airfoil, power density can be a varying configuration for the heaters covering the ice protection area. For instance, as in the experiment of Al-Khalil [42], seven different regions heat the surface with different power values as shown in figure 4.5. This example layout has been

investigated to optimize the power densities to minimize the energy consumption lately [44].

4.1.1.3 Fluid ice protection systems

This system of ice protection has the principle of avoiding the ice with a fluid acting as a Freezing Point Depressant (FBD). The water impinging the surface merges with FBD moves aft without freezing and leaves the surface through evaporation or shedding from the trailing edge. This system is sometimes referred to as weeping wing systems or by their trade name, TKS systems.

This solution is designed for anti-icing, but it is capable of de-icing, as well. The antifreeze fluid is pumped from the fluid tank through the meshed screen which has thousands of laser-drilled holes, way smaller than it is illustrated in the figure 4.6. With the help of the airstream, the fluid is dispersed all over the surface by coating it with the antifreeze solution.

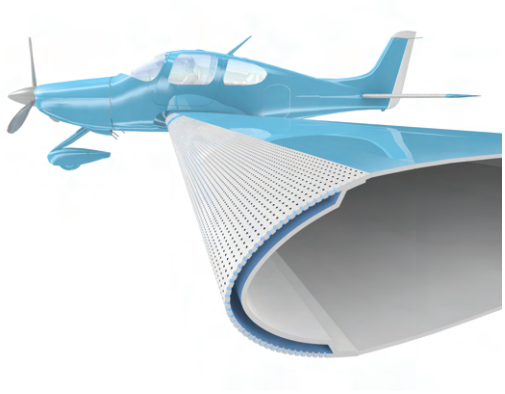

Figure 4.6: Illustration of TKS systems on the leading edge of the wing [45].

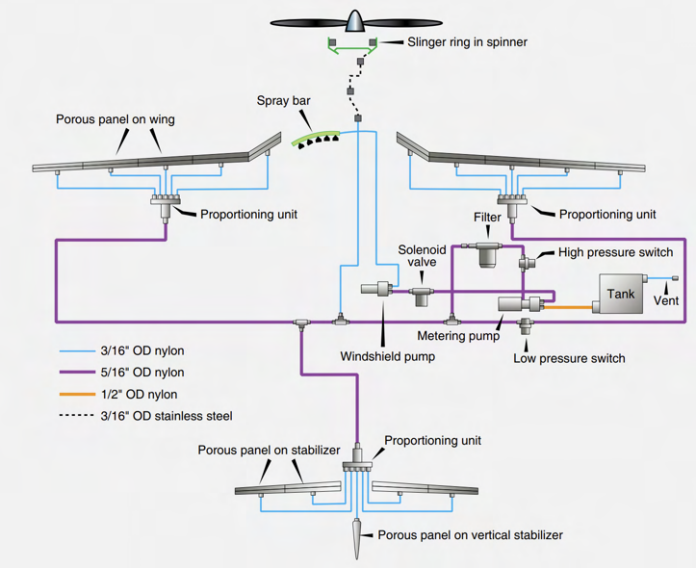

Figure 4.7: Fluid de-icing system [40].

In these systems, mostly glycol-based fluids are used since the freezing point of glycol is -12°C, and when mixed with the water in the same volume, it even decreases to -22°C to -40°C [46]. The location of the fluid tank is also critical in terms of tank refilling and strainer replacement, and the tank material must be corrosion-resistant such as aluminum, stainless steel, fiberglass, etc. The pump normally provides two different flow rates which are the normal flow rate in continuous maximum icing conditions and the higher flow rate in severe icing conditions. The general usage of TKS IPS is to operate during intermittent maximum icing conditions in the de-icing mode. Lately, the commonly used material for the mesh screen is titanium due to its low weight, great resistance to impact damage, and improved surface finish. In addition to titanium, carbon fiber reinforced polymer (CFRP) composite material is developed and enabled to utilize in TKS leading edge panels, as well [58].

The maintenance is relatively straightforward due to the long life cycle of the components. It has good reliability because the pump is the only moving part in the system; therefore, in case a high-quality pump is selected, the failure possibilities minimize. As a disadvantage of this IPS, the operation duration has a finite period due to the limited fluid supply.

4.1.1.4 Electro-impulse de-icing systems

Electro-impulse de-icing systems are physically simple models including a few components as seen in the basic circuit in figure 4.8.

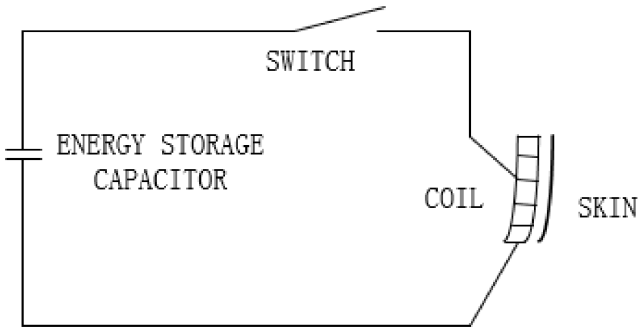

Figure 4.8: Basic circuit of electro-impulse systems [47].

The principle of this system is to discharge the high-voltage capacitors through the coils which are installed under the skin with an air gap shown in the figure 4.9, that results in a sudden electromagnetic field. According to Maxwell's law, this time-dependent magnetic field induces Eddy currents in the metal skin which generates a great instantaneous impulsive force in milliseconds. The resultant force creates a small deflection; however, the movement comes with a rapid acceleration that is sufficient enough to shatter the ice buildup on the leading edge. The real installation contains more than one coil on the surface of the aircraft and their cycle and firing sequence are controlled by the De-icing Control Unit (DCU).

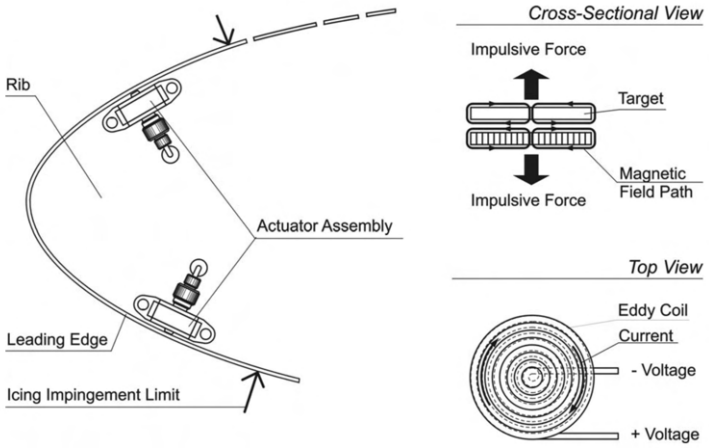

Figure 4.9: Electro-impulse de-icing system [48].

The power-and-sequencing box is usually located in the fuselage. It starts when the switch is on to discharge the capacitor. These switches are called Thyristor or SCR as in the figure 4.10 which abbreviates for Silicon-Controlled-Rectifier. The design of this IPS requires a sophisticated design including a structural dynamic analysis to develop the proper placement of the coils for the most efficient scenario. The preferred installation of the power and control system is where the capacitors are close to the inductor coils, and the power supply is close to the aircraft electrical generator; however far from the capacitors due to its trickle charge [49]. The layout is installed in the same manner in the figure 4.10 where the high energy electrical pulse distance is minimized.

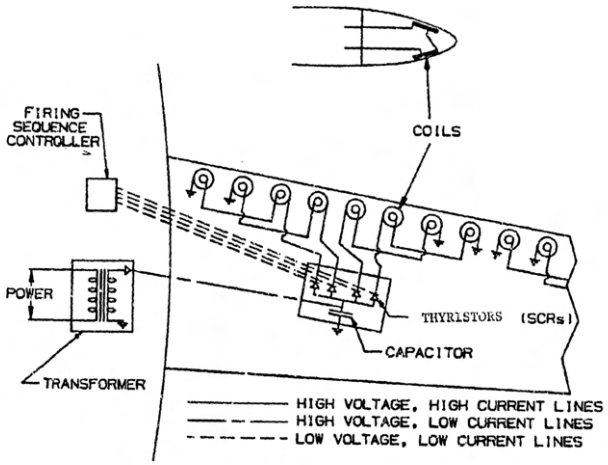

Figure 4.10: Electro-impulse system layout [49].

The power required for the electro-impulse IPS is relatively lower than the other systems and de-icing mode is operated reliably since it gets rid of the significant ice buildup. The surface is deflecting barely with the impulse which is why maintenance does not have much workload since it can be accepted that no parts are moving in the system. This small deflection also does not create an adverse aerodynamic effect

as the pneumatic boot de-icing systems.

On the other side, the electromagnetic field by discharging the coils can generate electromagnetic interference and disrupt the communication, navigation, and surveillance instruments by spamming signals. Another drawback of an electrical system is the possibility of experiencing a lightning strike which can end up bypassing the circuit. An addition, the discharging impulses can create disturbing noise for transport aviation especially if the aircraft is small. For a large transport airplane, they can be inaudible next to the other noises.

4.1.1.5 Hot air systems

As another thermal ice protection system, a source of heated air is used to prevent the icing. For the source, different options exist such as an extraction of engine compressor air. This is also known as bleed air and is commonly used on turbojet or turboprop aircraft. Other methods to obtain the hot air are compression of ram air with a compressor or heating the ram air with a combustion heater. On piston-drive engines, the exhaust gas can be recovered to use the waste heat.

The hot air is routed through components like ducts, manifolds, inlet lips, and valves that need to be anti-iced or de-iced. The figure 4.11 shows an example of the de-icing system by the bleed-air. The leading edge is separated by a two-layer diaphragm to prevent the leakage in reverse. Hot air is ejected into the piccolo tubes which guide the ventilation on the wingtips. In addition to the mechanical components, a temperature and/or pressure sensor must be implemented to control the air and the surface heated.

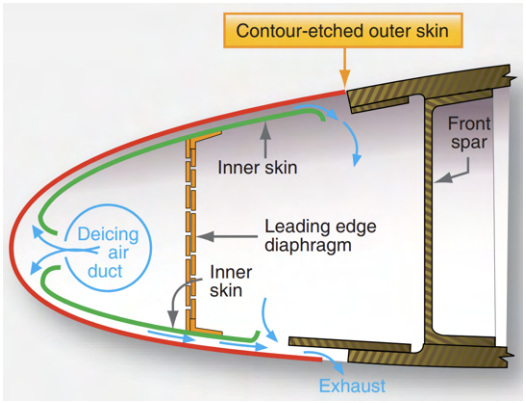

Figure 4.11: Hot-air de-icing system on the leading edge [40].

Hot air IPS can be used for both anti-icing and de-icing. Areas usually heated by anti-icing are engine inlets as shown in the figure 4.12, wing or empennage leading edges. The air enters to the leading edges chordwise near the stagnation point and exits through the gas passages at a non-critical location after flowing chordwise inside the skin. De-icing is done for the larger regions that support the continuously heated parting strips. The method is carried out in the same manner as the electrothermal IPS, only heated by a hot air source for this kind of system.

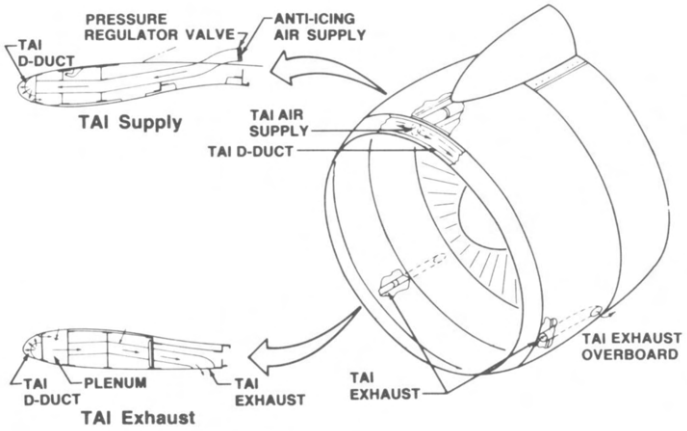

Figure 4.12: Engine inlet bleed air ice protection system [50].

The capabilities of bleed air anti-icing are given in figure 4.13 with flight test data of a B-747 airplane to compare [50]. It can be said that the system performs better in the areas of high impingement of droplets like around the stagnation point of the inlet lip. The longer protection segment, if possible, is preferred as it results in less runback ice on the cold surfaces aft of the heated inlet.

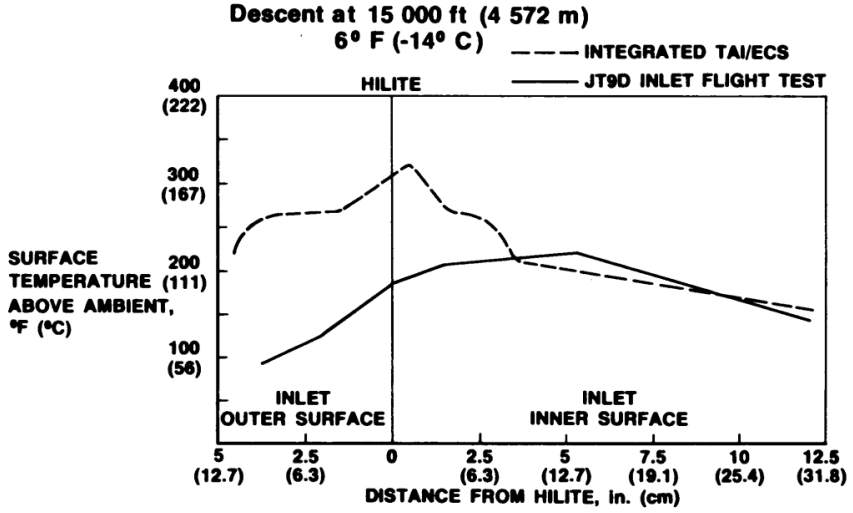

Figure 4.13: Engine inlet hot air anti-icing capabilities during descent power at 15,000 ft altitude [50].

This thermal ice protection system by hot air has no aerodynamic penalty for the anti-icing operation; however, runback ice is possible to form in the de-icing operations or not fully evaporative anti-icing operations. The runback ice can damage the airstream, cover the control surfaces, or form an obstruction when the retraction of an extended slat [49]. The usage of bleed air from the compressor can also result in a significant specific fuel consumption penalty. That is why, in the flight manual of B-747, the recommended usage of bleed air in ice protection concept is to activate it when the ambient temperature goes below 10 °C or in a visible precipitation scenario [50].

4.1.1.6 Hybrid systems

A hybrid ice protection system combines different systems and implements them in a way to create a more economical alternative where high power is not available or impractical. Several examples are given below to present the hybrid solutions.

Al-Khalil, Ferguson, and Phillips [51] developed a system where the airfoil leading edge is covered with the heated strips while electro-impulse actuators are implemented inside the skin as given in the figure 4.14. In case the runback ice forms due to the heated strips from the wingtip, the ice accumulated aft of the airfoil can be cleaned by the impulsive forces of the actuators periodically.

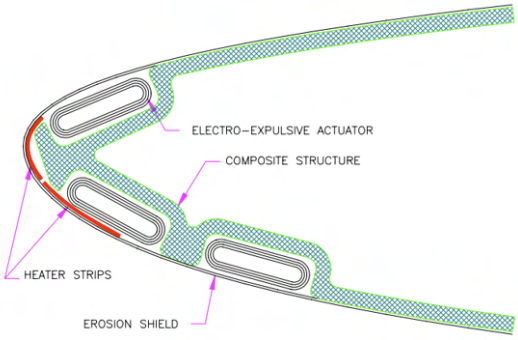

Figure 4.14: Hybrid system of electro-impulse and electro-thermal ice protection systems [51].

Another hybrid ice protection system is to use the bleed air from the engines inside the pneumatic boots by providing both mechanical and thermal de-icing. An example system architecture is shown in the figure 4.15. Bleed air is routed to two inboard and two outboard wing boots, two horizontal stabilizer boots, and to the brakes through the brake deice valves. In this combination, if any thin ice layer is left on the surface after inflating the boots, it can be melted by the heat being supplied through the bleed air.

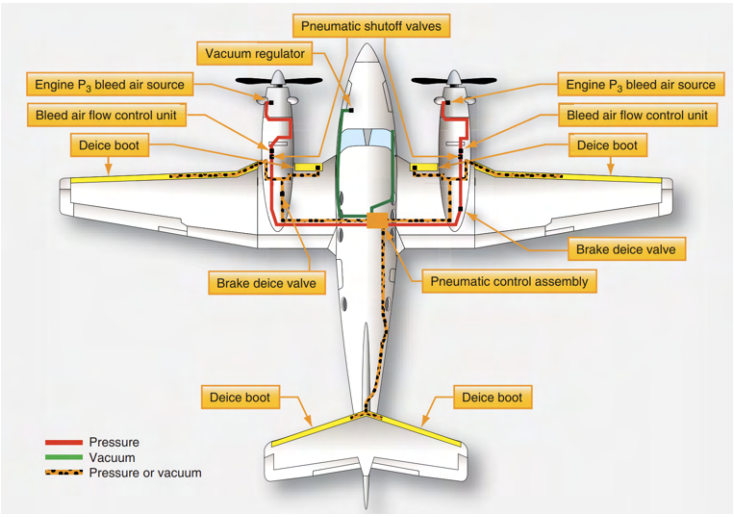

Figure 4.15: Hybrid system of hot-air and pneumatic ice protection systems [40].

4.1.1.7 Common usages of IPS

Some systems are preferred for specific regions for cost, sizing, or performance reasons. Common usages of ice protection systems specific to aircraft components are briefly explained in the Icing Handbook by FAA [49] and summarized in the table 4.2.

Table 4.2: Usages of ice protection systems.

	Pneumatic boots	**Electro thermal**	**Fluid**	**Electro impulse**	**Hot-air**
Airfoil and LE	Being used	Feasible for de-icing	Feasible	Feasible	Feasible
Windshields	Not applicable	Commonly used	De-icing is feasible	Not recommended	Feasible
Engine inlet lips	Limited to bypass inlets	De-icing provides good performance	Possible, risky for fluid ingestion	Recommended if ingestion for short cycle is acceptable	Feasible for inlet lips close to compressor
Turbofan components	Not been tried	Not common	Not been used	Not been applied	Commonly used
Propellers, spinners and nose	Feasible, not been tried	Commonly used	Feasible for propeller blades	Not applicable	Not the most preferred
Flight sensors	Not suitable	If needed, preferred	Not feasible	Not applicable	Not the most preferred
Radomes and antennas	May be installed but transmission losses can increase	Possible for antennas, not for radomes	Not feasible	Not applicable	Not the most preferred
Miscellaneous intakes and vents	May be feasible, not been tried	If needed, the most probable	Been tried on FOD deflector	Feasible for large components	Not been tried

These common usages will give an idea in the concept generation phase on adapting the feasible concepts to the current problem. When the focus is narrowed down to the inlet and lip IPS concept, the table 4.3 gives a general idea about the process.

Table 4.3: Inlet and lip focused common usage of existing IPS methods.

	Pneumatic boots	**Electro thermal**	**Fluid**	**Electro impulse**	**Hot-air**
Engine inlet lips	Limited to bypass inlets	De-icing provides good performance	Possible, risky for fluid ingestion	Recommended if ingestion for short cycle is acceptable	Feasible for inlet lips close to compressor
Miscellaneous intakes and vents	May be feasible, not been tried	If needed, the most probable	Been tried on FOD deflector	Feasible for large components	Not been tried

A detailed comparison and selection of the existing concepts special to ES-30 requirements are carried out in the chapter 4.2.

4.1.2 New concepts

Although there is no bleed air onboard due to lack of compressors, electric motors generate heat, as well which requires to be cooled by heat exchangers. This is an opportunity to use the waste heat for anti-icing of the inlet lip. Several concepts are built and presented in this chapter.

In figure 4.16, the simple loop shows that hot water is received from the heated electric motor for cooling purposes. On the way to the air-cooling heat exchanger, it is passed through the inlet lip and used for anti-icing. Then, the circuit is given to the heat exchanger back with a temperature drop, cooled, and transmitted to the electric motors back.

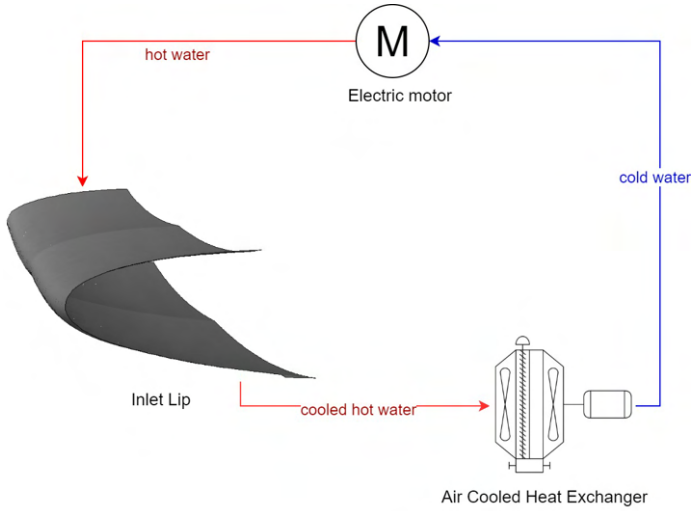

Figure 4.16: First concept using waste heat.

In figure 4.17, the concept involves utilizing the waste heat produced during electric motor operation. The difference lies in the placement of the inlet lip pipe. Heat exchangers are designed concerning various requirements. One parameter that affects the heat capacity is the temperature difference of the water before and after. It is preferred that this IPS be designed independently from the surrounding systems. To avoid the need for a unique heat exchanger design for different IPS requirements and to maintain efficiency, the inlet lip pipe is positioned after the heat exchanger in this concept. After the cooling heat exchanger, the chilled water is used inside the pipe and fed back into the loop.

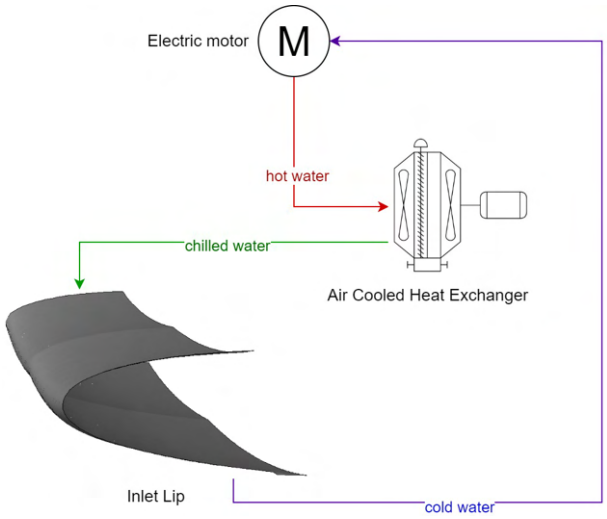

Figure 4.17: Second concept using waste heat.

The third concept is illustrated in figure 4.18 with a small addition to the second concept. In case the water coming out from the heat exchanger is not warm enough to prevent icing on the lip, the water can be heated, for instance by a heating element covering the pipe, and transmitted to the lip. A detailed computation will be carried out in the next chapter to determine if the water temperature in the second concept is adequate before implementing any enhancements as in this concept.

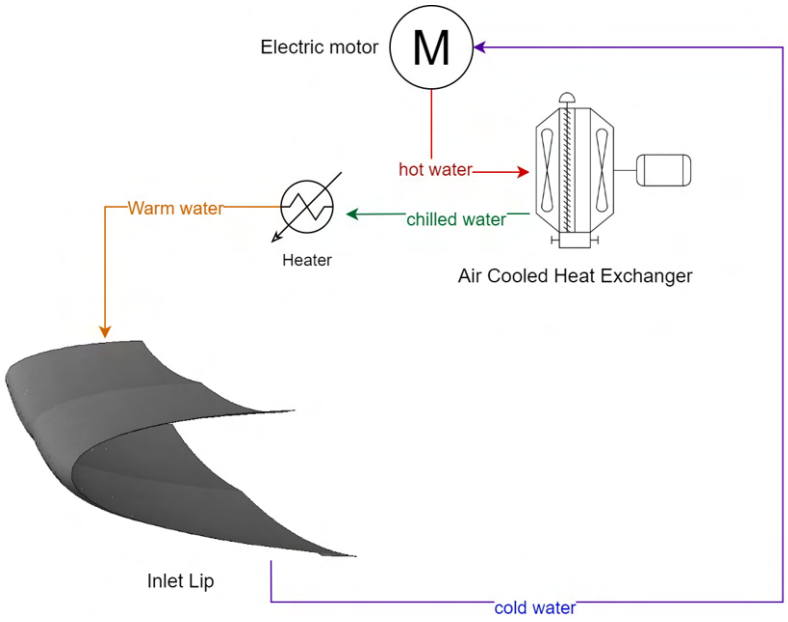

Figure 4.18: Third concept using waste heat.

4.2 Concept Selection

Existing and innovative concepts are evaluated in the previous chapter. A quantitative study is done on the possible solutions to move forward with the most promising ones to develop further. It is possible to continue with more than one concept when the solution is not obvious and needs more investigation.

First, the existing concepts are presented in the table 4.3. There are no solid applications with pneumatic boots used on the cooling intakes. It can weigh and cost much to install this system in a small region due to the necessary components described in 4.1.1.1. Using the fluid for anti-icing or de-icing can be tricky in terms of fluid ingestion by the intake. A storage place for the fluid is also required which is challenging to install for this type of intake. Electro-impulse IPS has the strong advantage of requiring very low power; however, implementing it on a small area, such as a sharp lip of cooling intake, may not be applicable. There is a possibility of electromagnetic interference which may pose a higher risk in a hybrid-electric aircraft. Hot air IPS is a good option for turboprop inlet since the compressor is at a close location and the power guiding the air into the lip is the only power needed. However, it is not feasible for the cooling intakes as they are usually located aft of the fuselage. For the inlet in this research, not having a compressor on the nacelle

is the main problem in applying this type of IPS. Because of the absence of bleed air, this option is eliminated before any further improvements are made. Electro-thermal IPS is a reliable and simple IPS, whereas it can cost much power if the region where it is going to be applied is large such as wings. For a small inlet lip, it can be a feasible solution. The anti-icing mode of this IPS is also applicable which is in favor of protecting the inlet from ice ingestion.

With these advantages and disadvantages, a summary of existing concepts is shown with the level of preferences in the table 4.4.

Table 4.4: Investigation of existing concepts for the air inlets of ES-30.

Not applicable Poor Fair Good

	Pneumatic boots	Electro thermal	Fluid	Electro impulse	Hot-air
Feasibility	Difficult but installable	Installable	Difficult but installable	Coils need space	No bleed air from the compressors
Performance	Shedded ice from de-icing	Runback ice	Cleans the ice	Shedded ice from de-icing	
Risk	Ice ingestion	Ice accumulation aft of lip	Fluid ingestion	Electromagnetic interference	
System complexity	Difficult due to limited space	Easy to transmit power due to location	Fluid storage place	Only power and sequencing box	
Maintenance	High	Low	High	Medium	
Weight	Medium	Light	Heavy	Light	

After selecting the electro-thermal IPS from the evaluation of existing IPS methods in the table 4.4, it is compared with the new concept where the lip is heated with the water of the cooling system. One of the most significant system considerations are the power required, the weight added, the complexity of the system, the cost of operating that type of IPS, and the possible risks. A qualitative matrix is presented in the table 4.5 where both concepts' criteria are given.

Table 4.5: Qualitative selection matrix.

Criteria	**Water-heated IPS**	**Electro-thermal IPS**
Power	Only to pump (waste heat is used)	Small amount due to small region
Weight	Additional pipes and pumps	Light mats
System complexity	Extra pipe interfaces and loops	Typical way of coatings
Cost of operation	Heat exchanger requirements changes	Power consumption from batteries
Risk	Heat supply need when motors are not running	Reliable

The features of both concepts do not give a prevailing solution as both concepts have different promising criteria. For instance, using the waste heat is a highly promising feature for water-heated IPS, and being used and suitable for these types of inlets is a reliable feature for electro-thermal IPS. Under these circumstances, both concepts are carried to the concept development and improved further.

4.3 Concept Development

On the second diamond of the framework, the concepts selected in the previous chapter are developed in detail. The critical conditions are identified, a generic inlet model is designed, and the ice accretion is analyzed without any ice protection in these critical conditions. Then, the required power is computed and validated by demonstrating the ice impingement differences after providing the heat. The system requirements of both IPS are presented to meet the power requirements. The results are discussed according to the ES-30 mission.

4.3.1 Critical icing conditions

The design for IPS is built according to the icing conditions that the aircraft is going to experience throughout the flight envelope. This intersection set defines the icing envelope of the aircraft. For ES-30, it is already presented in the figure 3.16 while explaining the boundary conditions. The details of simulation conditions are given in the table 4.6. For simplicity, the same calibrated airspeed is for three different scenarios which give different true airspeeds according to different atmospheric conditions. The two most common and critical MVD values are simulated for both CM and IM conditions. The selection of the temperatures is significant where the warmest and coldest points are chosen according to the icing envelope limits at the relevant altitudes. Middle points are selected to show the trends beside the values and the frequent icing conditions are taken as a guide which are given in the figure 2.6.

Table 4.6: Simulation conditions.

Altitude (ft)	MVD (μm)	KCAS (kts)	CM/IM	Ambient temperature (°C)
5000	20, 40	140	CM	-3, -10, -30
			IM	-3, -10, -12
10000	20, 40		CM	-3.6, -10, -30
			IM	-3.3, -10, -21.9
20000	20, 40		CM	-16.1, -20, -30
			IM	-19.2, -20, -30, -40

4.3.2 Intake design

The intake is designed based on the ESDU method explained in the section 2.3. As mentioned in the comparison of drag characteristics between scoop and flush inlets, the most suitable inlet type is selected as flush inlets for the required purposes of

ES-30. This flush inlet is designed with the rectangular planform as it gives a lower drag than the curved-divergent ramp planform type. The drag guides the design of the inlet in this research, and the calculations continue under this perspective. The purpose of this inlet is to provide sufficient airflow to the cooling system of the turbomachines, which guides the operating point to be at full captured mass flow rather than at maximum efficiency. ESDU has an example of dimensioning the inlet for this purpose which is taken as a guide.

First, the required mass flow is decided to provide sufficient airflow to the heat exchanger in the cooling system. With this value, a first approximation is done by setting,

$$A_1 = \frac{\dot{m}}{\rho_0 V_0} \tag{4.1}$$

the ρ_0 and V_0 are the air density and true airspeed values of the atmospheric conditions the inlet is designed for. In this case, it is carried out with the maximum cruise altitude and speed.

As the lip profile is elliptical,

$$d_{1fl} = d_t + 0.5t - l_l \tan\alpha \tag{4.2}$$

where the parameters of the flush inlet are defined and shown in the figure 2.28.

The width-to-height ratio also known as the throat aspect ratio is assumed as 4 as it is an optimal value for a good pressure recovery [15]. The ramp angle is taken a little larger than the typical values since the nacelle is already angled by 5°. By increasing the ramp angle until the maximum allowable value which is 11.5° in the design, the inlet area is intended to expand to catch more airflow. The lip is designed according to the architecture in the figure 3.10 given at [65]. With its guidance, calculations are continued with $l_l/d_t = 0.98$ and $t/d_t = 0.53$.

$$A_1 = w(d_t + 0.5t - l_l \tan\alpha) \tag{4.3}$$

d_t is found which gives the distance between upper and lower internal surfaces in the throat plane.

From the mass flow ratio plot, which is given in ESDU [15], with the fraction of boundary layer thickness, δ to d_t and the Mach number, $\dot{m}/\dot{m}_0$ is obtained which gives a final mass flow value. If the first area approximation gives a lower mass flow value than the required, the second approximation of the area is increased a little and the loop is repeated. The numerical procedure ends when the required mass flow is reached.

Table 4.7: Inlet parameters.

Width	0.203 m
Area	0.009 m^2
Lip area	0.02 m^2
Thickness	0.007 m
Mass flow	0.6 kg/s
Ramp angle	11.5°
Width-to-height ratio	4
Nacelle angle	5°

4.3.3 Ice accumulation on unheated inlet

Once the inlet design was finalized, the next step was to compute the impingement limits on the surface. For this, unheated wall simulations were performed for all the test cases in table B.4, allowing also to determine the heat transfer coefficient.

The chosen times for ice accretion range between 6 and 8. Analyzing the plots in figures 4.19 and Appendix D.2, which were obtained for different test cases of table B.4 representing CM and IM conditions at both 5,000 ft and 20,000 ft, it is possible to observe that the impingement limits extend further than the lip surface, this is due to a combination of different previously introduced parameters, such as flight speed or LWC which will induce more momentum into the droplets or increase water content, which combined with droplet inertia will change the momentum of the droplets and consequently changes the impingement limits on the surface. Larger droplets will impact the surface further aft whereas smaller ones might not even impact due to their low inertia. The surface accretes more ice on the external face of the lip due to the angle of attack that this submerged inlet has on the nacelle surface, which is an answer to the research question of this work. It is possible to observe that the ice thickness is also lower due to the lower LWC in the higher MVDs.

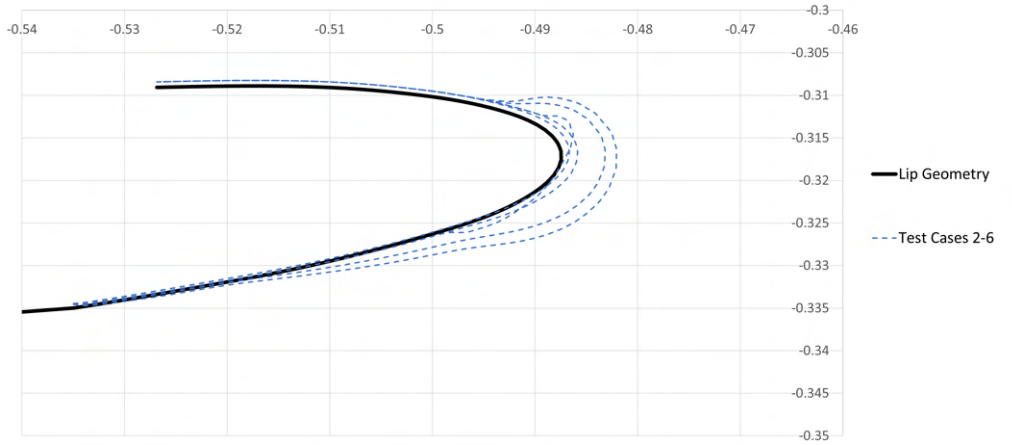

(a) CM conditions at 5000 ft

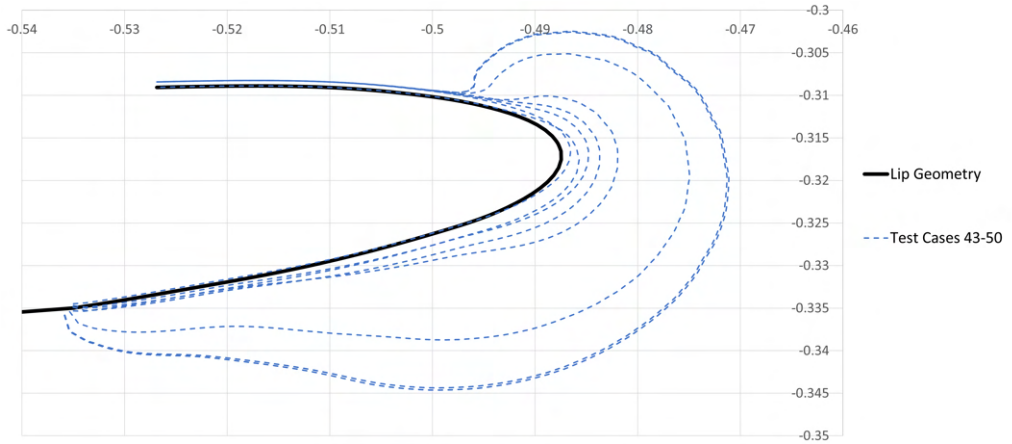

(b) IM conditions at 20000 ft

Figure 4.19: Ice shapes at the different conditions and altitudes described in table B.4

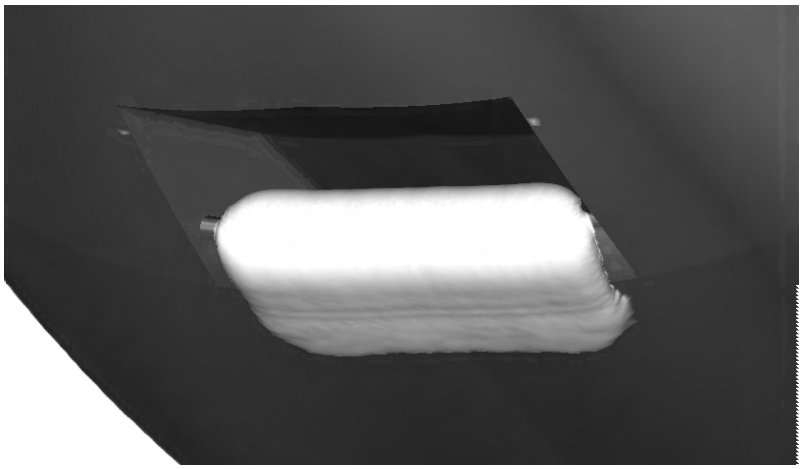

Figure 4.20: Ice accretion on lip surface for test case 1 ($M = 0.23$, $T_s = 270.15\ K$, $LWC = 0.574\ g/m^3$, $MVD = 20$)

For a fixed MVD, the collection efficiency is observed to decrease with temperature, this happens since the decrease in LWC with altitude has a stronger influence on collection efficiency than the increase in airspeed.

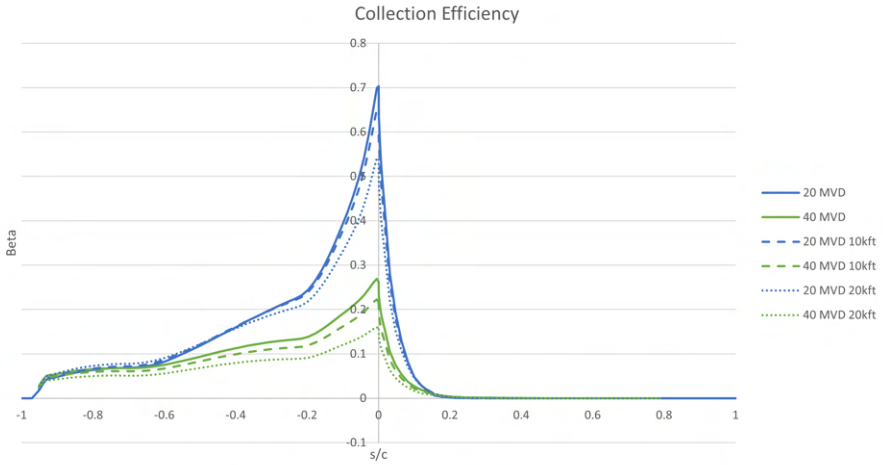

Figure 4.21: Collection efficiency variation with altitude and MVD for respectively test cases 1, 7, 8, 37 and 38 defined in table B.4

From the theory, it is known that a larger number of droplets is expected to impact the surface, increasing then the collection efficiency due to the higher inertia of larger droplets, with their momentum being less affected by flow disturbances, as stated previously. However, there is a relatively high reduction in the peak collection efficiency for higher MVDs. One possible reason for these results can be explained with the nacelle and inlet position in figure 4.22. The flow is being reoriented by the nacelle divergent shape starting from the spinner before the entry ramp begins close to the lip entry. Therefore, the flow reaches the ramp already oriented, parallel to the surface. More droplets overpass the lip surface due to referred higher inertia instead of curving into the ramp more easily like the lower 20 μm droplets, creating a shadow zone for higher inertia droplets.

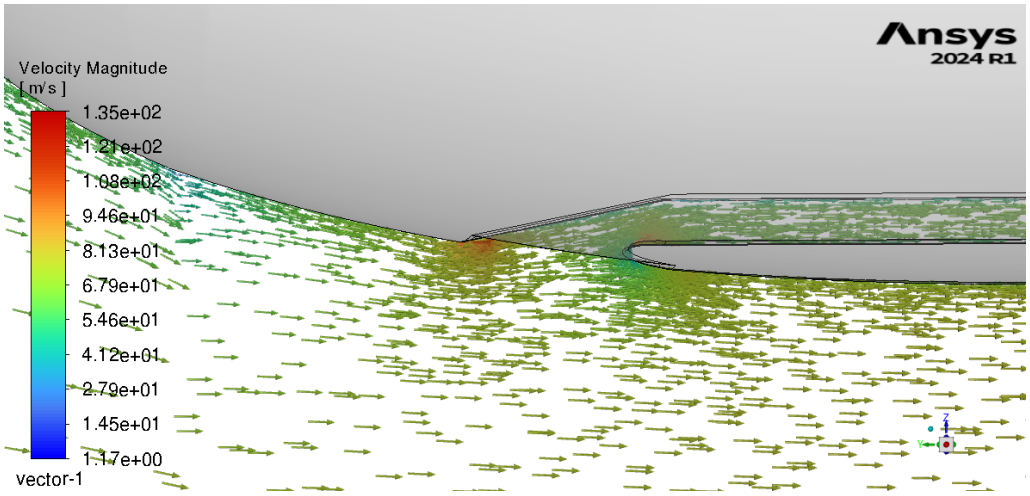

Figure 4.22: Velocity magnitude vectors for 0° of AoA.

The heat transfer coefficient remains relatively constant through the outside surface due to its smoother curvature. It drops towards the stagnation point due to the decrease in momentum and increases afterward into the inner duct due to the small curvature of the nose of the inlet which accelerates the flow since the stagnation point is located before it. The average values of 356, 300, and 212 W/m^2K are achieved for the 3 different altitudes and are represented by the dashed lines in figure 4.23.

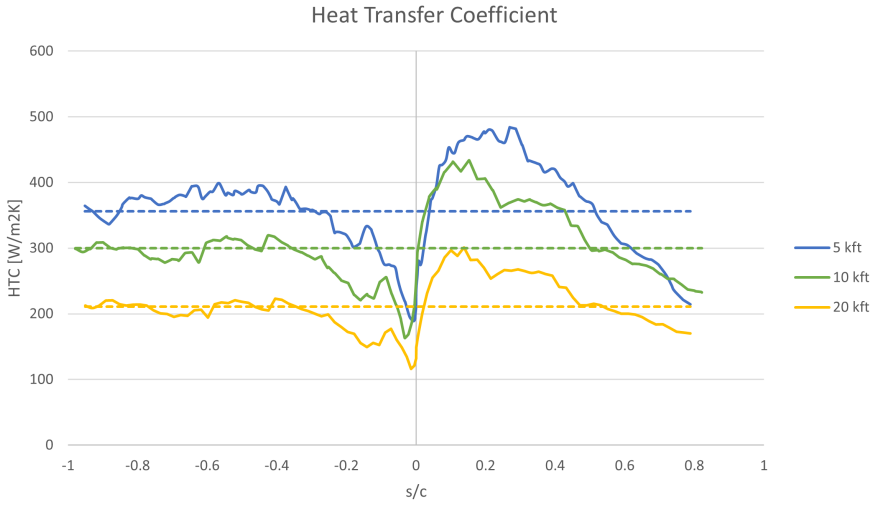

Figure 4.23: Heat transfer coefficient variation along the lip surface for test cases 1, 13 and 37 defined in table B.4.

The water caught or impingement rate represents the final parameter obtained after the collection efficiency, giving a good representative measure of the rate of water collected by the surface. From figure 4.24 it is possible to conclude that the decrease in collection efficiency observed in 4.21 is compensated with the increase in velocity as stated by equation 2.6 since LWC is only a function of temperature which is maintained the same for both cases.

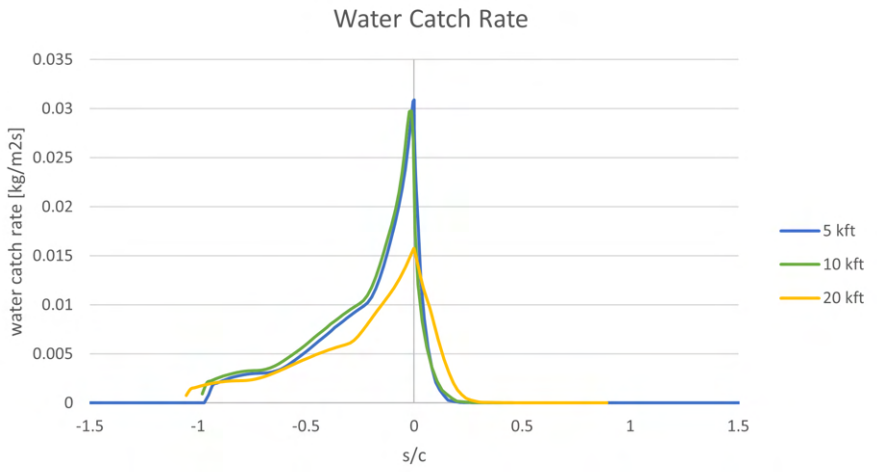

Figure 4.24: Water catch rate comparison between different altitudes for test cases 1, 13 and 37 defined in table B.4

For the 20,000-foot scenario, the warmest possible temperature is 257.05 K, which is lower than the previously evaluated cases. In this case, the decrease in LWC is significant enough to affect the water caught rate peak, with the collection efficiency change being higher than between the previous two altitude levels as shown in figure 4.21. Figure 4.25 confirms that temperature is indeed the variable that affects the water catch rate.

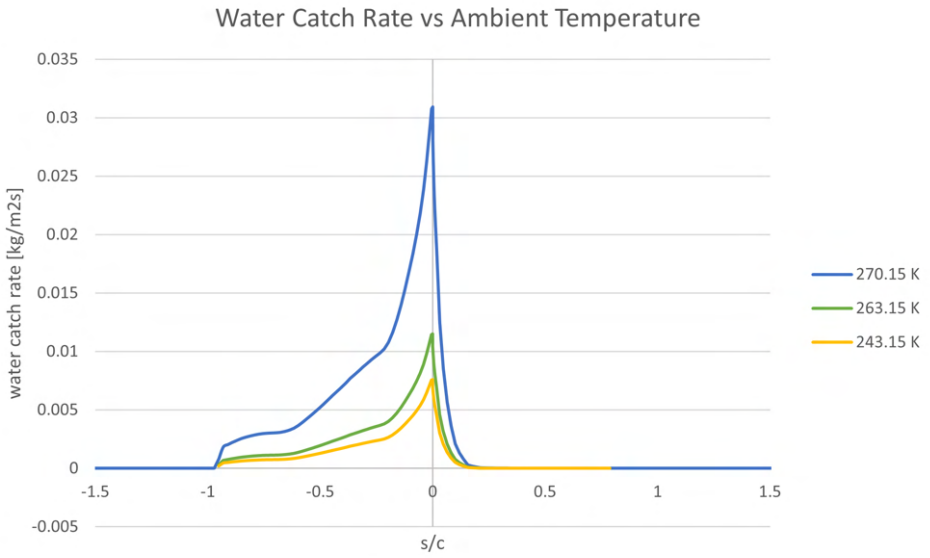

Figure 4.25: Water catch rate variation with temperature for respectively test cases 1, 3 and 5 defined in table B.4

All the previous parameters are time-independent. Thus, the thickness solutions are highly dependent on the time of accretion, and the following cases are obtained using a 6-minute time of accretion. Comparisons between CM and IM conditions

are made for altitude changes as well as shown in figure 4.26.

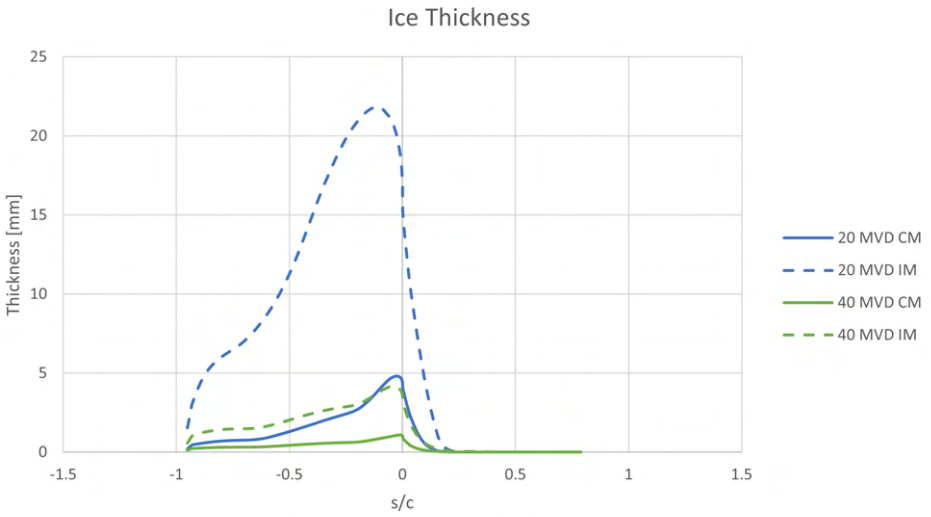

Figure 4.26: Ice thickness variation with CM/IM and MVD for respectively test cases 1, 2, 7, 8 in table B.4

MVD has the most meaningful impact on ice thickness as seen from figure 4.27, confirming the previous statements, which is also confirmed for altitude changes that inherently decrease the LWC content.

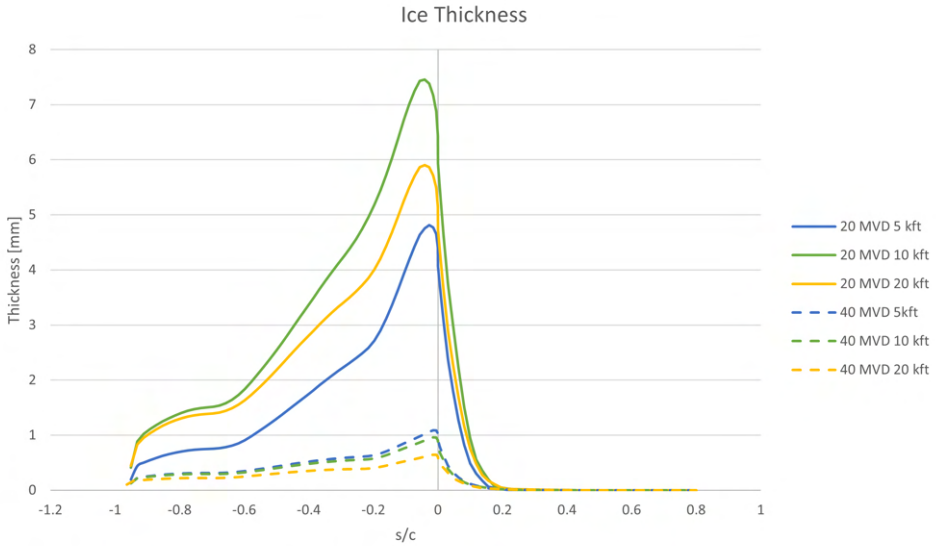

Figure 4.27: Ice thickness variation with MVD for respectively test cases 1, 2, 13, 14, 37 and 38 defined in table B.4

Another important parameter to be accounted for is the inflow angle on the surface of the nacelle. Naturally, the propellers will reorient the flow into the nacelle.

Nonetheless, this inflow might not be completely aligned, also wind gusts can happen during climbing changes thus the flow angle of attack into the nacelle; for this reason, flow solutions for 10, 20, and 30° of inflow angle of attack are calculated, and their collection efficiencies can be compared in 4.28.

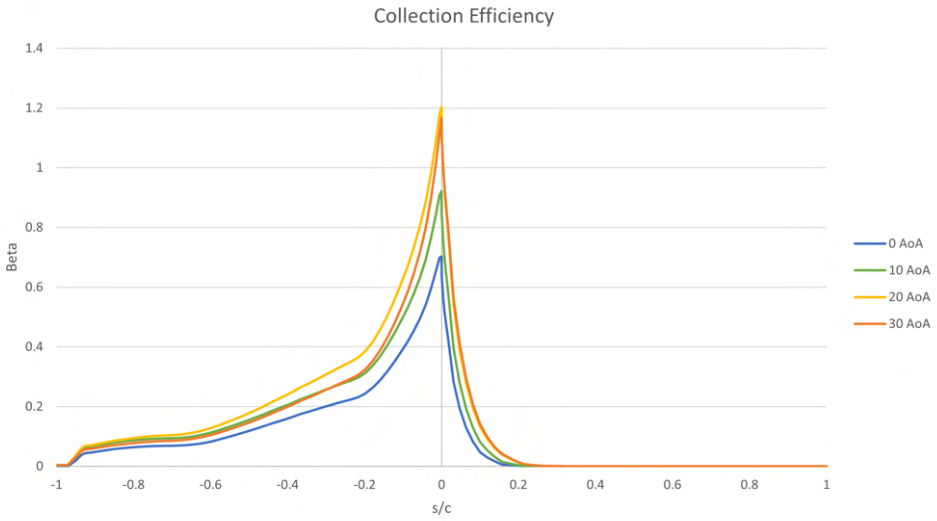

Figure 4.28: Collection efficiency variation with inflow angle of attack ($M = 0.23$, $T_s = 270.15\ K$, $LWC = 0.574\ g/m^3$, $MVD = 20$)

This collection efficiency is obtained for 20 μm droplets, and it can be observed that the collection efficiency increases with the AoA until at least 20° of inflow angle, then decreases for 30° as the flow starts to be unaligned with the inlet lip which is seen by comparing both figures 4.22 and 4.29.

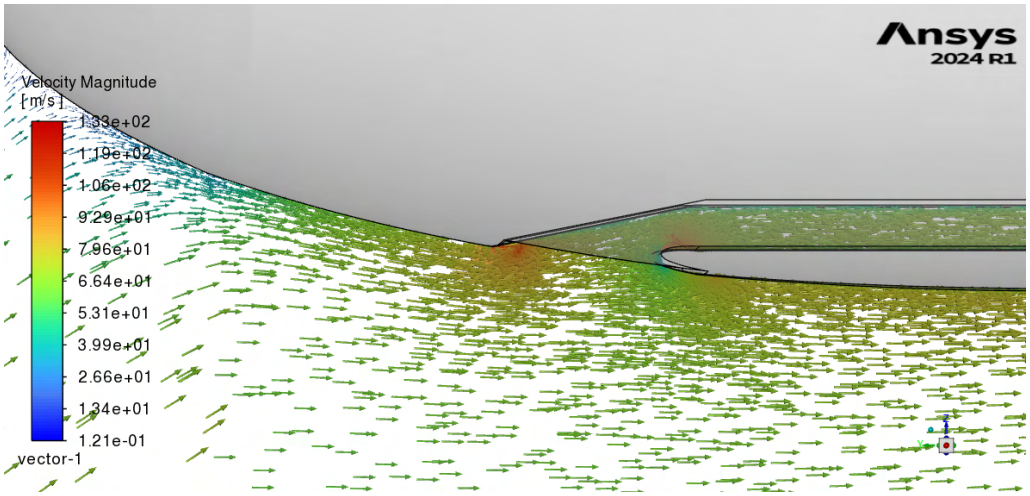

Figure 4.29: Velocity magnitude vectors for 30° of AoA.

A visual comparison between the different angles of attack can be seen in figures D.6. It can be concluded that if the inflow has an angle relative to the nacelle, the impingement limits will be greatly extended. Even though the thickness aft is small

compared with the ice accreted on the lip, it might be necessary to implement an icephobic coating on this area to prevent build-ups.

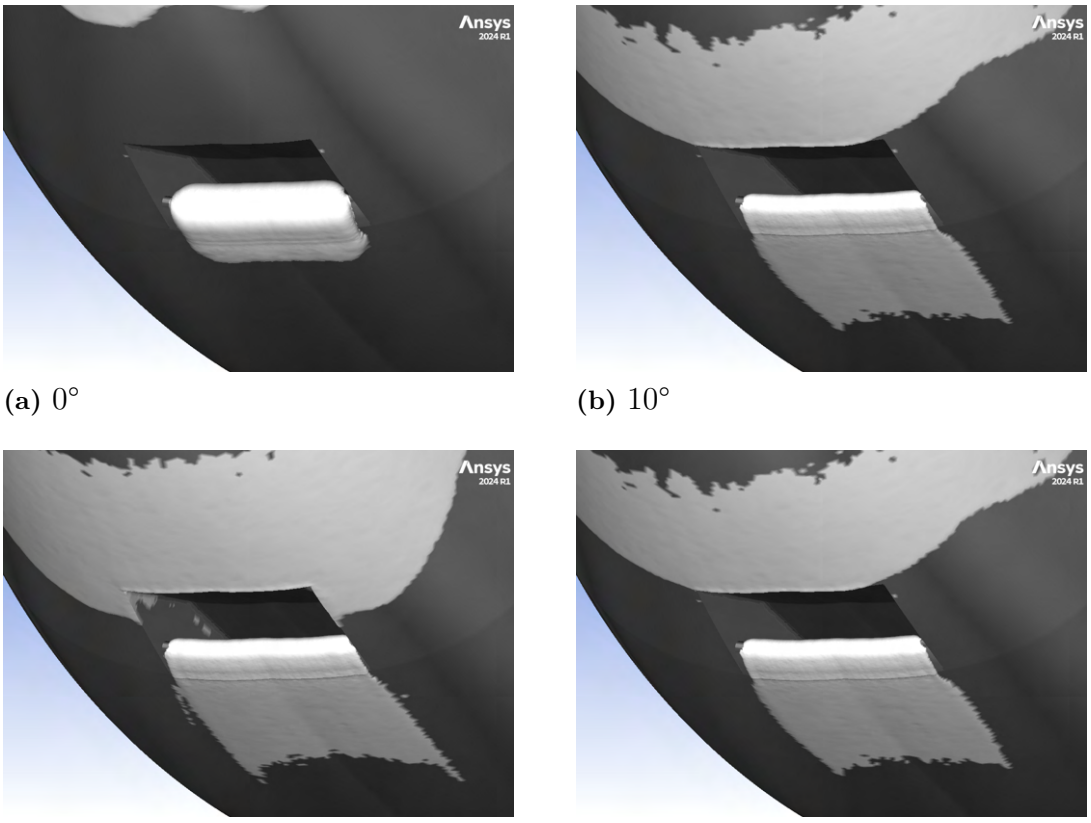

(a) 0° **(b)** 10°

(c) 20° **(d)** 30°

Figure 4.30: Ice accretion in 6 minutes for test case 1 ($M = 0.23$, $T_s = 270.15\ K$, $LWC = 0.574\ g/m^3$, $MVD = 20$)

Even though it is possible to adapt the model with a flat plate or cylinder and assume the heat transfer coefficient, the most accurate values can be taken from the flow solution obtained by the CFD model. That is why, heat transfer coefficients and collection efficiencies, which are highly related to the design of the model, are obtained and used in the Simulink computation model to calculate the power requirements. As the flow properties do not change significantly for different temperatures and to simplify the number of simulations, one heat transfer coefficient value for each case of altitude is computed from the warmest temperature value of the relevant altitude. The droplet impingement analysis (DROP3D) is relatively faster and easier than the flow solutions of FLUENT. Therefore, the true and distinct temperatures are considered with different MVDs, and various collection efficiencies are obtained as presented in table 4.8.

Table 4.8: Outputs from flow solutions for CM and IM.

Altitude (ft)	Heat transfer coefficient (W/m^2K)	MVD (μm)	Collection efficiency (β)
5000	356.082	20	0.703
		40	0.269
10000	299.758	20	0.652
		40	0.223
20000	212.238	20	0.540
		40	0.160

4.3.4 Power requirements

The required power to avoid icing on the inlet for the running-wet anti-icing mode is calculated for each critical condition, given in the table 4.6. Figure 4.31 presents the power for every altitude in continuous and intermittent maximum icing conditions at various ambient temperatures with an MVD of 20 μm.

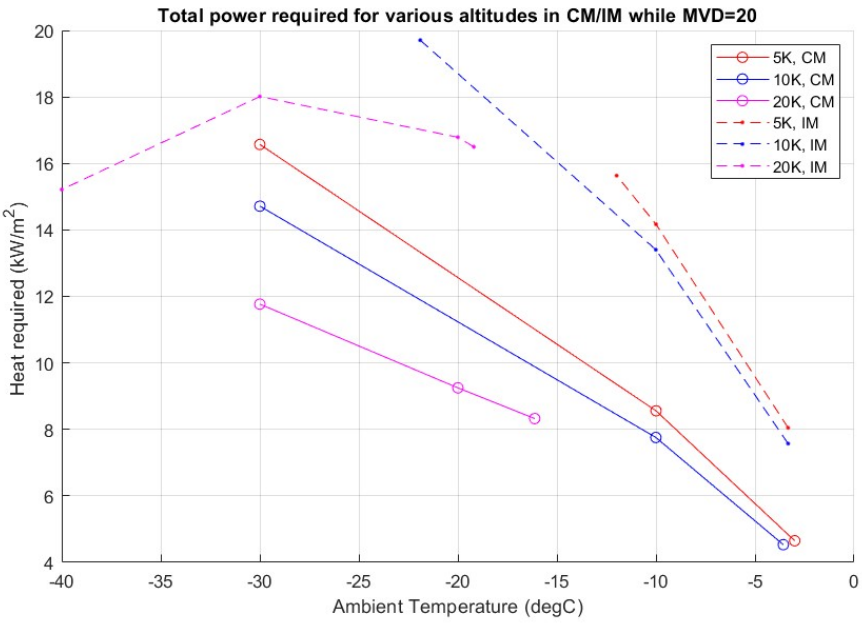

Figure 4.31: Total power required for various altitudes in CM/IM while MVD = 20 μm.

CM trends are parallel to each other for the decreasing temperature. The colder the atmosphere is the more power it is required for CM conditions at every altitude. It is also clear that the lower altitude needs more power since higher heat transfer coefficients cause more convection. To evaluate in detail, the energy balance terms are shown explicitly in figures 4.37 and 4.38 which is going to be discussed further.

IM trends, on the other side, show significant icing characteristics. Like in the CM trends, lower altitudes require more power; however, as the icing envelope of the IM

does not extend as CM boundaries, it is harder to see that trend. One important trend is from 20000 ft in IM conditions where the required power stops increasing with the decreasing temperature and starts decreasing around $40°F$. This is because of the extremely low liquid water content, which causes a low heat flux of the sensible heating term, which is explained and shown further in the next steps. As a result, the maximum power required is observed at 10000 ft in IM icing conditions with a value of 19.71 kW/m^2.

The first thing that is noticed when the MVD is increased to 40 μm is the required power for all the scenarios is less than the one when the MVD is equal to 20 μm. The reason for not having that much difference between CM and IM trends, in this case, is that LWC decreases much more rapidly when the MVD increases in IM conditions as seen from the figures 2.19. The other relations are similar to the one with 20 μm MVD such as requiring more power in lower altitudes and temperatures.

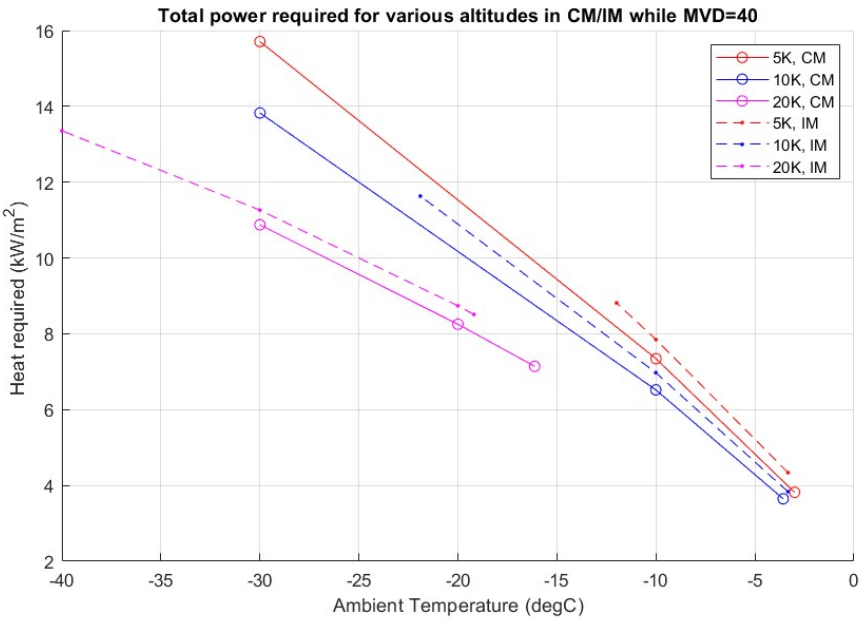

Figure 4.32: Total power required for various altitudes in CM/IM while MVD = 40 μm.

As observed from the figure 4.31 by changing the trend, the sensible heating is a significant parameter that is investigated and presented beside the total power. The sensible heating term effect is shown in the figures 4.33 and 4.34 which is computed from the equation 2.5

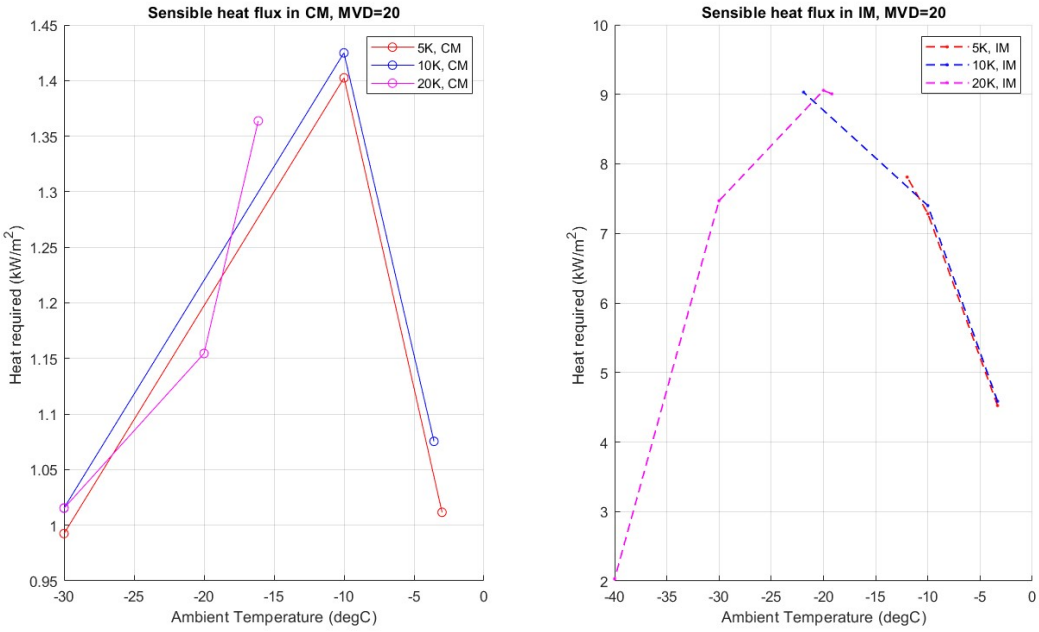

Figure 4.33: Sensible heat flux vs ambient temperature in CM/IM while MVD = 20 μm.

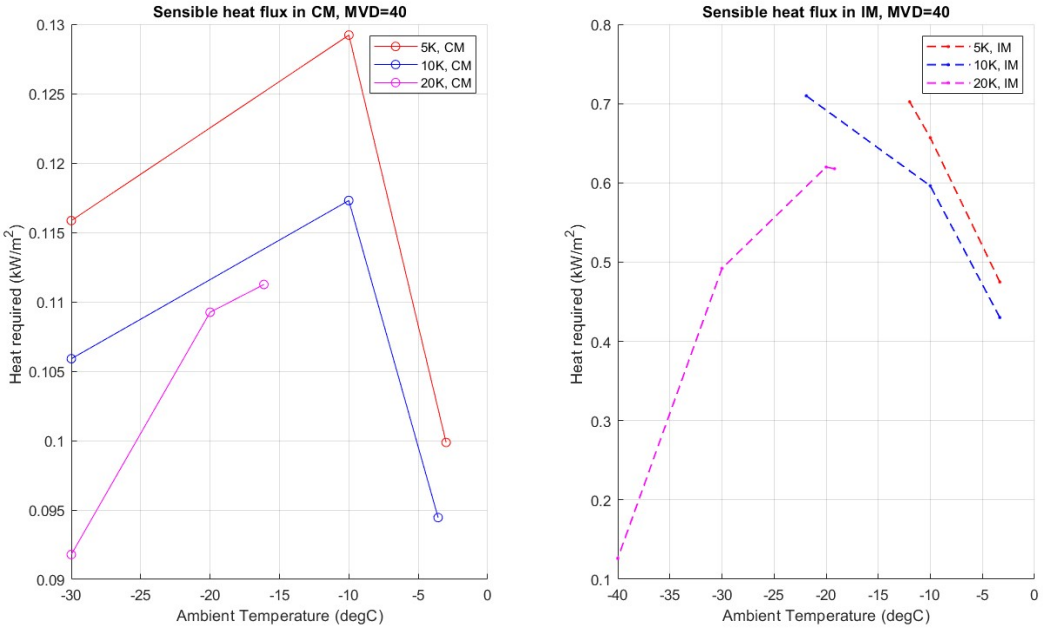

Figure 4.34: Sensible heat flux vs ambient temperature in CM/IM while MVD = 40 μm.

The sensible heating term does not have a linear trend opposite to the other heat flux terms. It peaks in the middle ambient temperatures which are around -10

$°C$ for CM and -20 $°C$ IM for MVD = 20 μm in figure 4.33. One important detail is the values between CM and IM conditions. IM values reach almost 5 times the CM values, which can be explained by way higher LWC values for IM conditions.

The same trend is seen in the figure 4.34 which the value of the heat fluxes should be noticed. For the MVD = 40 μm, the values are almost 10% of the values of MVD = 20 μm for both CM and IM, which is because of the lower LWC for higher MVD.

To explain why it peaks around the middle temperatures, the terms affecting are investigated which are the changing impingement rate $\dot{m}_{local}$, and the difference between ambient and skin temperature. The impingement rates are presented in the figures 4.35.

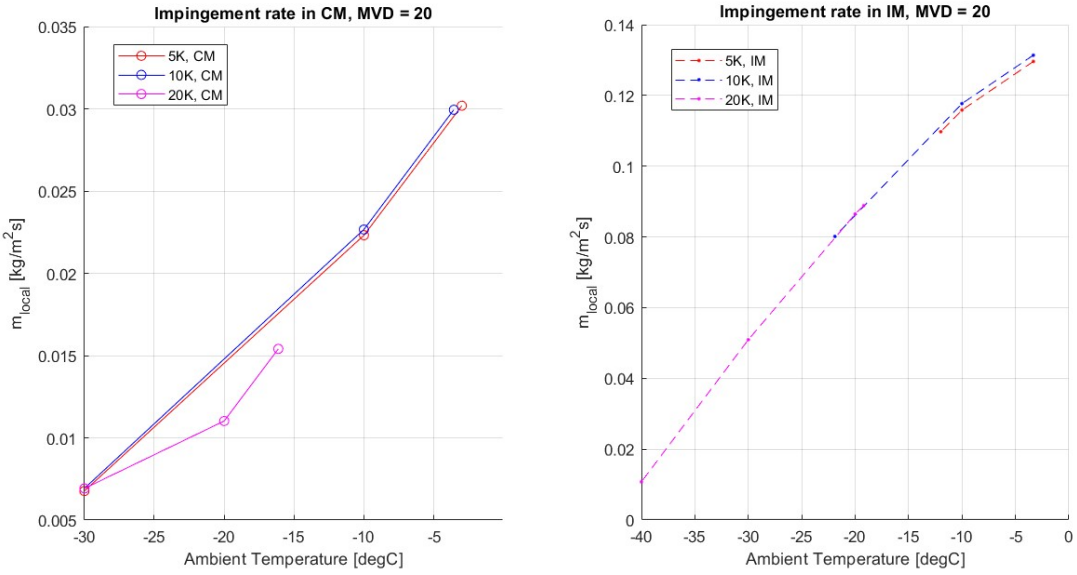

Figure 4.35: Impingement rate, in CM/IM, MVD = 20 μm.

The impingement rates have a linear trend with the ambient temperature. This term is computed from the collection efficiency, LWC, and the velocity as given in the equation 2.6. As the collection efficiencies used are taken as the same constant with the same velocity and varying ambient temperatures, the only factor is LWC shaping the trend of impingement rate. LWC and the temperature differences are in the figure 4.36. The peak value of multiplying the two values from two intervals is obtained by taking their intersecting values from a simple mathematical perspective. That is why, the peak values of sensible heat fluxes are seen at the intersecting ambient temperatures. The reason for the 20000 ft-CM trend is splitting away from the other trends in figure 4.35 is that the actual LWC trend for CM is as shown in figure 4.36. It is interpolated linearly for 5000 ft and 10000 ft due to no data in between. For the IM scenario, the trend is like the LWC trend as expected.

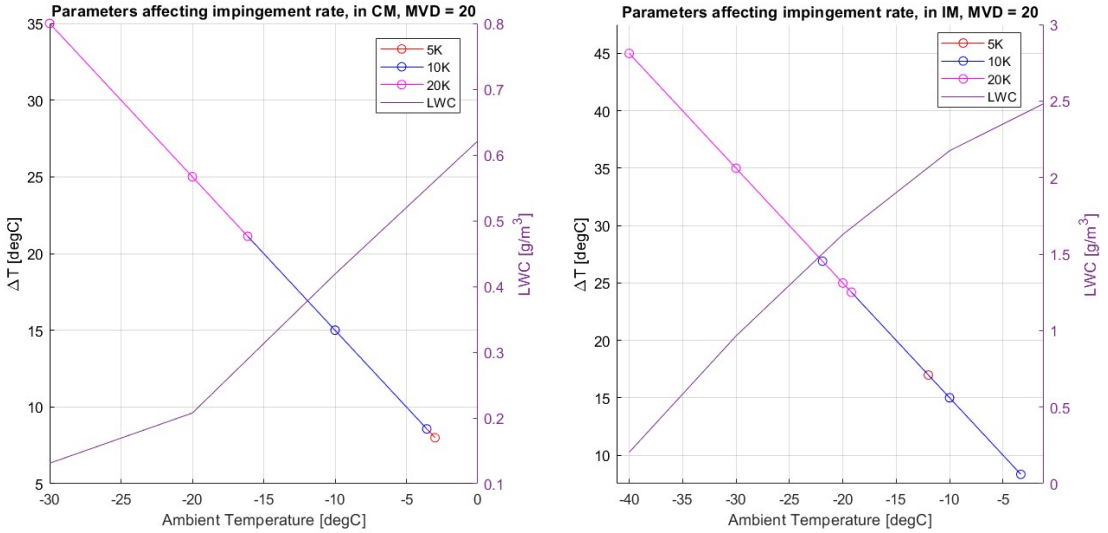

Figure 4.36: Parameters affecting impingement rate, in CM/IM, MVD = 20 μm.

As significant parameters shown above affecting the total power, it is presented in the figures 4.37 and 4.38 which parameters affect which energy balance terms and lead to the resulting power. Ambient temperature has a huge effect on convection, MVD and icing conditions such as CM or IM change the sensible heating term significantly, and altitude moderately affects convection implicitly since the heat transfer coefficient is the only variable on convection.

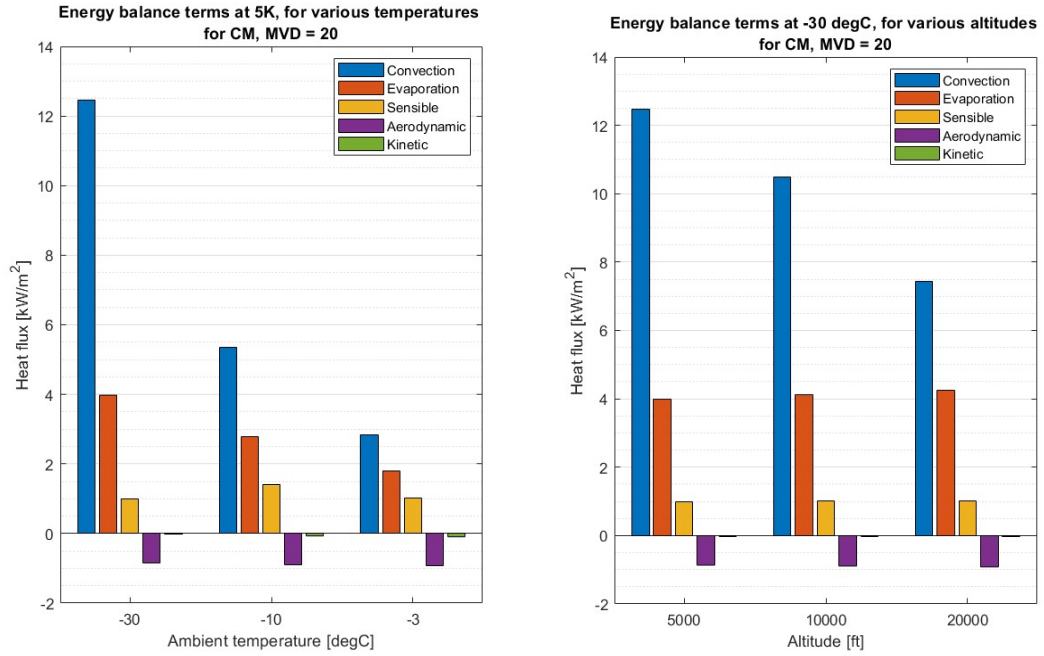

Figure 4.37: Energy balance terms at various temperatures and altitudes for CM, MVD = 20 μm.

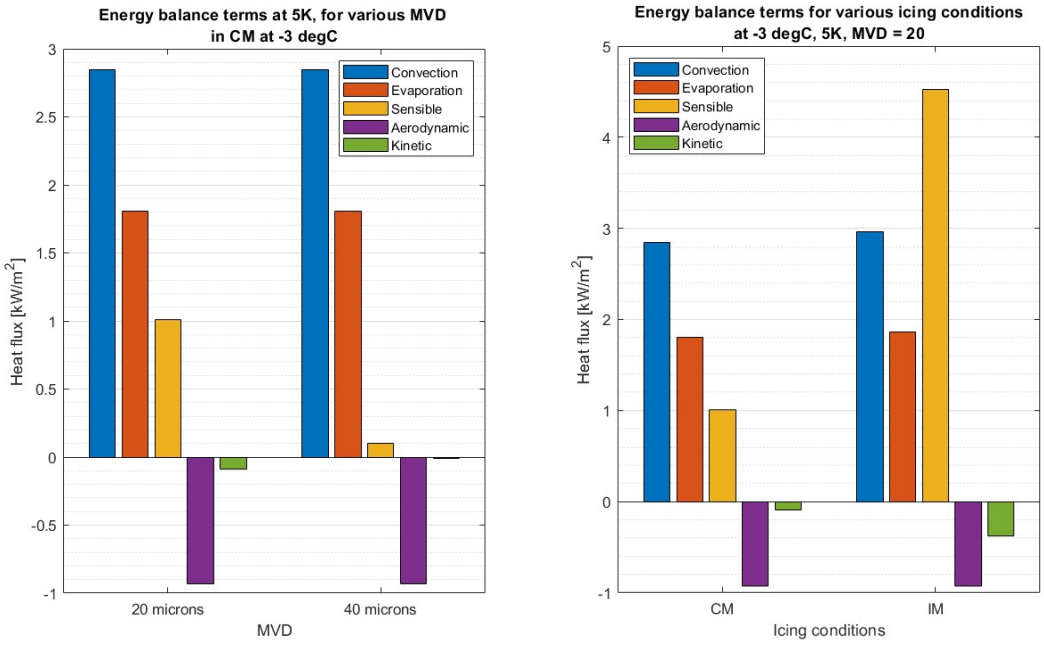

Figure 4.38: Energy balance terms at various MVD and icing conditions.

4.3.5 Validation with simulations

Having computed the required heat fluxes for each test case condition, the following conditions on table 4.9 are selected as the most critical conditions to validate due to their higher LWC values and/or the lowest heat fluxes of all the test cases, these combination was chosen since they were determined as the most critical ones to operation since with higher LWCs more liquid water will impact the surface and the lower heat fluxes can create more issues to remove the ice from it.

Table 4.9: Analyzed test conditions.

Test Cases	Altitude $[ft]$	TAS $[m/s]$	MVD $[\mu m]$	HTC $[kW/m^2K]$	Heat Flux $[kW/m^2]$	Power Required $[W]$
1	5000	76.59	20	356	4.650	86.04
3	5000	73.92	20	356	8.560	158.39
7	5000	76.29	20	356	8.050	148.95
14	10000	83.74	40	300	3.650	67.54
16	10000	81.22	40	300	6.520	120.64
20	10000	83.80	40	300	3.830	70.87
22	10000	81.22	40	300	6.970	128.97
24	10000	80.86	40	300	11.630	215.20
44	20000	99.09	40	212	8.510	157.46
50	20000	94.95	40	212	13.360	247.21

Figures 4.39 and 4.40 show the difference in ice build-up between CM and IM conditions for the warmest possible temperature at 5000 feet. In Appendix D.3, a more detailed view of the other test cases is shown. The results of these simulations showed that a complete ice removal of the lip surface area is possible by these values which are applied by defining it into that surface boundary.

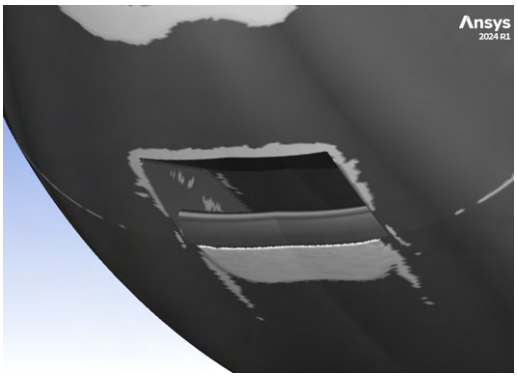

Figure 4.39: Ice cover heated surface for test case 1 in table B.4

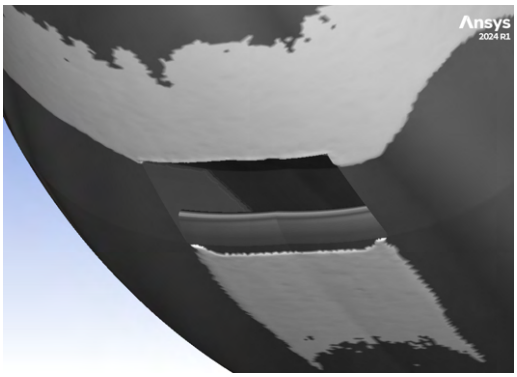

Figure 4.40: Ice cover heated surface for test case 7 in table B.4

Nonetheless, it is important to investigate the actual temperature reached by the surface. If the temperature is too high, a lower heat flux can be provided, resulting in a decrease in power consumption, which is an extremely relevant parameter for the ES30 energy management. On the other hand, high temperatures may compromise the structure of the nacelle itself.

Comparison between surface temperature distribution is given in figure 4.41 of test cases 1, 14, and 16 from the table B.4 shows that the average temperatures across the surface are maintained around average values of around 4.58, 7.55, and 3.34$°C$, respectively, confirming that the provided heat fluxes calculated by the implementation of Messinger's [33] mathematical model on Simulink, and provided here as a numerical boundary condition to the surface during the ice accretion simulation.

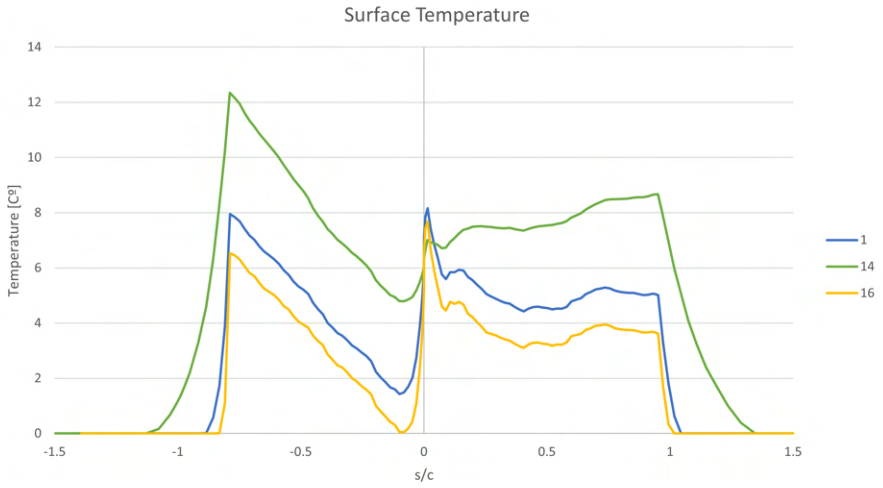

Figure 4.41: Surface temperature distribution for test cases 1, 14, and 16 described in table B.4.

For the ice thickness, it is possible to visualize the figure 4.42 that after providing the required heat flux for that operation condition the area covered by the heater is completely free of ice, having now ice build-ups which extend further into the aft

of the surface, outside of the heated area, but have greatly decreased in thickness. This can be explained by the water film model solved from ICE3D which creates water runback and refreeze once the surface temperature drops below 0°.

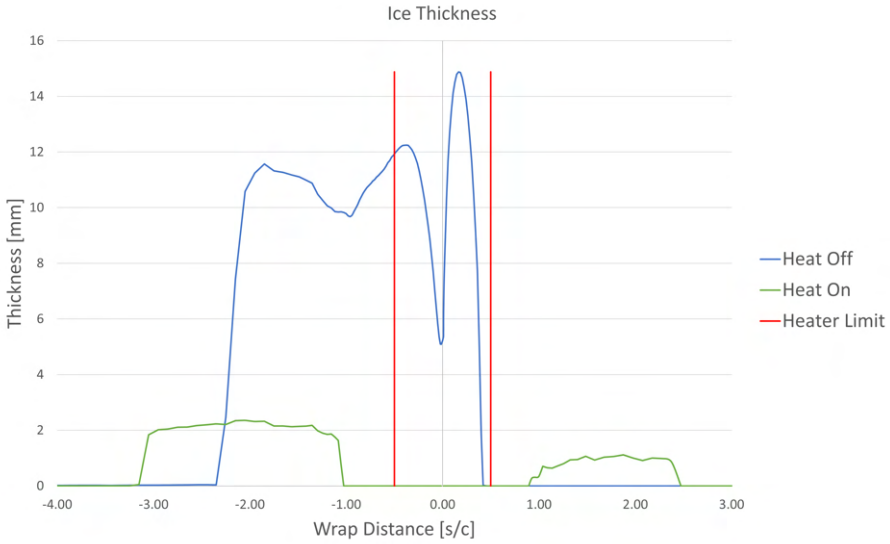

Figure 4.42: Ice thickness comparison with the heater on or off for test case 1 ($M = 0.23$, $T_s = 270.15\ K$, $LWC = 0.574\ g/m^3$, $MVD = 20$).

This ice buildup is relatively small, having only a maximum of 2 mm in thickness, and to avoid extending the heated area since that will increase the power consumption of the IPS.

4.3.6 IPS results

The ice protection system architectures, their system requirements, functions, implementations, and outcomes are presented in this chapter.

4.3.6.1 Electro-thermal IPS

The electro-thermal IPS is modeled as the existing and used implementation following the standard material layering in the table 4.1. These heaters cover the whole lip area as presented in figure 4.43 independent of the impingement limits which is not the common way how they are implemented. This approach is chosen to simplify the model, and the results of this decision will be discussed later. The system function is to provide continuous heat to the lip surface to meet the requirement that keeps the surface temperature above 5° to avoid any ice accretion. The heat is computed by the running-wet anti-icing method and applied throughout the inlet lip area.

The heat is provided through the heater element to both the outer and inner sides of the layers as shown in figure 4.43. Even though the material selections lead the majority of the supplied heat to the outer surface by the thermal conductivities and thicknesses, there will be a heat loss that goes towards the inner lip. The simple

thermal model starts where the heat comes from the heater element. This heat is coming from the power requirements directly assuming it is 100% efficient.

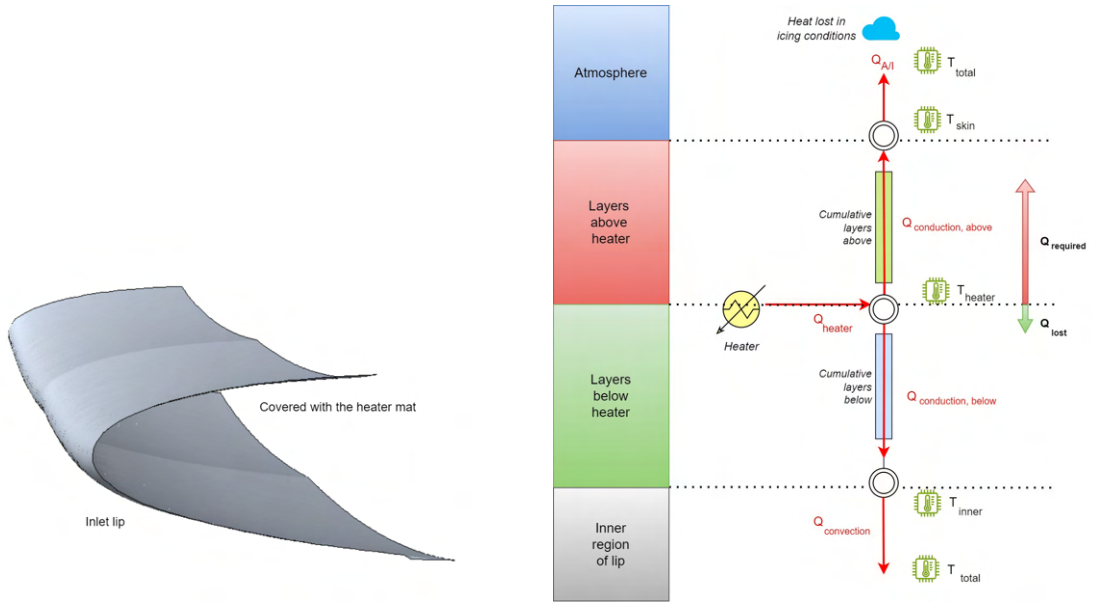

(a) Heater mat implementation on inlet lip

(b) System layout.

Figure 4.43: Electro-thermal IPS system implementation.

Then, this heat flux is separated outer and inner sides according to the thermal conductivity constituents of both sides. These heat fluxes are going to decrease a little by heating the materials and be transmitted to the skin and inner surfaces, respectively. The heat flux on the skin is going to balance the required heat in icing conditions, and the inner heat flux is going to balance with a constant temperature. Those heat fluxes defining the efficiency are named $Q_{required}$ and Q_{lost}.

The thermal efficiency factor is computed for each simulation condition from the equation 4.4. The minimum efficiency is considered by providing heat to the system.

$$\eta_{th} = \frac{\text{Heat required}}{\text{Heat supplied}} = \frac{Q_{required}}{Q_{lost} + Q_{required}} \tag{4.4}$$

Thermal efficiency values varied through different simulation conditions concerning different factors. As seen from the figures 4.44, (a) shows the efficiency depending on CM or IM at the same altitude and MVD. It is clear that the ambient temperature has a significant effect and when the atmosphere is colder, efficiency is lower which means more heat is lost to the inner side of the layers for both CM and IM. (b) shows another factor which is the heat required by the system. When the icing conditions are worse and more heat is required on the skin of the lip, the efficiency increases, which can be observed from most of the efficiency maps. This is mostly due to sucking more heat flow through the skin when there is a higher heat loss due to icing.

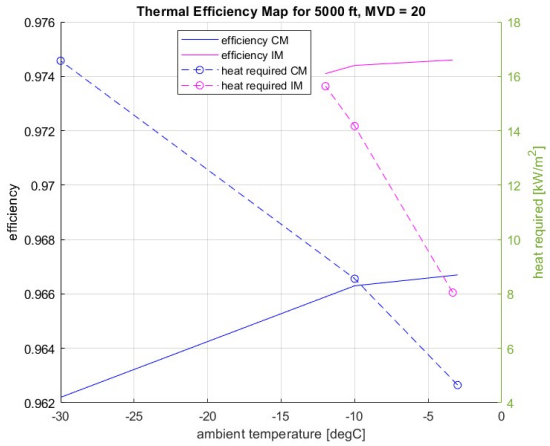

(a) CM/IM variation on efficiency at 5000 ft for MVD = 20 μm

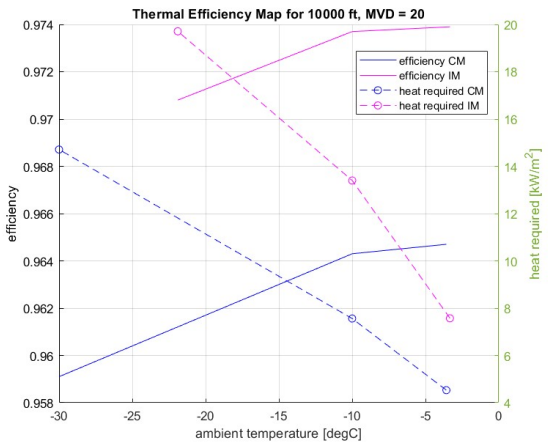

(b) CM/IM variation on efficiency at 10000 ft for MVD = 20 μm

Figure 4.44: Effects of ambient temperature and heat required on thermal efficiency in electro-thermal IPS.

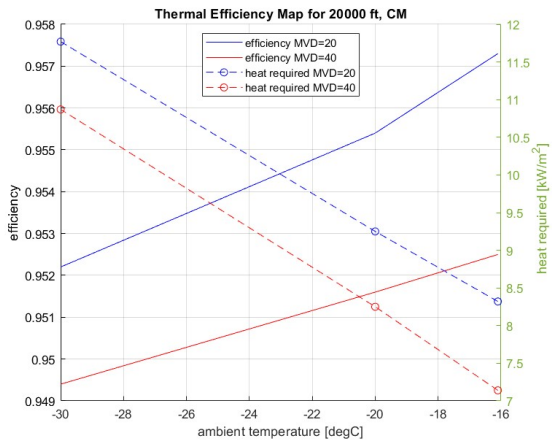

(a) MVD variation on efficiency at 20000 ft in CM

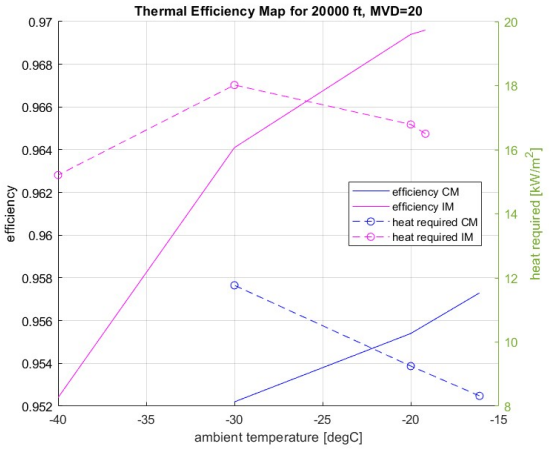

(b) CM/IM variation on efficiency at 20000 ft for MVD = 20

Figure 4.45: MVD and CM/IM effect on thermal efficiency in electro-thermal IPS.

Another factor affecting the efficiency is MVD in a roundabout way. In figure 4.45 (a), it can be seen that a better efficiency is obtained with MVD = 20 μm than with MVD = 40 μm at the same ambient temperature. This is valid for every altitude and CM or IM conditions. The effect of MVD on efficiency is parallel to having a higher efficiency when more heat is required. When the lowest ambient temperature combines with a lowering heat required as in (b) at the coldest scenario, it gives the lowest efficiency of that altitude envelope in IM conditions. When the heat supplied is calculated for each scenario, the design point still needs the highest heat. Therefore, the efficiency value at the design point is taken as the thermal

efficiency and the temperatures are checked if heat supplied with this added margin is overheating the materials.

$$\eta_{th,@design,point} = 0.96 \tag{4.5}$$

$$Q_{supplied,max} = \frac{Q_{required,max}}{\eta_{th,@design,point}} = 20.303 \, \frac{kW}{m^2} \tag{4.6}$$

For an example of how the other materials are affected by the heat, a simulation output is given in the figure 4.46 when the heater starts to run while the system is at ambient temperature.

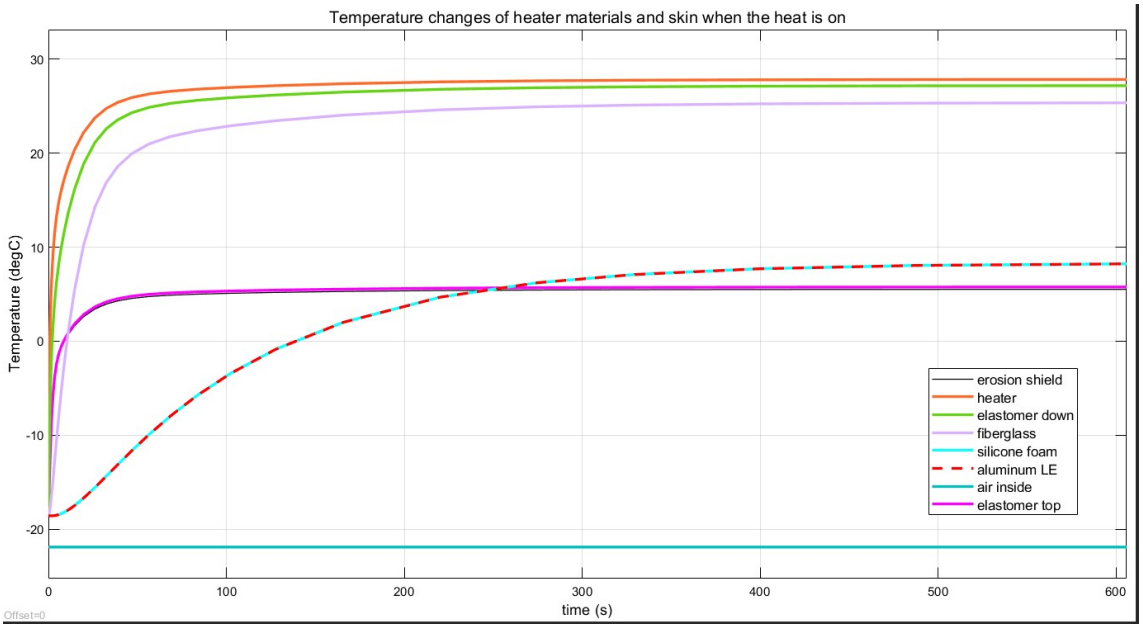

Figure 4.46: Converged temperatures of heater layers at 10000 ft, -21.9°C, in IM, MVD = 20

The legend of the plot is ordered from top to bottom layers. As requested, the skin, shown as an erosion shield in the plot, is heated up to 5 °C. The layer just below the skin, elastomer is evaluated in two half parts as the heater is installed into the elastomer. The elastomer on the top is almost at the same temperature as the skin but a little higher as it is closer to the heater and not exposed to the atmosphere. One layer below is the location of the heater. The heater is heating up the most than the other materials as the heat is distributed from this level to upper and lower levels. The elastomer part below the heater behaves like the heater but is a little cooler. Then, the fiberglass heats up like the other lower layers but less than the one above as it is further to the heater. Then, the silicone foam insulation has the thermal properties where it traps the heat due to a low thermal conductivity. So, it converges more slowly and drags the aluminum leading edge with it since the aluminum has a high thermal conductivity. Finally, the air inside of the lip is assumed to always stay at ambient temperature. This scenario is where the most heat is required and checked if the layers are heating the most. However, there are

no issues as the hottest temperature is less than 30°C.

The coldest scenario in IM at 20000 ft is also checked to see how fast the heat can be transmitted in the worst conditions. It is seen that in 80 seconds, it reaches 4 °C and with a slow increment, it ends up at 5 °C in a total of 5 minutes which becomes significant while implementing the control systems and the required time margin to the system.

Even though the materials are not overheated at a dangerous level, the system should consider a monitor system to assure performance and detect and prevent overheating events.

4.3.6.2 Water-heated IPS

This concept is based on anti-icing the lip by using the heat of hot liquid that is circulating in the cooling system of the engines. The engines are cooled by an air-water heat exchanger placed behind the inlet. The concept is to implement another pipe from the pipe coming from the air-cooled heat exchanger which will pass through the inlet lip. Then, the pipe will be implemented back to the pipe going to the engines. First, in the concept generations, it is suggested to take the incoming pipe before the air-water heat exchanger but it is updated in order not to decrease the efficiency of the heat exchanger by decreasing the water temperature difference. In this final concept, there can be several architectures to place the pipe inside the lip. The advantages and disadvantages of the installation concepts are presented. The factors affecting the performance or design of the system, such as water flow rate and water temperature, are explained. The selected fluid for the cooling system and anti-icing the lip is introduced briefly. This concept is energy-efficient since it does not require electrical power from the batteries but uses waste heat.

4.3.6.2.1 Liquid properties

The liquid that will be used in anti-icing is the one in the cooling system of the electric motor. This model uses a 60:40 glycol-water mixture because of its beneficial thermodynamic properties [70]. When the ethylene glycol is diluted with water, the boiling point heightens while the freezing point drops which is desirable for the systems including hot and cold conditions in a short time. An improved thermal performance also has a significant effect on having this fluid. While glycol has a lower heat capacity and higher viscosity, the solution with water has a stronger heat transfer capacity. Viscosity decreases by including water and increases the efficiency of the cooling system. This saves the system from implementing a pump to compensate for the required flow rate. Mixing water with ethylene glycol helps to reduce the overall corrosion rate of metals by providing a less reactive environment.

The 50:50 ratio is also a good balance and moderately improves thermal performance. The 60:40 ratio gives high performance for heavy-duty applications. To ensure the system operates well under extreme conditions, the 60:40 ratio glycol-water

mixture is used in the model. The specific heat values according to the temperature and pressure inputs of the flight scenarios are implemented from the Thermal Liquid Properties block of Simscape [69] as shown in the figure 4.47.

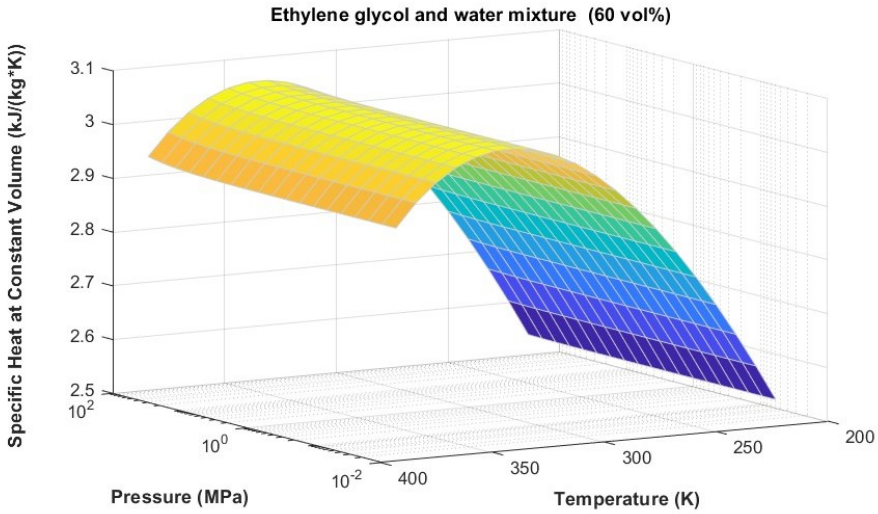

Figure 4.47: Ethylene glycol-water mixture (60:40) properties [69].

4.3.6.2.2 Pipe configurations

Circular pipe

This pipe configuration is reminiscent of piccolo tubes inside the airfoils. It is rather easier to manufacture and connect it with the upcoming pipes from the cooling system loop. The pipe is installed such that it touches the skin covering the nose diameter as seen in figure 4.48.

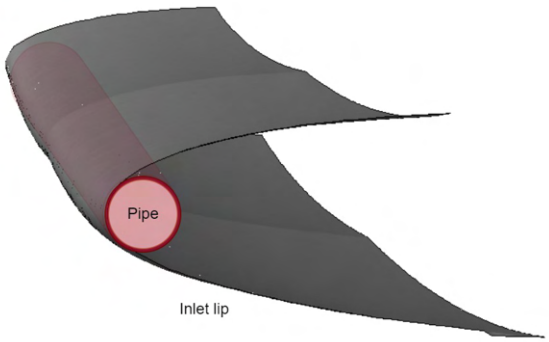

Figure 4.48: Circular pipe implementation on inlet lip.

One drawback of this concept is that the heat is applied to a specific region of the lip including the stagnation line which is favorable considering the amount of ice accretion. However, the aft of the lip stays unprotected and there is runback ice risk

due to having a circular pipe in the elliptical lip. A larger pipe can be installed in the middle of the lip without touching the stagnation line; however, it would also create a risk of ice accretion on the stagnation line and a smaller heated region. To place the pipe covering the largest region, the diameter of the pipe is selected as the possible maximum value.

Pipe properties are mostly the same for both pipe configurations. The material is aluminum due to its resistance to high temperatures, low cost, and easiness of manufacture.

Table 4.10: Circular pipe properties.

Thickness	1 mm
Diameter	6 mm
Cross-sectional area	19.635 mm^2
Thermal conductivity	200 W/mK
Density	2700 kg/m^3
Specific heat	900 J/kgK

To build a detailed system architecture such as the minimum water flow required or water temperature, the critical icing condition is identified. The expected critical condition is where the power requirement is maximum in the coldest icing conditions at 10,000 ft and the results confirm. The effect of different water flow rates and temperatures on lip temperature is being studied. Applicable intervals for these two variables are used in the iteration of this study. A feasible design point can be chosen according to the resulting lip temperature with the water mass flow and temperature values. In terms of icing limits, this target lip temperature is 5 degC. Values providing a higher lip temperature will confirm successful anti-icing protection.

The water temperature is highly dependent on the heat capacity of the air-water heat exchanger and the water flow of the cooling loop. With the value of heat dissipated in the cruise condition, a temperature of 70°C cools the motor and inverters. In the following water flow investigation in the pipe is done with this water temperature.

Figure 4.49 shows the variation of water mass flow. The lip and pipe temperatures with varying water flow can be seen through the left axis. Another important parameter, the temperature drop in the pipe due to the heat lost because of anti-icing, can be also seen through the right axis. It is significant to choose a design point where the temperature drop is low. Otherwise, a relatively colder water merging with the cooling system can disrupt the heat transfer properties of the flow. The main requirement is to have a water flow that heats the lip above 5°C, which represents a minimum of 0.74 L/min as seen from the figure. At this water flow, a temperature drop of 2°C occurs.

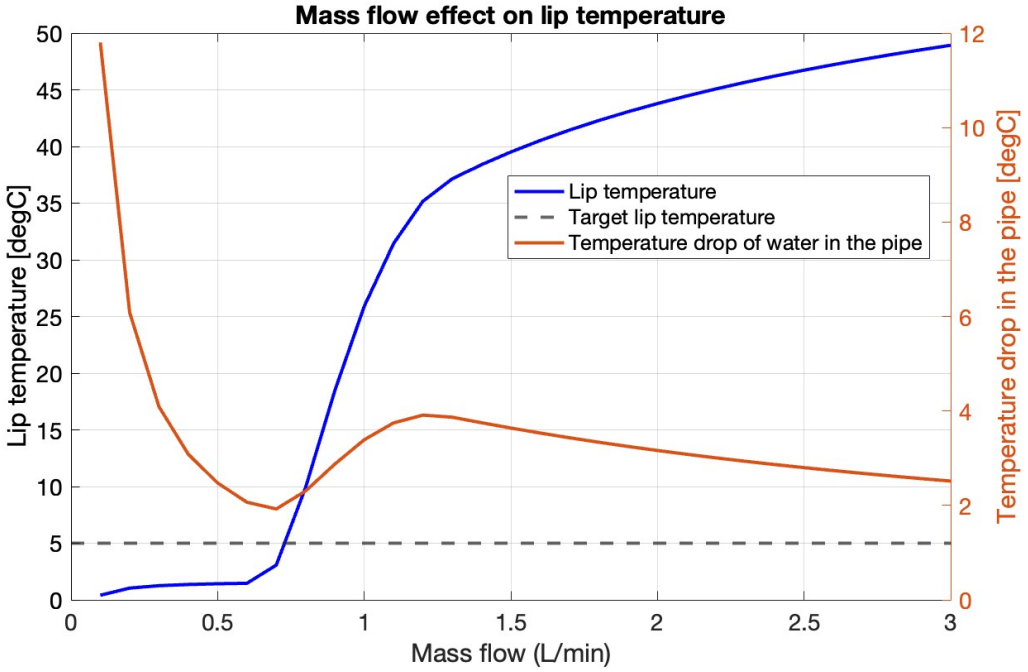

Figure 4.49: Water mass flow effect on lip temperature and temperature drop in the pipe for the circular pipe.

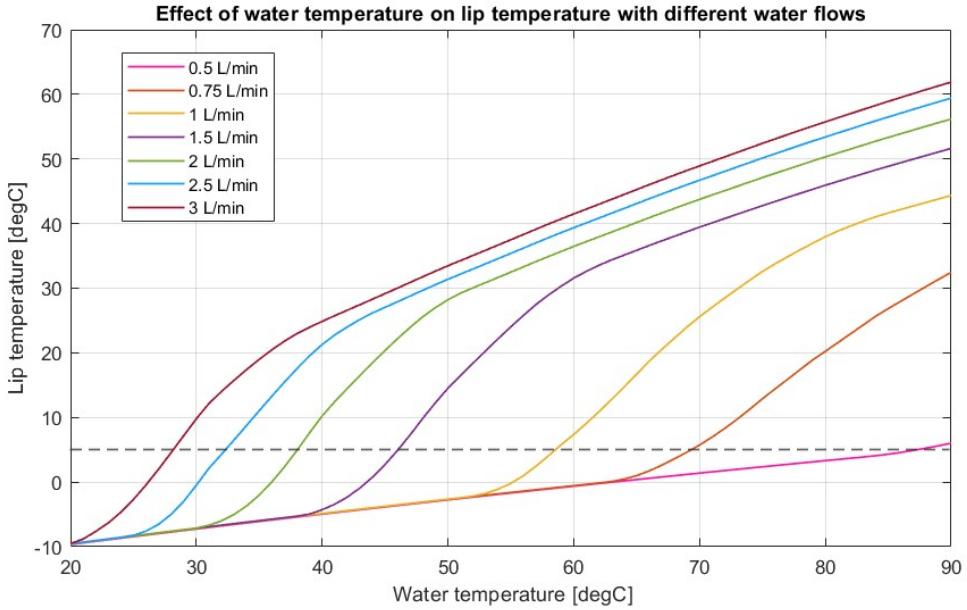

Figure 4.50: Effect of water temperature on lip temperature with different water flows for the circular pipe.

Since the power of electric motors can change during the whole flight envelope, the temperature of the water heated by the motor is going to change at the different phases of the mission. That is why, a variety of temperatures are given as input for different mass flow values in figure 4.50. As it can be seen even a 30°C of water can

be enough to heat the water above 5°C when the mass flow is around 2.5 L/min. Since the cooling loop's water flow is much higher than this value, it can be clearly said that there is more than sufficient waste heat that can be used in anti-icing.

One important detail to note is that the circular pipe does not cover the whole lip and it will not be able to succeed in protecting the region properly. If the lip is designed with a rounded lip design, this pipe can be more applicable and efficient in heat transfer. In the current case, another configuration suggested is a C pipe.

C pipe

This pipe configuration is implemented under the inlet lip like a coat without any air gap between, as illustrated in figure 4.51. Its thickness is very small so that all the water flowing in transfers the heat immediately and does not require a lot of water mass flow.

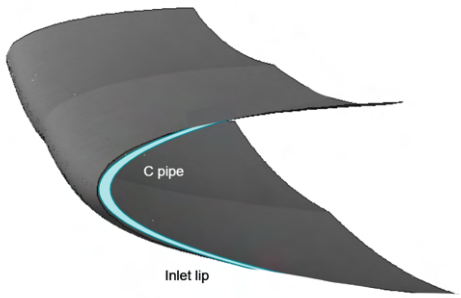

Figure 4.51: C pipe implementation on inlet lip.

The outer diameter of this pipe is the inner diameter of the skin where they are installed one under the other. In this configuration, the cross-sectional area becomes 5 times larger than the circular pipe. However, the icing condition the pipe will experience is the whole lip region which is 10 times larger. Most of the properties are the same as the circular pipe due to the same material as given in table 4.11.

Table 4.11: C pipe properties.

Thickness	1 mm
Inner width	1 mm
Cross-sectional (chordwise) length	103 mm
Cross-sectional area	103 mm^2
Thermal conductivity	200 W/mK
Density	2700 kg/m^3
Specific heat	900 J/kgK

As the circular pipe, a 70° water temperature is given to the pipe, and lip temperature is observed. It can be seen that while 0.74 L/min is required for the circular

pipe, less than 0.25 L/min is enough when the pipe is having a lip shape. Temperature drop, on the other side, is much higher than the one in a circular pipe. That is why, even though the water flow is enough, the design point would be a higher mass flow than the one providing 5°C lip temperature, as shown in the figure 4.53.

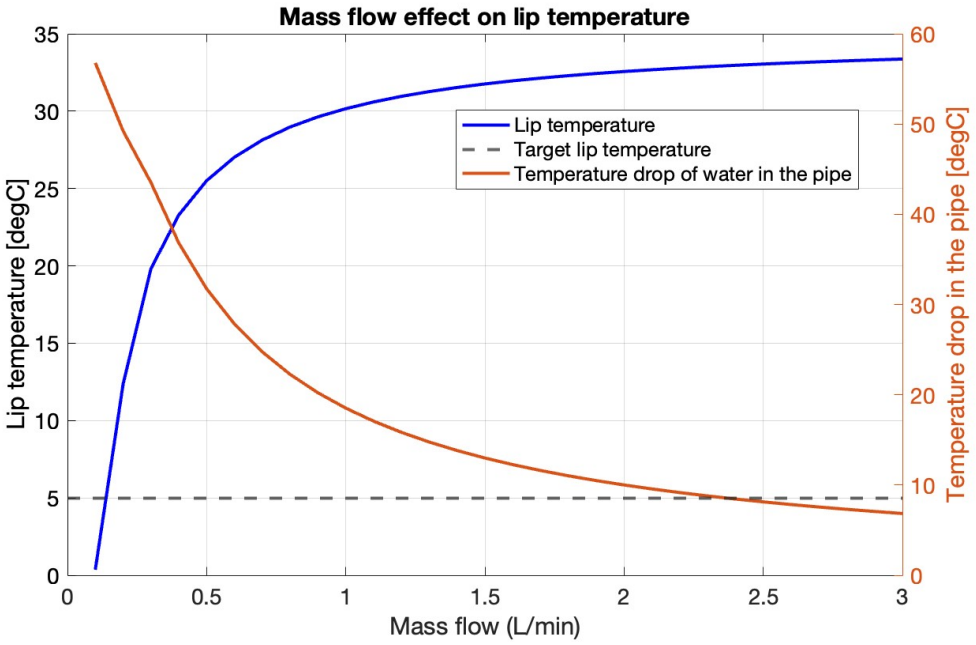

Figure 4.52: Water mass flow effect on lip temperature and temperature drop in the pipe for the C pipe.

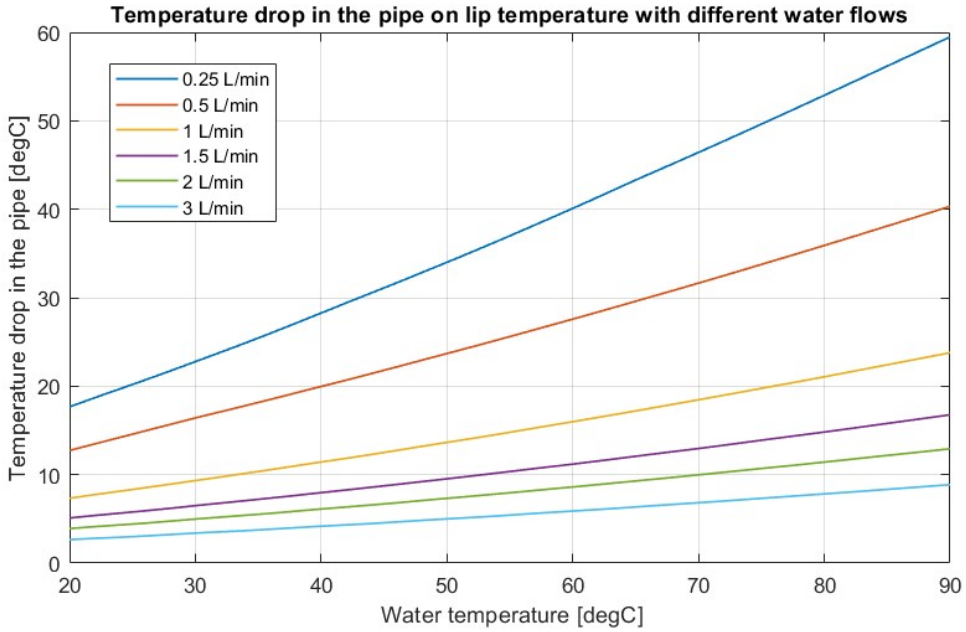

Figure 4.53: Temperature drop in the pipe on lip temperature with different water flows for the C pipe.

For various water temperatures and mass flows, the system is simulated and the same conclusion can be made. The anti-icing with the pipe from the waste heat coming from the electric motor cooling system is possible in terms of heat capacity. As an advantage, this configuration would protect the whole region of the inlet lip.

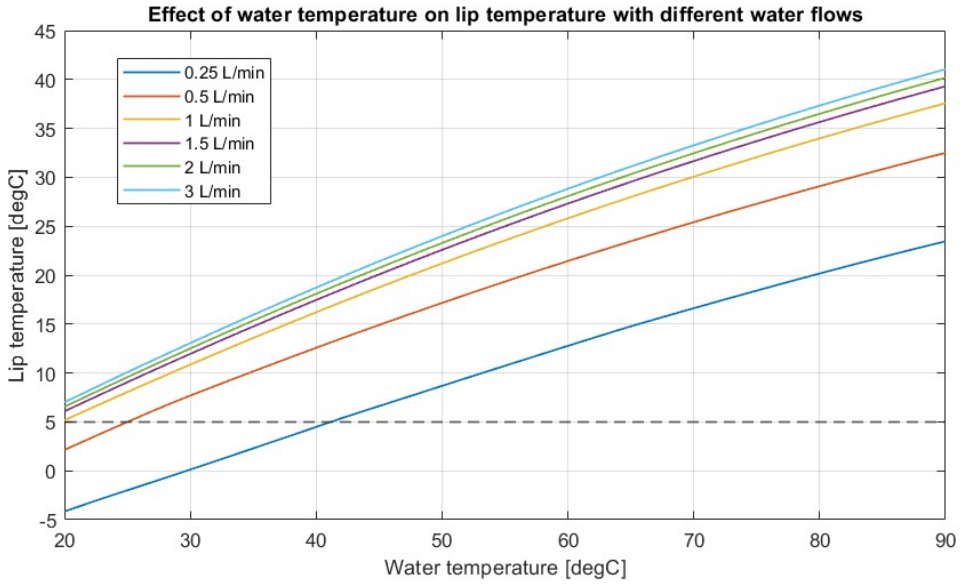

Figure 4.54: Effect of water temperature on lip temperature with different water flows for the C pipe.

The challenge of this type of IPS is the manufacturing and implementation of the inlet lip. The circular pipe is easier as the configuration is being used. In addition, the interface is easier where the circular pipe is merged with the supporting pipes which carry the water from the main cooling loop to the inlet lip. On the other side, C pipe requires a unique design for each type of inlet lip design. 3D printing can provide accurate work with laser drilling techniques for the inner side of the pipe. Unlike the circular pipe, a specific interface should be added to carry the water with typical circular pipes throughout the nacelle till the inlet lip to provide precise work only for the lip.

4.3.7 IPS Selection

To select the final proposed IPS, additional considerations are made such as the power consumption of peripherals included in the system architecture of the water-heated IPS, and the weight effects of the systems.

Figure 4.55 shows the schematic view of the main components employed in the waste heat architecture highlighting the components that are already part of the required cooling system and the newly added ones. Where the green line represents the standard cooling loop to dissipate the rejected heat by the electric propulsion unit, whereas the blue line represents the required added loop to implement this solution.

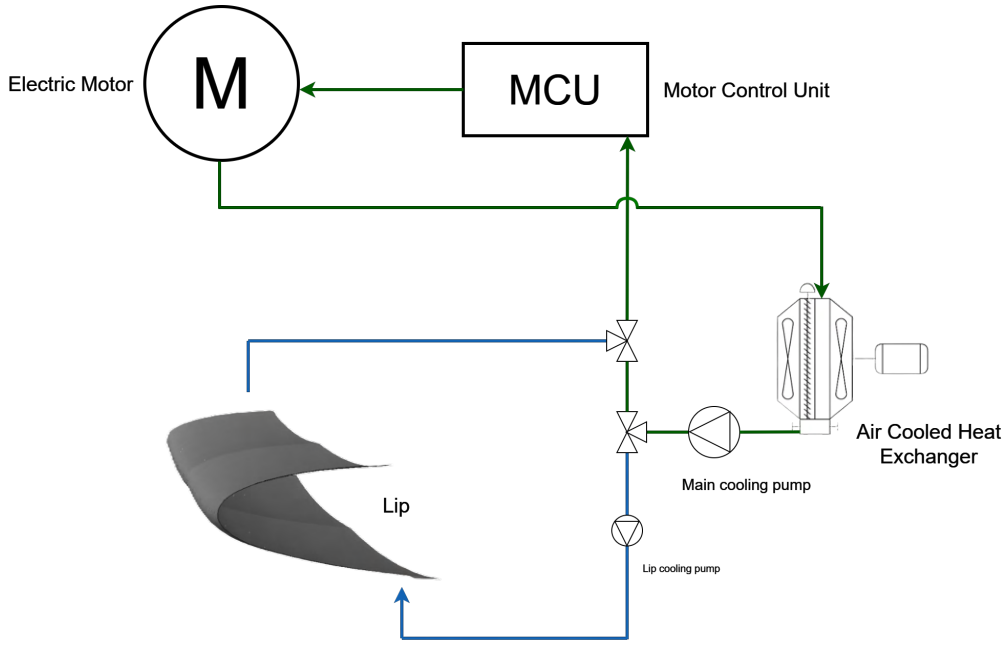

Figure 4.55: System components of water-heated IPS.

It is estimated that this extra pipe would have approximately 1.6 m and would have an internal diameter of 5 mm to allow the interface of the tube and the lip to be mounted as close as possible to the lip's leading edge. With this and by fixing the mass flow an estimation for the required lip cooling pump power can be done using Bernoulli's energy conservation equation 4.7 and Moody's diagram given in figure 4.56.

$$P_1 + \frac{1}{2}\rho v_1^2 + \rho g h_1 = P_2 + \frac{1}{2}\rho v_2^2 + \rho g h_2 \tag{4.7}$$

By fixing a mass flow of 1 L/min, the velocity can be easily calculated, which then allows one to compute the Reynolds, and finally, with the surface roughness for plastic perspex of $\epsilon = 0.0025$ fixes the relative pipe roughness.

$$V = \frac{\dot{m}}{rho \cdot A} = 0.868\ m/s \tag{4.8}$$

$$A = \pi \cdot r^2 = 1.963e-5\ m^2 \tag{4.9}$$

$$Re = \frac{V \cdot D}{\nu} \approx 3500 \tag{4.10}$$

$$\frac{\epsilon}{d} = \frac{0.0025}{5} = 5e-4 \tag{4.11}$$

$$\Delta P = f \cdot \frac{L}{D} \cdot \frac{V^2}{2 * g} \approx 0.5107 \tag{4.12}$$

Giving a friction factor of approximately $f \approx 0.0475$, leading to the calculation of the pressure drop due to friction inside the pipe in equation 4.12.

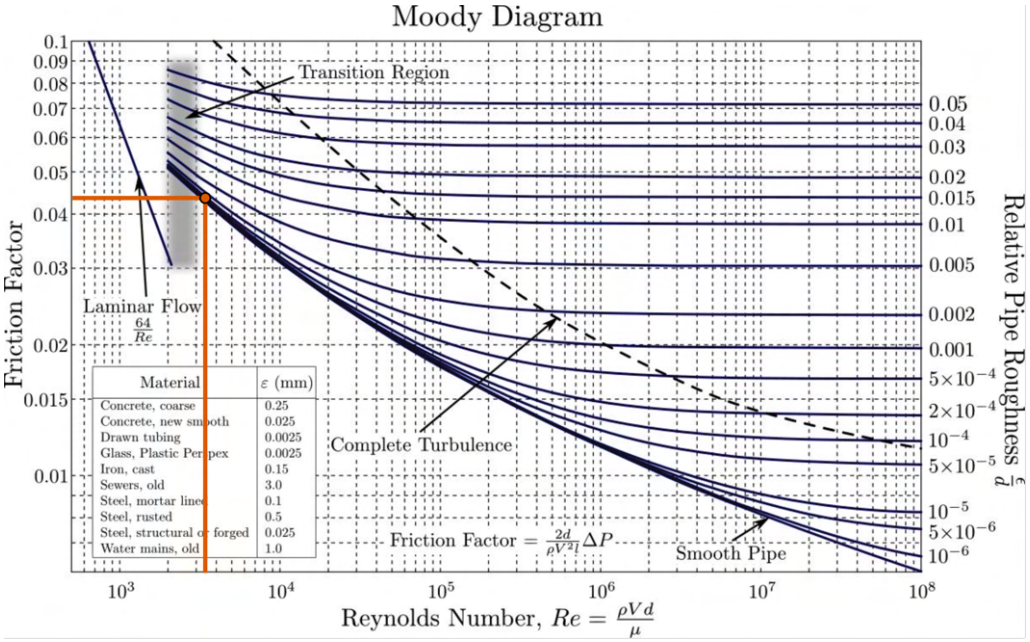

Figure 4.56: Moody's diagram.

The loop should be composed of 4 connecting valves, 2 elbow-like on the lip, and 2 T-like on the 3-way valves represented in figure 4.55. The head loss of these components is then,

$$h_{elbow} = k \cdot \frac{V^2}{2g} = 1.5 \cdot \frac{0.868^2}{9.81} \approx 0.1152 \tag{4.13}$$

$$h_T = k \cdot \frac{V^2}{2g} = 2 \cdot \frac{0.868^2}{9.81} \approx 0.1536 \tag{4.14}$$

$$h_{total} = h_{elbow} + h_T = 0.7795 \tag{4.15}$$

The pump power is then calculated using equation 4.16, which, as it can be seen, is considering a pump efficiency of unity. However, at the same time, the power consumption is negligible, even considering an efficiency of 50% for example. For this reason, we do not consider the power consumption increase in the table 4.12. Nonetheless, it is an important step to check since, in the end, different architectures or mass flows might lead to values that might need to be taken into account.

$$P = V \cdot A \cdot \rho \cdot g \cdot H \approx 0.129\ W \tag{4.16}$$

Another important outcome of this is that a well-designed system might be able to run only with the main cooling pump by equalizing the resistance of the lip loop and the main loop, avoiding cooling fluid stagnation on the lip loop.

In terms of weight added to the system is calculated as an approximate location of the cooling systems and the connections. For water-heated IPS, only the pipe inside the lips weighs 4.7 grams, and 112.9 grams for circular and C pipe respectively. As the circular pipe covers only the nose of the lip while the C pipe covers all the cross-sectional length, it is an expected difference. The additional pipe connecting these

to the main cooling loop is going to be around 1 meter for an outward and return path. This is calculated as a circular pipe with the same dimension as the circular lip pipe, which weighs 32.7 grams. For the C pipe, there will be an interface addition connecting these two different configurations. This interface length is calculated as 3.39 g by estimation from Udeotok [75] around 3% of the pipeline length.

For the weight of the electro-thermal IPS, in addition to the heater mat structure, a temperature sensor with 20 g is added.

Table 4.12: Comparison of IPS architectures.

Criteria	**Circular pipe water-heated IPS**	**Rating**	**C pipe water-heated IPS**	**Rating**	**Electro-thermal IPS**	**Rating**	**Weight**
Power	0.129 W	5	0.129 W	5	415 W	4	20%
Weight	**94.4 g total** 32.7 g connecting pipe including interface 4.7 g lip pipe 46 g pump 14 g extra liquid	5	**164.98 g total** 32.7 g connecting pipe 112.9 g lip pipe 3.39 g interface 46 g pump 16 g extra liquid	4	**152 g total** 132 g mat structure 20 g sensor	4	20%
Performance	Only anti-icing around the stagnation line	2	Evaporative anti-icing potential	5	Running-wet anti-icing power	4	20%
System complexity	Welded interface and pipe manufacturing, heat exchanger adaptation	4	3D laser-cut unique and lip-shaped interface and pipe manufacturing, heat exchanger adaptation	3	Typical and simple heater coatings	5	15%
Cost of operation	Pressure drop, flow distortion in cooling loop, less place in the nacelle	3	Pressure drop, flow distortion in cooling loop, less place in the nacelle	3	Range drop due to power usage	4	10%
Risk	Leakage in the interfaces, flow staying stationary on the lip region	3	Leakage in the interfaces, flow staying stationary on the lip region	3	Runback ice	4	15%
Weighted score	**3.4**		**4**		**4.2**		**100**%

where 1 represents "unacceptable," 2 for "potential blocker, 3 for "acceptable, 4 for "good," and 5 for excellent in the assessment scale.

5
Conclusion

The study revealed the need for ice protection technologies in hybrid-electric aircraft, particularly caused by the electric propulsion systems. The investigation focused on designing and evaluating a submerged cooling air intake model, highlighting the necessity of IPS, due to the novel placement under an angled nacelle.

In-flight icing simulations by CFD, droplet impingement, and thermal analysis validated the heat balance model on the inlet lip. To avoid the icing, both feasible existing concepts and new concepts are generated and compared. It is indicated that the heat dissipated from the electric motor/inverters is sufficient enough to prevent icing with an additional loop to the cooling system. Despite the added system complexity, this IPS concept introduces a significant potential to electric aircraft. The findings and comparison propose the electro-thermal IPS as the most viable solution from the existing methods, balancing power consumption, weight, performance, system complexity, cost of operation, and risk. This study contributes to the goal of having a sustainable aviation industry by ensuring that electric aircraft can operate safely and efficiently, devoid of icing hazards.

5.1 Research Output

The work yields the following results:

- The necessity of actively protecting lip surface area to avoid ice accretion for a submerged inlet under an angled nacelle is verified.
- The development and validation of a methodology that accurately calculates the required power a surface requires to avoid ice accretion for different types of conditions
- The waste heat of the electric motors is found to be sufficient to prevent ice formation on the lip surface.
- The waste heat anti-icing system has the potential to be competitive with electro-thermal solutions since it does not utilize any power from the system.
- The water-heated IPS can provide more heat to the systems with larger pipes if needed.
- For flight phases with higher angles of attack or a more angled nacelle design, ice accretion may occur farther aft the inlet's lip, even if in lower thicknesses compared to the actual lip. To address that, ice-phobic coatings can be considered to maintain power consumption and keep the surface clean from ice.

5.2 Future Development

The topic of the work is extensive and multidisciplinary, which then creates space for other fields to be explored to improve and use the results obtained here. Some of the intended future developments would be:

- Implementing the heaters in a way covering impingement limits, where it can cover more outside, and less inside regions.
- Considering the shadow zone by installing the heater structures where the ice is not accumulating on the edges of the lip near the rectangular walls to optimize the power consumption.
- Improving the system implementation of both IPS concepts by considering all sorts of missions that the electric aircraft will experience such as reserve missions in case the power supplied changes throughout the different mission modes.
- For the larger inlet lips, evaluating a power-varying heater mat structure chord-wise to optimize the power supply since this research focuses on the anti-icing computations on the stagnation line for a small inlet lip due to simplicity and less value of the return.
- Evaluating the water-heated IPS solutions in a way that increases the effective area of the pipe to the leading edge, optimizing the surface temperature with the water mass flow rates, and considering the effect on the heat exchanger on the inlet.
- Optimizing the inlet and lip geometry for better aerodynamic performance and less exposure to ice accretion.
- Analysing a rounded lip design to implement the circular pipe more suitably.

Bibliography

[1] K.R. Petty and C.D.J. Floyd. A Statistical Review of Aviation Airframe Icing Accidents in the U.S. *11th Conference on Aviation, Range, and Aerospace Meteorology*, 54(March 1997), 2004.

[2] "Aircraft Technology Roadmap to 2050: IATA," Docslib. [Online]. Available: https://docslib.org/doc/1789734/aircraft-technology-roadmap-to-2050-iata.

[3] H. Ritchie, "What share of global CO2 emissions come from aviation?" Our World in Data, Apr. 2024, Available: https://ourworldindata.org/global-aviation-emissions.

[4] EASA, "European Aviation Environmental Report," 2022. Available: https://www.easa.europa.eu/eco/sites/default/files/2023-02/230217_EASA%20EAER%202022.pdf.

[5] A4E, ACI-E, ASD, CANSO, and ERA, "Destination 2050 Report," 2021. Available: https://www.destination2050.eu/wp-content/uploads/2021/03/Destination2050_Report.pdf.

[6] Roland Berger GmbH, "Aircraft Electrical Propulsion – The Next Chapter of Aviation?," Think:Act, Sep. 2017, Available: https://tinyurl.com/3kkh243h.

[7] D. Perry, "Heart reveals ES-30 redesign as it switches to off-the-shelf hybrid powertrain," Flight Global, May 15, 2024. https://www.flightglobal.com/air-transport/heart-reveals-es-30-redesign-as-it-switches-to-off-the-shelf-hyb\rid-powertrain/158291.article.

[8] W. M. Leary, "We Freeze to Please": A History of NASA's Icing Research Tunnel and the Quest for Flight Safety. National Aeronautics and Space Administration, 2002.

[9] T. P. Ratvasky, J. F. Van, and J. J. Riley, "NASA/FAA Tailplane Icing Program overview," Jan. 1999, doi: https://doi.org/10.2514/6.1999-370.

[10] M. Papadakis, Hsiung Wei Yeong, M. Vargas, and M. Potapczuk, "Aerodynamic Performance of a Swept Wing with Ice Accretions," 41st Aerospace Sciences Meeting and Exhibit, Jan. 2003, doi: https://doi.org/10.2514/6.2003-731.

[11] T. P. Ratvasky and R. J. Ranaudo, "Icing effects on aircraft stability and control determined from flight data - Preliminary results," Jan. 1993, doi: https://doi.org/10.2514/6.1993-398.

[12] "Icing Research Tunnel." https://www.nasa.gov/directorates/armd/aetc/icing-research-tunnel/.

[13] "Deicing and Anti-Icing Equipment," www.aopa.org, Jul. 30, 2020. https://www.aopa.org/training-and-safety/online-learning/safety-spotlights/weather-wise-precipitation-and-icing/deicing-and-anti-icing-equipment.

[14] European Aviation Safety Agency (EASA). Certification Specifications and Acceptable Means of Compliance for Large Aeroplanes, CS-25, Amendment 28; Cologne, Germany, 2021.

[15] ESDU, 1986, Drag and pressure recovery characteristics of auxiliary air inlets at subsonic speeds, Item No. 86002 with amendments A to D, July 1996, Engineering Sciences Data Unit, London.

[16] R. Stull, "UBC ATSC 113 - Stratiform Clouds," www.eoas.ubc.ca, 2020. https://www.eoas.ubc.ca/courses/atsc113/flying/met_concepts/01-met_concepts/01a-clouds/stratiform.html

[17] R. Stull, "UBC ATSC 113 - Cumuliform Clouds," www.eoas.ubc.ca, 2020. https://www.eoas.ubc.ca/courses/atsc113/flying/met_concepts/01-met_concepts/01a-clouds/cumuliform.html

[18] R. K. Jeck, "A new data base of supercooled cloud variables for altitudes up to 10,000 feet AGL and the implications for low altitude aircraft icing," Federal Aviation Administration Technical Center, 1983.

[19] P. T. Hacker and R. G. Dorsch, "A Summary of Meteorological Conditions Associated with Aircraft Icing and a Proposed Method of Selecting Design Criterions for Ice Protection Equipment," vol. NACA-TN-2569, 1951, Available: https://ntrs.nasa.gov/citations/19810068848.

[20] Heinrich, A., Ross, R., Zumwalt, G., Provorse, J., Padmanabhan, V., Thompson, J., and Riley, J., "Aircraft Icing Handbook - Volume 1 of 3," DOT/FAA/CT-88/8- I, Department of Transporation, Federal Aviation Administration Technical Center, 1991.

[21] Schlichting, H. Grenzschicht-Theorie, 5th edn, Braun, Karlsruhe, 1965

[22] Y. Cao, G. Zhong, and C. Ma, "Numerical simulation of ice accretion prediction on multiple element airfoil," Science China Technological Sciences, vol. 54, pp. 2296–2304, Sep. 2011, doi: https://doi.org/10.1007/s11431-011-4434-9.

[23] I. Langmuir and K. Blodgett, A mathematical investigation of water droplet trajectories. Army Air Forces Headquarters, Air Technical Service Command, 1946.

[24] "Airworthiness Standards: Transport Category Airplanes," U.S. Department of Transportation, Federal Aviation Administration, Federal Aviation Regulations, FAR Part 25, Washington, D.C., 1985.

[25] C. B. Neel, Jr., N. R. Bergrun, D. Jukoff, and B. A. Schlaff, "Calculation of Heat Required for Wing Thermal Ice Prevention in Specified Icing Conditions," Dec. 1947, doi: https://doi.org/10.4271/480204.

[26] D.T. Bowden, A.G. Gensemer, C.A. Sheen, Engineering summary of airframe icing technical data, FAA Technical Report ADS-4, 1963.

[27] R. J. Ranaudo, "Discoveries on Ice," Flight Safety Foundation, Feb. 21, 2017. https://flightsafety.org/asw-article/discoveries-on-ice/.

[28] W. Baars, R. Stearman, and C. Tinney, "Wind tunnel studies employing higher order statistics to detect icing induced upsets," 2009.

[29] K. Wang, Y. Xue, H. Tian, M. Wang, and X. Wang, "The Impact of Icing on the Airfoil on the Lift-Drag Characteristics and Maneuverability Characteristics," Mathematical Problems in Engineering, vol. 2021, pp. 1–16, Jun. 2021, doi: https://doi.org/10.1155/2021/5568740.

[30] M. B. Bragg, "A similarity analysis of the droplet trajectory equation," AIAA Journal, vol. 20, no. 12, pp. 1681–1686, Dec. 1982, doi: https://doi.org/10.2514/3.8004.

[31] Society of Automotive Engineers, "SAE Aerospace Applied Thermodynamics Manual, ice, rain, fog, and Frost Protection," (AIR 1168/4C), 2021. doi:10.4271/air1168/4c.

[32] M. Ali, A. Mohiudeen, and K. Kara, Determination of Water Droplet Collection Efficiency: An Empirical Model. 2017. doi: https://doi.org/10.2514/6.20171869.

[33] T. G. Myers, "Extension to the Messinger model for aircraft icing," AIAA Journal, vol. 39, pp. 211–218, Jan. 2001, doi: https://doi.org/10.2514/2.1312.

[34] L. Makkonen, Estimating intensity of atmospheric ice accretion on stationary structures, vol. 20, Journal of Applied Meteorology, 1981, pp. 595–600.

[35] O. Meier and D. Scholz, "A Handbook Method for the Estimation of Power Requirements for Electrical De-Icing Systems," Deutscher Luft-und Raumfahrtkongress, 2010.

[36] S. Bansmer, Aircraft Icing. A Challenging Problem of Fluid Mechanics, 1st ed. Göttingen, Germany: Cuvillier Verlag, 2020, p. 23.

[37] F. P. Incropera, D. P. DeWitt, T. L. Bergman, and A. S. Lavine, Fundamentals of Heat and Mass Transfer, 6th ed. John Wiley & Sons, Inc., 2007.

[38] S. W. Churchill and M. Bernstein, "A Correlating Equation for Forced Convection From Gases and Liquids to a Circular Cylinder in Crossflow," Journal of Heat Transfer, vol. 99, no. 2, pp. 300–306, May 1977, doi: https://doi.org/10.1115/1.3450685.

[39] "Aircraft Ice Protection", Advisory Circular 20-73 (1971), Federal Aviation Administration, Washington, D.C. 20591.

[40] FAA, Aviation Maintenance Technician Handbook– Airframe, FAA-H-8083-31A., vol. 2. FAA, 2012, p. Chapter 15: Ice and Rain Protection. Available: https://www.faa.gov/sites/faa.gov/files/2022-06/amt_airframe_hb_vol_2.pdf

[41] A. Shinkafi and C. Lawson, "Enhanced Method of Conceptual Sizing of Aircraft Electro-Thermal De-icing System," Zenodo (CERN European Organization for Nuclear Research), vol. 8, no. 6, May 2014, doi: https://doi.org/10.5281/zenodo.1092896.

[42] K. Al-Khalil et al., "Validation of NASA thermal ice protection computer codes. III - the validation of Antice," 35th Aerospace Sciences Meeting and Exhibit, Jan. 1997. doi:10.2514/6.1997-51.

[43] The Engineering ToolBox (2009). Air - Thermal Conductivity vs. Temperature and Pressure. [online] Available at: https://www.engineeringtoolbox.com/air-properties-viscosity-conductivity-heat-capacity-d_1509.html.

[44] B. Arizmendi Gutiérrez, A. Della Noce, M. Gallia, and A. Guardone, “Optimization of a Thermal Ice Protection System by means of a genetic algorithm.,” *In: International Conference on Bioinspired Methods and Their Applications. Cham: Springer International Publishing*, pp. 189–200, 2020.

[45] B. Whitfield, “How It Works: TKS Ice Protection System,” Flying, Oct. 25, 2016. https://www.flyingmag.com/how-it-works-tks-ice-protection-system/.

[46] D. R. Cordray, L. R. Kaplan, P. M. Woyciesjes, and T. F. Kozak, “Solid-liquid phase diagram for ethylene glycol + water,” Fluid Phase Equilibria, vol. 117, Art. no. 1, 1996, doi: https://doi.org/10.1016/0378-3812(95)02947-8.

[47] X. Jiang and Y. Wang, “Studies on the Electro-Impulse De-Icing System of Aircraft,” Aerospace, vol. 6, no. 6, p. 67, Jun. 2019, doi: https://doi.org/10.3390/aerospace6060067.

[48] Z. Goraj and Warsaw University of Technology, “An Overview of the Deicing and Anti-icing Technologies with Prospects for the Future,” presented at the 24th International Congress of the Aeronautical Sciences, 2004.

[49] Heinrich, A., Ross, R., Zumwalt, G., Provorse, J., Padmanabhan, V., Thompson, J., and Riley, J., “Aircraft Icing Handbook - Volume 2 of 3,” DOT/FAA/CT-88/8- I, Department of Transporation, Federal Aviation Administration Technical Center, 1991.

[50] A. D. Shah, “Integrated Engine Inlet Thermal Anti-Icing and Environmental Control System (TAI/ECS),” SAE Transactions, Vol. 85, Section 3: 760430–760707 (1976), pp. 1738-1743, Feb. 1976, doi: https://doi.org/10.4271/760517.

[51] K. Al-Khalil, T. Ferguson, and D. Phillips, “A hybrid anti-icing ice protection system,” 35th Aerospace Sciences Meeting and Exhibit, Jan. 1997, doi: https://doi.org/10.2514/6.1997-302.

[52] Ansys Inc., "ANSYS FENSAP-ICE User Manual", Release 18.1, 2017

[53] William Wright, "User’s Manual for LEWICE Version 3.2", QSS Group, Inc., Cleveland, Ohio, 2008

[54] Y. Cao, W. Tan, and Z. Wu, “Aircraft icing: An ongoing threat to aviation safety,” Aerospace Science and Technology, vol. 75, pp. 353–385, Apr. 2018. doi:10.1016/j.ast.2017.12.028

[55] E. P. Lozowski and M. M. Oleskiw, “Computer modeling of time-dependent rime icing in the atmosphere,” Jan. 1983.

[56] K. M. Al-Khalil, T. G. Keith, K. J. DeWitt, J. K. Nathman, and D. A. Dietrich, “Thermal analysis of engine inlet anti-icing systems,” Journal of Propulsion and Power, vol. 6, no. 5, pp. 628–634, Sep. 1990, doi: https://doi.org/10.2514/3.23264.

[57] L. Bennani. Two Dimensional modelling of electrothermal ice protection systems. Modeling and Simulation. INSTITUT SUPERIEUR DE L’AERONAUTIQUE ET DE L’ESPACE (ISAE), 2014. English.

[58] K. Shimoi and CAV Systems, “Development and Application of a Fluid-Based Nacelle Ice Protection System,” presented at the International Conference on Icing of Aircraft, Engines, and Structures.

[59] K. T. Ulrich and S. D. Eppinger, Product Design and Development. McGraw-Hill/Irwin, 2000.

[60] Design Council, “Eleven lessons: managing design in eleven global brands - A Study of the Design Process. ,” 2005, Available: https://www.designcouncil.org.uk/our-resources/framework-for-innovation/.

[61] Heart Aerospace, “ES-30 | Heart Aerospace.” https://heartaerospace.com/es-30/.

[62] J. S. Dennard, “The Total-Pressure Recovery and Drag Characteristics of Several Auxiliary Inlets at Transonic Speeds,” no. NASA-MEMO-12-21-58L, Mar. 1959.

[63] H. Mason, “Boeing 737 AEW&C Wedgetail Walk Around Page 2,” www.primeportal.net.https://www.primeportal.net/hangar/howard_mason5/boeing_737_aewc_wedgetail/index.php?Page=2 (accessed May 13, 2024).

[64] “Passenger-Ready 787 Dreamliner Is Ready to Board,” forum.lowyat.net, 2011. https://forum.lowyat.net/topic/1993678/all(accessed May 13, 2024).

[65] "NACA Submerged Duct Construction," Bill Whitehouse Glastar builder https://cozyserenity.weebly.com/uploads/2/1/8/0/21804934/__naca_duct_design.pdf(accessed May 13, 2024)

[66] "ANSYS FLUENT 12.0 User’s Guide," https://www.afs.enea.it/project/neptunius/docs/fluent/html/ug/main_pre.htm(accessed May 15, 2024)

[67] H. Vömel, “Water Vapor Pressure Formulations,” www.eas.ualberta.ca. https://www.eas.ualberta.ca/jdwilson/EAS372_15/Vomel_CIRES_satvpformulae.html.

[68] AOPA Air Safety Foundation, “Aircraft Icing,” Safety Advisor, vol. Weather No. 1, no. SA11-04/08, 2008, Available: https://www.aopa.org/-/media/Files/AOPA/Home/Pilot-Resources/ASI/Safety-Advisors/sa11.pdf.

[69] “Preset fluid properties for the simulation of a thermal liquid network - MATLAB - MathWorks Nordic,” se.mathworks.com. https://se.mathworks.com/help/hydro/ref/thermalliquidpropertiestl.html#d126e292494.

[70] D. Sawicka, Cieśliński, Janusz T, and S. Smolen, “A comparison of empirical correlations of viscosity and thermal conductivity of water-ethylene glycol-al2o3 nanofluids,” Nanomaterials, vol. 10, Art. no. 8, 2020, doi: https://doi.org/10.3390/nano10081487.

[71] 1995-2024 Auld Srinivas, Aerodynamics for students "Blade Element Theory for Propellers", https://www.aerodynamics4students.com/propulsion/blade-element-propeller-theory.php.

[72] Markus Rütten, Holger Wendland, "Performance Enhancement of Auxiliary Air Intakes Using Vortex Generators," 50th AIAA Aerospace Sciences Meeting including the New Horizons Forum and Aerospace Exposition, January 2012 https://www.researchgate.net/publication/269057085_Performance_Enhancement_of_Auxiliary_Air_Intakes_Using_Vortex_Generators.

[73] Nicolas J. Pignier, Ciarán J. O’Reilly, Susann Boij, "Aerodynamic and aeroacoustic analyses of a submerged air inlet in a low-Mach-number flow," April 2016 https://www.sciencedirect.com/science/article/pii/S004579301630113X.

[74] Charles L. Ladson "Effects of independent variation of Mach and Reynolds numbers on the low-speed aerodynamic characteristics of the NACA 0012 airfoil section, " October 1, 1988 https://ntrs.nasa.gov/citations/19880019495

[75] Native Dynamics, “Calculating Interface Volumes for Multi-product Pipelines | Neutrium,” neutrium.net, 2013. https://neutrium.net/fluid-flow/calculating-interface-volumes-for-multi-product-pipelines/.

A

Droplet impingement physics

A.1 Droplet trajectory equation

As supercooled droplets have considerably small diameters, typically less than 60 μm, eventually, the Reynolds number they experience is small to assume that droplets are considered spherical. In this case, the trajectory equation by Newton's Second Law for the droplet is given in the equation A.1.

$$m\frac{d^2\vec{x}}{dt^2} = \vec{P} + \vec{M}_a + m\vec{g} + \vec{B} + \vec{D} \tag{A.1}$$

where $\vec{x}$ is the position vector of the droplet, t is time, $\vec{P}$ is the pressure gradient, $\vec{M}_a$ is the apparent mass, m is the mass of the droplet, $\vec{g}$ is the gravitational constant, $\vec{B}$ is the Bassett (unsteady) history force, and $\vec{D}$ is the drag force [20].

The $\vec{P}$ and $\vec{M}_a$ are neglected as the density of the droplet is significantly higher than that of the air. The $m\vec{g}$ is also neglected due to the comparatively small mass of the droplet. The Bassett force is essentially a correction term to the drag for an accelerating sphere. It can be negligible in case the density of the droplet is the same as the fluid it is in or the droplet has enormous accelerations. The initial condition is not valid here. For the latter case, there has been much research about if supercooled droplets are involved in this condition. It is said that for most of the cases, neglecting this term is not going to affect the accuracy of the computations [55]. Therefore, this term is going to be omitted for the following equations.

The drag term is defined as

$$\vec{D} = \frac{1}{2}\rho C_D S \left|\vec{u} - \frac{d\vec{x}}{dt}\right| \left(\vec{u} - \frac{d\vec{x}}{dt}\right) \tag{A.2}$$

where $\vec{u}$ is the local flowfield velocity vector, S is the cross-sectional area and C_D is the drag coefficient. With the omitted terms and the substitution of the equation A.2, the equation A.1 becomes

$$\frac{d^2\vec{x}}{dt^2} = \frac{3}{4}\frac{\rho_a C_D}{\delta\rho_w} \left|\vec{u} - \frac{d\vec{x}}{dt}\right| \left(\vec{u} - \frac{d\vec{x}}{dt}\right) \tag{A.3}$$

where the δ is the droplet diameter, ρ_{w} is the air density, and ρ_{a} is the droplet density. A standard drag curve for a sphere with many research results is given in the figure A.1.

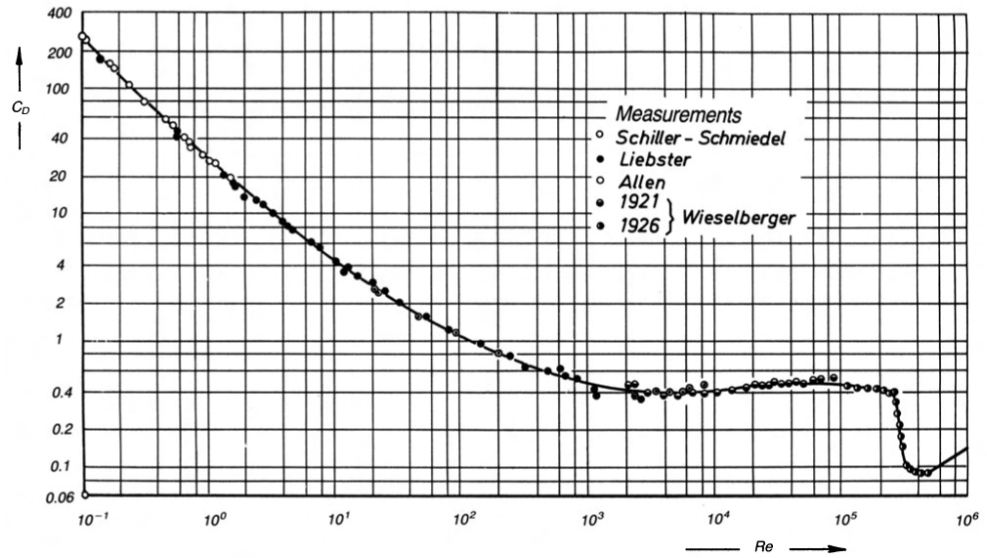

Figure A.1: Drag coefficient vs Reynolds number for a sphere [21].

A.2 Modified droplet inertia parameter

Equation A.3 is nondimensionalized. Accepting the x and y are the components of the vector $\vec{x}$, nondimensional variables are expressed as $x^* = x/c, y^* = y/c, t^* = t/\left(c/V_\infty\right)$, where c is the characteristic length, and V_∞ is the freestream airspeed. In this way, an inertia parameter, K, and a modified inertia parameter, K_0 are introduced as seen in the equation A.4.

$$\frac{d^2\vec{x}}{dt^2} = \frac{1}{K}\frac{C_D R_l}{24}\left(\vec{u} - \frac{d\vec{x}}{dt}\right) \tag{A.4}$$

With all the nondimensional components, the local relative Reynolds number of the droplet can be stated as

$$\mathrm{Re}_l = \frac{\rho_\mathrm{a}\delta\left|\vec{u} - \frac{\mathrm{d}\vec{x}}{\mathrm{dt}}\right|}{\mu_\mathrm{a}} \tag{A.5}$$

where the μ_a is the dynamic viscosity of the air.

K can be taken from the equation A.4 and A.5.

$$K = \frac{1}{18}\frac{\delta^2 V_\infty \rho_w}{c\mu_\mathrm{a}} \tag{A.6}$$

From the equation A.4, it is seen that the variables K and $C_D R_l/24$ shapes the trajectory. It turns out that, $C_D R_l/24$ depends upon the free stream Reynold number of the droplet, which is

$$\mathrm{Re} = \frac{\rho_\mathrm{a}\mathrm{V}_\infty\delta}{\mu_\mathrm{a}} \tag{A.7}$$

As a result, the only variables of the trajectory is Re and K. The effect of these variables are combined in one parameter called the modified inertia parameter, K_0,

by Langmuir and Blodgett [23], which is given as

$$K_0 = K\left(\frac{\lambda}{\lambda_3}\right) \tag{A.8}$$

The parenthesis in the equation A.8 represents the droplet range ratio and is defined as the trajectory distance of the droplet in the still air with an initial Reynolds number divided by the trajectory distance when the drag term obeys the Stokes law. This parameter can be seen from the numerical computations in the figure A.2.

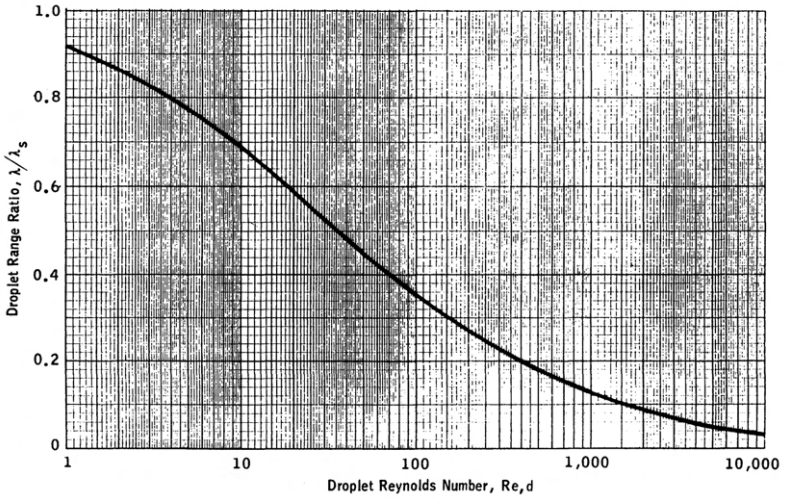

Figure A.2: Droplet range ratio as a function of droplet Reynolds number [26].

With an interpretation of the equation A.4,

$$\left[\frac{K}{C_D\,\mathrm{Re}_l\,/24}\right]\frac{d^2\vec{x}}{dt^2} = \vec{u} - \frac{d\vec{x}}{dt} \tag{A.9}$$

The droplet path can be expressed by only this parameter and it can be assumed as average under typical icing conditions with Bragg's derivation [30].

$$\mathrm{K_0} = 18\ \mathrm{K}\left[\mathrm{Re}^{-2/3} - \frac{\sqrt{6}}{\mathrm{Re}}\,\mathrm{Arctan}\,\frac{\mathrm{Re}^{1/3}}{\sqrt{6}}\right] \tag{A.10}$$

When combined with the equation A.6,

$$\mathrm{K_0} = \frac{\delta^2 V_\infty \rho_w}{c\mu_\mathrm{a}}\left[\mathrm{Re}^{-2/3} - \frac{\sqrt{6}}{\mathrm{Re}}\,\mathrm{Arctan}\,\frac{\mathrm{Re}^{1/3}}{\sqrt{6}}\right] \tag{A.11}$$

From K_0, it can be understood which is the dominating force in the flow path. If K_0 is sufficiently small around 0.005, droplet inertia is too ineffective under the drag forces; therefore, the droplet follows the streamlines around the body. On the other hand, if K_0 is large around 1.0, the droplet inertia is large enough to break off from the flow streamlines when it gets closer to the body. The figure A.3 gives an example how K_0 changes the trajectory of a droplet. As seen, the larger modified

inertia parameter ends up hitting the airfoil by its high droplet inertia while the other drop follows the streamline.

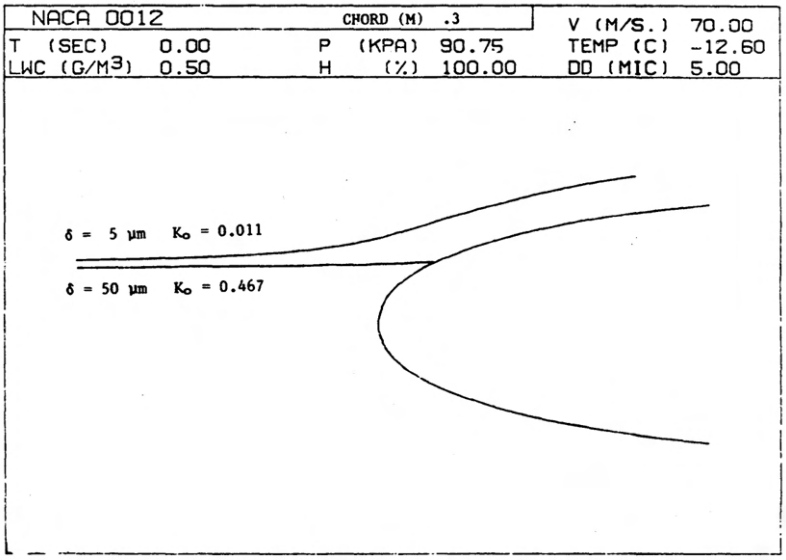

Figure A.3: Comparison of droplet trajectories with respect to modified inertia parameter [20].

In the calculation of K_0 through the equations A.6 and A.10, characteristic length is an important variable. The table A.1 gives conventional values to choose the characteristic length for the several bodies.

Table A.1: Characteristic lengths for several bodies for calculation K_0 [20].

Body	**Characteristic length**
Airfoil	Chord, c
Cylinder	Radius, $D/2$
Ribbons	Half width, $b/2$
Semi-infinite rectangle	Half width
Ellipsoids (10%, 20%) A/B = 10, 5	Body length, L_{el}
Ellipsoids A/B = 2, 3, 5	Half body length, $L_{el}/2$
Cones	Cone length
Elbow	Arbitrary length, L_{eb}, (proportional to elbow size)

Bragg derived another parameter to approximate K_0, $\overline{\mathrm{K}}$, that is expressed in the equation A.12 which has not been that commonly used as K_0. In this equation, significant relations can be observed. $\overline{\mathrm{K}}$, consequently K_0, is proportional to $\delta^{5/3}$, $U^{1/3}$ and 1/c.

$$\overline{\mathrm{K}} = \frac{1}{18}\left(\frac{\rho_{\mathrm{w}}^{3}\delta^{5}\mathrm{U}}{\mathrm{c}^{3}{\mu_{\mathrm{a}}}^{2}\rho_{\mathrm{a}}}\right)^{\frac{1}{3}} \tag{A.12}$$

The figure A.4 shows K_0 values for different MVD for the chords of an airfoil, a full scale horizontal stabilizer and a full scale wing, from top to bottom. This shows that chord size has a strong effect on K_0 as a confirmation to the equation A.12. MVD also contributes considerably but aircraft velocity does not affect the modified inertia parameter significantly.

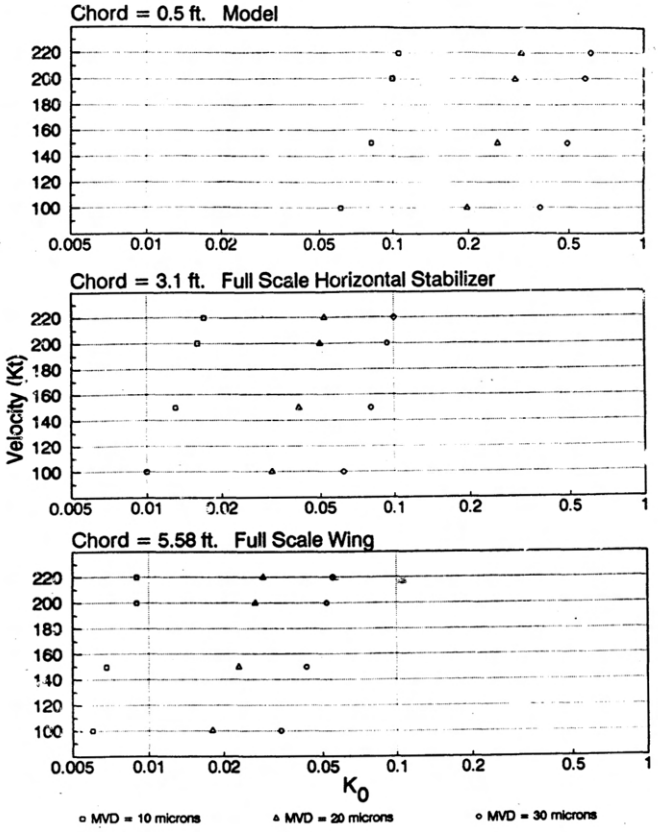

Figure A.4: K_0 based on MVD for several chord sizes [20].

B

Simulation conditions

Table B.1: Coordinates of stations on x and y axes [65].

Station X axis	**Upper surface Y axis**	**Lower surface Y axis**
0.000	0.197	0.197
0.125	0.087	0.325
0.250	0.056	0.375
0.375	0.036	0.412
0.500	0.021	0.440
0.625	0.012	0.462
0.750	0.006	0.481
0.875	0.002	N/A
1.000	0.000	N/A

Table B.2: Experimental icing conditions from [42].

Icing Condition	Total Temperature (°F)	Velocity (mph)	LWC (g/m^3)	MVD (μm)	Angle of Attack (°)
1	20	100	0.78	20	0
2	20	100	1.1	20	0
3	20	200	0.39	20	0
4	0	100	0.78	20	0
5	0	100	1.1	20	0
6	0	200	0.39	20	0
7	20	200	0.55	20	0
8	0	200	0.55	20	0
9	20	100	0.78	20	−2
10	20	100	0.78	20	−4
11	20	100	0.90	40	0
12	−22	200	0.39	20	0
13	15	100	2.0	20	0
14	0	100	0.78	20	−2
15	0	100	0.78	20	−4

Table B.3: Thermal setup for icing condition evaluation [42].

Icing Condition	Run # (TTMS#)	Anti-Icing Mode	Zone A		Zone B		Zone C		Zone D		Zone E		Zone F		Zone G	
			T_s	q	T_s	q	T_s	q	T_s	q	T_s	q	T_s	q	T_s	q
1	22 (70,71)	Evap Wet	117	38	147	40	150	40	160	40	162	39	157	40	156	38
2	48 (75,76)	Evap Wet	116	37	158	39	163	40	169	39	172	39	165	38	164	39
3	53 (80,81)	Evap Wet	92	36	97	38	100	38	103	37	106	36	100	35	101	35
4	35 (63,64)	Evap Wet	112	36	144	38	151	39	154	38	157	38	150	36	149	36
5	58 (114,115)	Evap Wet	112	38	133	41	155	40	163	42	174	40	153	41	159	40
6	63 (116,117)	Evap Wet	92	47	98	48	102	49	102	47	105	47	93	46	89	46
7	65 (101,102)	Evap Wet	102	38	128	39	135	39	145	38	151	38	142	37	136	37
8	67 (104,105)	Evap Wet	91	42	97	43	99	45	100	43	101	42	94	38	95	42
9	69 (92,93)	Evap Wet	117	38	164	40	163	40	170	40	172	40	164	39	169	39
10	71 (95,96)	Evap Wet	117	39	154	41	151	39	154	41	160	40	147	40	135	40
11	73 (98,99)	Evap Wet	116	40	141	41	150	42	157	42	168	40	157	41	154	41
12	75 (124,125)	Evap Wet	91	45	122	47	125	47	132	46	132	45	116	44	102	45
13	87 (110)	Evap Wet	–	37	–	39	-	39	–	39	-	39	–	38	–	38
14	89 (119)	Evap Wet	114	–	175	–	168	–	190	–	192	–	167	–	168	–
15	91 (122,123)	Evap Wet	113	40	160	43	151	42								

IX

Table B.4: Test conditions.

Fensap Code	Flight Phase	Altitude [ft]	KCAS [kts]	KTAS [kts]	TAS [m/s]	Mach	MVD [microns]	IM/CM	Ambient Temperature [Kelvin]
1	Hold	5000	140	148.9	76.59	0.2355	20	CM	270.15
2							40		
3				143.7	73.92	0.2318	20		263.15
4							40		
5				140.86	72.46	0.2318	20		243.15
6							40		
7				148.3	76.29	0.2317	20	IM	269.82
8							40		
9				146.5	75.36	0.2317	20		263.15
10							40		
11				145.9	75.05	0.2317	20		261.16
12							40		
13	Loiter	10000		162.8	83.74	0.2575	20	CM	269.57
14							40		
15				157.9	81.22	0.2547	20		263.15
16							40		
17				154.7	79.58	0.2546	20		243.15
18							40		
19				162.9	83.80	0.2545	20	IM	269.82
20							40		
21				157.9	81.22	0.2547	20		263.15
22							40		
23				157.2	80.86	0.2545	20		251.25
24							40		
25	Cruise	20000		193.8	99.69	0.3102	20	CM	257.05
26							40		
27				192.34	98.94	0.3102	20		253.15
28							40		
29				188.5	96.96	0.3102	20		243.15
30							40		
31				192.64	99.09	0.3102	20	IM	253.98
32							40		
33				192.34	98.94	0.3102	20		253.15
34							40		
35				188.5	96.96	0.3102	20		243.15
36							40		
37				184.58	94.95	0.3102	20		233.15
38							40		

C

3D surfaces

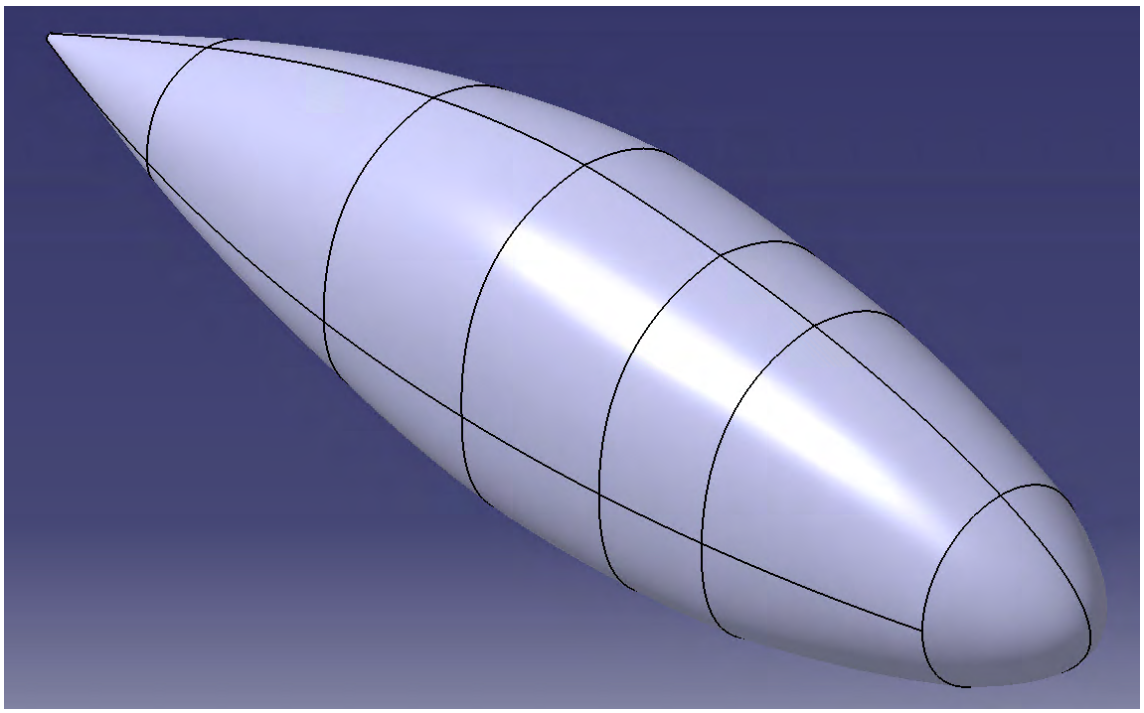

Figure C.1: Final nacelle design.

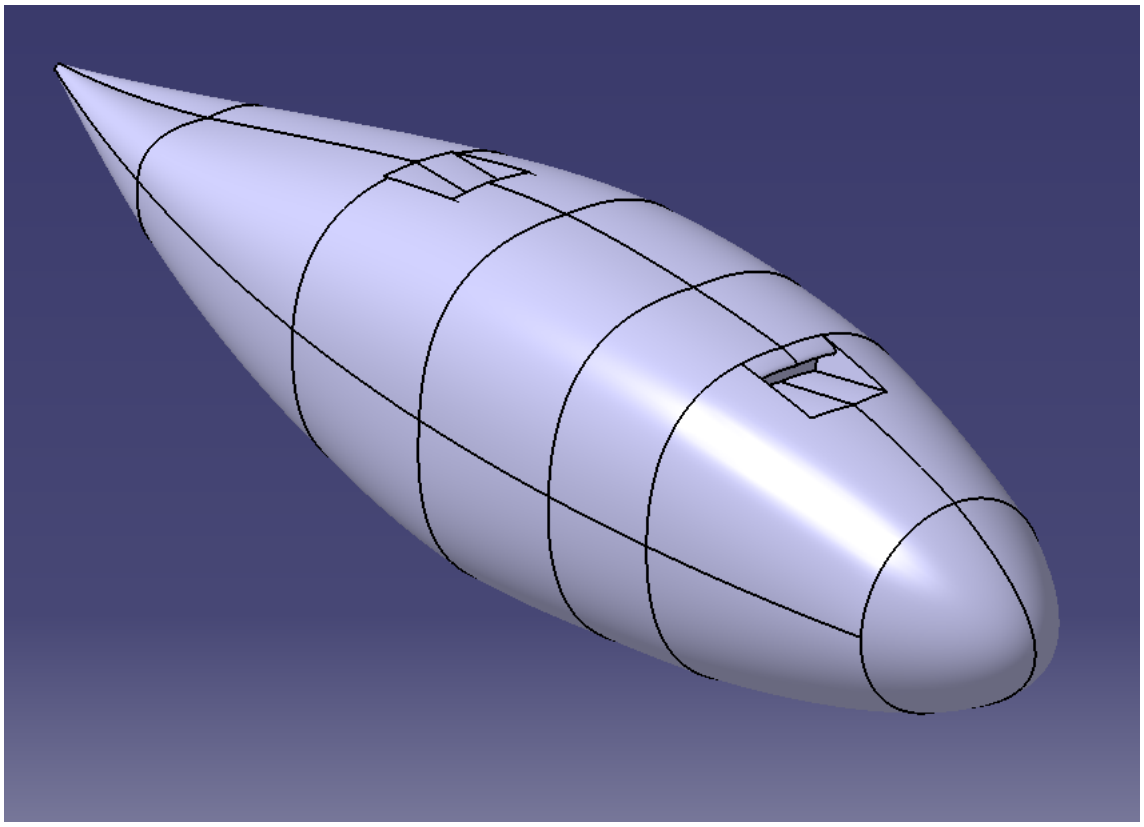

Figure C.2: Inlet view.

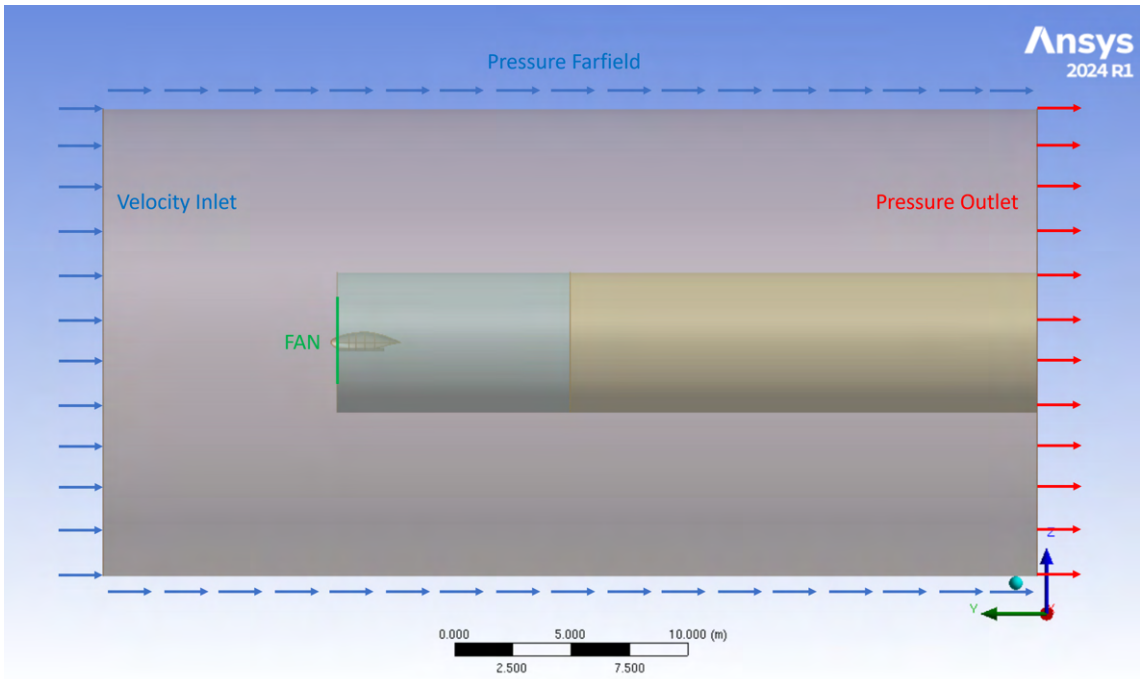

Figure C.3: Domain boundary conditions.

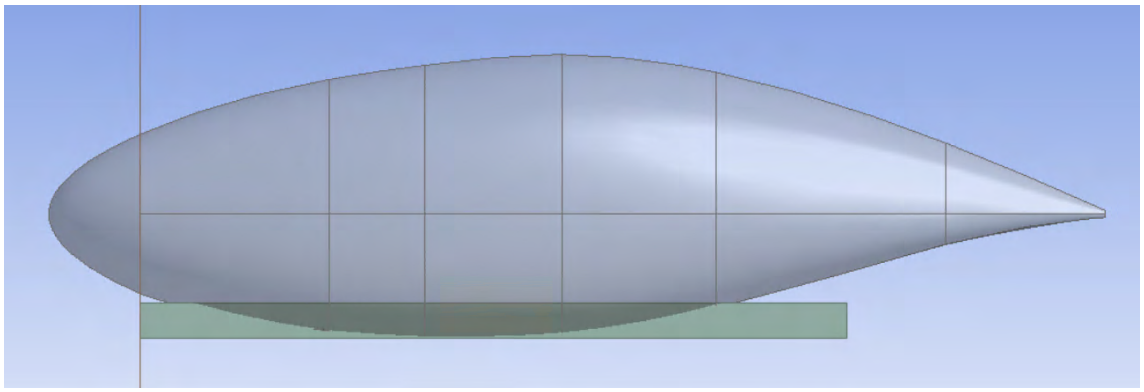

Figure C.4: Nacelle refinement zone near the inlet entry through the duct and exit.

D

Ice accretion results

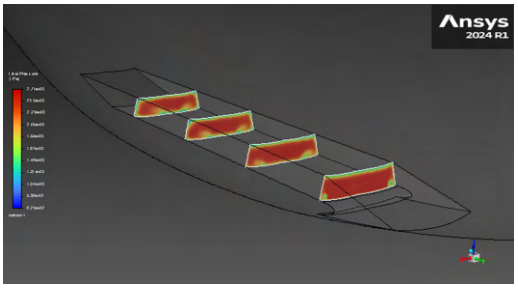

(a) 5 kft, $TAS = 76.59\ m/s$, $T_0 = 273.15\ K$

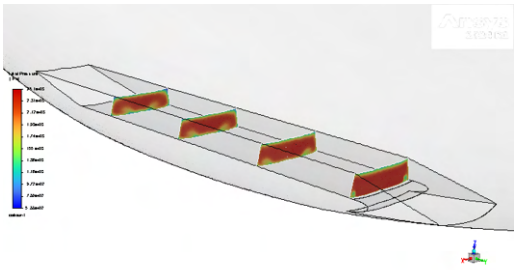

(b) 10 kft, $TAS = 83.74\ m/s$, $T_0 = 273.15\ K$

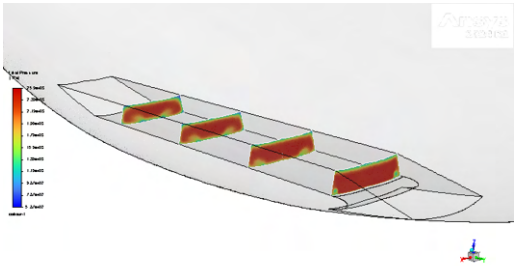

(c) 20 kft, $TAS = 99.69\ m/s$, $T_0 = 262\ K$

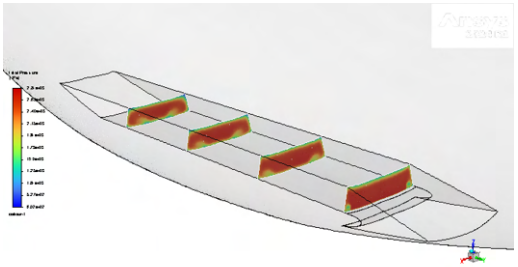

(d) 5 kft, $TAS = 76.59\ m/s$, $T_0 = 273.15\ K$, $AoA = 10\,\text{deg}$

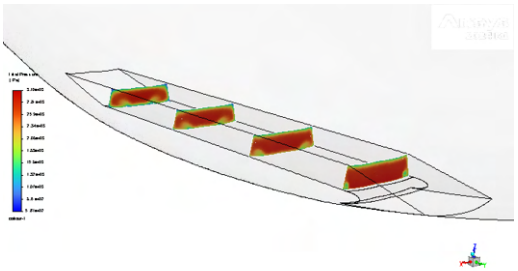

(e) 5 kft, $TAS = 76.59\ m/s$, $T_0 = 273.15\ K$, $AoA = 20\,\text{deg}$

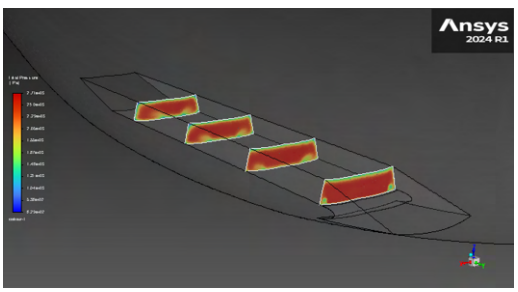

(f) 5 kft, $TAS = 76.59\ m/s$, $T_0 = 273.15\ K$, $AoA = 30\,\text{deg}$

Figure D.1: Total pressure evolution across the duct for different conditions.

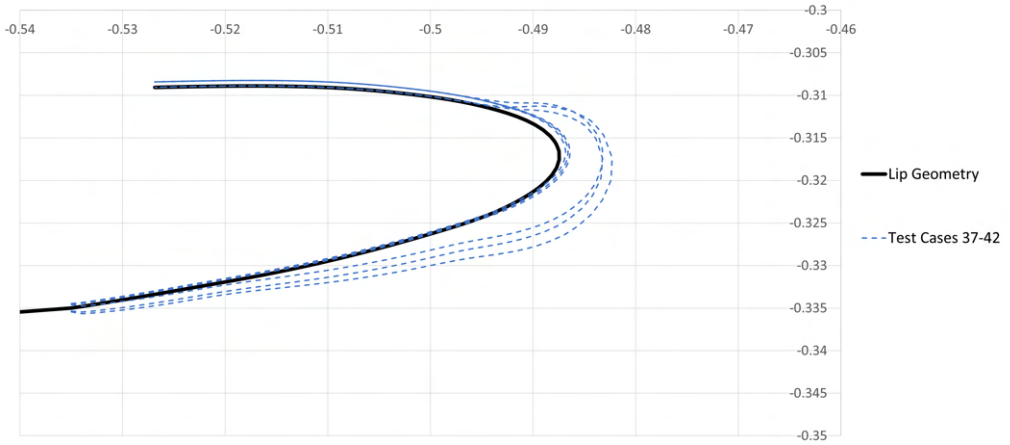

(a) CM conditions at 20000 ft

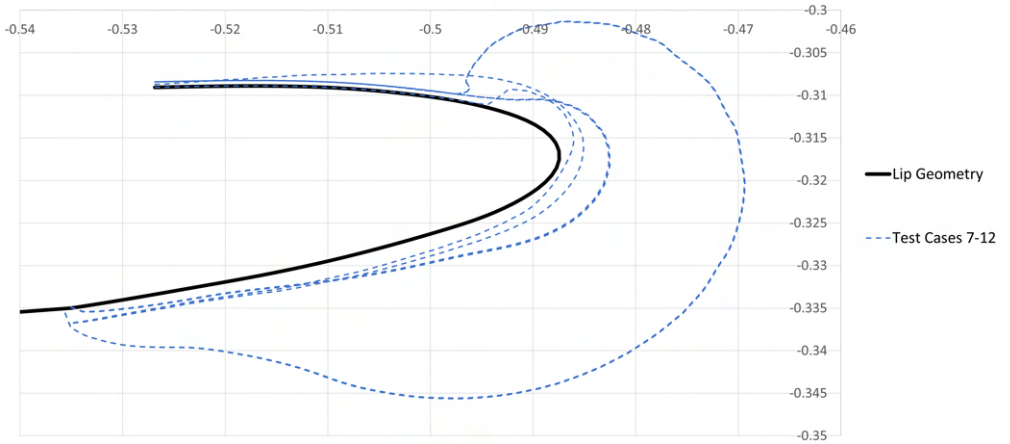

(b) IM conditions at 5000 ft

Figure D.2: Ice shapes at the different conditions and altitudes described in table B.4

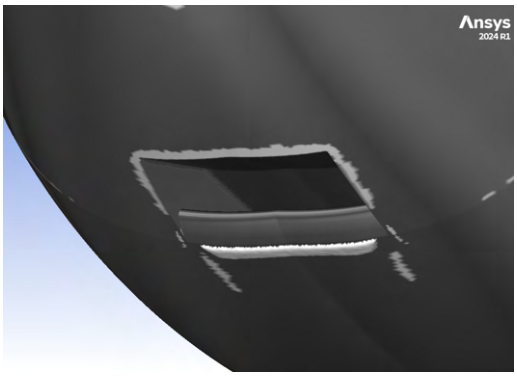

(a) Test point 3.

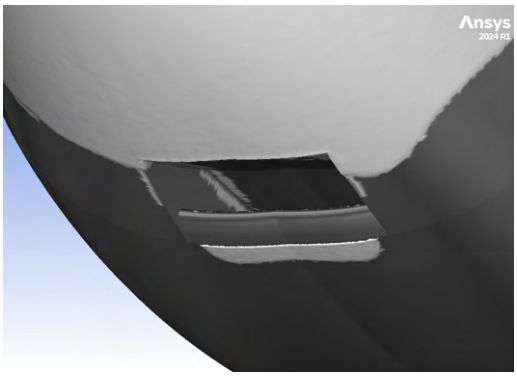

(b) Test point 14.

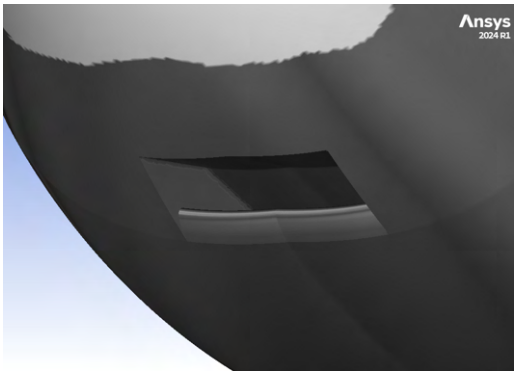

(c) Test point 16.

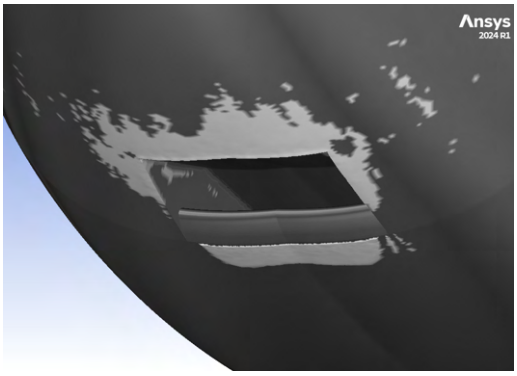

(d) Test point 20.

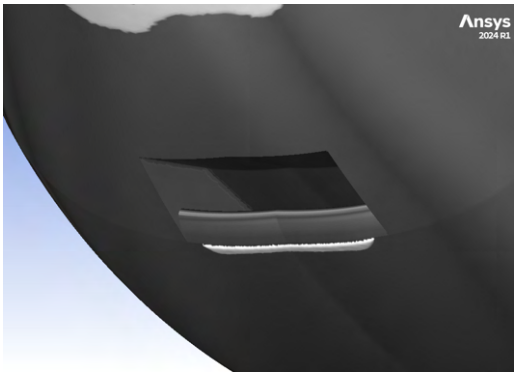

(e) Test point 22.

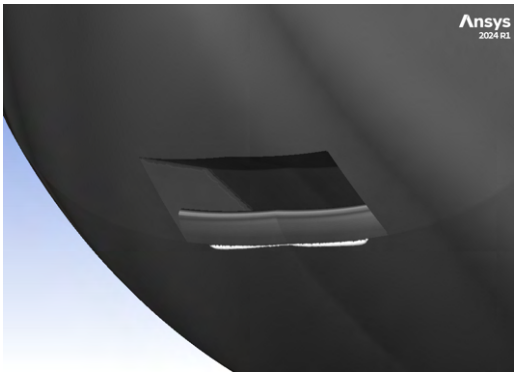

(f) Test point 24.

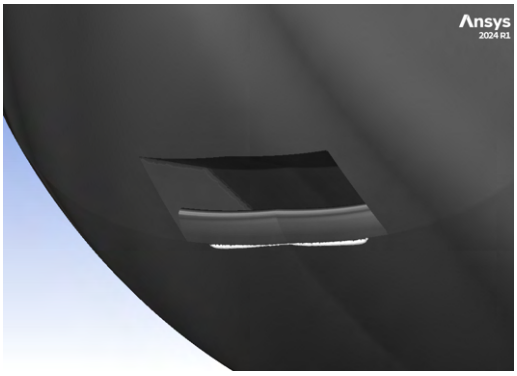

(g) Test point which.

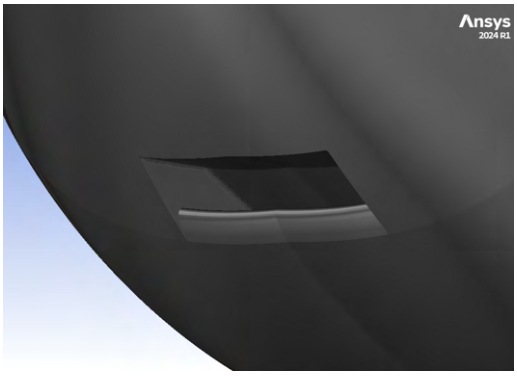

(h) Test point which.

Figure D.3: Heated surface ice accretion in 6 minutes for different test points.

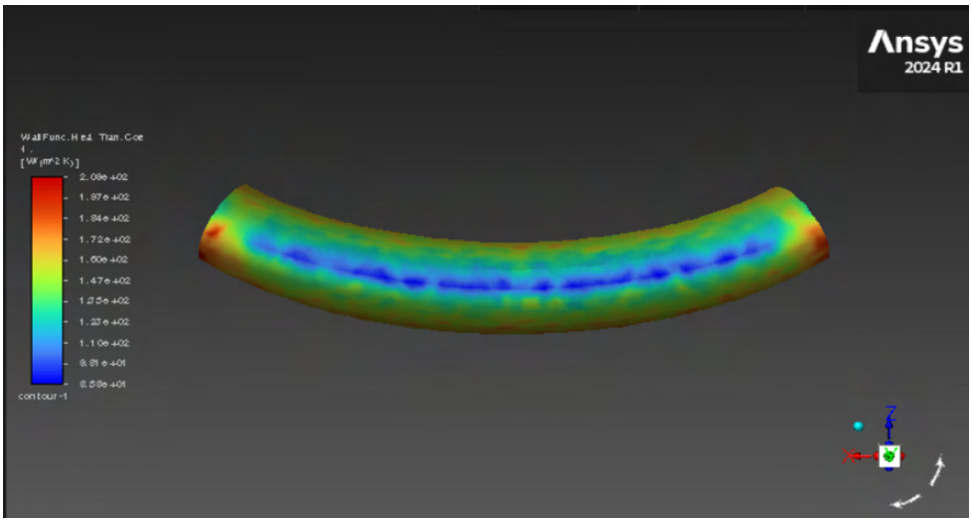

(a) Mesh number 2.

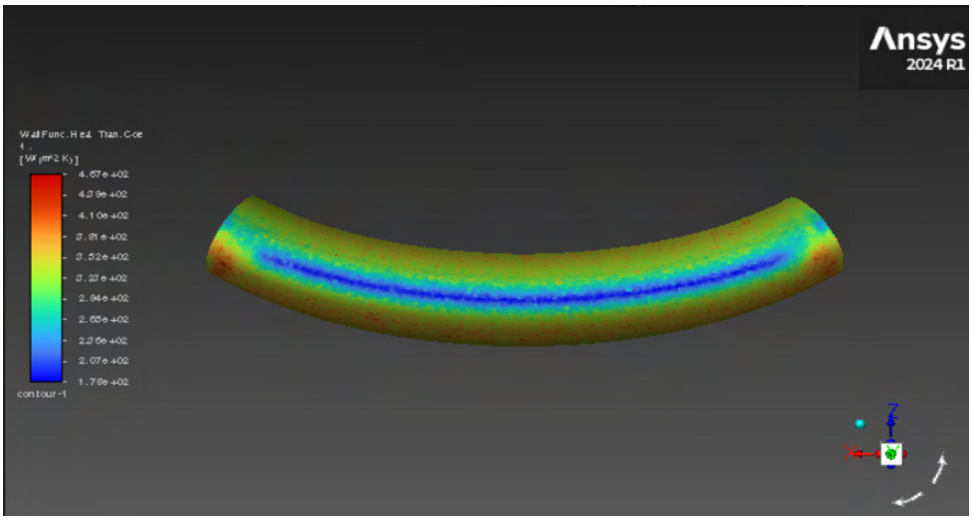

(b) Mesh number 3.

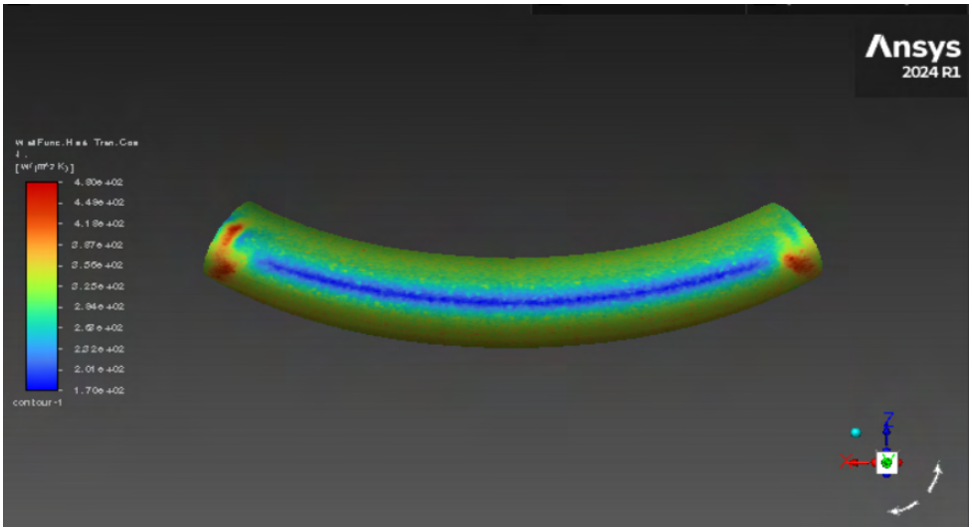

(c) Mesh number 4.

Figure D.4: Heat transfer coefficient contours on lip surface.

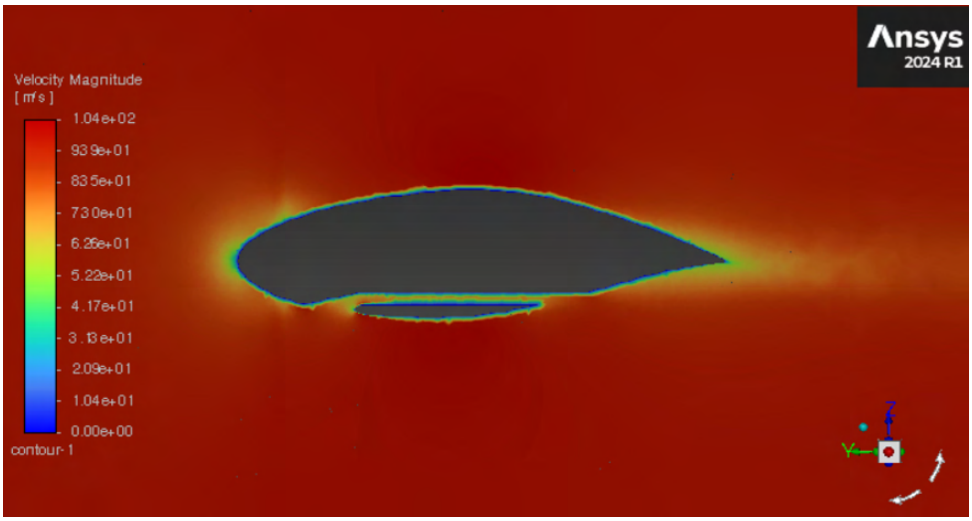

(a) Mesh Number 1

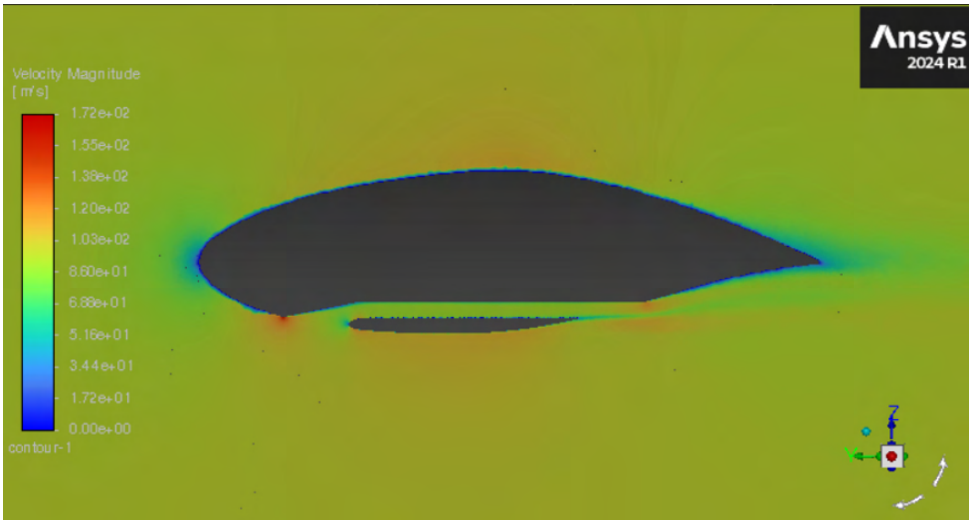

(b) Mesh Number 3

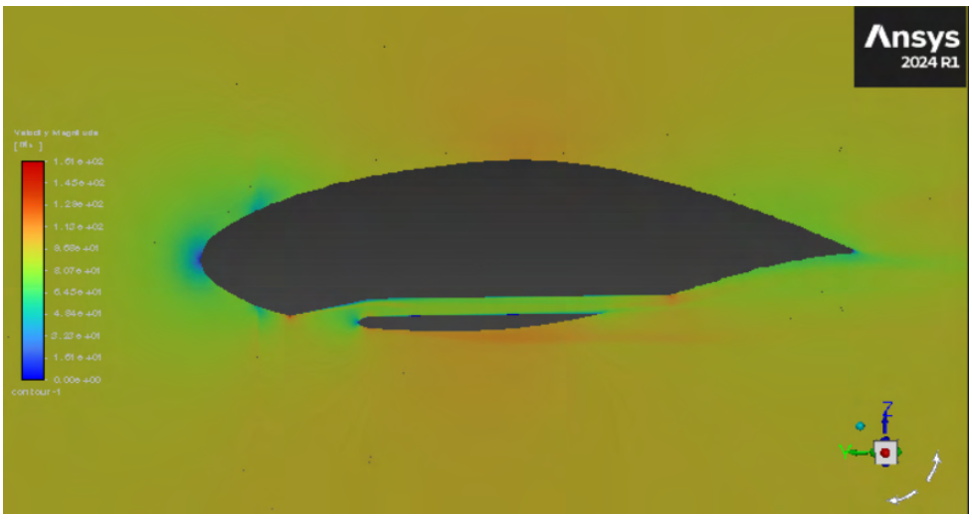

(c) Mesh Number 4

Figure D.5: Velocity magnitude contours along the cross-section of the nacelle.

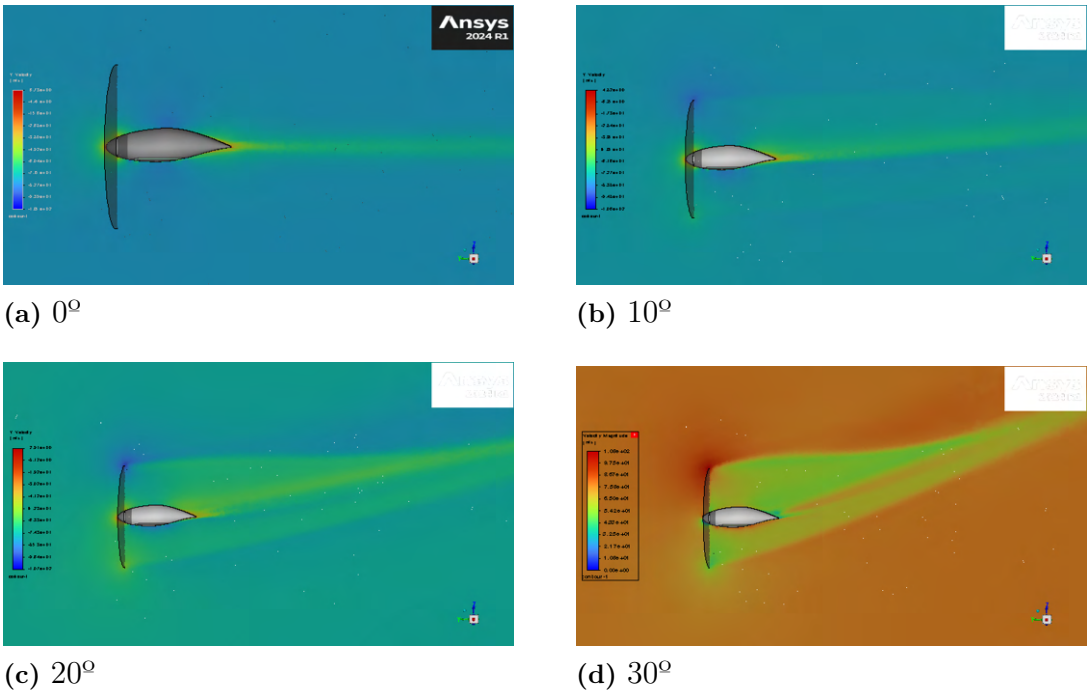

(a) 0º **(b)** 10º

(c) 20º **(d)** 30º

Figure D.6: Velocity magnitude change with AoA.

DEPARTMENT OF MECHANICS AND MARITIME SCIENCES
CHALMERS UNIVERSITY OF TECHNOLOGY
Gothenburg, Sweden
www.chalmers.se

CHALMERS
UNIVERSITY OF TECHNOLOGY